

DISSERTATION IN ASTRONOMY

SUBMITTED TO THE
COMBINED FACULTIES OF THE NATURAL SCIENCES AND MATHEMATICS
OF THE
RUPERTO-CAROLA-UNIVERSITY OF HEIDELBERG
GERMANY

FOR THE DEGREE OF
DOCTOR OF NATURAL SCIENCES

PUT FORWARD BY

ALEX BÜDENBENDER, M.Sc.
BORN IN KÖLN, GERMANY

ORAL EXAMINATION: 16 JULY 2015

Enlighten the dark in the Milky Way with dynamical models

Alex Büdenbender
Max-Planck-Institut für Astronomie

**Referees: Dr. Glenn van de Ven
Prof. Justin I. Read**

Abstract

Since the first studies of galactic rotation curves we have seen evidence of a dark mass component in the halos of galaxies we can not observe directly. As the motion of astronomical objects are sensitive to the underlying gravitational potential, we can use dynamical models to infer the distribution of dark matter in galaxies including the Milky Way. An accurate determination of the dark matter density in the solar neighbourhood is therefore important for understanding the nature and distribution of dark matter in the universe.

We begin by analysing the coupled motion of G-type dwarf stars in the solar neighbourhood using data from the Sloan Extension for Galactic Understanding and Exploration survey. The coupling is illustrated by the tilt of velocity ellipsoid, which we find to be close to the alignment with the spherical coordinate system and hence pointing to the Galactic centre.

We proceed then by introducing a novel axisymmetric Jeans model that accounts for the tilt of the velocity ellipsoid. We apply it to the sample of G-type dwarf stars and make use of a discrete likelihood method to measure the local dark matter density to be $\rho_{\text{dm}} = (0.013 \pm 0.0015) \text{ M}_{\odot}\text{pc}^{-3}$ and the baryonic surface density to be $\Sigma_{\text{b}} = (52 \pm 3) \text{ M}_{\odot}\text{pc}^{-2}$. If we ignore the coupled motion in the axisymmetric Jeans model, we will underestimate the local dark matter density by at least 33%.

We next measure the dark matter distribution in the Galactic halo by applying our axisymmetric Jeans model to K-giants out to a heliocentric distance of 100 kpc. As the halo contains many substructures affecting the velocity distribution of our K-giants, we develop a model that accounts for the variable velocity distribution of the largest of them, the Sagittarius stream. In this way, we are able to robustly estimate the mass profile of the galaxy of $M(r < 100 \text{ kpc}) = (8.8 \pm 0.7) \cdot 10^{11} \text{ M}_{\odot}$. At the same time, we estimate the virial mass and the mass concentration of the dark halo to be $M_{200} = (12.6 \pm 1.8) \cdot 10^{11} \text{ M}_{\odot}$ and $c_{200} = 15.3 \pm 2.3$.

We conclude that a sensible value for the tilt in dynamical models is as important as the correct characterisation of the tracer density. If we consider our estimated halo mass, we cannot relax the tension on the cosmological small scale problem, in which the number of predicted sub-halos in cosmological simulations differ from the number of observed satellite galaxies of the Milky Way. Furthermore, it is unlikely with a total mass within 200 kpc of $(12.5 \pm 1.2) \cdot 10^{11} \text{ M}_{\odot}$ that the distant satellite galaxy Leo I is bound.

Zusammenfassung

Seit den ersten Arbeiten über Rotationskurven von Galaxien gab es immer mehr Hinweise auf eine dunkle Materiekomponente in den Halos von Galaxien, die wir auf direktem Weg nicht beobachten können. Wir können allerdings mit Hilfe von dynamischen Modellen auf die Verteilung dieser Dunklen Materie in der Milchstraße sowie in anderen Galaxien schließen, weil die Bewegung astronomischer Objekte von Gravitationspotentialen beeinflusst wird - auch von denen der Dunklen Materie. Darum ist eine genaue Bestimmung der Dichte der Dunklen Materie in unserer Sonnenumgebung essentiell, um mehr über ihre Natur und Verteilung im Universum zu erfahren.

Zuerst haben wir die Abhängigkeit der radialen und vertikalen Bahnbewegung anhand von Zwergsternen der Spektralklasse G in der Sonnenumgebung analysiert, wobei wir Daten aus dem Sloan Extension for Galactic Understanding and Exploration Survey verwendet haben. Die Abhängigkeit wird durch den Tilt des Geschwindigkeitsellipsoids veranschaulicht, der nach unseren Ergebnissen fast an dem sphärischen Koordinatensystem ausgerichtet ist bzw. in Richtung Galaxienzentrum zeigt.

Anschließend entwickeln wir ein achsensymmetrisches Jeansmodell, das den Tilt des Geschwindigkeitsellipsoids in der Bahnbewegung der Sterne mitberücksichtigt und wenden es auf die G Zwergsterne an. Mit Hilfe einer diskreten Likelihood Methode gelingt es eine lokale Dunkle Materiedichte von $\rho_{\text{dm}} = (0.013 \pm 0.0015) M_{\odot} \text{pc}^{-3}$ und die Oberflächendichte der Baryonen ($\Sigma_{\text{b}} = (52 \pm 3) M_{\odot} \text{pc}^{-2}$) zu bestimmen. Würden wir die Abhängigkeit der Bahnbewegung in den achsensymmetrischen Jeansmodellen ignorieren, würden wir die tatsächliche Dichte der Dunklen Materie um mindestens 33% unterschätzen.

Als Nächstes untersuchen wir die Verteilung der Dunklen Materie im galaktischen Halo, indem wir unser achsensymmetrisches Jeansmodell auf Riesen der Spektralklasse K anwenden, die sich auf bis zu 100 kpc vom galaktischen Zentrum entfernt erstrecken. Der Halo enthält viele Substrukturen, wie vom Gravitationspotential der Milchstraße eingefangene und zerrissene Zwerggalaxien, in denen sich auch einige unserer K Riesensterne befinden. Weil diese die Geschwindigkeitsverteilung unseres Samples modifizieren, haben wir ein Modell entwickelt, das die Geschwindigkeitsverteilung der größten Substruktur, dem Sagittarius Stream, berücksichtigt. Damit können wir dann zuverlässig das Massenprofil der Galaxie mit $M(r < 100 \text{ kpc}) = (8.8 \pm 0.7) \cdot 10^{11} M_{\odot}$ bestimmen. Dabei ergibt sich die Virialmasse zu $M_{200} = (12.6 \pm 1.8) \cdot 10^{11} M_{\odot}$ und ein dazugehöriger Massenkonzentrationskoeffizient von $c_{200} = 15.3 \pm 2.3$.

Aus unserer Arbeit geht hervor, dass ein sinnvoller Wert für den Tilt in dynamischen Modellen genauso wichtig ist wie die richtige Charakterisierung der Dichteverteilung der Tracerobjekte. Desweiteren können wir unter Berücksichtigung der Halomasse die Diskrepanz zwischen der von kosmologischen Simulationen vorhergesagten Anzahl kleinerer Halos und der bisher beobachteten Anzahl, die in den Halo der Milchstraße eingebettet sind, nicht verringern. Außerdem scheint es aufgrund der Masse der Milchstraße von nur $(12.5 \pm 1.2) \cdot 10^{11} M_{\odot}$ innerhalb von 200 kpc unwahrscheinlich, dass die weit entfernte Satellitengalaxie Leo I an die Milchstraße gebunden ist.

CONTENTS

1	INTRODUCTION	1
1.1	DARK MATTER	2
1.1.1	EVIDENCE ON THE GALACTIC SCALE	2
1.1.2	DARK MATTER ON COSMOLOGICAL SCALES	5
1.1.3	THE DARK MATTER HALO OF THE MILKY WAY	8
1.1.4	NATURE AND DETECTION OF DARK MATTER	9
1.2	THE MILKY WAY	10
1.2.1	BULGE	10
1.2.2	DISK	12
1.2.3	HALO	15
1.3	DYNAMICAL MODELS	16
1.3.1	DISTRIBUTION FUNCTION BASED METHODS	17
1.3.2	ORBIT-BASED METHODS	18
1.3.3	PARTICLE-BASED METHODS	19
1.3.4	MOMENT-BASED METHODS	20
1.4	AIMS AND STRUCTURE OF THE THESIS	22
2	DATA & MODEL	25
2.1	STARS AS TRACERS FOR THE GRAVITATIONAL POTENTIAL	25
2.2	THE SLOAN DIGITAL SKY SURVEY	26

2.2.1	<i>SEGUE</i> G-TYPE DWARF STARS	28
2.2.2	THE SELECTION FUNCTION	29
2.3	<i>SEGUE-2</i> K-GIANTS AND THEIR SELECTION CRITERIA	31
2.4	AXISYMMETRIC JEANS MODEL	32
2.4.1	PROLATE SPHEROIDAL COORDINATES	34
2.4.2	PROLATE SPHEROIDAL JEANS EQUATIONS	36
3	THE TILT OF THE VELOCITY ELLIPSOID IN THE MILKY WAY DISK	41
3.1	LOCAL STELLAR KINEMATICS	42
3.1.1	VELOCITY ELLIPSOID IN THE MERIDIONAL PLANE	43
3.1.2	EXTRACTING VELOCITY MOMENTS	43
3.2	VERTICAL JEANS MODEL	46
3.2.1	GRAVITATIONAL POTENTIAL	46
3.2.2	TRACER POPULATIONS	48
3.2.3	VERTICAL VELOCITY DISPERSION	50
3.3	VELOCITY ELLIPSOID TILT	51
3.3.1	VELOCITY ELLIPSOID OF DIFFERENT SUB-SAMPLES	52
3.3.2	TILT ANGLE	52
3.3.3	LITERATURE COMPARISON	56
3.4	DISCUSSION AND CONCLUSION	60
4	THE DARK MATTER DENSITY IN THE SOLAR NEIGHBOURHOOD FROM AXISYMMETRIC JEANS MODELS	65
4.1	SETUP OF THE JEANS MODEL	67
4.1.1	TRACER POPULATION	67
4.1.2	GRAVITATIONAL POTENTIAL	70
4.1.3	VELOCITY DISTRIBUTION	72
4.1.4	ACCELERATED COMPUTATION	73
4.2	LOCAL DARK MATTER DENSITY	75
4.2.1	TRACER DENSITY AND KINEMATICS: SEPARATE VERSUS SIMULTANEOUS FIT	75
4.2.2	PARAMETER RANGES	76
4.2.3	THE VELOCITY ELLIPSOID TILT	81
4.2.4	INFLUENCES OF PARAMETERS	84

4.3	DISCUSSION AND CONCLUSION	85
5	MASS OF THE DARK HALO	89
5.1	EXTRACTING THE LINE-OF-SIGHT VELOCITY DISPERSION	91
5.1.1	SAGITTARIUS MEMBERSHIP PROBABILITY	92
5.2	DYNAMICAL MODEL INGREDIENTS	98
5.2.1	FLATTENED DENSITY PROFILES AND THE GRAVITATIONAL POTENTIAL	100
5.2.2	PROJECTION OF THE VELOCITY DISPERSION TENSOR	103
5.2.3	BREAKING THE DEGENERACY BETWEEN M_{200} AND c_{200}	103
5.3	MILKY WAY'S HALO MASS	104
5.3.1	LINE-OF-SIGHT VELOCITY DISPERSION	104
5.3.2	THE HALO MASS	108
5.4	DISCUSSION AND CONCLUSION	115
6	SUMMARY AND OUTLOOK	121
6.1	TILT OF THE VELOCITY ELLIPSOID	121
6.2	LOCAL DARK MATTER DENSITY	123
6.3	MASS PROFILE OF THE DARK HALO	125
6.4	FUTURE PROSPECTS	127
	ACKNOWLEDGEMENTS	131
	BIBLIOGRAPHY	133
	LIST OF TABLES	143
	LIST OF FIGURES	145

The field of galactic dynamics strives to solve the questions of how galaxies are structured and what are the mechanisms that lead to the build up and evolution of components like the thin and the thick disk, the bulge, the spiral arms within the disk and the stellar halo. The Milky Way is unique for these studies as we are able to observe the three-dimensional position and motion of individual stars together with detailed chemical abundances from their spectra. Thanks to modern Galactic surveys like the Sloan Extension for Galactic Understanding and Exploration (SEGUE, [Yanny et al. 2009](#)) and the RAdial Velocity Experiment ([Kordopatis et al. 2013](#)), which completed their mapping of Milky Way stars in the past decade, it has become possible to push the investigations of the assembly history of the Milky Way and the recovery of the gravitational potential to the next level.

When studying galaxies in general, we primarily want to know how galaxies formed and evolve over time, but we cannot directly *see* the evolution of a galaxy that we observe. Therefore, we need to piece the various evolutionary stages together by observing many galaxies and comparing the gathered information. At the same time, we also want to know how the Milky Way compares to other galaxies. Specifically, is our galaxy like many others or is it in some sense unique? There are two quantities from which we can deduce many relevant properties of a galaxy; these are the chemo-orbital distribution function and the gravitational potential.

The “missing satellites” and “too big to fail” problems are still not fully solved (see [Section 1.1.3](#)), partially because the mass estimates for the dark halo do still not agree and exhibit a large spread in literature ([Wang et al. 2015](#)). The reason for this may be due to one part in the different tracer populations used and to a second part in the various model approaches, where the systematic errors of some of them have not been completely understood yet.

The uncertainty in the density profile of the dark halo affects the direct and indirect searches for dark matter as well. From these searches, we hope to gain more insights into the nature of dark matter, which are believed to be some kind of exotic particles not belonging to the standard

model of particles (Feng 2010). Stellar remnants, planets and very faint stars, which cannot be detected yet, could in principle also count toward the dark matter. However, their total mass cannot account for the additional mass that is needed to explain galactic rotation curves or the unexpected large velocities of galaxies within clusters.

Most importantly, knowledge of the potential allows us to determine the distribution of dark matter, which is our best connection to cosmology. Helping us to understand the evolution of galaxies, are *ab initio* simulations of galaxy formation - most of which include both dark matter and the complex hydrodynamical interactions of baryonic matter. Ten years ago, it was still a problem to create Milky Way-like galaxies with a thickened disk and a small bulge. The disks were too small and the bulges too large and roundish as it is the case for classical bulges. Galaxy simulations have only been able to reproduce a Milky Way-like galaxy in the last years (e.g. Agertz et al. 2011; Martig et al. 2012). One important ingredient, missing in former simulations, has turned out to be radiative feedback, which weakens the cooling of gas and suppresses star formation (Nath & Silk 2009). Unlike observations, N-body simulations have the big advantage that they return full information in every time step. But the way how to test the impact of the ingredients of formation models, such as the diverse feedback mechanisms, on observational data is still subject of debate. Nonetheless, it is clear that the gravitational potential will play an essential role in this comparison.

The gravitational potential is also necessary for the calculation of orbital parameters, like eccentricity, angular momentum or energy of the orbit. Orbital parameters in combination with chemical information have shown to be useful in the identification of fossil remnants (Minchev et al. 2014). These are stars having their origin in former satellite galaxies that merged with the Milky Way. Figure 1.1 illustrates the separation of different stellar groups in the halo with most of them originating from satellites. We can reconstruct the formation of the Milky Way and in particular of the stellar halo with the help of these remnants. Orbital parameters and chemical abundances of stars are also used to disentangle radial migration from other processes, which could have created the thick disk (Liu & van de Ven 2012). This helps to better understand the process of radial migration and the strength of its influence on disk heating.

1.1 DARK MATTER

1.1.1 EVIDENCE ON THE GALACTIC SCALE

The need for dark matter became inevitable when Zwicky (1937) studied the masses of galaxy clusters. He measured the velocity of galaxies within a cluster and estimated the total mass of the cluster from the virial theorem. Then he compared this mass to the summed mass of the galaxies, which he estimated from the integrated light of the cluster and the number of galaxies. The two

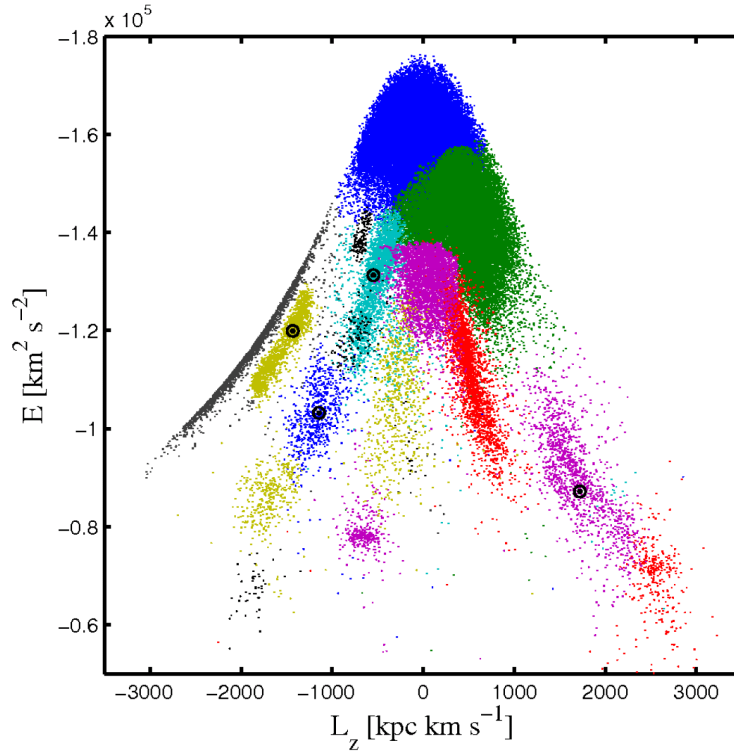


Figure 1.1: Orbital energy versus angular momentum of simulated particles in the halo as observed by Gaia (Gómez et al. 2010). The particles originate from satellites each indicated by different colours that got disrupted in a Milky Way-like halo. Without additional information like chemical abundances to colour observed stars, only very few satellites can be distinguished.

mass estimates differed by two orders of magnitude. The galaxies were moving too fast in the cluster suggesting that the cluster could not be bound by the luminous mass only. This was one of the first indications of the existence of a massive, non-luminous mass-component.

Subsequently, measurements of Galactic rotation curves show that stars in the outskirts of a spiral galaxy rotate with roughly the same velocity around the Galactic centre, giving rise to a flat rotation curve (Rubin & Ford 1970; Bosma 1981). From Newtonian dynamics one would expect a declining rotation curve, as is the case for the stellar disk component in Figure 1.2. The observed rotation curves can be explained if the galaxy resides in a large and massive dark matter halo, which provides the additional gravitational force to sustain the large circular velocity of the stars. The analysis of the rotation curve or the velocity dispersion of tracer populations requires an assumption of dynamical equilibrium and other model dependent assumptions.

The Phenomenon of gravitational lensing provides a useful technique to infer the mass of a dark halo with only a few assumptions. The gravitational field of a highly concentrated mass acts like a lens and deflects the light of a background source. The deflection angle depends on the strength of the gravitational field. As such, galaxy clusters and dense cores in massive galaxies

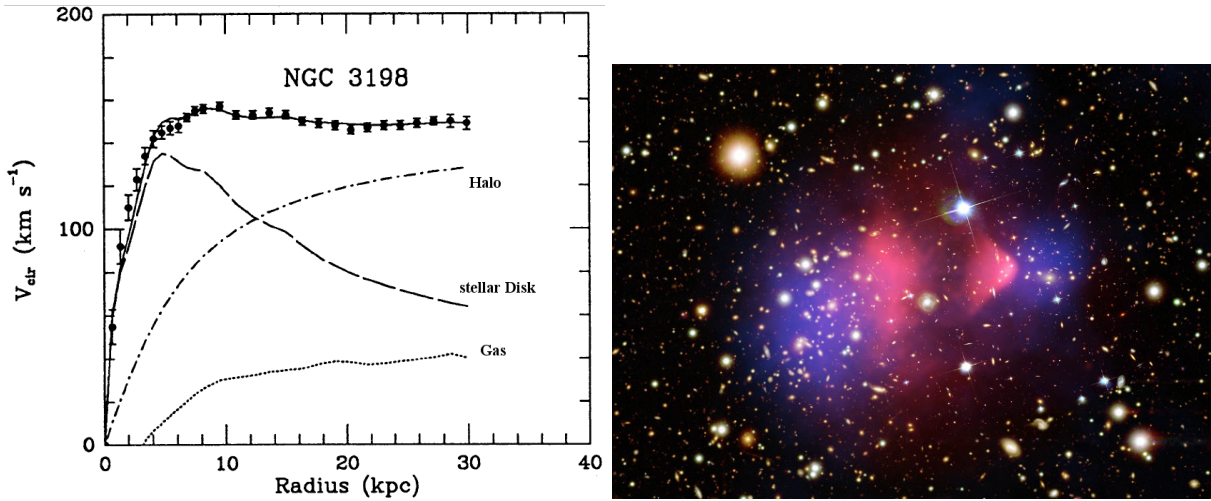


Figure 1.2: *Left:* Generic rotation curve of a spiral galaxy measured from the 21cm line of neutral hydrogen. The total rotation curve (solid line) has contributions from gas, the stellar disk and the dark halo (Begeman et al. 1991). *Right:* The Bullet Cluster, a collision between two galaxy clusters; The gas (red) is shock heated and lags behind the dark matter (violet), whose distribution is reconstructed by strong lensing. (Markevitch et al. 2002)

can focus the light rays of the background source, so that we can observe multiple images of the same source. These images are distorted into stretched arcs, that are either magnified or demagnified depending on the path the light takes around the lensing object. This kind of lensing is called strong lensing and the mass of the lensing object is estimated from the deflection angle of the images and the magnification factor, but strong lensing can only provide the mass within the Einstein radius of the lens system. Furthermore, it is hard to disentangle the luminous and dark mass of the galaxy or cluster from gravitational lensing. Kinematical information used with a dynamical model can help to separate the two components (van de Ven et al. 2010).

One of the strongest pieces of evidence for dark matter is found in cluster mergers. The most prominent one is the Bullet Cluster (Figure 1.2, right panel) consisting of two clusters that collided with a speed of 4700 km/s about 150 million years ago (Koda et al. 2008). Galaxy clusters contain a large amount of gas between the individual galaxies. The gas particles of both clusters interact and transform kinetic into thermal energy through electromagnetic forces during the collision. This causes the gas in both clusters to slow down. Strong lensing reveals that the large majority of the mass resides far away from the X-ray gas, whereas the X-ray gas is concurrent with the majority of luminous matter. The dark matter must have maintained its velocity, as it is not subjected to electromagnetic interactions. Thus, the observed offset can be explained (Paraficz et al. 2012).

Strong lensing is quite rare in the line-of-sights towards us. If the light passes a galaxy only through the outer halo or far away from a cluster, we call this weak lensing. The deflection is

orders of magnitude smaller and it does also not generate multiple images. The luminosity of the background galaxy increases only slightly and the deflection shears the shape a little. But it is almost impossible to measure these effects on individual galaxies.

Galaxies have already intrinsically a variety of different shapes and the inclination angle is also an unknown factor. Therefore, the weak lensing signal can only be measured from an ensemble of adjacent¹ lensed background galaxies, for which the average shear is determined. The shear pattern of a field of galaxies around the lens object is then proportional to the second derivative of the potential, which indirectly results in the mass. With weak lensing, it is possible to measure the dark matter distribution further away from a galactic centre than is possible with kinematic measurements or strong lensing [Gavazzi et al. \(2007\)](#).

1.1.2 DARK MATTER ON COSMOLOGICAL SCALES

Λ Cold Dark Matter (Λ CDM) is the cosmological standard model. It describes the evolution of a universe with only a few parameters and whose matter content is dominated by cold² dark matter and is driven by a progressive expansion of the universe caused by a yet unknown form of dark energy. Measurements of the Cosmic Microwave Background radiation (CMB, [Penzias & Wilson 1965](#); [Dicke et al. 1965](#)) have shown that dark energy clearly dominates the energy content of the universe. The total density of the universe Ω consists of the density of baryons $\Omega_b = 0.0486 \pm 0.0007$, the density of dark matter $\Omega_{\text{dm}} = 0.26 \pm 0.006$ and the dark energy density $\Omega_\Lambda = 0.6911 \pm 0.0062$ ([Planck Collaboration et al. 2015](#)). If $\Omega = 1$, then Ω_b , Ω_{dm} and Ω_Λ can be interpreted as fractions of the critical density and the universe is flat. Non-baryonic (dark) matter makes up about 85% of the total matter in the Universe and only 15% is made of baryonic matter. The cosmological parameters are highly correlated when only one method is used to measure them. For this reason, tight constraints can only be achieved if different methods complement each other.

The distribution of dark matter that formed the cosmic web was already imprinted in space before the recombination of baryons. Quantum fluctuations in the energy density of the primordial plasma created microscopic regions of slightly larger density. The rapid phase of inflation ([Guth 1981](#)) extended these regions. When the fluctuations are Fourier transformed into plane waves, a wave-mode is assigned to each fluctuation. The dark matter particles rested within these overdensities because of their cold nature and attracted additional baryons. The baryons contracted due to the increasing gravitational force until radiation pressure exceeded gravity and forced the baryons to expand again, sending a sound wave into the surrounding medium. This is the baryonic acoustic oscillation (BAO), as the baryons oscillate in the potential wells of the

¹Adjacent in the sense, that the images of these galaxies are closely located on the sky

²The velocity dispersion of the dark matter particles is small.

dark matter. The wave-modes of the fluctuations determine if these oscillations happen more than once before they stop at the time of recombination.

The distance a sound wave can travel in the plasma is called the sound horizon³, and there should be a sphere of small overdensity at this distance. The overall density fluctuations grew under the influence of gravity to today's large-scale structure, while the universe was expanding (Springel et al. 2006). So the sound horizon stretched as well to 150 Mpc distance scale. Eisenstein et al. (2005) were the first to discover these overdense shells in a large sample of galaxies in SDSS with the complication that there was not just one density fluctuation that emitted such a sound wave. The sound waves superimposed and smoothed these shells at large scales. But the overdensity is still measurable on small scales. They were also able to measure the mean density $\Omega_m = \Omega_b + \Omega_{\text{dm}}$ of matter in the universe, which provides a sensible constraint on Ω_{dm} . Recent galaxy surveys like the Baryon Oscillation Spectroscopic Survey (Dawson et al. 2013) as part of SDSS-III, designed to measure the BAO signal, are also able to determine the distance-redshift relation as a measure of the expansion of the universe to a precision of 1% (Anderson et al. 2014).

The density fluctuations grew after recombination to the large-scale structure in a non-linear regime, so that large cosmological N-body simulations are required to predict their appearance today. Springel et al. (2005) were the first to accurately visualise the structure formation within their cosmological ‘‘Millennium’’ simulation, where they used $\approx 10^{10}$ dark matter particles in a cubic box of $500h^{-1}$ Mpc⁴ side length. The comparison with the structure clustering in the 2dF Galaxy Redshift Survey (Norberg et al. 2002) and in the Sloan Digital Sky Survey (Zehavi et al. 2002) confirmed the predicted structure formation of the Λ CDM model.

When light of very distant galaxies travels towards us, it passes through several structures of predominantly dark matter. The light is weakly lensed in all of these dark matter halos, whereby it is possible to reconstruct the large-scale structure with an analysis of the weak lensing signal (Massey et al. 2007). The so quantified clustering agrees with the Millennium simulation as well. In addition, it is possible to estimate Ω_m from weak lensing (Mandelbaum et al. 2013), though with a large scatter.

The Lyman- α forest provides another validation for the large-scale structure formation in the Λ CDM model. Quasars are one of the most distant galaxies. Their emitted light has to travel through large amounts of intergalactic gas, whose distribution varies along the line-of-sight to the quasar. At wavelengths shorter than the Lyman- α line, one can find many absorption lines lying close together that have their origin in the absorption by neutral hydrogen in the intergalactic medium. The gas follows the potential wells of the dark matter and is hence distributed in the filaments of the cosmic web. Thus, the large-scale structure can be extracted from the Lyman- α forest in the quasar spectra by comparing the spectra with predictions of hydrodynamical

³sometimes also acoustic scale

⁴h is the Hubble constant H_0 in units of $100 \text{ km s}^{-1} \text{ Mpc}^{-1}$

simulations, which simulate the distribution of gas along the filaments based on a cosmological simulation (Borde et al. 2014).

However, the CMB provides the best constraints on the cosmological parameters except of Ω_Λ . The CMB radiation emerged from the baryonic acoustic oscillations at early times. The anisotropy map of the CMB in the left panel of Figure 1.3 reflects the temperature fluctuations in the plasma right before photons and baryons decoupled. The last process of oscillation is still imprinted in the photons. By transforming the temperature fluctuations into a power spectrum, we can compare it to models with and without dark matter and those with dark matter are strongly preferred. The power spectrum in the right panel of Figure 1.3 contains the latest Planck results (Planck Collaboration et al. 2015), from which we can infer the curvature Ω_K of the universe, Ω_b and Ω_{dm} amongst others.

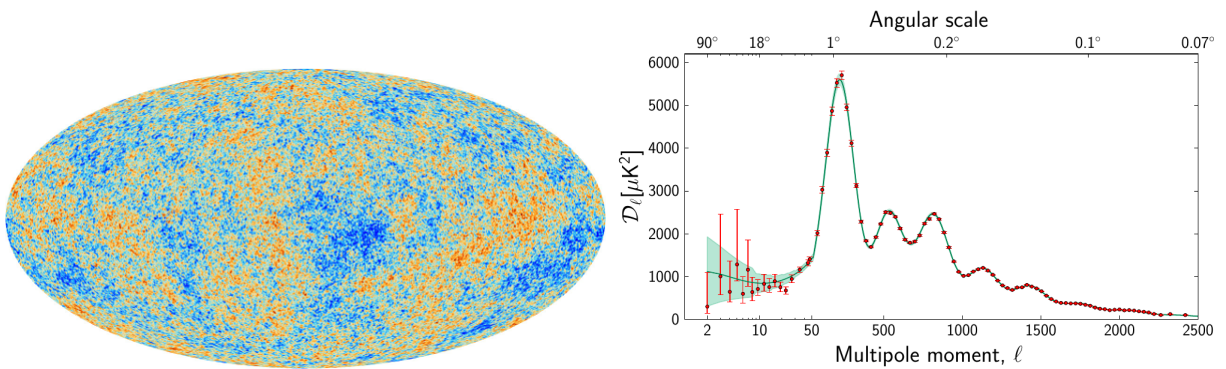


Figure 1.3: *Left:* Anisotropy map of the CMB observed by Planck (Planck Collaboration et al. 2011). The colour code represents microscopic temperature fluctuations corresponding to regions of slightly different mass densities, which had already imprinted the large scale structures of the cosmic web and the empty voids of today’s universe. *Right:* Planck CMB temperature angular power spectrum (Planck Collaboration et al. 2014). The first three peaks are sensitive to the curvature of the universe, the baryonic density and the dark matter density.

The location of the first peak in the power spectrum is a measure of the curvature of the universe, although the location is slightly degenerate with the baryon density. The baryon density Ω_b mainly influences the amplitude of the odd in comparison to the even peaks, but at the same time the peaks shift a little to higher multipoles.

The amplitude of the third peak in comparison to the second peak indirectly measures the dark matter density, as it actually measures the non-relativistic matter density. In combination with the baryon density, one can deduce the density of dark matter. The constraint on Ω_Λ from the CMB power spectrum is only loose, so that other methods are needed, like from BAO measurements and from distant Supernovae type-Ia.

Type-Ia supernovae type-Ia (SN-Ia) are powerful probes of the expansion of the universe. We use type-Ia instead of type-II supernovae, since SN-Ia are brighter and thus also visible at

redshifts beyond 1. Supernovae of the same type are appreciated as “standard candles”, because almost all of them have the unique absolute brightness at the peak. The expansion is inferred from a fit of the Λ CDM model to the Hubble diagram. This diagram displays the relative brightness and the redshift of the supernovae. The brightness can be regarded as a measure of time due to their unique absolute brightness. The fainter a Supernova appears, the farther away it is and hence the further back in time it happened. In addition, one can also estimate Ω_m and Ω_K , though Ω_K is least constraint. The SN-Ia measurements together with the BAO measurements give the best constraints on Ω_Λ (Perlmutter et al. 1999; Betoule et al. 2014).

In conclusion, we cannot directly measure Ω_{dm} , but if we know the total matter density Ω_m and the density of all baryons Ω_b , we can simply calculate it. Weak lensing, CMB, BAO and Supernovae measurements provide good constraints on Ω_m and the CMB can precisely measure Ω_b . Since $\Omega_m \neq \Omega_b$ and the baryonic matter constitutes only a small portion of the total matter, the preponderant part must be non-baryonic dark matter consisting of some non-standard particles. The Λ CDM theory succeeds on these independent tests on large scales and shows excellent agreement with observations. This demonstrates that we are on the right path with our theory of cold dark matter. In order to better understand the nature of dark matter we have to study its behaviour on small scales as well. However, predictions of Λ CDM exhibit discrepancies with observations on galactic scales.

1.1.3 THE DARK MATTER HALO OF THE MILKY WAY

Structures in the Λ CDM cosmology forms hierarchically. Small structures formed first in a time, when the universe was still very dense. Hence, their mass is more concentrated. Subsequently, these structures merge to create larger halos like the one around the MW. But some small structures survived and reside in big halos, now. Almost all of them would have been disrupted by the large tidal forces of the bigger halos, if they did not have high mass concentrations (Kauffmann et al. 1993). We know from observations of the Milky Way halo that it is rich in substructures like the remnants of accreted dwarf spheroidal galaxies and stellar streams. In contrast to large massive spiral galaxies, the surviving dwarf galaxies are thought to be dark matter dominated (Burkert 1997), which makes them good test objects of the Λ CDM model.

Klypin et al. (1999) and Moore et al. (1999) highlighted a problem with the CDM theory, which they dubbed the “missing satellites” problem. They estimated from numerical simulations that a halo as big as the Milky Way should host more than 100 satellite galaxies with a luminosity $L > 10^6 L_\odot$. The problem was that we have not observed this many satellites yet. Kauffmann et al. (1993) were the first to encounter this problem and they explained the discrepancy with small sub-halos not being efficient enough in forming stars and retaining gas. Wadepuhl & Springel (2011) argued that cosmic rays could be responsible for the suppression, as they heat the gas in these systems. As the detection limit of the telescopes has advanced in the last years,

many new faint satellites have been discovered (e.g. [Willman et al. 2005](#); [Willman 2010](#); [The DES Collaboration et al. 2015](#); [Koposov et al. 2015](#); [Laevens et al. 2015](#)). But a factor of $\sim 5 - 20$ times as many faint galaxies could remain undetected at present because of incomplete sky coverage, luminosity bias, and surface brightness limits ([Walsh et al. 2009](#); [Bullock et al. 2010](#)). This would solve the problem at the low mass end but not at the high mass end.

The Aquarius simulation ([Springel et al. 2008](#)) predicted that the Milky Way should host around 8 massive satellite galaxies. However, there are actually only three of them: the small and large Magellanic Clouds and the Sagittarius dwarf spheroidal galaxy. Also, [Boylan-Kolchin et al. \(2011\)](#) pointed out that the massive sub-halos in the Aquarius simulation are denser and probably more massive than the most massive satellites around the Milky Way. This issue is referred to as the “too big to fail” problem in literature, which includes the question why the most massive sub-halos as seen in simulations fail to host luminous components. As the number of sub-halos and the size of the largest ones depends on the mass of the host halo, the “missing satellites” and the “too big too fail” problems could be solved if the Milky Way had a mass less than $\approx 10^{12} M_{\odot}$ ([Wang et al. 2012](#)).

1.1.4 NATURE AND DETECTION OF DARK MATTER

Although many independent observations strongly support the existence of dark matter, it is still unclear what its nature is. Particle physicists have suggested a comprehensive collection of candidates ranging from weakly-interacting massive particles (WIMPs) to axions. All of them have in common that they are cold, long-lived, usually collisionless and weakly interacting. The possible ways to detect one of them are either with direct or indirect detection methods.

There are two ways to detect a dark matter candidate directly. For the first one, the candidate has to be able to scatter off standard particles. Very sensitive detectors that are only exposed to low background radiation can then capture a signal from this scatter. The second direct detection method involves a high energy particle collider, where dark matter candidates are produced by particle collisions.

Even when dark matter candidates will not be directly detectable, we should see special signatures of standard particles that are involved in this interaction. The indirect detection requires that dark matter particles decay or annihilate, producing specific X-ray signals. Those signals could be best observed in dwarf spheroidal galaxies, which contain a large fraction of dark matter, so that the X-ray flux from the galaxy itself does not cover these specific X-ray signals.

For a successful detection of dark matter particles, particle physicists need to know the cross-section of the candidate as well as the local dark matter density near the sun or in such dwarf galaxies. Both quantities are required to calculate the expected interaction rate of the candidate

with a standard particle. However, the local dark matter density is strongly degenerate with the ratio of the cross-section to the dark matter particle mass in the interaction rate. Hence, an independent measurement of the local dark matter density is needed to break the degeneracy, which we provide using dynamical models and astronomical data. A more detailed description of the candidates and the possibilities to detect them is given in [Feng \(2010\)](#) and [Strigari \(2013\)](#). In this thesis, we will focus on the determination of the dark matter density from the kinematics and the density distribution of stars in the solar neighbourhood that serve as tracers of the gravitational potential of the Milky Way. We will explain the principle in more detail in [Section 1.3.4](#) and [Section 2.4](#).

1.2 THE MILKY WAY

The gravitational potential in dynamical models is often expressed as a superposition of the individual components of the Milky Way. [Figure 1.4](#) displays a sketch of the galaxy showing various ingredients and components. We will solely focus on the three main components, disk, bulge and halo, as they are the important ones for dynamical models.

Our galaxy has an exponential disk which one might split into a thin and thick disk with different kinematics and density profiles. The latter are described by double exponentials in radius and height regarding the thin disk as well as the thick disk. The centre is dominated by a barred, rotating bulge. Both, disk and bulge are again embedded in a flattened halo with an old, metal-poor stellar population, but strongly dominated by dark matter. Although we know already quite a lot about the properties of these components, their formation scenarios and evolutionary processes are still subjects of ongoing research. We give a short overview of the components in this section.

1.2.1 BULGE

The bulge in the Milky Way as well as in most other later-type galaxies is small and box/peanut-shaped with a more elongated bar-like structure rather than spherically symmetric ([Freeman 2014](#)). The stellar orbits which are responsible for the peanut-shape are X-type orbits. The major axis of the barred bulge is turned with respect to our line-of-sight to the Galactic centre by an angle of about 27 degrees and extends ~ 3 kpc from the centre.

The bulge is made of multiple populations that show a significant α -enhancement. However, [Ness et al. \(2013\)](#) recently found besides two strong α -enhanced populations, also a weakly α -enhanced, very metal-rich population. The stars inside the bulge seem to be mostly older than 9 Gyrs and born at early times of the galaxy. [Zoccali et al. \(2003\)](#) interpreted this as a sign for a classical merger-driven formation scenario, in which the bulge formed rapidly in the early epoch

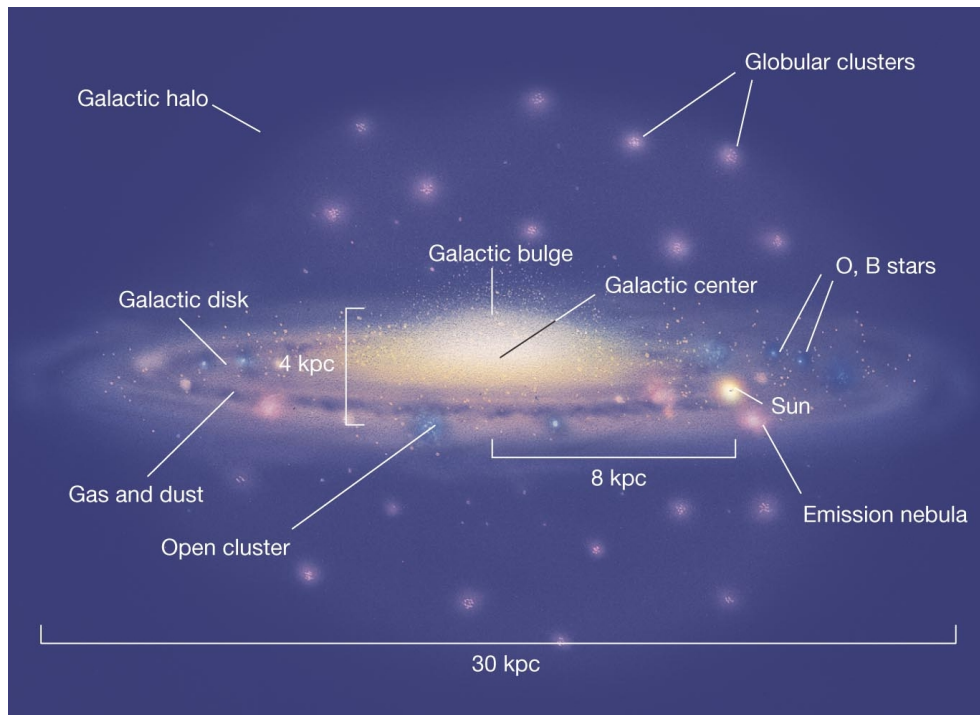


Figure 1.4: A sketch of the galactic structure emphasising the individual components and ingredients of the Milky Way.

of the galaxy. In contrast, [Bensby et al. \(2013\)](#) observed a range of ages for the metal-rich end of the bulge stars using microlensing events. This contradicts the possible merger-driven scenario that requires all bulge stars to be old.

Another controversial signature is the vertical metallicity gradient. [Ness et al. \(2013\)](#) find 5 chemically different populations that are spatially distinct in the vertical direction. They argue that the changing fractions of these populations with vertical height mimics the gradient. The two more metal-rich populations having nearly solar $[\text{Fe}/\text{H}]$ dominate the X-shaped orbits of the bulge stars. [Ness et al. \(2013\)](#) associate them with the early thin disk, while they assign the other three populations to the thick disk and the inner halo with $[\text{Fe}/\text{H}] < -0.5$.

The second favoured formation scenario for the bulge is through secular evolution of a bar. N-Body models show that the bar can form from an unstable, rotating disk within 1 Gyr and afterwards undergo a vertical buckling phase from which the box/peanut-shaped bulge emerges. One necessary condition for the bar to form is a cold disk. Then, disk stars are trapped in the bar at time of formation while increasing their vertical energy to follow the asymmetric bar potential. Thus the disk stars became fossil records of the disk when the bar-buckling occurred. Boxy bulges are believed to be connected to bar-buckling instabilities of disks ([Combes & Sanders 1981](#)).

We have now strong evidence in favour of the disk instability scenario from new observations. [McWilliam & Zoccali \(2010\)](#) observe a bimodal luminosity distribution of red clump stars within a line-of-sight at higher Galactic latitudes, indicating the X-shape of the bulge. The second evidence comes from the density profile, which falls off exponentially along the bar axis ([Wegg & Gerhard 2013](#)). Furthermore, [Kormendy & Illingworth \(1982\)](#) first discovered that the bulge rotates cylindrically, i.e. the mean rotational velocity depends mainly on the radius. This is also directly connected to boxy bulges, as classical bulges do not show cylindrical rotation. N-body simulations of isolated disks are already able to reproduce all of these observational constraints, when the bulge is naturally formed by disk instabilities. [Ness et al. \(2014\)](#) also verifies in their simulation the occurrence of different ages in the bulge.

1.2.2 DISK

The Galactic disk contains a full variety of stars with a large range of ages, masses and chemical abundances. In between, gas and dust is located in a thin layer in the mid-plane of the disk. Dust has a large opacity and obscures light especially in the optical wavelength range. The sun directly sits within this thin layer, which makes it hard to observe the Galactic centre and the regions at the other side of the galaxy. We can bypass this limitation by observing in the infrared and radio domain - two techniques which made possible the discovery of the central supermassive black hole and the outstanding findings of the bulge.

New stars are steadily born within dense gas clouds with a rate of $\approx 1M_{\odot}/\text{yr}$. The largest hatchery of stars are the spiral arms, which therefore harbour the youngest stars. Spiral arms are concentrated regions of atomic and molecular gas, which rotate differentially such that the inner galactic parts rotate with a larger angular velocity than the outer ones. The rotation of spiral disks can be explained by the formation of the galaxy. After dark matter coalesced to build the large, concentrated structures, the deep potential well attracted the baryonic matter, which fell into the dark matter halo following the dark matter filaments. During this infall, the baryonic matter must have had already an angular momentum, which was conserved as the gas settled and collapsed into a thin disk. As of now, it is not clear how many spiral arms the Milky Way has. This is important insofar as the number of spiral arms is a crucial hint towards their mechanism of creation. For now, we believe that the spiral arms have rather a flocculent pattern with 4 arms than a grand design structure. For an extensive review on the creation and the dynamics of spiral arms see [Dobbs & Baba \(2014\)](#).

The outer parts of the disk beyond $R_{gc} = 15$ kpc exhibit a clear warp. On the one side of the disk, there are more stars above $z = 1$ kpc than below and on the other side, there are more stars below $z = -1$ kpc than near the mid-plane. It is obvious that the warp can only have an external origin. Two scenarios seems likely: a merger with debris from a satellite that fell in on a low-latitude, low-eccentric prograde orbit ([Peñarrubia et al. 2005](#)) or the a tidal interaction with

the Large Magellanic Cloud which circled the Milky Way on its vertical orbit with respect to the disk (Momany et al. 2006).

Before 1980 the disk was modelled as a single component with an exponential density profile in radius and height. Subsequently Gilmore & Reid (1983) found that the luminosity function changes its slope beyond $|z| = 1$ kpc. This suggested that the disk may actually consist of a two distinct components, a thin and a thick disk. In the next decades, scientists found more and more evidence not only in star counts, but also in metallicity space (Lee et al. 2011), in kinematics (Chiba & Beers 2000) like the rotational velocity or velocity dispersions and age (Bensby et al. 2004).

Stars of the thin and thick disk are different in many respects. Thick disk stars are “hotter”, which means that their velocity dispersion is larger. Moreover they are more metal-poor and α -enhanced, consistent with thick disk stars being on average older. Roughly 10 million years after the first massive stars formed in the galaxy, these first massive stars exploded in a supernova type II and enriched the interstellar gas with α elements. The stars born thereafter are therefore strongly α -enhanced. The thick disk stars must have formed within the first 1 Gyr after the galaxy had settled in the dark matter potential well and star formation had started, because then supernova type Ia events occurred, which produce large amounts of iron in comparison to α elements. Hence, the $[\alpha/\text{Fe}]$ ratio dropped and the $[\text{Fe}/\text{H}]$ ratio increased, so that stars born thereafter are metal-rich and have only a weak α enhancement. Those stars would correspond to the thin disk.

The velocity dispersion also depends on age. In a picture, in which stars born in a low dispersion gas cloud are in equilibrium, the newly formed stars will take over the small dispersion, but subsequently will increase the dispersion the longer they live. In general, the gas clouds are confined to the meridional plane on low eccentricity. For this reason, thin disk stars show a similar orbital structure, while the orbits of thick disk stars are more eccentric and reach a larger height above the plane.

The responsible processes for the disk heating and the resulting formation of the thick disk are still a topic of debate. Minor mergers could have heated the pristine disk (e.g. Quinn et al. 1993; Villalobos & Helmi 2008). We think that the Milky Way has grown in size by minor mergers and we know that such events are still ongoing. One example is the Sagittarius dwarf galaxy (Purcell et al. 2011; Gómez et al. 2012). Another possibility of this kind could be a gas-rich merger that would thicken the disk and would make it rather clumpy than smooth. Then the old, metal-poor stars, we see in the thick disk today, would be born in a burst of star formation (Brook et al. 2007). It might also be likely that the thick disk stars were born in a turbulent, thickened gaseous disk (Bournaud et al. 2009), which would lead to initially large velocity dispersions. Or they were already born in a satellite galaxy, that was later accreted contributing their stars to the stellar population of the thick disk (Abadi et al. 2003).

Alternatively, internal galactic processes might be responsible, like radial migration. During the latter process, stars scatter at the co-rotation radius of transient spiral arms (Sellwood & Binney 2002) or at the resonances of the bar and spiral arms (Minchev & Famaey 2010). The scattering changes the angular momentum L_z of the orbit or the mean orbital radius respectively, while the orbital random energy is unchanged. Liu & van de Ven (2012) concluded from an analysis of G-type dwarf stars in the solar neighbourhood, that radial migration might have shaped the more metal-rich part of the thick disk, while the old, metal-poor stars probably have their origin in a gas-rich merger in the early phase of the galaxy. The change in angular momentum due to radial migration has additionally a dramatic effect on galactic archaeology, which has amongst others, the goal of finding the birth places of stars in order to recover the formation history of galactic components like the thick disk. The angular momentum can not be used to find the birth radius of a star, because it is simply not conserved due to the scattering. Radial migration does not only have an effect on disk heating but also on the metallicity distribution, making it primarily broader without changing the radial gradient much (Minchev et al. 2013; Grand et al. 2015).

Given all possible mechanisms for disk heating, it is in the end most likely that not only one process is responsible, but a combination of them. It is an important challenge for future studies and galactic surveys to clarify to what extent the individual processes have contributed to the heating of the disk.

In summary, there are three main pieces of observational evidence in favour of a distinct thin and thick disk: The split in vertical scale heights, the split in velocity dispersion and a bimodal distribution in $[\alpha/\text{Fe}]$.

Bovy et al. (2012a) recently put the thin/thick disk concept into question as they showed that the mass-weighted surface density distribution of several sub-populations is a smooth function of the scale height, which would normally show a bimodal distribution in the thin-thick disk picture. They falsified the bimodal distribution in $[\alpha/\text{Fe}]$, when they pointed out that the bimodality will vanish if the distribution is correctly mass-weighted according to the selection function. Without the weighting, the sample showed the known bimodality in $[\alpha/\text{Fe}]$. Next, Bovy et al. (2012c) could characterise the MAPs as single-exponentials in the number density. They falsified the split in scale heights, as their determined scale heights and scale lengths vary smoothly as a function of both $[\alpha/\text{Fe}]$ and $[\text{Fe}/\text{H}]$. So, the scale height varies continuously from the α -old, metal-poor stars, which are radially concentrated and vertically thick, to the α -young, metal-rich stars, which are radially extended and vertically thin. These results also support the hypothesis of an inside-out growth of the disk. Finally, Bovy et al. (2012b) investigated the kinematical structure of the MAPs and found an almost isothermal behaviour of the radial and vertical velocity dispersion in the vertical direction. Similar to the density parameters, they could also show that the dispersions smoothly changes from a higher dispersion in the α -old, metal-poor MAPs to a lower dispersion in the α -young, metal-rich MAPs.

With the release of considerably larger datasets with higher precision that allows to better identify the individual sub-populations of the disk spectroscopically, it seems to crystallise that the disk is in reality a single, albeit complex system, whose sub-populations can not be differentiated by a simple hard cut.

1.2.3 HALO

The stellar halo holds one of the most informative keys to the formation of our galaxy. As an example, fossil records can be used to disentangle the different formation processes. While stars in the disk quickly lose the knowledge of their origin, stars in the halo remember it much longer because of the extended dynamical timescales. Thus, signatures in velocity space are longer preserved and can be used to identify substructures of accreted satellites ([Helmi & White 1999](#)).

If we know how the Milky Way formed, we can draw conclusions for the formation of other spiral galaxies, however different environments will also play a role, with galaxies near large clusters having different encounter rates than galaxies in the field. The Milky Way is unique in the sense that we can resolve individual stars, even spectroscopically, of a large part of the halo. The study of the stellar halo in other galaxies is a much harder challenge, because their halos have a much lower surface brightness and we can only observe the light integrated by several stars or the emission from gas present in the halo.

There are two favoured formation scenarios for the stellar halo, in which the stars are either born in situ in a rapid starburst at early times or, as proposed by [Searle & Zinn \(1978\)](#), slowly accreted from other satellite galaxies. The simulation of [Bullock & Johnston \(2005\)](#) suggests, that about 50-80% of the stellar halo is built up more than 9 Gyrs ago by probably more massive satellites while the time after, the accretion of smaller satellites slowly continues until today. The Sagittarius dwarf galaxy, the progenitor of the Sagittarius stream, was the first still ongoing accretion event to be discovered in the Milky Way halo ([Ibata et al. 1994](#)). Since then, many more substructures of tidally interacting satellites and overdensities have been found, like the Monoceros stream ([Rocha-Pinto et al. 2003](#)), the Virgo Stellar Stream ([Duffau et al. 2006](#)), the Orphan stream ([Belokurov et al. 2007](#)) and the Pisces overdensity ([Watkins et al. 2009](#)).

The Sagittarius stream is by far the largest stream extending 360° around the Milky Way and its orbit can be accurately reconstructed ([Sanders & Binney 2014](#)), from which one can infer the gravitational potential and the shape of the halo. [Helmi \(2004\)](#) found indications for a prolate halo, while [Fellhauer et al. \(2006\)](#) contradicted this result by finding an almost spherical halo. [Smith et al. \(2009\)](#) draw the same conclusion using the measured velocity ellipsoid of halo subdwarfs. They also measured the orientation of the velocity ellipsoid, and found it spherically aligned. Recent studies suggest on the other hand an oblate shaped halo ([Sesar et al. 2011](#); [Vera-Ciro & Helmi 2013](#)).

The density distribution of the stellar halo was characterised as a single power law in early work (Sommer-Larsen 1987; Wetterer & McGraw 1996). However, Carollo et al. (2007) indicated that the halo is split into an inner and an outer component. Their stellar sample, obtained from SDSS, reaches distances up to 4 kpc from the sun and exhibit a break in the spatial density profile with a flatter profile of the inner halo. In addition, the two components have different stellar orbits and metallicities. Stars of the inner halo have mainly high eccentric orbits, while outer halo stars show a broader range of eccentricities. Deason et al. (2011) ascertained the transition between the inner and the outer halo to be around $r_{\text{gc}} = 30 \text{ kpc}$ ⁵. de Jong et al. (2010) measured a mean metallicity of $[\text{Fe}/\text{H}] \sim -1.6$ for the inner and $[\text{Fe}/\text{H}] \sim -2.2$ for the outer halo. The consequential metallicity gradient is then just a result of the changing fractions of inner and outer halo stars when moving outwards in radius. This is supported by the observation that the inner and outer halo stars alone do not exhibit such a gradient (Ivezić et al. 2008; Carollo et al. 2012). The kinematical properties of the halo encounter a dichotomy as well. The velocity dispersion of halo stars drops from $\approx 110 \text{ km/s}$ at $r_{\text{gc}} = 15 \text{ kpc}$ to $\approx 85 \text{ km/s}$ at 80 kpc (Brown et al. 2010) and the outer halo shows a significant net retrograde rotation, whereas the inner halo seems to have no rotation (Carollo et al. 2010).

With larger samples and more accurate distance and proper motion measurements even out to 40 kpc from the upcoming Gaia and Large Synoptic Survey Telescope (LSST, Ivezić et al. 2008) surveys, we should be able to confirm the above discoveries with higher significance and to solve the inconsistent determinations of the halo shape. Furthermore, we might finally answer the question of how the halo formed by determining the fraction of accreted versus in situ born stars. On the basis of our current knowledge, it is very likely that the outer halo was formed through merged satellites only and the inner halo is composed of some accreted stars and stars born in situ.

1.3 DYNAMICAL MODELS

When estimating the potential of a simulated N-body galaxy we can simply add the point-mass potential of all particles. In a real galaxy, most of the baryonic mass resides in stars. But adding the point-mass potentials of all stars is not feasible, because there are $\approx 10^{11}$ of them and dust extinction and brightness limits of the telescopes prevent us from seeing all of them. Instead, it is sufficient to follow tracers in a smooth potential and match the density distribution and kinematics of the tracers.

In this section we present a brief overview of the available methods in literature to recover the potential from phase-space information of individual stars. We will especially emphasise the Jeans model, since it is the model of choice in this dissertation.

⁵ r_{gc} is the distance from the galactic centre

1.3.1 DISTRIBUTION FUNCTION BASED METHODS

The collisionless Boltzmann equation is a fundamental equation in stellar dynamics, describing the motion of stars in a stellar system.

$$\frac{\partial f}{\partial t} + \vec{v} \cdot \nabla f - \nabla \Phi \cdot \frac{\partial f}{\partial \vec{v}} = 0 \quad (1.1)$$

The equation assumes that the stars do not collide with each other. The assumption is clearly valid for galaxies, because the relaxation time⁶ is longer than the age of the galaxy. This might only become problematic in a very dense system like a (nuclear) star cluster.

When looking at the gravitational forces acting on a single star, it becomes obvious that the major contribution comes from the many distant stars. Gravity is a long range force, which is why the few nearby stars does not carry as much weight. For this reason we can neglect local fluctuations of the potential caused by nearby stars and assume steady state equilibrium to solve the collisionless Boltzmann equation. The solution results in the distribution function (DF) which provides the probability to find a star in the spatial interval $(\vec{x}, \vec{x}+d^3x)$ with velocities $(\vec{v}, \vec{v}+d^3v)$, i.e. a 6-dimensional phase-space. The Jeans' theorem proves that any combination of isolating integrals of motion solves the collisionless Boltzmann equation. In general, the energy $E = (v_R^2 + v_\phi^2 + v_z^2)/2 + \Phi(R, z)$ and angular momentum belong to the integrals of motion and are called classical integrals. The symmetry of a stellar system dictates the type of integrals of motion. A spherical system has four integrals of motion, the energy and the angular momentum vector; an axisymmetric system has three integrals of motion, the energy, the angular momentum $L_z = Rv_\phi$ parallel to the symmetry z -axis and a third yet unknown integral I_3 ; a triaxial system has three integrals of motions as well, but of them only the energy is known. The other two I_2 and I_3 are non-classical integrals, just as the third one in the axisymmetric system.

Several observable quantities can be computed directly from the DF including the density at position \vec{x} , the mean velocity of stars and the velocity dispersion. With that, the model in terms of the DF can be fitted to these quantities to find the underlying DF. However, this approach is not contemporary in Milky Way dynamics anymore, since discrete data of individual stars have become easily accessible. Instead, the parameters of the DF and the gravitational potential are optimized in a maximum likelihood approach, in which $\mathcal{L}(f(\vec{x}, \vec{v})|\Phi(\vec{x}))$ the likelihood of the DF given the potential is maximised. Then the position and velocities of the individual stars are directly used as input for the model. While an analytic solution to the collisionless Boltzmann equation in spherical systems can be expressed through the classical integrals of motion, the orbits in axisymmetric systems admit a third non-classical integral, which does not have an analytic expression. The only case in which the orbits in such a system can be described

⁶The relaxation time specifies the time in which multiple encounters have changed the star's orbit significantly. The orbital energy and angular momentum changes in this case as well. So the integrals of motion would not be conserved.

with E and L_z only, is when the velocity is isotropic in the radial and vertical direction, i.e. $\overline{v_R^2} = \overline{v_z^2}$.

Fortunately, there is a way out of this dilemma. Actions are integrals of motion as well and in action-angle space, the three integrals of motions are known. The actions portray the strength of oscillations that a star can do in a specific direction. They have various advantages as opposed to the classical integrals:

- (i) Due to the fact that the actions together with the angle coordinates form a complete set of canonical coordinates, the orbits in action-angle space are extremely simple (McMillan & Binney 2008);
- (ii) Orbits in action space occupy a volume of $(2\pi)^3 d^3 J$, independent of the potential. For this reason, the density of stars only depends on the distribution function, $(2\pi)^3 N f(\vec{\theta}, \vec{J})$;
- (iii) Actions are adiabatic invariants, that is even if the orbit changes due to a slow change of the potential, the actions remains the same.

The drawbacks are that the mathematical form of the DF has to be known a priori and there is a complicated and computationally expensive coordinate transformation $(\vec{\theta}, \vec{J}) \leftrightarrow (\vec{x}, \vec{v})$ involved, in order to compare the model with the data. This transformation depends on the potential and to make it worse, it is only analytic for a small set of potentials. In the last years, some techniques were developed to improve on this (McMillan & Binney 2008; Binney 2010; Binney & McMillan 2011; Sanders 2012). Among them is for example a numerical approximation of an arbitrary axisymmetric potential with Stäckel potentials (Binney 2012). Until now, only axisymmetric potentials can be used with action-based distribution functions.

1.3.2 ORBIT-BASED METHODS

Schwarzschild (1979) introduced a method that sidesteps the ignorance about the non-classical integrals of motion. The integrals of motion cover a hypersurface in phase space such that the energy, for instance, is everywhere the same on this hypersurface and stars only orbit on this surface. Hence, a large enough number of orbits would be able to trace the DF.

Schwarzschild's idea was to construct a library of different orbits computed in an arbitrary gravitational potential and find the weight to each orbit that best reproduces all available data at the same time. The orbit library should contain all possible orbits that the given potential can generate. Subsequently, the potential is adjusted in an iterative process to find the best match to the data. The weights can be regarded as the number of stars occupying each orbit.

The method was originally designed to reconstruct the observed light distribution of external galaxies. In order to have sufficient signal-to-noise, the galaxy is separated into cells and the light of each pixel⁷ within a cell is added. The orbit-model is therefore implemented such that

⁷The pixels on the detector unit of a telescope.

it reproduces the integrated light in every cell. However, it is rarely used in combination with discrete tracers to fit the positions and velocities of individual stars in the bulge or disk directly due to a lack of working implementations. So far, solely [Chanamé et al. \(2008\)](#) has implemented a working discrete Schwarzschild code.

A big advantage of this method is that neither the DF nor any information on the integrals of motion is required. The DF can be deduced from the weights of the orbits with only a few assumptions. It assumes steady state and a specific symmetry. All kinds of symmetries are supported, even triaxiality ([van den Bosch et al. 2008](#)) and assumptions on the anisotropy or the coupling of motions are not necessary. Nevertheless, Schwarzschild modelling is computationally expensive since every time a new potential is tried, the orbit library needs to be recomputed. A few orbits do not suffice, because the orbits should sample well the phase space.

[McMillan & Binney \(2008\)](#) has developed another orbit based method, called torus modelling. The main difference between the Schwarzschild model and this method is the way orbits are treated. The torus model transfers the orbits in action-angle space, whereas the orbits are time series of phase space points in the Schwarzschild model. The name torus model is motivated by the toroidal object the orbit forms in phase space while moving in action-angle space. The reader is referred to [Binney & McMillan \(2011\)](#) for a detailed comparison of the two methods.

1.3.3 PARTICLE-BASED METHODS

Inspired by N-body simulations, the made-to-measure method (M2M) ([Syer & Tremaine 1996](#)) introduces a technique to modify a N-body model so that it recovers the structure and gravitational potential of a real galaxy. An existing N-body simulation provides the starting point, which has already created a galaxy morphologically similar to the target galaxy. It works by assigning a weight to each particle and adjusting the weights to match the density and kinematics, while the particles move on orbits in a self-consistent gravitational potential.

The original M2M method was only capable of using photometry to match the density profile of the target galaxy. The NMAGIC code ([de Lorenzi et al. 2007](#); [Morganti & Gerhard 2012](#)) has included the ability to treat observational errors and it was the first using constraints on the line-of-sight velocity. But it was designed to applying on external galaxies, not able to handle discrete Milky Way data. The development of M2M for the Milky Way has just started. [Bissantz et al. \(2004\)](#) made the first attempt by tuning the original M2M method to analyse the barred bulge of the Milky Way. [Long et al. \(2013\)](#) and [Portail et al. \(2015\)](#) focused on the bulge as well and [Hunt & Kawata \(2013, 2014\)](#) were the first to apply the M2M method to N-body simulated disk stars as they would be observed with Gaia.

The M2M method consumes less memory than Schwarzschild's method, because it does not need to store the full orbits of the particles. On the other side, it has to follow the orbit of a particle for a longer time to reach a comparable accuracy, so that the M2M method is even more computationally expensive than the Schwarzschild method.

1.3.4 MOMENT-BASED METHODS

The moment-based method avoids the trouble with the distribution functions. The method is based on the Jeans equations, which are derived from the collisionless Boltzmann equation. The collisionless Boltzmann equation in cylindrical coordinates is given by.

$$\frac{\partial f}{\partial t} + v_R \frac{\partial f}{\partial R} + \frac{v_\phi}{R} \frac{\partial f}{\partial \phi} + v_z \frac{\partial f}{\partial z} + \left(\frac{v_\phi^2}{R} - \frac{\partial \Phi}{\partial R} \right) \frac{\partial f}{\partial v_R} - \frac{1}{R} \left(v_R v_\phi + \frac{\partial \Phi}{\partial \phi} \right) \frac{\partial f}{\partial v_\phi} - \frac{\partial \Phi}{\partial z} \frac{\partial f}{\partial v_z} = 0 \quad (1.2)$$

The second moments of this particular collisionless Boltzmann equation are the Jeans equations given in equations 2.7 and 2.8. We outline the Jeans equations in cylindrical coordinates in more detail in Chapter 2.

The Jeans equations have a problem of closure. There are four unknown second order velocity moments $\overline{v_R^2}$, $\overline{v_z^2}$, $\overline{v_\phi^2}$ and $\overline{v_R v_z}$, but only two equations. This means, one has to make assumptions about the velocity anisotropy, or in other words the shape and alignment of the velocity ellipsoid. In only a few cases, it is possible to find a closed solution, e.g. [Binney & Mamon \(1982\)](#) for a solution in a spherical system.

Considering only the second equation 2.8, the one-dimensional vertical Jeans equation 3.11 results from neglecting the first term. In this case, the crossterm $\overline{v_R v_z}$ is assumed to be negligible near the mid-plane of the galactic disk. We will demonstrate in Chapter 3 when this assumption breaks down and the vertical Jeans model yields biased results.

The basic idea behind the Jeans models is that the gravitational potential is deduced given the velocity dispersion and the number density distribution of a stellar tracer population. Poisson's equation relates Φ to the total mass density $\rho_{\text{tot}} = \rho_{\text{lum}} + \rho_{\text{dark}}$:

$$4\pi G \rho_{\text{tot}} = \frac{\partial^2 \Phi}{\partial z^2} + \frac{1}{R} \frac{\partial}{\partial R} \left(R \frac{\partial \Phi}{\partial R} \right), \quad (1.3)$$

where G is Newton's gravitational constant. It is common to spatially bin the data and to compare the velocity dispersion of each bin to the predicted velocity dispersion of the Jeans model. Instead, it is more reasonable to use an approach that is capable of using discrete data to avoid a potential loss of information during the binning process. The discrete modelling approach has also the advantage that outliers and interlopers can be taken into account without making hard cuts. than the majority of the tracers.

Kuijken & Gilmore (1989b) revolutionised the vertical Jeans analysis by adding a correction term to account for the radial dependence of the vertical force and assuming a crossterm $\overline{v_R v_z}$ for which the velocity ellipsoid points to the Galactic centre. This is actually a reasonable assumption as we will show in Chapter 3. The work of Kuijken & Gilmore (1989b,a, 1991) has pointed the way for the last two decades (Fuchs & Flynn 1994; Holmberg & Flynn 2000; Bienaymé et al. 2006; Zhang et al. 2013).

Cappellari’s 2008 JAM models have become very popular in the analysis of external stellar systems (i.a. Watkins et al. 2013; Adams et al. 2014; Nguyen et al. 2014; Posacki et al. 2015). The axisymmetric Jeans equations are solved under the assumption that the velocity ellipsoid is aligned with the cylindrical coordinate system. This may be only a reasonable assumption if stars close to the mid-plane dominate the light-weighted line-of-sight kinematics, where the cross-term $\overline{v_R v_z} \approx 0$ due to the symmetry.

In case of Stäckel potentials the equations of motions are separable in confocal ellipsoidal coordinates (λ, μ, ν) , so that in the general triaxial case there are three Jeans equations and three unknown (diagonal) second order velocity moments. The general solution of these Jeans equations has been derived by van de Ven et al. (2003), who also give the solution in case of oblate axisymmetry. Even though Stäckel models have density distributions that are cored in the centre and hence are unable to describe a possible density cusp in the centre of the Milky Way, they should be able to give a realistic prescription of the mass distribution in the Solar Neighbourhood and beyond. We will derive a new solution of the axisymmetric Jeans equations in the prolate spheroidal coordinate system using characteristics in Section 2.4. The solution will allow for an arbitrary potential, that can include a central cusp.

Jeans models need more assumption than most other dynamical models. To recap, these are assumptions on steady state, symmetry, the coupling of motion and the velocity anisotropy. Moreover, they are not so flexible, which makes it difficult to incorporate the survey selection function or chemical information. One of the more important downsides is that the underlying distribution function cannot not be guaranteed to be non-negative. In the other above presented dynamical models, the final potential is a result of the marginalisation over all possible DFs and one can assure that the DF is always positive.

Despite of this all, Jeans models are frequently applied to external galaxies and globular clusters, because the available data is still limited and the Jeans equations have analytic solutions and are fast to compute in these cases. The vertical Jeans model has mostly been the preferred choice when focusing on the vertical force only, because the model is simple and very fast while seemingly providing a reasonable estimate on the vertical force and density.

With future, even larger and more accurate data sets for the Milky Way, we should move to more sophisticated models, like Schwarzschild’s method. However, the computational effort is much larger. From this perspective, our axisymmetric Jeans model is a real alternative to the more general models. In addition, it is especially good for constraining the parameter space of

the potential before running the more general methods. In this way, the initial potential in the more general models is already close to the true potential and the run time will be noticeably reduced.

1.4 AIMS AND STRUCTURE OF THE THESIS

Experiments designed to detect dark matter particles will only be able to constrain their properties if the dark matter density in the Solar Neighbourhood is accurately known. This requires a precision determination of the local gravitational potential, yielding the total mass density from which the luminous density is subtracted to recover the dark matter density. Stellar populations tracing the potential are inevitable for this task. The selection function of a corresponding survey only affects the density profile of the tracers, but not the velocity distribution. Nevertheless, the selection function plays an important role in the modelling process.

The “vertical” Jeans equation relates the gravitational potential directly to the observable number density and velocity dispersion of stars above the Galactic plane. While straightforward, this approach assumes that the motion in height z and radius R are decoupled. This is a viable assumption for tracers near the mid-plane of the disk. But in order to precisely determine the local dark matter density, we need to break the degeneracy between the baryonic matter in the disk and the dark matter in the halo, which is only possible with tracers well above the mid-plane, where the dark halo starts to dominate. For this reason, the tilt of the velocity ellipsoid cannot be neglected in dynamical models when using these tracers. The dramatic increase in quantity and quality of discrete stellar data over the last few years makes it possible to verify this assumption and go beyond it.

To overcome the limitations of vertical Jeans models, we develop an axisymmetric Jeans model that accounts for the tilt of the velocity ellipsoid and thus we can take advantage of the extended volume in the disk observed by modern surveys like SEGUE. Such a model also provides the opportunity to use tracers in the stellar halo and to estimate the mass of the dark halo, which puts constraints on Milky Way-like galaxies in cosmological simulations and galaxy formation models, especially in combination with the local dark matter density (see also [Section 6.4](#) for considerations on the shape of the local dark halo).

The thesis is organised as follows:

- [Chapter 2](#) presents the SEGUE G-type dwarf sample and explains the selection function of the SEGUE survey, which accounts for the selection biases of the survey and is needed to correctly determine the number density distribution. Moreover, it introduces our axisymmetric Jeans model, for which the Jeans equations are solved in the prolate spheroidal coordinate system. We will then use the model in [Chapters 4](#) and [5](#) to determine the local dark matter density and the mass of the dark halo.

- Chapter 3 quantifies the coupling between the motion in R and z . We have already known for some decades that this coupling exists, but so far its vertical profile has not been properly measured. We start by introducing a technique to extract the axisymmetric second velocity moment tensor from a local sample of G-type dwarf stars from the SEGUE-I survey. Then we describe the vertical Jeans model and show, that it breaks down for tracers 1 kpc above the mid-plane due to the coupled motion in R and z . To investigate whether the latter coupling depends on the age of the stars, we split the sample into seven bins in the measured α -abundance-metallicity space and measure the velocity dispersions and the coupling as a function of height at the solar radius.
- Chapter 4 moves beyond the vertical Jeans model and proposes an axisymmetric Jeans model, which accounts for the coupled motion and the anisotropy between the radial and vertical motion. We present a set of gravitational potentials and the tracer density, which are used in the axisymmetric Jeans model. Then we apply it to the extended G-type dwarf sample to estimate the local dark matter density and the surface density of the disk. At the same time, we investigate the effect of the tilt of the velocity ellipsoid and other parameters that are fixed in the model on the determination of the dark matter density.
- Chapter 5 applies the axisymmetric Jeans model to a sample of K-giants in the Galactic halo to derive a robust measurement of the dark halo mass. For this purpose, we consider different density profiles for the K-giants to check their implication on the dark halo mass estimate. The density distribution of tracers can introduce the a large biases in dynamical models. Besides, the sample contains a non-negligible fraction of stars from substructures, which can bias the mass estimate as well. Since the Sagittarius stream is the largest of them, we suggest a method to identify those stars and properly account for them in the model process without the need to remove them from the sample. Subsequently, we demonstrate the reliability of the method by comparing the results to a sample of definitely identified members of Sagittarius from the literature.
- Chapter 6 gives a summary of the work and also draws attention to the next steps in dynamical modelling.

2.1 STARS AS TRACERS FOR THE GRAVITATIONAL POTENTIAL

We cannot see dark matter as we can see stars and gas clouds. It does not emit or reflect light. We only know that dark matter interacts gravitationally with baryonic matter, which we can actually see. The only chance we have to find out more about its distribution in and around galaxies is to observe the way it influences the motion of the baryonic matter. As all objects in a galaxy have to follow the same gravitational field, we can use stars as tracers for the gravitational potential.

Eligible stars should be bright, so that we can even observe them on large distances, and they should be common as well as dynamically relaxed. The attribute “common” assures that the stars are not only present in the centre of the galaxy or near the mid-plane, but instead spread over the entire galaxy. Beside the dispersal, the number of stars in a sample matters for the statistics in dynamical models. The attribute “dynamically relaxed” assures that the stars have lived long enough to complete ample orbits in order to validate the assumption of dynamical equilibrium in the models.

G and K type dwarfs and giants, Blue Horizontal Branch (BHB) and variable stars like RR Lyrae belong to those stars that fulfil these requirements. Giants, BHBs and variable stars are sufficiently present in the halo and are therefore well suited to trace the dark matter halo. Variable stars have the advantage that absolute magnitudes are accurately measurable, thus enabling reliable distance estimates. G- and K-dwarfs are very frequent in the disk and therefore best suited for disk studies, but likewise can be used to estimate the local dark matter density, for which G-dwarfs are more eligible as they reach larger heights above the mid-plane. The dark matter fraction is higher there, so that the degeneracy between the disk and the halo in dynamical models is reduced. Although stars are the most commonly used tracers in the Milky Way, gas, stellar streams in the halo, dwarf galaxies and globular clusters are used as well.

To determine the gravitational potential it would be simplest to directly measure the accelerations, because they are linearly related to the gradient of the potential. However, we can only see a snapshot of the galaxy which is expressed by the current position of the stars. For spectroscopically observed stars we can measure the line-of-sight velocity from Doppler-shifts of their spectra. If stars are close enough we can detect a change of position after several years from which we deduce the proper motion. This gives us then in combination with the line-of-sight velocity and distance the full three dimensional velocity. But we cannot directly measure the accelerations of stars. Instead, we have to infer it from dynamical modelling.

Tracer objects constitute in this way an essential part in the determination of the potential. However, there is not a unique potential describing the stellar motions. Several different potentials can be fitted equally well to the data. In order to compare studies done with different potentials qualitatively, they are often described by properties of the Galactic components, like the surface density, mass, circular velocity, local dark matter density or scale height and scale length. The latter, though, depends on the form of potential again.

In the 1990s, the HIPPARCOS survey (Perryman et al. 1997) was a milestone in the determination of precise parallaxes, although the data have only contained nearby stars within a 100 pc sphere around the sun's position. SEGUE and RAVE recently pushed the available data to a more spatially extended sample covering large parts of the local disk and a large volume in the stellar halo. Moreover, Gaia, started in 2014, is gathering data for 1 billion stars with yet unreached precision on photometric parallaxes. This will allow for an unprecedented investigation of the Milky Way's internal dynamics.

2.2 THE SLOAN DIGITAL SKY SURVEY

The observations from the Sloan Digital Sky Survey (SDSS, York et al. 2000) are performed with a 2.5m telescope located at Apache Point Observatory. The telescope is equipped with a 120 megapixel camera and 5 different photometric filters (*ugriz*). It also has a spectrograph that is fed by optical fibres.

SDSS is organised in three phases with each of them having several sub surveys with distinct science goals. Among the ones relevant for dynamical modelling the Milky Way are the Sloan Extension for Galactic Understanding and Exploration (SEGUE-I and -II) and the APO Galactic Evolution Experiment (APOGEE). APOGEE operates in the near-infrared using a high-resolution spectrograph to draw a clearer picture of the bulge region and the lower latitude disk, where dust obscuration normally penalties the optical bands. The two sub surveys relevant for this thesis are SEGUE-I and -II. These are spectroscopic follow-up surveys of the first phase of SDSS, which was mainly designated to study the local group and distant galaxies.

Thus, the pointing of the first phase avoids the dusty lower latitude part ($b < 30^\circ$) of the Milky Way. SEGUE complements the photometric dataset of stars from SDSS in the upper thin and thick disk and the halo with medium resolution ($R \sim 2000$) spectra that cover a wavelength of 3,800-9,200 Å. SEGUE-I concentrated the observations on the upper thin and thick disk, whereas SEGUE-II had the goal to learn more about the growth of the halo. So we use G-type dwarf stars in chapters 3 & 4 and K-giants in Chapter 5. SEGUE observed over 350,000 stars in total and an automated pipeline extracted stellar parameters (Lee et al. 2008), like effective temperature, surface density and metallicity. The errors of the parameters depend on the signal-to-noise ratio, but are on average $\sigma(T_{eff}) = 200$ K, $\sigma(\log(g)) = 0.3$ dex and $\sigma([Fe/H]) = 0.2$ dex, respectively. Lee et al. (2011) extracted sufficiently good α -abundances in a separate analysis having errors below 0.1 dex. Line-of-sight velocities are estimated as well. They depend on spectral type, e.g. for stars brighter than $r \sim 18$ mag, the velocity error is normally smaller than 5 km/s; it rises to ≈ 20 km/s for stars with $r \sim 20$ mag.

In summary, SEGUE gives positions, colours and metallicity as well as line-of-sight velocities. The only quantity missing are the proper motions in order to retrieve full 6D phase-space information. For that, SDSS and USNO-B (US Naval Observatory) observations were matched and proper motions calculated from the difference in position of the stars in the two catalogues (Munn et al. 2004). The USNO-B catalogue is based on photographic plates of the Palomar Observatory Sky Survey (POSS), which was carried out more than 50 years ago. This guarantees an excellent baseline for the proper motions. The resulting errors are about 3 mas/year at the bright end and ≈ 6 mas/year at the faint end.

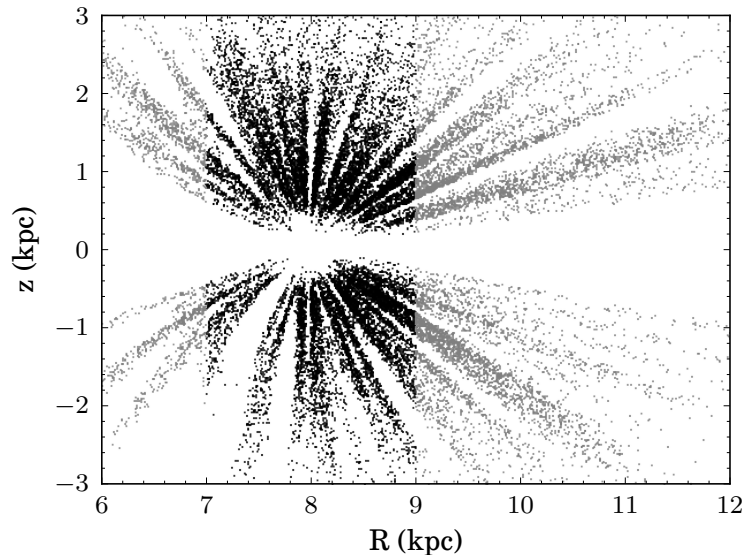


Figure 2.1: The distribution of the G-dwarf sample in the radial and vertical plane. The black points mark the stars inside the region which is used in Chapter 3, while Chapter 4 employs the total sample consisting of the black and the grey points.

2.2.1 *SEGUE* G-TYPE DWARF STARS

Of the wide variety of stars covered by *SEGUE* (Yanny et al. 2009), we focus on G-dwarfs as they are abundant and have been targeted for spectroscopy with minimal selection biases. Among possible stellar tracers of the disk dynamics, G-dwarfs are the brightest with main-sequence lifetimes long enough to validate the assumption of dynamical equilibrium. Moreover, their rich metal-line spectrum enables reliable line-of-sight velocities, metallicities $[\text{Fe}/\text{H}]$, and abundances $[\alpha/\text{Fe}]$, with typical uncertainties for $\text{S/N} > 15$ of $2\text{--}5 \text{ km s}^{-1}$, 0.2 dex, and 0.1 dex respectively (Lee et al. 2011).

We make use of the G-type dwarf sample extracted from *SEGUE*-I by Liu & van de Ven (2012). Their selection criteria were as following: (1) absorption-corrected and dereddened colour index $(g - r)_0$ between 0.48 and 0.55, equal to the *SEGUE* targeting condition for G-dwarfs; (2) colour cuts $0.6 < (u - g)_0 < 2.0$ and $-0.1 < (r - i)_0 < 0.4$ to ensure normal stars; (3) $\log g < 3.75$ to eliminate giant stars; (4) $E(B - V) < 0.3$ to minimize effects due to uncertainty in extinction; (5) signal to noise $\text{S/N} > 15$; (6) availability of heliocentric velocities and proper motions; (7) each line-of-sight has at least 100 G-dwarfs. The last criterion is required to correct the incompleteness in the spectroscopic survey.

Figure 2.1 illustrates the distribution of the sample in the local volume: black points are those we consider to be within the solar neighbourhood and are used for our analysis in Chapter 3, while we use the whole range in Chapter 4. We show the distribution of the resulting sample in $[\text{Fe}/\text{H}]$ and $[\alpha/\text{Fe}]$ space in the top panel of Figure 3.2.

We augment our kinematic data with proper motions from the USNO-B survey, while distances based on the photometric colour-metallicity-absolute-magnitude relation of Ivezić et al. (2008) have relative errors of $\sim 10\%$. The line-of-sight velocities and proper motions of the stars are transformed into the three velocity components along cylindrical coordinates, namely radial velocity v_R , azimuthal or rotational velocity v_ϕ , and vertical velocity v_z . Taking into account the errors in line-of-sight velocities, proper motions and distances, the resulting uncertainties in the velocity components in cylindrical coordinates are on average 10 km s^{-1} . At the furthest distances of $\sim 3 \text{ kpc}$, the velocity error can increase to 40 km s^{-1} , but no biases are introduced as the velocity error remains smaller than the intrinsic velocity dispersion of the stars.

In Chapter 3, we focus our analysis on vertical gradients, so as to avoid biases due to radial gradients we concentrate on the Solar cylinder with stars between 7 and 9 kpc from the Galactic centre. In the end, the sample then consists of a total of 16,276 stars between 0.5 and 3.0 kpc away from the mid-plane. In Chapter 4, we extend the radial range of the sample and include all stars between 6 and 12 kpc. With that, we cannot only better measure the radial disk scale length

with our dynamical model, but also the strength of the coupling between the radial and vertical motion.

2.2.2 THE SELECTION FUNCTION

It is clear that we can not observe every star in a galaxy even in the Milky Way. This is maybe true for a specific population of stars within their effective radius, that is the radius which is set by the apparent magnitude of the star and the brightness limit of the telescope. If the apparent magnitude exceeds the brightness limit, the star will be too faint and hence too far away from earth. Photometric surveys reach very high levels of completeness over a large volume. SDSS is for example complete to more than 95% in point sources. Spectroscopic surveys on the other side can only observe a sub-sample of those stars.

First of all, the science goals of such a spectroscopic survey mostly drive the primary selection. Secondly, the brightness limit is usually lower than for photometric surveys and even if a star is observed, the spectra sometimes do not satisfy the desired accuracy because of a too small signal-to-noise ratio or inconsistent estimates of stellar parameters. In these cases the stars will still be listed in the photometric catalogue. But when selecting stars for the spectroscopic sample, they are excluded. Thus the distribution functions of the density, metallicity and age are under- or overestimated and do not reflect the true distributions.

The selection function accounts for this imbalance by weighting the individual stars according to their probability to finally have ended up in the sample. But there is not one weighting method applicable to all samples. The spectroscopic sample can only be weighted if we know how it was selected from the photometric catalogue, that is which cuts are applied. In principle, every selection cut introduces a bias, that differs in size. Some biases may be very small, so that is not implicitly necessary to correct for them.

SEGUE identifies targets in the SDSS photometry catalogue by using a quantified target selection algorithm based on photometric and proper motion criteria. The stars for the spectroscopic observation were for each line of sight randomly selected. There are two plates for each line of sight, a bright plate and a faint plate. Each plate covers a circular area of 7 square degree on the sky and has 640 fibres available of which a specified number is reserved for the individual target types, e.g. stars being targeted as G-dwarfs get 375¹ fibres. The exact number of fibres per target category can slightly vary from plate to plate.

The assignment of fibres to different target categories leads to the first selection bias. The target type criteria are not strictly separated from each other. Thus it happens that the stars are classified in multiple categories. The main bias from this side originates for G- and K-dwarfs in the low metallicity and the K-giant category, since their classification criteria overlap strongly.

¹This is the number of fibres on the bright and faint plate together

The G- and K-dwarfs are the only target types classified only by their colour ($g - r$) and r magnitude. G-type stars have a colour range of $0.48 \leq g - r \leq 0.55$ and a magnitude range of $14.0 < m_r < 20.1$. Unfortunately, many other categories overlap within these photometric ranges. Stars labelled with multiple categories have thus a higher probability to get a fibre in the spectroscopic survey. That could result in an overrepresentation of metal-poor stars.

A second bias arrives, because each plate has a limited number of fibres so that not every star in the photometric catalogue can be observed. This yields to a latitude effect, because a fixed number of stars is observed on each line-of-sight. At lower latitude, many more stars are present than at higher latitude. The underlying population can therefore be sampled more extensive at higher latitude, just because less stars are missed in relation to the total number in that latitude.

The third bias is caused by the colour cut applied to the G- and K-dwarf sample. It isolates a different range of masses at every metallicity. Thus stars with high metallicity are in general more massive than those with low metallicity. The mass function predicts more low mass than high mass stars yielding to a bias of more metal-poor stars in the sample. In order to correct this, the spectroscopic sample shall reflect in every metallicity bin the same portion of the mass function.

THE APPLIED WEIGHTING METHOD TO THE G-TYPE STARS

We apply the weighting method of [Zhang et al. \(2013\)](#), where the star counts in a spatial bin are divided by the effective volume of that bin in order to reproduce the correct density distribution. In the following, we will summarise the method.

We will split the G stars sample in metallicity and α -abundance. We will then calculate for each of these sub-samples the density distribution as a function of radius and height. The effective volume in a given radial and height bin pair (R_m, z_i) is the summation over the effective sub-volumes of all line-of-sights of all G-type stars in the radial bin.

$$V_{\text{eff}}^{\text{sub}}(R_m, z_i) = \sum_{q=1}^{n_{\text{sub}}} V_{\text{eff},q} \quad (2.1)$$

n_{sub} is the number of stars in the radial bin. Each line-of-sight is part of a specific plate, so the plate weight, which is the ratio of spectroscopic to photometric targets of a plate, is also included in the effective volume.

$$W_{\text{plate},q} = \frac{N_{\text{spec},q}}{N_{\text{photo},q}} \quad (2.2)$$

Whether a line-of-sight contributes to the effective volume depends on the apparent magnitude limit of the corresponding plate. The distance modulus of a star is linked to its apparent magnitude and if this is inside the magnitude limit, the line-of-sight contributes, which is expressed with the parameter W_q . Since the absolute magnitude of a star also depends on the metallicity,

the third bias, which influences the metallicity-mass function, affects the distance and, hence, the 3D position as well. Zhang et al. (2013) adopted the average metallicity of the sub-sample to calculate the distance modulus in order to correct for the third bias. We obtain the absolute magnitude from the Ivezić et al. (2008) photometric colour-metallicity-absolute-magnitude relation (their equation A7). The effective sub-volume is then computed from

$$V_{\text{eff},q} = W_{\text{plate},q} \cdot W_q \cdot \frac{\sin \theta}{\sin(b_q)} \cdot \frac{\pi}{6} \left[\cot(b_q - \theta) - \cot(b_q + \theta) \right] (z_{\text{upper}}^3 - z_{\text{lower}}^3) \quad (2.3)$$

where $\theta = 1.49^\circ$ is the diameter of the SEGUE spectroscopic plate and b_q the latitude of the line-of-sight. Furthermore,

$$W_q = \begin{cases} 0, & \text{for } z_i \leq z_q \leq z_{i+1} \\ 1, & \text{otherwise} \end{cases} \quad (2.4)$$

$$\begin{aligned} z_{\text{upper}} &= \min(z_{i+1}, d_{r_{\text{max}}} \sin(b_q)) \\ z_{\text{lower}} &= \max(z_i, d_{r_{\text{min}}} \sin(b_q)) \end{aligned} \quad (2.5)$$

$$\begin{aligned} d_{r_{\text{min}}} &= 10^{(r_{\text{min}} - M_q + 5) \cdot 0.2} \text{ pc} \\ d_{r_{\text{max}}} &= 10^{(r_{\text{max}} - M_q + 5) \cdot 0.2} \text{ pc} \end{aligned} \quad (2.6)$$

with $r_{\text{min}} = 14.0$ (17.8) and $r_{\text{max}} = 17.8$ (20.1) being the magnitude limit of the bright (faint) plates. z_q is the height above the mid-plane under the assumption that the corresponding line-of-sight has the same metallicity as the average metallicity of the entire sub-sample. W_q will be one if z_q is inside the vertical bin range. Otherwise, the particular line-of-sight does not contribute. A small effective volume means, that the star count is stronger underestimated in the (R,z)-bin than in case of a large effective volume.

2.3 SEGUE-2 K-GIANTS AND THEIR SELECTION CRITERIA

Giant, BHB and RR Lyrae stars are the most readily useable tracers in the stellar halo. They are bright enough to observe spectra with high signal to noise ratio and to measure reliable distances even out to 100 kpc. We choose K-giants because of their well defined selection function in SEGUE-2. The sample includes the same stars as in Xue et al. (2015). SEGUE-2 identifies K-giants according to the following magnitude and colour cuts: $15 < g_0 < 18.5$, $r_0 > 15$, $0.7 < (u - g)_0 < 3$, $0.5 < (g - r)_0 < 0.8$, $0.1 < (r - i)_0 < 0.6$ and $l\text{-colour}^2 > 0.09$.

Nevertheless, pure photometric criteria are not confident enough to identify giants. Xue et al. (2014) describe how to select giants more robustly by the Magnesium (Mg) index and

²The l-colour is an empirical metallicity indicator based on photometry for stars in the colour range $0.5 < (g - r)_0 < 0.8$, which is used to select metal-poor stars.

the stellar atmospheric parameters determined from the spectra. Figure 2.2 shows the spatial distribution of the sample in the x-y and x-z plane in the Cartesian coordinate system as well as the LOSV as function of galactocentric radius and the pencil-beam character of SEGUE-2 in the top left panel. The mean metallicity of the K-giant sample is $[\text{Fe}/\text{H}] = -1.75$ dex and the most metal-poor K-giants have $[\text{Fe}/\text{H}] \gtrsim -3.5$. Distances are very important for the determination of the density profile and the correct density profile is crucial in turn to estimate the mass, which is why we only select those K-giants with accurate distance estimates from Xue et al. (2014).

The basis of the selection function is the plate-dependent ratio of the spectroscopically to photometrically targeted stars. The photometric targets are all K-giants of SDSS in our case. Despite the magnitude and colour cuts of SEGUE-2 to select K-giants, the probability of a K-giant to be observed in SEGUE-2 is independent of magnitude and colour. This implies that the selection function is simplified as it is constant with apparent magnitude and colours, but it still varies with the plate and the star's position. Xue et al. (2015) reports the exact details of the selection function and how to robustly derive the density profile. The final sample contains 6036 K-giants, which we use in dynamical models to constrain the halo mass in Chapter 5.

2.4 AXISYMMETRIC JEANS MODEL

In this section, we derive based on the collisionless Boltzmann equation the axisymmetric Jeans model that we use in Chapter 4 to determine the local dark matter density and in Chapter 5 to estimate the mass profile of the dark halo. Let us consider an axisymmetric stellar system in which both the potential $\Phi(R, z)$ and distribution function (DF) are independent of azimuth ϕ and time. Under the assumption that the stars in the galaxy are in steady state, the time-dependent term in the collisionless Boltzmann equation 1.2 vanishes. To eliminate the derivatives regarding ϕ and the velocities, we multiply the collisionless Boltzmann equation by v_R and v_z and integrate over all velocities. Then we obtain two Jeans equations (see also Binney & Tremaine 2008, eq. 4-29) with the intrinsic number density $\nu(R, z)$ of a tracer population.

$$\frac{\partial(R\nu\overline{v_R^2})}{\partial R} + R\frac{\partial(\nu\overline{v_R v_z})}{\partial z} - \nu\overline{v_\phi^2} + R\nu\frac{\partial\Phi}{\partial R} = 0, \quad (2.7)$$

$$\frac{\partial(R\nu\overline{v_R v_z})}{\partial R} + R\frac{\partial(\nu\overline{v_z^2})}{\partial z} + R\nu\frac{\partial\Phi}{\partial z} = 0, \quad (2.8)$$

Due to the assumed axisymmetry, all terms in the third Jeans equation, that follows from multiplying by v_ϕ , vanish. By Jeans' theorem the DF only depends on the isolating integrals of motion $f(E, L_z, I_3)$, as already mentioned in Section 1.3.1. The unknown third integral I_3 is usually³ invariant under the change $(v_R, v_z) \rightarrow (-v_R, -v_z)$. This implies that the mean velocity in the radial

³If resonances are present, I_3 may lose this symmetry.

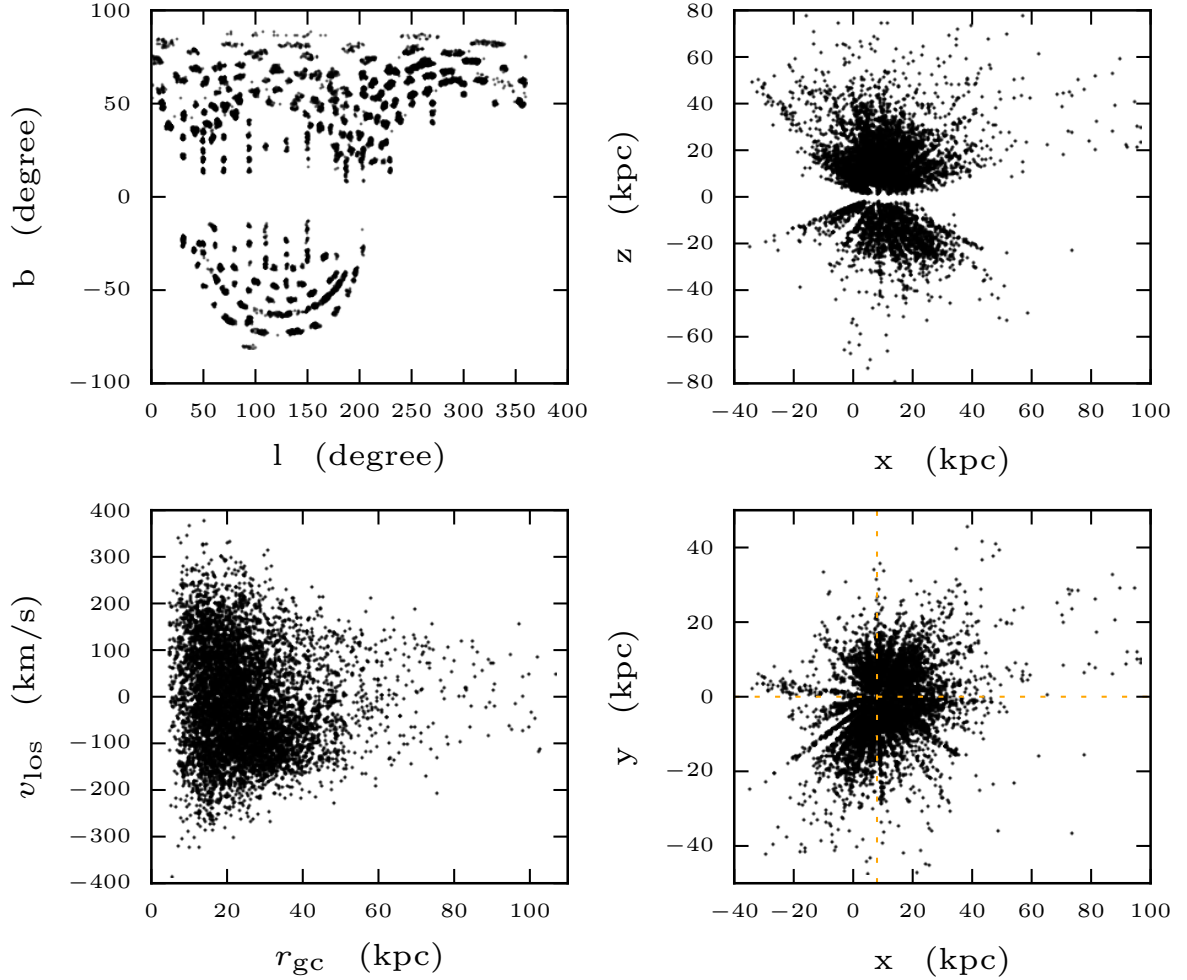


Figure 2.2: *Top left:* The K-giant sample in Galactic longitude and latitude. SEGUE is a pencil-beam survey and the individual pointings are nicely visible in this plot. *Top right:* Distribution in the x-z plane. The stars are all above $|z| > 2$ kpc and 238 stars are in between $2 < |z| < 4$ kpc. *Bottom right:* Distribution in the x-y plane. The orange dashed cross guides the eye to the position of the sun in the Galactic plane. *Bottom left:* LOSV as function of galactocentric distance. The K-giants come as close as 5 kpc to the centre and there are 283 (43) stars farther than 50 (80) kpc from the centre. The majority of stars is in the range $10 < r_{\text{gc}} < 35$ kpc.

and vertical direction is zero ($\overline{v_R} = \overline{v_z} = 0$) and the velocity ellipsoid is aligned with the rotation direction ($\overline{v_R v_\phi} = \overline{v_\phi v_z} = 0$).

The velocity ellipsoid is an illustrative construct to depict the tensor of the second velocity moment. Its diagonal components in cylindrical coordinates ($\overline{v_R^2}$, $\overline{v_\phi^2}$, $\overline{v_z^2}$) span the axes of the ellipsoid and the orientations of the ellipsoid in the R-z, R- ϕ and ϕ -z planes represent the covariances between the stellar velocity components (v_R , v_ϕ , v_z). The ellipsoid can be orientated between two extrema: aligned with the radial axis of the cylindrical coordinate system; pointing to the Galactic centre.

In the simplest case the velocity ellipsoid is aligned with the cylindrical coordinate system, which means that $\overline{v_R v_z} = 0$. Then $\overline{v_R^2}$ is related to $\overline{v_z^2}$ via a constant fraction. However, we show in Chapter 3 that the velocity ellipsoid tilts away from the Galactic plane towards the radial axis of the cylindrical coordinate system.

We construct dynamical models based on the solution of the axisymmetric Jeans equations. When we use a prolate spheroidal coordinate system instead of the cylindrical one, we are able to solve the two Jeans equations 2.7 and 2.8 by aligning the velocity ellipsoid with the prolate spheroidal coordinate system. Note, that the axes are not fixed in contrast to the axes of the cylindrical coordinates. We can change the focal point of the axes with the parameters α and q^2 and thus their bending. This has the advantage that the tilt of the velocity ellipsoid becomes adjustable. Our axisymmetric Jeans model requires only a few assumptions:

- The MW is axisymmetric.
- The system is in a steady state; neglecting time-dependent changes in the potential.
- The velocity anisotropy increases with radius and only slowly decreases with height.

Thus, it overcomes most of the assumptions made in vertical Jeans models. The third assumption will be adaptable, if we change the functional form of the anisotropy. Arnold (1995) gives two other functions that leads to a mainly vertical gradient or an anisotropy changing similiary with radius and height. Then new solutions to the Jeans equations must be derived with the alternative anisotropy function.

2.4.1 PROLATE SPHEROIDAL COORDINATES

The prolate spheroidal coordinates are given by (λ, ϕ, ν) , with the same azimuthal angle ϕ as in the cylindrical coordinate system, while λ and ν are the two roots of

$$\frac{R^2}{\tau - 1} + \frac{z^2}{\tau - q^2} = 1, \quad (2.9)$$

with τ being one of λ or ν and constants α and q^2 such that $q^2 \leq \nu \leq 1 \leq \lambda$. We normalise (λ, ϕ, ν) and (R^2, z^2) by $-\alpha$ and make them dimensionless. We denote the normalised (R^2, z^2) as $\tilde{R}^2 = -\frac{R^2}{\alpha}$ and $\tilde{z}^2 = -\frac{z^2}{\alpha}$, where α is taken to be negative and has the dimension of kpc^2 . Surfaces of constant λ and ν are thus ellipses and hyperbolae in the meridional plane, with foci on the z -axis at $\Delta = \pm\sqrt{-\alpha(1-q^2)}$. For $\lambda = 1$, the prolate spheroidal coordinate surfaces reduce to the part of the z -axis between the foci, while the part beyond the foci is reached if $\nu = 1$. The equatorial plane $z = 0$ corresponds to $\nu = q^2$. Toward the centre ($\lambda = 1, \nu = q^2$) the prolate spheroidal coordinate system approaches the cylindrical coordinate system, whereas at large radii it approaches the spherical coordinate system. As a result, the velocity ellipsoid will be cylindrically aligned at small radii and radially aligned at large radii, which is typically very close to the behaviour of the velocity ellipsoid in real galaxies (e.g. Merritt 1980; Richstone 1982; Dehnen & Gerhard 1993; Cretton et al. 1999).

The relation between (λ, ϕ, ν) and the usual cylindrical coordinates (\tilde{R}, \tilde{z}) is given by

$$\tilde{R}^2 = \frac{(\lambda - 1)(\nu - 1)}{q^2 - 1}, \quad \tilde{z}^2 = \frac{(\lambda - q^2)(\nu - q^2)}{1 - q^2}. \quad (2.10)$$

The inverse relation follows as

$$\lambda = \frac{1}{2}(\tilde{R}^2 + \tilde{z}^2 + q^2 + 1 + \Delta), \quad \nu = \frac{1}{2}(\tilde{R}^2 + \tilde{z}^2 + q^2 + 1 - \Delta), \quad (2.11)$$

where, using $\tilde{z}_0^2 \equiv -\frac{\Delta^2}{\alpha} = 1 - q^2$, we have defined

$$\Delta^2 \equiv (\tilde{R}^2 - \tilde{z}^2 + \tilde{z}_0^2)^2 + 4\tilde{R}^2\tilde{z}^2. \quad (2.12)$$

The corresponding transformation between the velocity components is given by

$$v_R = A v_\lambda - B v_\nu, \quad v_z = B v_\lambda + A v_\nu, \quad (2.13)$$

where A and B are defined as

$$A^2 = \frac{(\lambda - q^2)(\nu - 1)}{(\lambda - \nu)(q^2 - 1)} = \frac{1}{2} \left(1 + \frac{\tilde{R}^2 - \tilde{z}^2 + \tilde{z}_0^2}{\Delta} \right) \quad (2.14)$$

$$B^2 = \frac{(\lambda - 1)(\nu - q^2)}{(\lambda - \nu)(1 - q^2)} = \frac{1}{2} \left(1 - \frac{\tilde{R}^2 - \tilde{z}^2 + \tilde{z}_0^2}{\Delta} \right) \quad (2.15)$$

As a consequence, with $\overline{v_\lambda v_\nu} = 0$, the second order velocity moments are related as

$$\begin{aligned} \overline{v_R^2} &= A^2 \overline{v_\lambda^2} + B^2 \overline{v_\nu^2}, \\ \overline{v_z^2} &= B^2 \overline{v_\lambda^2} + A^2 \overline{v_\nu^2}, \\ \overline{v_R v_z} &= AB \left(\overline{v_\lambda^2} - \overline{v_\nu^2} \right). \end{aligned} \quad (2.16)$$

The angle θ of the velocity ellipsoid with respect to the equatorial plane is given by

$$\tan 2\theta = \frac{2\overline{v_R v_z}}{v_R^2 - v_z^2} = \frac{2AB}{A^2 - B^2} = \frac{2Rz}{R^2 - z^2 + \Delta^2}. \quad (2.17)$$

The focal point Δ^2 of the coordinate system controls in this way the tilt of the velocity ellipsoid.

2.4.2 PROLATE SPHEROIDAL JEANS EQUATIONS

The two non-trivial axisymmetric Jeans equations 2.7 & 2.8 in (λ, ϕ, ν) are

$$\begin{aligned} \frac{\partial T_{\lambda\lambda}}{\partial \lambda} + \frac{T_{\lambda\lambda} - T_{\phi\phi}}{2(\lambda + \alpha)} + \frac{T_{\lambda\lambda} - T_{\nu\nu}}{2(\lambda - \nu)} &= -v_l \frac{\partial \Phi}{\partial \lambda}, \\ \frac{\partial T_{\nu\nu}}{\partial \nu} + \frac{T_{\nu\nu} - T_{\lambda\lambda}}{2(\nu - \lambda)} + \frac{T_{\nu\nu} - T_{\phi\phi}}{2(\nu + \alpha)} &= -v_l \frac{\partial \Phi}{\partial \nu}. \end{aligned} \quad (2.18)$$

where we have defined $T_{\tau\tau} = \overline{v_l v_\tau^2}$ for $\tau = \lambda, \phi, \nu$. While $T_{\lambda\lambda}$ is perpendicular to the part of the z -axis between the foci, $T_{\nu\nu}$ is perpendicular to the part of the z -axis beyond the foci. Stäckel potentials have the remarkable property that they are separable in (λ, ϕ, ν) . [Dejonghe & de Zeeuw \(1988\)](#) (their Appendix D) found a general solution in the axisymmetric case by integrating along characteristics and [Evans \(1990\)](#) derived a numerical algorithm to solve the spherical Jeans equations. A fully general solution to the triaxial case was given by [van de Ven et al. \(2003\)](#).

On the other hand, [Arnold \(1995\)](#) computed a solution of the axisymmetric Jeans equations using characteristics without assuming a separable potential.

Here, we apply the same approach with the following definition for the flattening of the velocity ellipsoid in the meridional plane

$$\beta_{\lambda\nu} \equiv 1 - \frac{T_{\nu\nu}}{T_{\lambda\lambda}} = \kappa \frac{\lambda - 1}{\lambda - p^2}. \quad (2.19)$$

The constant $-\infty \leq \kappa \leq 1$ controls the anisotropy at large radii from fully tangential anisotropic ($\kappa = -\infty$), to isotropic ($\kappa = 0$) to fully radial anisotropic ($\kappa = 1$). The velocity ellipsoid is isotropic ($\beta_{\lambda\nu} = 0$) along the part of the z -axis between and at the foci. The constant p^2 controls the turn-over of the anisotropy with radius. It is allowed to take values between 0 and 1. If p^2 is close to 1, the anisotropy will change slower with radius and it will be constant overall in the case $p^2 = 1$.

Figure 2.3 illustrates the behaviour of the anisotropy within the cylindrical coordinate system (bottom) in comparison to within the spheroidal system (top). To calculate the spheroidal anisotropy, we assume $\alpha = -50 \text{ kpc}^2$, $p^2 = 0.65$ and $\kappa = 1$. This κ belongs to a strong radial anisotropy. The transformation from the spheroidal anisotropy $\beta_{\lambda\nu}$ to the cylindrical anisotropy β_{Rz} involves the gravitational potential and the axisymmetric Jeans model. We convert $\beta_{\lambda\nu}$ into β_{Rz} by using the

parameters in Table 4.1.

The anisotropy increases mainly with radius R , but we see in β_{Rz} a light bending of the iso-contour lines, that leads to a moderate decrease of the anisotropy in height z . If κ becomes more isotropic, this bending will strenghten. In contrast, the behaviour of $\beta_{\lambda\nu}$ is very simple in the solar neighbourhood; it changes with radius only.

Eliminating $T_{\phi\phi}$ from the two Jeans equations 2.7 & 2.8, yields the following mixed first-order partial differential equation

$$(\lambda - 1)\frac{\partial T_{\lambda\lambda}}{\partial \lambda} - (\nu - 1)(1 - \beta_{\lambda\nu})\frac{\partial T_{\lambda\lambda}}{\partial \nu} + \beta_{\lambda\nu}T_{\lambda\lambda} = -\Psi, \quad (2.20)$$

where the potential term is defined as

$$\Psi(\lambda, \nu) = \nu_l \left[(\lambda - 1)\frac{\partial \Phi}{\partial \lambda} - (\nu - 1)\frac{\partial \Phi}{\partial \nu} \right], \quad (2.21)$$

Substituting our choice for the anisotropy solutions derived by [Arnold \(1995\)](#), we obtain

$$\begin{aligned} T_{\lambda\lambda}(\lambda, \nu) &= \int_{\lambda}^{\infty} d\lambda' \left(\frac{\lambda' - p^2}{\lambda - p^2} \right)^k \frac{\Psi(\lambda', \hat{\nu})}{\lambda' - 1}, \\ &= \int_0^{\infty} d\eta \left[e^{\eta} + \frac{1 - p^2}{\lambda - p^2} (1 - e^{\eta}) \right]^k \Psi(\lambda', \hat{\nu}). \end{aligned} \quad (2.22)$$

The second line follows upon substitution of $\lambda' = 1 + (\lambda - 1)e^{\eta}$, which might facilitate the numerical evaluation of the integral as the integrand is expected to fall off steeply with increasing radius. As a result, the solutions for the intrinsic second velocity moments can be obtained through single numerical integrals for given intrinsic number density ν_l and gravitational potential Φ . If Φ depends on R and z only through their squared values, we can simplify the potential term 2.21 with the help of the expressions 2.10 of λ and ν to

$$\Psi(\lambda, \nu) = (\lambda - \nu) \nu_l \frac{\partial \Phi}{\partial z^2}. \quad (2.23)$$

If the solution for $T_{\lambda\lambda}$ is known, the anisotropy term 2.19 will directly link $T_{\nu\nu}$ to $T_{\lambda\lambda}$, so that no additional integral is needed to compute $T_{\nu\nu}$. The drawback is that the shape of the anisotropy profile is fixed, in this case to a rising anisotropy from the centre to a slowly approaching maximal

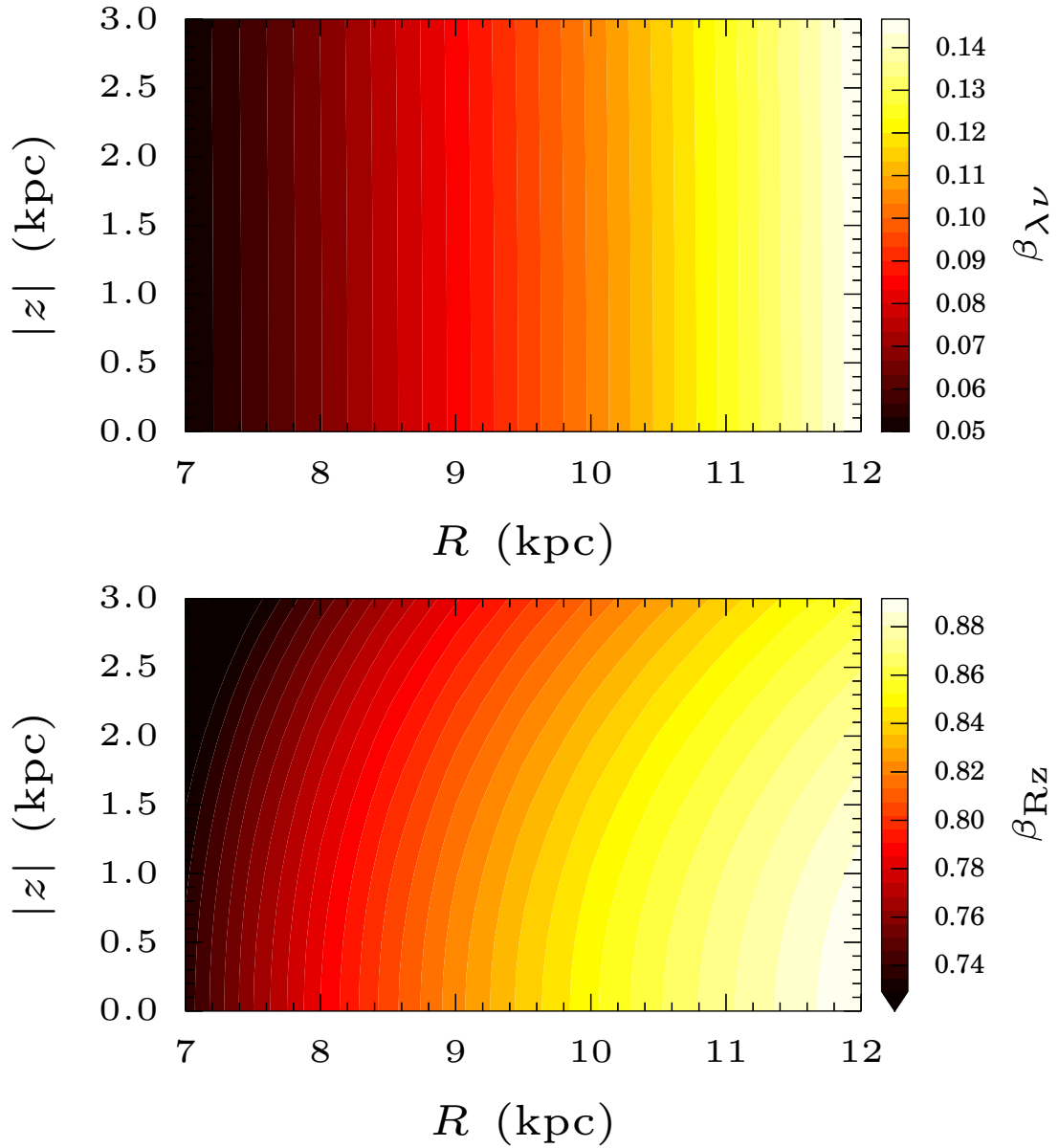


Figure 2.3: Anisotropy map as function of radius and height; (*top*) prolate spheroidal anisotropy $\beta_{\lambda\nu}$; (*bottom*) cylindrical anisotropy β_{Rz} . We compiled the maps with the parameters $\alpha = -50 \text{ kpc}^2$, $p^2 = 0.65$, $\kappa = 1$ and the ones given in Table 4.1.

value κ , due to the specific solution 2.22 under the assumption of the anisotropy relation 2.19. The general solution for $T_{\phi\phi}$ follows directly from the second Jeans equation 2.18 as

$$\begin{aligned}
 T_{\phi\phi}(\lambda, \nu) &= \left(1 - \beta_{\lambda\nu} + \beta_{\lambda\nu} \frac{\nu - 1}{\lambda - \nu}\right) T_{\lambda\lambda} + 2(1 - \beta_{\lambda\nu})(\nu - 1) \frac{\partial T_{\lambda\lambda}}{\partial \nu} \\
 &\quad + 2(\nu - 1)v_l \frac{\partial \Phi}{\partial \nu} \\
 &= (1 - \beta_{\lambda\nu}) \int_0^\infty d\eta \left(\frac{e^\eta(\lambda - 1) + 1 - p^2}{\lambda - p^2} \right)^\kappa \left[2(\hat{\nu} - 1) \frac{\partial \Psi(\lambda', \hat{\nu})}{\partial \hat{\nu}} \right. \\
 &\quad \left. + \left(1 + \frac{\beta_{\lambda\nu}(\nu - 1)}{(1 - \beta_{\lambda\nu})(\lambda - \nu)}\right) \Psi(\lambda', \hat{\nu}) \right] + 2(\nu - 1)v_l \frac{\partial \Phi}{\partial \nu}, \tag{2.24}
 \end{aligned}$$

where we substitute λ' with η in the second line again, to obtain a faster convergence of the numerical integral. The anisotropy $\beta_{\lambda\nu}$ is given in equation 2.19.

Throughout the following chapters we adopt 8 kpc for the Sun's distance to the Galactic centre, and 220 km s^{-1} for the circular velocity of the local standard of rest (LSR) (Kerr & Lynden-Bell 1986). We adopt for the Sun's peculiar velocity relative to the LSR the common values of (10.00, 5.25, 7.17) km s^{-1} in the radial, azimuthal and vertical direction, respectively (Dehnen & Binney 1998).

THE TILT OF THE VELOCITY ELLIPSOID IN THE MILKY WAY DISK

The concordance cosmological model is based on collisionless dark matter particles, of yet unknown nature, which cannot be detected directly, but which interact through gravity. Various direct detection experiments aim to uncover the nature of these particles, in particular their mass, but, since the signal will depend strongly on their distribution in the Solar neighbourhood, the local dark matter density needs to be measured independently and accurately (e.g. [Peter 2011](#)). Such a local measurement is also essential to constrain the overall dark matter distribution in the Milky Way as good measurements of the Galactic rotation curve exist but these do not allow the separation of luminous and dark matter due to the so-called disk-halo degeneracy (e.g. [Dutton et al. 2011](#)).

The traditional approach adopted to measure the local dark matter density is through the vertical force, i.e., the derivative of the gravitational potential away from the Galactic disk plane, inferred from a population of stars with observed vertical number density profile and vertical velocity dispersion profile (e.g. [Kuijken & Gilmore 1989b](#)). Recent surveys such as the Sloan Extension for Galactic Understanding and Exploration (*SEGUE*; [Yanny et al. 2009](#)) make it possible to extract robust vertical density and dispersion profiles even for chemically different subpopulations, providing independent tracers of the same gravitational potential. However, even with many thousands of stars the uncertainties on the dark matter density are still substantial and systematic differences between studies remain even if similar data sets are being used (e.g. [Zhang et al. 2013](#)).

Most investigations of the local dark matter density to date have used the vertical Jeans equation, which relates the gravitational potential directly to observable vertical profiles without having to specify the phase-space distribution function of the tracers. Unfortunately, the inference of the vertical profiles is often based on taking statistical moments of discrete data within a certain bin, which not only implies loss of information, but is also very sensitive to interlopers.

*This chapter is adapted from [Büdenbender et al. \(2015\)](#)

Moreover, the motions of stars in the vertical and radial directions are typically coupled, however often a simple approximation is adopted or the coupling is neglected altogether.

This radial-vertical coupling is reflected in the tilt of the velocity dispersion ellipsoid with respect to the Galactic mid-plane. In turn, this tilt is related to the shape of the gravitational potential, but also depends on the phase-space distribution function. Only in the case of a Stäckel potential can the shape of the gravitational be directly constrained from the tilt of the velocity ellipsoid (e.g. [Binney & McMillan 2011](#)). Even so, aside from measuring the local dark matter density, the velocity ellipsoid is also important for constraining dynamical heating processes (e.g. [Fuchs & Wielen 1987](#)), including those that might have led to the thickened Milky Way disk (e.g. [Liu & van de Ven 2012](#); [Bovy et al. 2012a](#)). The velocity ellipsoid also enters directly into the asymmetric drift correction of the azimuthal to circular velocity ([Dehnen & Binney 1998](#)). Finally, deviations from axisymmetry due to, for example, spiral structure are encoded in the velocity ellipsoid components ([Binney & Tremaine 2008](#)).

Previous measurements of the local velocity ellipsoid, and in particular its tilt, have been either over a broad range in height (e.g. [Siebert et al. 2008](#); [Carollo et al. 2010](#); [Casetti-Dinescu et al. 2011](#)) and/or with very large error bars (e.g. [Smith et al. 2012](#)). These limitations are partly driven by the limited availability of large samples of stars with reliable photometric and kinematic measurements. The method used to extract the velocity moments also plays an important role, so we introduce a discrete likelihood method that explicitly accounts for interlopers and uses a Bayesian inference of the velocity moments.

We describe the G-dwarf sample and kinematic extraction method in [Section 3.1](#) and construct vertical Jeans models for chemically different sub-samples in [Section 3.2](#). Even though they are tracers of the same gravitational potential, the inferred value of local dark matter density varies substantially, which we believe mainly to be a consequence of the invalid assumption of decoupled vertical and radial motion. In [Section 3.3](#), we indeed confirm that the tilt of the velocity ellipsoid for each sub-sample is non-zero and similarly pointing toward the Galactic centre. In [Section 3.4](#), we discuss how this strongly-improved measurement of the velocity tilt provides important constraints on dynamical models of the Milky Way disk. In [Section 3.3.2](#), we show that our measurements in the meridional (R, z)-plane under the assumption of axisymmetry are affected neither by motion in the azimuthal direction nor by a slight non-zero vertical and radial mean velocities.

3.1 LOCAL STELLAR KINEMATICS

We briefly introduce the kinematic extraction algorithms we use to probe the dynamics in a local volume of about 1 kpc in radius around the Sun and from about 0.5 to 2.5 kpc away from the mid-

plane. The sample of G-type dwarf stars, that we use in this chapter, is presented in Chapter 2 with a short overview on the related SEGUE survey.

3.1.1 VELOCITY ELLIPSOID IN THE MERIDIONAL PLANE

We treat the Milky Way disk as an axisymmetric system in a steady state, so that the potential $\Phi(R, z)$ and the distribution function do not vary with azimuth ϕ or time. [Jeans \(1915\)](#), pointed out that the distribution function depends only on isolating integrals of the motion: energy $E = \frac{1}{2}(v_R^2 + v_\phi^2 + v_z^2) + \Phi(R, z)$, angular momentum $L_z = Rv_\phi$, and a third integral I_3 whose form is not generally known. However, in the absence of resonances, I_3 is invariant under the change $(v_R, v_z) \rightarrow (-v_R, -v_z)$, from which it follows that the mean velocity is in the azimuthal direction ($\overline{v_R} = \overline{v_z} = 0$) and the velocity ellipsoid is aligned with the rotation direction ($\overline{v_R v_\phi} = \overline{v_\phi v_z} = 0$).

The remaining second velocity moment $\overline{v_R v_z}$ then quantifies the coupling between the radial and vertical motions, and, in combination with the radial and vertical velocity dispersion, σ_R and σ_z yields the tilt of the velocity ellipsoid. We extract the latter velocity moments from the observed radial and vertical velocities, v_R and v_z , but do not need to consider the observed azimuthal velocities v_ϕ , if the Milky Way disk is axisymmetric locally. In [Section 3.3.2](#), we show that excluding or including the azimuthal velocities yields consistent results for σ_R , σ_z and $\overline{v_R v_z}$. Thus, we exclude the azimuthal velocities from the remainder of the current analysis; this is particularly convenient because it is well known that the distribution in v_ϕ is non-Gaussian.

The distribution in v_R and v_z , on the other hand, is well described by a bi-variate Gaussian. However, $\overline{v_R}$ and $\overline{v_z}$ are observed to be mildly non-zero especially closer to the mid-plane ([Williams et al. 2013](#)), in line with deviations from axisymmetry due to spiral structures ([Faure et al. 2014](#)). Even so, in [Section 3.3.2](#), we show that, at the heights $0.5 < |z|/\text{kpc} < 2.5$ probed by the G dwarfs, the deviations are so small that they do not affect the inferred second velocity moments. So to decrease the statistical uncertainty on particular $\overline{v_R v_z}$ and, hence, on the subsequent tilt angle measurement, we set $\overline{v_R} = \overline{v_z} = 0$ for this chapter and [Chapter 4](#).

The only non-zero velocity moments are, thus, second moments σ_R , σ_z , $\overline{v_R v_z}$. To determine these velocity moments for a subset of stars (typically selected, in this paper, to have similar heights, metallicities and α -element abundances), we use a maximum likelihood approach, which we discuss below.

3.1.2 EXTRACTING VELOCITY MOMENTS

Consider a dataset of N stars where the i th star has velocity vector \mathbf{v}_i and uncertainty matrix Δ_i . Now suppose that the velocity distribution in the disk may be modelled as a multivariate

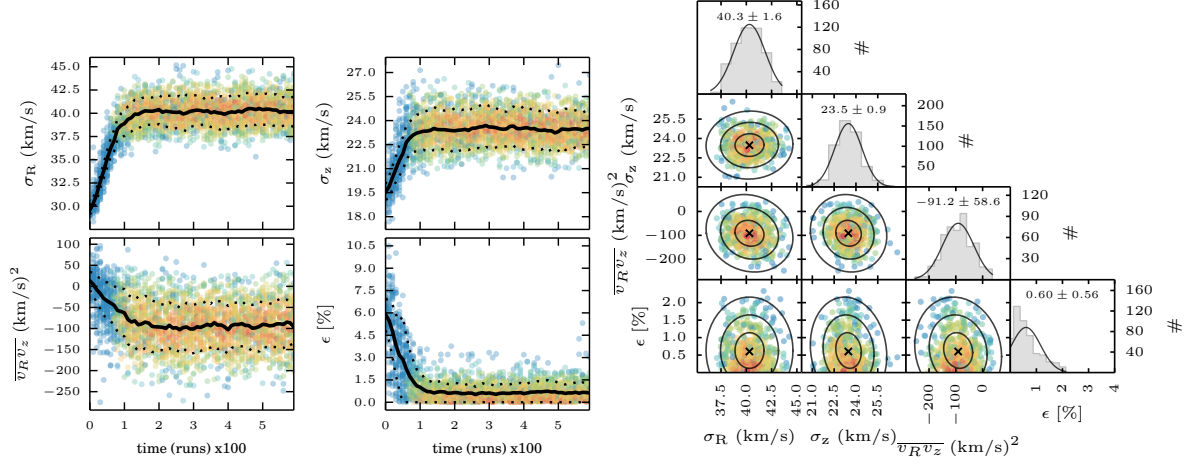


Figure 3.1: *Left:* Parameter evolution in a typical MCMC run. The points show the values visited by the walkers at each step and are coloured by likelihood from red (high) to blue (low). The solid lines show the means at each step and the dotted lines show the dispersions. All parameters converge quickly and tightly. *Right:* Post-burn parameter distributions from a typical MCMC run. The scatter plots show the projected two-dimensional distributions of the parameters, with the points coloured by likelihood (red high and blue low). The crosses indicate mean values and the ellipses encompass the 1–3 σ regions. The histograms show the projected one-dimensional parameter distributions with lines representing gaussians with the same mean and standard deviation. We also give the one-dimensional mean and uncertainty for each of the parameters. We do not see significant correlations between the parameters.

Gaussian j of rank n with mean $\boldsymbol{\mu}_j$ and variance $\boldsymbol{\Sigma}_j$. We wish to know what is the likelihood that star i came from the disk distribution predicted by Gaussian j , which can be written as

$$\begin{aligned} \mathcal{L}_{ij}^{\text{disk}} &= \mathcal{L}(\mathbf{v}_i | \boldsymbol{\mu}_j, \boldsymbol{\Sigma}_j, \Delta_i) \\ &= \frac{1}{(2\pi)^{\frac{n}{2}} |\boldsymbol{\Sigma}'_j|^{\frac{1}{2}}} \exp\left(-\frac{1}{2} (\mathbf{v}_i - \boldsymbol{\mu}_j)^T \boldsymbol{\Sigma}'_j{}^{-1} (\mathbf{v}_i - \boldsymbol{\mu}_j)\right). \end{aligned} \quad (3.1)$$

where $\boldsymbol{\Sigma}'_j = \boldsymbol{\Sigma}_j + \Delta_i^2$ results from the convolution of the intrinsic variance of the Gaussian and the observed uncertainties. Here, $\boldsymbol{\mu}_j$ and $\boldsymbol{\Sigma}_j$ are unknown parameters that we wish to determine.

Our dataset is also contaminated by Milky Way halo stars, which we assume to have a Gaussian velocity distribution with a mean of zero and variance $\boldsymbol{\Sigma}_{\text{halo}}$. we also need to consider the likelihood of observing star i given the halo population, which is written as

$$\begin{aligned} \mathcal{L}_i^{\text{halo}} &= \mathcal{L}(\mathbf{v}_i | \boldsymbol{\Sigma}_{\text{halo}}, \Delta_i) \\ &= \frac{1}{(2\pi)^{\frac{n}{2}} |\boldsymbol{\Sigma}'_{\text{halo}}|^{\frac{1}{2}}} \exp\left(-\frac{1}{2} \mathbf{v}_i^T \boldsymbol{\Sigma}'_{\text{halo}}{}^{-1} \mathbf{v}_i\right). \end{aligned} \quad (3.2)$$

where $\Sigma'_{\text{halo}} = \Sigma_{\text{halo}} + \Delta_i^2$ results from the convolution of the variance of the halo distribution and the observed uncertainties.

We adopt a canonical single halo model with dispersions $\sigma_{R,\text{halo}} = 157 \pm 10 \text{ km s}^{-1}$ and $\sigma_{z,\text{halo}} = 75 \pm 8 \text{ km s}^{-1}$ (Schönrich et al. 2011), where $\sigma_{R,\text{halo}}^2$ and $\sigma_{z,\text{halo}}^2$ are the diagonal elements of Σ_{halo} while the cross term is assumed to be zero. We show in Section 3.4 that neither a dual-halo contamination model (e.g. Carollo et al. 2007, 2010) nor the presence of a metal-weak tail to the thick disk (e.g. Chiba & Beers 2000) effects our results.

If we assume that a (small) fraction ϵ_j of the stars are halo stars – and so fraction $(1 - \epsilon_j)$ are disk stars – then the total likelihood of star i is given by

$$\mathcal{L}_{ij} = (1 - \epsilon_j) \mathcal{L}_{ij}^{\text{disk}} + \epsilon_j \mathcal{L}_i^{\text{halo}} \quad (3.3)$$

The halo fraction ϵ_j will be another free parameter in our models. The total likelihood of model j is the product of the model likelihoods for each star

$$\mathcal{L}_j = \prod_{i=1}^N \mathcal{L}_{ij}. \quad (3.4)$$

The best model is that which maximises \mathcal{L}_j .

In general, the free parameters are μ_j , Σ_j and ϵ_j . However, as we discussed in Section 3.1.1, we can assume that all components of μ_j and a number of elements of Σ_j are zero. So, in practice, there are only four free parameters for each model j : σ_R , σ_z , $\overline{v_R v_z}$ and ϵ . In order to efficiently sample the parameter space as we search for the best model, we use a Markov Chain Monte Carlo (MCMC) analysis; we use the `emcee` package developed by Foreman-Mackey et al. (2013), which is an implementation of the affine-invariant MCMC ensemble sampler by Goodman & Weare (2010). Our MCMC chains use 100 walkers and run for 600 steps. We consider the first 500 steps as the burn-in phase that finds the region of parameter space where the likelihood is highest. The final 100 steps then constitute the post-burn phase that explores the high-likelihood region.

Figure 3.1 illustrates the output from an MCMC run on a typical subset of our kinematic data (around 500 stars). The left-hand panels show the evolution and eventual convergence of the MCMC chain. The coloured points show the values sampled by the walkers at each step with the colours representing the likelihood of the model (red high and blue low). The solid lines show the means of the walker values and the dotted lines show the 1σ dispersions of the walker values. All of the parameters converge tightly. The right-hand panels show the post-burn parameter distributions. The scatter plots show the two-dimensional distributions of the parameters, again with points coloured according to their likelihoods (red high and blue low). The ellipses show the 1σ , 2σ and 3σ regions of the covariance matrix for the post-burn parameter distribution, projected into each 2D plane. The crosses mark the means of the parameter distributions.

The histograms show the one-dimensional distributions of the parameters; the solid black lines represent Gaussians with the same mean and standard deviation. The histogram panels also give the one-dimensional mean and uncertainty for each of the parameters.

3.2 VERTICAL JEANS MODEL

We use dynamical models to link observable quantities (such as stellar number density ν and velocity dispersion σ) with quantities that we wish to know but are not able to measure directly (such as mass density ρ and potential Φ).

Stellar sub-samples with different origins as reflected in their different ages and/or chemical properties, will have different spatial distributions (ν) and different kinematics (σ). Nevertheless, they feel the same underlying total mass density that gives rise to the same underlying gravitational potential. So, in theory, if the observed kinematics of a number of sub-samples are independently used to find the best-fit density distribution in the solar neighbourhood, all sub-samples should return the same answer. However, in practice, we will only obtain consistent results from the different sub-samples if the assumptions we make in the modelling are correct.

Our goal here is to assess the validity of the assumption that the radial and vertical motions of stars in the Milky Way disk are decoupled. As such, we first select two sub-samples of G-dwarf stars based on their [Fe/H] metallicities and $[\alpha/\text{Fe}]$ abundances. Then we model the local mass density independently for the two sub-samples, assuming that the vertical and radial motions are decoupled, and test the agreement of the two best-fit models.

3.2.1 GRAVITATIONAL POTENTIAL

The total mass density in the solar neighbourhood has contributions from both luminous and dark matter. [Jurić et al. \(2008\)](#) calculated photometric parallax distances for ~ 48 million stars selected from the SDSS to determine the 3-dimensional number density distribution of the Milky Way. Using a sub-sample of nearby M-dwarfs, they found that the solar neighbourhood mass density is best described as two exponential disks: a thin disk with density ρ_{thin} and a thick disk with density ρ_{thick} , where the fraction of thick disk stars relative to thin disk stars in the plane at the solar radius R_{\odot} is $f = 0.12$. The thin disk component has a vertical scale height $h_{\text{thin}} = 300$ pc and the thick disk component has a vertical scale height $h_{\text{thick}} = 900$ pc. We adopt this as the stellar density distribution for our analysis¹. Dark matter also makes a contribution ρ_{dm} to the local density distribution; as the radial extent of our data is small and the vertical extent is less

¹Note, we assume that all of our stars are at the solar radius, so we neglect any radial variations in disk density.

than 2 kpc, we can assume that this is constant throughout the region of interest. Thus the total mass density in the solar neighbourhood is given by

$$\rho_{\odot}(z) = \rho(R_{\odot}, z) = \rho_{\text{thin}}(R_{\odot}, z) + \rho_{\text{thick}}(R_{\odot}, z) + \rho_{\text{dm}} \quad (3.5)$$

where the thin and thick disk densities are given by

$$\rho_{\text{disk}}(R_{\odot}, z) = \rho_{\text{disk}}(R_{\odot}, 0) \exp\left(-\frac{z}{h_{\text{disk}}}\right) \quad (3.6)$$

and where $\rho_{\text{disk}}(R_{\odot}, 0)$ is the density of the disk component in the plane at the solar radius.

Recalling that we know the local normalisation fraction f of the thick disk relative to the thin disk in the plane

$$f = \frac{\rho_{\text{thick}}(R_{\odot}, 0)}{\rho_{\text{thin}}(R_{\odot}, 0)}, \quad (3.7)$$

then

$$\rho_{\odot}(z) = \rho_0 \left[\exp\left(-\frac{z}{h_{\text{thin}}}\right) + f \exp\left(-\frac{z}{h_{\text{thick}}}\right) \right] + \rho_{\text{dm}} \quad (3.8)$$

where $\rho_0 = \rho_{\text{thin}}(R_{\odot}, 0)$.

The potential generated by this density distribution can then be calculated via Poisson's equation

$$\nabla^2 \Phi = 4\pi G \rho_{\odot}. \quad (3.9)$$

It is not possible to measure Φ directly. Instead, we use dynamical models to predict the observable quantities generated in a given potential, then we compare the values we actually observe with those we predict. For this present thesis, we use the Jeans equations to carry out the dynamical modelling.

Under the assumption of axial symmetry, the vertical first moment Jeans equation in cylindrical polars is

$$\frac{1}{R} \frac{\partial}{\partial R} (R v \overline{v_R v_z}) + \frac{\partial}{\partial z} (v \sigma_z^2) + v \frac{\partial \Phi}{\partial z} = 0. \quad (3.10)$$

If we assume that the velocity ellipsoid is aligned with the cylindrical coordinate system (and hence that radial and vertical motions can be decoupled) then $\overline{v_R v_z} = 0$. Our sample is restricted to the solar neighbourhood and we assume that all stars are at the solar radius R_{\odot} . Hence, the vertical Jeans equation becomes

$$\frac{d}{dz} (v \sigma_z^2) + v \frac{d\Phi}{dz} = 0. \quad (3.11)$$

As one can see, we are actually interested in the first derivative of the potential here, which we calculate from equations 3.8 and 3.9 as

$$\begin{aligned} \frac{d\Phi}{dz}(z) = & 4\pi G\rho_0 \left\{ h_{\text{thin}} \left[1 - \exp\left(-\frac{z}{h_{\text{thin}}}\right) \right] \right. \\ & \left. + f h_{\text{thick}} \left[1 - \exp\left(-\frac{z}{h_{\text{thick}}}\right) \right] \right\} + 4\pi G\rho_{\text{dm}}z. \end{aligned} \quad (3.12)$$

Finally, we need the tracer number density ν and the vertical velocity dispersion σ_z ; both of which we are able to calculate from observations. Note that different stellar populations may have different number density profiles and different dispersion profiles due to differences in their origins, however they all orbit within the same potential. This point is key to our analysis. By applying these models to multiple stellar sub-samples independently, we can obtain multiple independent estimates for the potential of the system. If the assumptions we have made in the modelling are correct – principally that the radial and vertical motions may be decoupled – and equation 3.11 is a good representation of reality, then the estimates of the potential should be in good agreement. However, if the potential estimates we recover do not agree, then we can conclude that our assumptions were incorrect.

3.2.2 TRACER POPULATIONS

The top panel of Figure 3.2 shows the $[\alpha/\text{Fe}]$ abundances and $[\text{Fe}/\text{H}]$ metallicities of the stars in our sample. The stars have been binned into pixels of 0.025 dex by 0.0125 dex and the pixels coloured according to the number of stars in that pixel as shown by the colour bar. α -element and iron abundances are particularly useful as they can be used as a proxy for age: stars towards the top-left of parameter space as plotted are older, in general, than the stars towards the bottom-right (Loebman et al. 2011). In our sample, there are two clear overdensities: the first occurs at high $[\alpha/\text{Fe}]$ and low $[\text{Fe}/\text{H}]$, representing an older population; the second occurs at high $[\text{Fe}/\text{H}]$ and low $[\alpha/\text{Fe}]$, representing a younger population.

We select two sub-samples centred on these overdensities: the α -old sample contains stars with $0.3 < [\alpha/\text{Fe}]$ and $-1.2 < [\text{Fe}/\text{H}] < -0.3$; the α -young sample contains stars with $[\alpha/\text{Fe}] < 0.2$ and $[\text{Fe}/\text{H}] > -0.5$. These selection boxes are shown in the top panel of Figure 3.2, with the α -old selection shown in red and the α -young selection shown in blue. For consistency, these colours will be used in all plots comparing results from these two sub-samples.

We assume that the number density ν of stars in each tracer sub-sample follows an exponential profile such that

$$\nu(z) = \nu_0 \exp\left(-\frac{z}{\zeta_{\text{tr}}}\right) \quad (3.13)$$

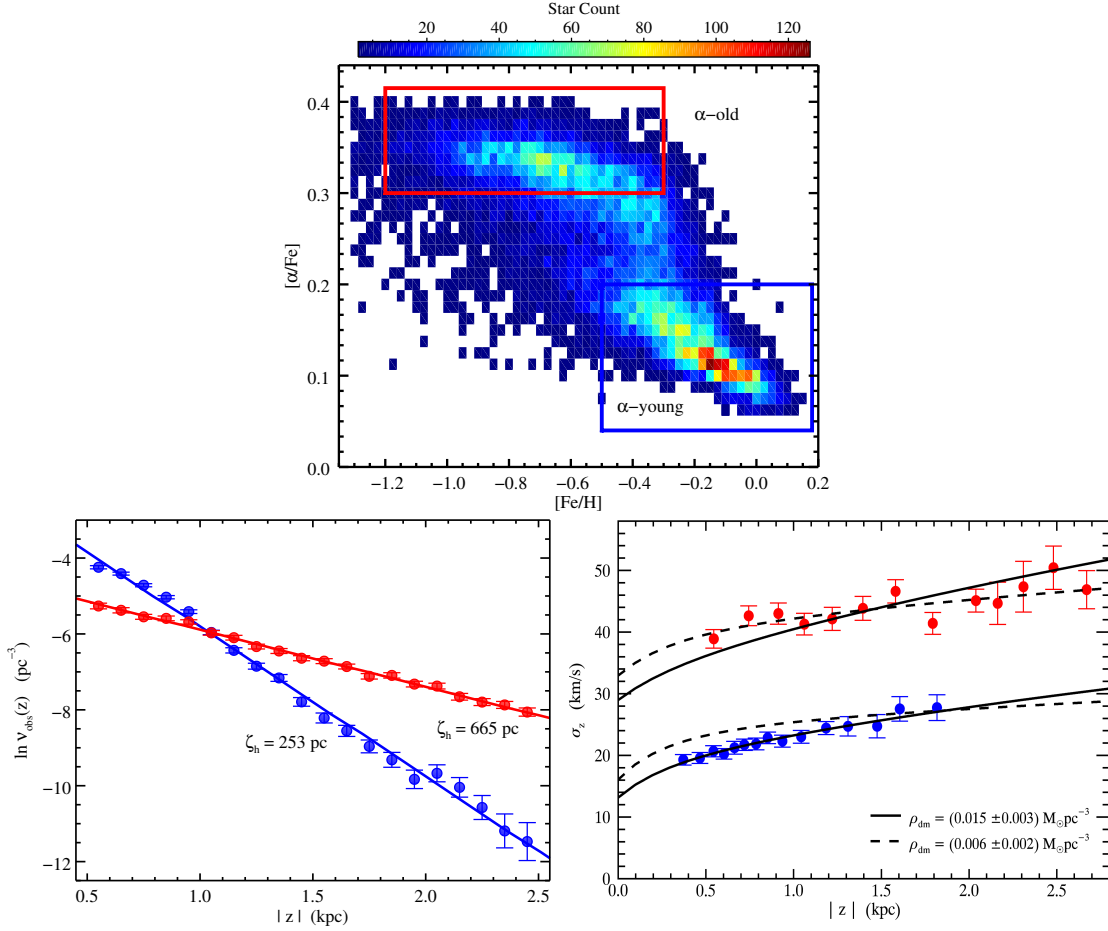


Figure 3.2: *Top:* $[\alpha/\text{Fe}]$ abundances and $[\text{Fe}/\text{H}]$ metallicities of 16,276 SDSS/SEGUE G-dwarf stars, binned in 0.025 dex by 0.0125 dex pixels. The pixel colours represent the number counts, as shown by the colour bar. The selection boxes used to extract the two sub-samples we use in this section are shown as red and blue rectangles. α -element and iron abundances can be used as a proxy for age; the sub-sample with high $[\alpha/\text{Fe}]$ and low $[\text{Fe}/\text{H}]$ we call the α -young sub-sample and the sub-sample with low $[\alpha/\text{Fe}]$ and high $[\text{Fe}/\text{H}]$ we call the α -old sub-sample. *Bottom left:* The selection-function-corrected number density profiles of the α -old sub-sample (red) and α -young sub-sample (blue). The solid lines are exponential fits with scale heights ζ_h indicated. *Bottom right:* Vertical velocity dispersion as a function of height. The α -old sub-sample (red) is best fit by a model with negligible dark matter (upper dashed line) and α -young sub-sample (blue) is best fit by a model including dark matter (lower solid line). To aid visual comparison of the models, the upper solid line (lower dashed line) shows the best-fitting α -young (α -old) density model using the α -old (α -young) tracer density. As the sub-samples orbit in the same underlying potential, they should make consistent predictions about the local dark matter density. These models assume that the radial and vertical motions can be decoupled; the discrepancy in the fits indicates that this assumption is incorrect.

where ν_0 is the number density in the Galactic plane and the ζ_{tr} is the scale height of the tracer sample. To determine the scale-height parameters for each sub-sample, we calculate the number density of stars in a series of height bins and find the best-fitting exponential profile. The number density is highly sensitive to the selection function for SEGUE; to correct for this, we adopt the approach outlined in Section 2.2.2 and originally introduced by Zhang et al. (2013) in their Section 3.1.2. The bottom left panel of Figure 3.2 shows the logarithm of the corrected number density as a function of vertical distance from the plane for the two sub-samples. The α -old sub-sample is shown in red and the α -young sub-sample is shown in blue. The data are shown as symbols and the best-fit profiles are shown as solid lines. we find a best-fitting scale height of $\zeta_{\text{tr}} = 253 \pm 6$ pc for the α -young sub-sample and $\zeta_{\text{tr}} = 665 \pm 11$ pc for the α -old sub-sample.

3.2.3 VERTICAL VELOCITY DISPERSION

Now that we have a functional form for the tracer density (equation (3.13)), we can substitute this and the first derivative of the potential from equation (3.12) into the vertical Jeans equation (3.11). Rearranging and performing the necessary integration, we obtain a prediction for the vertical velocity dispersion as a function of height

$$\begin{aligned} \sigma_z^2(z) = & 4\pi G \rho_0 \zeta_{\text{tr}} \left\{ h_{\text{thin}} \left[1 - \frac{h_{\text{thin}}}{h_{\text{thin}} + \zeta_{\text{tr}}} \exp\left(-\frac{z}{h_{\text{thin}}}\right) \right] \right. \\ & \left. + f h_{\text{thick}} \left[1 - \frac{h_{\text{thick}}}{h_{\text{thick}} + \zeta_{\text{tr}}} \exp\left(-\frac{z}{h_{\text{thick}}}\right) \right] \right\} \\ & + 4\pi G \rho_{\text{dm}} \zeta_{\text{tr}} (z + \zeta_{\text{tr}}). \end{aligned} \quad (3.14)$$

There are two free parameters in this expression: the local thin disk density in the plane ρ_0 and the local dark matter density ρ_{dm} .

To obtain vertical velocity dispersion profiles for our data, we bin the stars in height and use the maximum likelihood method described in Section 3.1.2 to calculate the velocity dispersion in each bin. we use 10 bins, with the bin boundaries selected so that each bin contains an equal number of stars. This is done independently for each of our sub-samples. Note that, although we are only interested here in the vertical velocity dispersion σ_z , our maximum likelihood analysis uses all of the data available and fits for the radial dispersion, the covariance and the background fraction² as well. The bottom-right panel of Figure 3.2 shows the vertical velocity dispersion profiles for our two sub-samples; the α -young sample is shown in blue and the α -old sample is shown in red.

We wish to compare the model predictions against our data and determine which $(\rho_0, \rho_{\text{dm}})$ values provide a best fit to the observed profile for each sub-sample. We do this using a non-linear least squares (NNLS) fit.

²The estimated background fraction varies little from bin to bin and never exceeds 5%.

We find that the α -old sample is best described by a model with central disk density $\rho_0 = 0.12 \pm 0.011 M_\odot \text{pc}^{-3}$ and local dark matter density $\rho_{\text{dm}} = 0.0024 \pm 0.0021 M_\odot \text{pc}^{-3}$. This model is shown as dashed lines in the bottom-left panel of Figure 3.2. The upper dashed line is plotted using the value of ζ_{tr} found to best fit the α -old sample; as expected, this is an excellent fit to the α -old dispersion profile. In order to show the ability of this model to reproduce the α -young profile, the lower dashed line is plotted using the α -young ζ_{tr} . This is a very poor fit to our α -young sample.

We find that the α -young sample is best described by a model with central disk density $\rho_0 = 0.06 \pm 0.011 M_\odot \text{pc}^{-3}$ and local dark matter density $\rho_{\text{dm}} = 0.014 \pm 0.004 M_\odot \text{pc}^{-3}$. This model is shown as solid lines in the bottom-left panel of Figure 3.2. Again, we plot this model using both the α -old ζ_{tr} (upper solid line) and the α -young ζ_{tr} (lower solid line). This model is an excellent approximation to the α -young sample, but fails to reproduce the α -old sample.

As we previously discussed, the α -old and α -young sub-samples feel the same underlying dark-matter density. If our modelling approach is correct and the radial and vertical motions can be decoupled, then the best-fit models determined from the two sub-samples should be consistent. However, we find that the dark matter densities estimated by the two sub-samples are inconsistent: the α -young sub-sample favours a model with small but non-negligible local dark matter density, whereas the α -old sub-sample favours a model that is consistent with no local dark matter. From this we conclude that our assumption was incorrect and, thus, that the radial and vertical motions cannot be treated independently. This, in turn, implies that the velocity ellipsoid is tilted.

3.3 VELOCITY ELLIPSOID TILT

The coupling between the radial and vertical motions is characterised by the tilt angle α_{tilt} of the velocity ellipsoid defined as

$$\tan(2\alpha_{\text{tilt}}) = \frac{2\overline{v_R v_z}}{\sigma_R^2 - \sigma_z^2}. \quad (3.15)$$

It is expected that σ_R and σ_z are larger for an older population of stars as a result of internal and external dynamical heating mechanisms over time (e.g. Carlberg & Sellwood 1985), as well as due to the possibility that the earliest stars were born dynamical hotter from a more turbulent disk at higher redshift (e.g. Förster Schreiber et al. 2009). However, the tilt angle can still be and remain the same for different populations, and, actually, if the (local) potential is of separable Stäckel form, has to be same. Hence, we now investigate the velocity ellipsoid for different sub-samples independently and find that, within the measurement uncertainties, the tilt angle is the same. We then combine the sub-samples to arrive at a measurement of the tilt angle, which we show to be consistent but significantly more precise than previous determinations.

3.3.1 VELOCITY ELLIPSOID OF DIFFERENT SUB-SAMPLES

As shown in the top-left panel of Figure 3.3, we divide our sample of G dwarfs into seven sub-samples in the plane of $[\alpha/\text{Fe}]$ versus $[\text{Fe}/\text{H}]$; The Voronoi binning scheme (Cappellari & Copin 2003) ensures comparable number of stars per sub-sample. We then sub-divide each sub-sample further in height $|z|$ away from the mid-plane so that each bin contains approximately 500 stars. This number of stars ensures that the MCMC discrete likelihood fits (see Section 3.1.2) yield robust results per bin on the three velocity ellipsoid components σ_R , σ_z and $\overline{v_R v_z}$. In particular, an accurate measurement of the latter cross term is essential to infer the tilt angle α_{tilt} with a precision of $\lesssim 4^\circ$, indicated by the black error bar in the top-right panel of Figure 3.3. The results from this analysis is provided in Table 3.1.

The corresponding uncertainties on the radial and vertical dispersions, shown in the bottom panels of Figure 3.3, are only $\lesssim 2\text{km s}^{-1}$. Although the dispersions change from bin to bin, within each sub-sample the dispersion is nearly constant with $|z|$, consistent with earlier findings of vertically near-isothermal behaviour of mono-abundance populations (e.g. Liu & van de Ven 2012; Bovy et al. 2012b). For the α -older and more metal-poor stars with somewhat larger Voronoi bins, the remaining variation might be ascribed to a change with height in the relative contribution of stars with different kinematics. However, for the α -younger and more metal-rich stars that are probing lower heights, a decrease in dispersion toward the mid plane is expected, but the amplitude will depend on the amount of dark matter (see also the solid and dashed curves in Figure 3.2) as well as the tilt of the velocity ellipsoid.

The top-right panel of Figure 3.3 shows a clear non-zero tilt that increases in magnitude away from the mid-plane. Since the α -older stars are typically probing larger heights, the assumption of decoupled radial and vertical motion in the above vertical Jeans analysis is likely to be more incorrect than for the α -younger stars. So the inference that we made in Section 3.2.3 – that a gravitational potential with a significant presence of dark matter is more plausible – is perhaps too premature; though we note that the velocity ellipsoid tilt is also significantly non-zero for the α -younger stars, which casts doubt on our conclusions for that sub-sample as well. we have shown here that, within the measurement uncertainties, the tilt angle at a given height is consistent between the different sub-samples. Thus, henceforth, we shall consider the sample of G dwarfs together to improve the statistical precision on the measured velocity ellipsoid tilt.

3.3.2 TILT ANGLE

The left panel of Figure 3.4 shows the tilt angle α_{tilt} of the velocity ellipsoid as function of height $|z|$ away from the mid-plane at the solar radius. The measurements are based on the MCMC discrete likelihood fitting (see Section 3.1.2), with around 1500 G-type dwarf stars per bin in height. The vertical error bars indicate the standard deviation around the mean in the α_{tilt} values

Table 3.1: Measured velocity ellipsoid components as function of height above the Galactic plane for chemically different sub-samples from Figure 3.3. The seven sub-samples are ordered in this table top down from metal-rich and α -poor to metal-poor and α -rich. The stars within each sub-sample are subdivided in different height ranges (with mean and spread indicated) after which the velocity ellipsoid components in the meridional plane are computed using the likelihood approach described in Section 3.1.2; the mean and standard-deviation of the MCMC post-burn parameter distribution are given. The tilt angle α_{tilt} follows from combing the velocity ellipsoid components as in equation (3.15).

$[\text{Fe}/\text{H}]$ (dex)	$[\alpha/\text{Fe}]$ (dex)	z (pc)	σ_{R} (km s $^{-1}$)	σ_z (km s $^{-1}$)	$\langle v_{\text{R}}v_z \rangle$ (km s $^{-1}$)	α_{tilt} (deg)	ϵ (%)
-0.07	0.11	449 \pm 124	33.5 \pm 1.3	19.0 \pm 0.8	-40 \pm 40	-3.0 \pm 2.9	1.7 \pm 0.8
		565 \pm 89	34.5 \pm 1.4	18.9 \pm 0.9	-61 \pm 42	-4.1 \pm 2.8	1.7 \pm 0.8
		667 \pm 83	37.1 \pm 1.5	19.6 \pm 0.9	-84 \pm 45	-4.8 \pm 2.6	1.2 \pm 0.8
		766 \pm 97	37.8 \pm 1.5	20.3 \pm 0.9	-92 \pm 46	-5.1 \pm 2.5	1.3 \pm 0.7
		966 \pm 357	38.1 \pm 1.3	21.3 \pm 0.8	-110 \pm 45	-6.3 \pm 2.5	1.0 \pm 0.5
-0.21	0.14	447 \pm 125	41.1 \pm 1.6	19.4 \pm 0.9	-60 \pm 46	-2.6 \pm 2.0	1.0 \pm 0.7
		563 \pm 83	40.7 \pm 1.6	20.8 \pm 0.9	-10 \pm 48	-0.5 \pm 2.2	0.9 \pm 0.6
		650 \pm 71	41.3 \pm 1.6	21.1 \pm 0.9	25 \pm 49	1.2 \pm 2.2	0.5 \pm 0.4
		739 \pm 73	43.7 \pm 1.9	21.2 \pm 1.0	-87 \pm 54	-3.4 \pm 2.1	1.0 \pm 0.9
		826 \pm 78	43.8 \pm 1.7	24.7 \pm 1.0	-177 \pm 61	-7.6 \pm 2.5	0.5 \pm 0.5
		928 \pm 104	42.9 \pm 1.6	23.8 \pm 1.0	-7 \pm 61	-0.3 \pm 2.7	0.8 \pm 0.6
		1082 \pm 158	41.9 \pm 1.6	24.9 \pm 1.0	28 \pm 63	1.4 \pm 3.2	0.5 \pm 0.4
1328 \pm 394	43.3 \pm 1.9	26.6 \pm 1.1	-106 \pm 68	-5.1 \pm 3.2	0.4 \pm 0.4		
-0.36	0.18	499 \pm 205	37.0 \pm 1.5	22.4 \pm 1.0	-47 \pm 50	-3.1 \pm 3.3	1.9 \pm 1.0
		637 \pm 176	39.4 \pm 1.6	24.7 \pm 1.0	-105 \pm 53	-6.3 \pm 3.1	1.0 \pm 0.7
		761 \pm 195	40.5 \pm 1.6	24.4 \pm 1.1	-131 \pm 57	-7.1 \pm 3.0	0.9 \pm 0.7
		893 \pm 264	40.5 \pm 1.7	23.5 \pm 1.1	-105 \pm 59	-5.5 \pm 3.0	0.8 \pm 0.7
		1188 \pm 640	41.2 \pm 1.6	24.8 \pm 1.0	-153 \pm 56	-7.9 \pm 2.8	3.1 \pm 1.1
-0.35	0.28	685 \pm 158	49.5 \pm 1.9	33.9 \pm 1.3	-58 \pm 86	-2.5 \pm 3.8	0.5 \pm 0.5
		892 \pm 104	50.0 \pm 1.9	32.7 \pm 1.3	-66 \pm 87	-2.6 \pm 3.4	1.1 \pm 0.8
		1106 \pm 106	51.5 \pm 2.1	34.0 \pm 1.4	-74 \pm 97	-2.8 \pm 3.7	0.8 \pm 0.8
		1362 \pm 134	55.7 \pm 2.4	34.9 \pm 1.5	-199 \pm 116	-6.0 \pm 3.4	1.4 \pm 1.2
		1830 \pm 489	54.5 \pm 2.6	35.3 \pm 1.4	-442 \pm 114	-13.5 \pm 3.1	1.4 \pm 1.1
-0.51	0.29	558 \pm 179	40.2 \pm 1.7	30.8 \pm 1.3	-147 \pm 72	-11.9 \pm 5.3	3.2 \pm 1.5
		734 \pm 139	43.8 \pm 2.0	32.8 \pm 1.5	-139 \pm 88	-9.1 \pm 5.6	2.8 \pm 1.6
		898 \pm 136	47.4 \pm 2.0	36.4 \pm 1.4	9 \pm 97	0.6 \pm 6.0	1.0 \pm 0.9
		1065 \pm 149	48.1 \pm 2.3	34.7 \pm 1.6	-42 \pm 99	-2.2 \pm 5.1	2.6 \pm 1.6
		1254 \pm 174	45.8 \pm 2.5	33.0 \pm 1.5	-130 \pm 99	-7.2 \pm 5.4	4.0 \pm 1.7
		1490 \pm 232	46.4 \pm 2.5	36.4 \pm 1.6	-15 \pm 111	-1.0 \pm 7.6	1.8 \pm 1.4
		1977 \pm 587	53.8 \pm 3.0	39.6 \pm 1.7	-290 \pm 116	-11.8 \pm 4.4	3.1 \pm 2.0
-0.68	0.32	623 \pm 223	55.5 \pm 2.4	39.4 \pm 1.6	-217 \pm 116	-7.9 \pm 4.1	1.7 \pm 1.4
		822 \pm 148	53.9 \pm 2.3	40.4 \pm 1.6	-222 \pm 120	-9.6 \pm 4.9	2.0 \pm 1.3
		986 \pm 146	54.8 \pm 2.5	41.4 \pm 1.8	-160 \pm 130	-7.0 \pm 5.5	3.9 \pm 2.0
		1169 \pm 156	57.0 \pm 2.4	39.0 \pm 1.8	-251 \pm 127	-8.1 \pm 4.0	3.1 \pm 1.8
		1367 \pm 178	62.2 \pm 2.6	42.9 \pm 1.8	-456 \pm 151	-12.1 \pm 3.7	1.8 \pm 1.5
		1580 \pm 201	61.2 \pm 3.0	45.1 \pm 1.9	-480 \pm 161	-14.6 \pm 4.2	2.2 \pm 1.8
		1857 \pm 256	61.9 \pm 2.9	43.7 \pm 1.8	-221 \pm 149	-6.5 \pm 4.2	1.5 \pm 1.4
2225 \pm 449	64.5 \pm 3.2	43.8 \pm 1.8	-608 \pm 171	-14.2 \pm 3.5	1.7 \pm 1.5		
-0.89	0.34	817 \pm 272	65.1 \pm 3.2	46.3 \pm 1.9	-407 \pm 179	-10.6 \pm 4.3	4.5 \pm 2.6
		1093 \pm 230	66.6 \pm 3.8	46.5 \pm 1.9	-344 \pm 179	-8.5 \pm 4.2	4.6 \pm 2.7
		1378 \pm 242	67.1 \pm 4.0	48.9 \pm 2.0	-468 \pm 202	-12.0 \pm 4.7	5.9 \pm 3.5
		1675 \pm 251	71.4 \pm 3.3	46.0 \pm 1.9	-337 \pm 186	-6.4 \pm 3.4	2.1 \pm 1.9
		2113 \pm 583	74.4 \pm 3.7	49.0 \pm 2.0	-927 \pm 68	-15.3 \pm 1.4	4.4 \pm 3.4

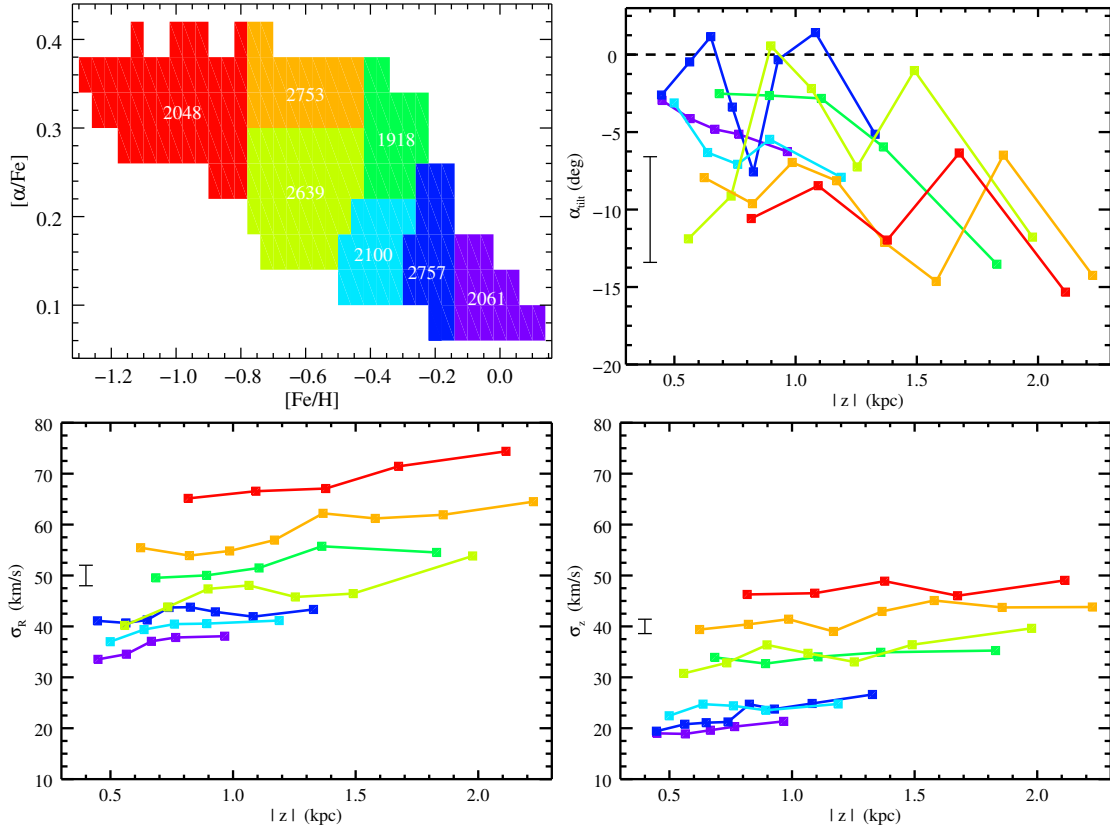


Figure 3.3: *Top left:* The sub-division of SDSS/SEGUE G-dwarf stars in the Solar neighbourhood according to their measured $[\alpha/\text{Fe}]$ abundance and $[\text{Fe}/\text{H}]$ metallicity, with the number of stars per sub-sample indicated. Position in the $[\alpha/\text{Fe}]$ - $[\text{Fe}/\text{H}]$ plane can be used as a proxy for age, which is reflected in the colours, such that from purple to red the stars become older, on average. *Top right:* Non-zero tilt angle of the velocity ellipsoid for each sub-sample as function of height away from the Galactic mid-plane. *Bottom:* Nearly flat radial (left) and vertical (right) velocity dispersion as function of height for each sub-sample. We provide the values of the above measurements in Table 3.1.

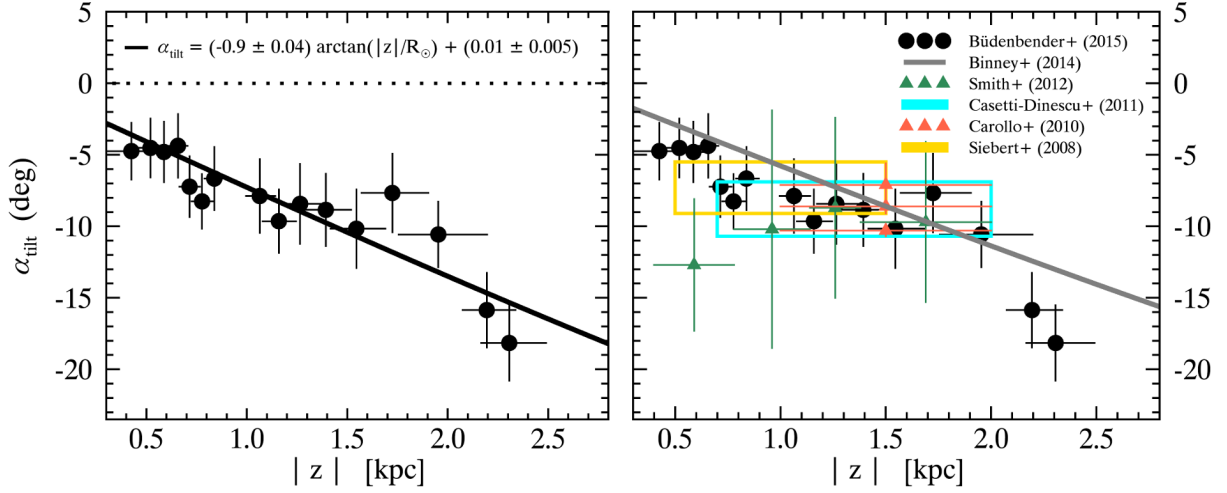


Figure 3.4: Tilt angle α_{tilt} of the velocity ellipsoid as function of height $|z|$ away from the mid-plane at the Solar radius. The filled circles are measurements with uncertainties indicated by the vertical error bars based on ~ 1000 G-dwarf stars per bin in height with the bin-size indicated by the horizontal error bars. *Left:* The tilt angle is significantly non-zero everywhere with best-fit arctan relation as indicated by the solid curve that is close to spherical alignment. *Right:* The tilt angle measurements are consistent with previous determinations, but significantly improved. The measurements of the tilt angle as well as halo contamination fraction are provided in Table 3.2.

of the MCMC chain after convergence; the horizontal error bars indicate the size of the bin in $|z|$ around the median value (see also Table 3.2).

Over the full range in height probed from about 0.4 to 2.0 kpc, the tilt angle is significantly non-zero and, thus, everywhere inconsistent with the assumption of decoupled radial and vertical motion. Whereas the latter would imply cylindrical alignment of the velocity ellipsoid, the measurements are instead consistent with a velocity ellipsoid pointing toward the Galactic centre: the solid curve represents the best-fit of the relation

$$\alpha_{\text{tilt}} = (-0.90 \pm 0.04) \arctan(|z|/R_{\odot}) - (0.01 \pm 0.005), \quad (3.16)$$

which is close to the case of alignment with the spherical coordinate system for which $\alpha_{\text{tilt}} = \arctan(|z|/R_{\odot})$.

In the case that the (local) potential is of separable Stäckel form and axisymmetric, the velocity ellipsoid is aligned with the prolate spheroidal coordinate system (e.g. de Zeeuw 1985). Expressed in cylindrical coordinates, the tilt angle is then given by

$$\tan(2\alpha_{\text{tilt}}) = \frac{2Rz}{R^2 - z^2 + \Delta^2}, \quad (3.17)$$

where $\Delta \geq 0$ is the focus of the prolate spheroidal coordinate system. The uncertainties in the tilt angle measurements allow for $\Delta/R_{\odot} \lesssim 0.24(0.42)$ within 1σ (3σ) confidence limits, which includes the limiting case of spherical alignment with $\Delta = 0$.

EFFECT OF NON-AXISYMMETRY ON TILT ANGLE

As described in Section 3.1.1, the tilt of the velocity ellipsoid is independent of the azimuthal velocity in case of axisymmetry. In the bottom panels of Figure 3.5, we show that excluding or including v_ϕ yields consistent results for the velocity ellipsoid components in the meridional plane, σ_R , σ_z and $\overline{v_R v_z}$, that make up the tilt angle. For an α -old (red) and an α -young (blue) sub-sample selected as indicated in the top-left panel, the open circles adopt a multivariate Gaussian of rank 2 in the likelihood fitting described in Section 3.1.2, while the filled squares include the azimuthal velocities in the fit by adopting a multivariate Gaussian of rank 3. The inferred values are nearly indistinguishable, so that including v_ϕ is not needed and actually would lead to slightly larger uncertainties as well as the complication that the distribution in v_ϕ is typically non-Gaussian. Even so, the inferred azimuthal mean velocity $\overline{v_\phi}$ and velocity dispersion σ_ϕ , shown in the top-middle and top-right panel, are as expected for a dynamical warmer α -old sub-sample with $\overline{v_\phi}/\sigma_\phi$ smaller than an dynamically colder α -younger sub-sample.

Restricting to the meridional plane, the mean radial and vertical motion are zero in case of axisymmetry and hence should not effect the tilt angle. In Figure 3.6, we show that even though $\overline{v_R}$ and $\overline{v_z}$ are observed to be mildly non-zero there is no significant effect on the velocity ellipsoid components and corresponding tilt angle. For the same α -old (red) and an α -young (blue) sub-sample as in Figure 3.5, the open circles show the latter quantities measured in case we set $\overline{v_R} = \overline{v_z} = 0$, while in case of the filled squares the means of the bivariate Gaussians are free parameters. The measured velocity ellipsoid components and corresponding tilt angle are again nearly indistinguishable, so that the means of the bivariate Gaussians can be safely set to zero; the number of free parameters are reduced, so that the statistical uncertainty on particular $\overline{v_R v_z}$ and thus also the tilt angle decrease. When left free, both $\overline{v_R}$ and $\overline{v_z}$ show small but significant deviations of a few km s^{-1} from zero, consistent with earlier findings (e.g. Williams et al. 2013) and in line with deviations from axisymmetry due to spiral structures (Faure et al. 2014).

3.3.3 LITERATURE COMPARISON

In the right-panel of Figure 3.4, we compare our estimate of the tilt angle as a function of distance from the mid-plane with estimates from previous studies.

Siebert et al. (2008) used 580 red-clump stars below the Galactic mid-plane from the second data release of the RAdial Velocity Experiment (RAVE), to infer a tilt angle of $7.3 \pm 1.8^\circ$ for heights $0.5 < |z|/\text{kpc} < 1.5$. Casetti-Dinescu et al. (2011) combined data from the fourth release of the Southern Proper Motion Program and the same second release of RAVE for 1450 red-clump stars above and below the Galactic mid-plane to find a tilt angle of $8.6 \pm 1.8^\circ$ for heights $0.7 < |z|/\text{kpc} < 2.0$. After accounting for the flip in sign of α_{tilt} from below to above the Galactic

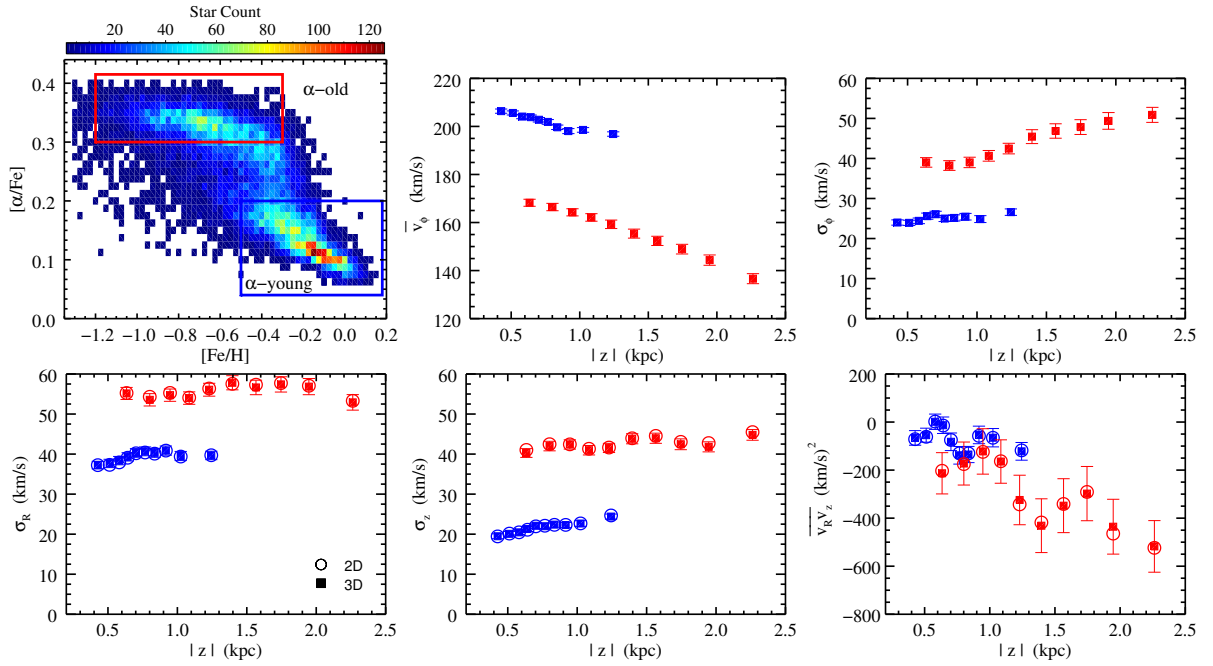


Figure 3.5: Top left: $[\alpha/\text{Fe}]$ abundances and $[\text{Fe}/\text{H}]$ metallicities of the G-dwarf stars, identical to Figure 3.2. The red and blue boxes show the selections for the α -old and α -young sub-samples, respectively. These same colours are used in all other panels. Top middle and right: Azimuthal mean velocity and velocity dispersion as function of height $|z|$ away from the mid-plane at the Solar radius. Bottom row: Radial and vertical velocity dispersion and their correlated second velocity moment for the two sub-samples. The open symbols show the results for the multivariate Gaussian velocity distribution of rank 2, while the filled symbols show the corresponding results of a multivariate Gaussian of rank 3.

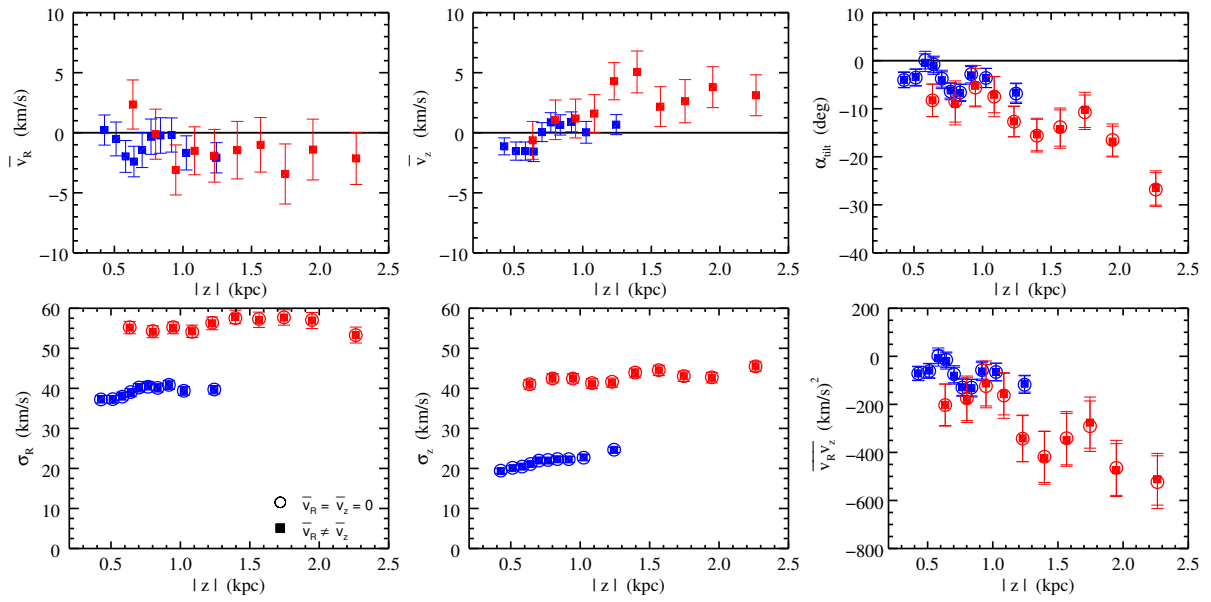


Figure 3.6: Dynamical profiles for the α -old (red) and α -young (blue) as a function of distance from the mid-plane at the solar radius. Top left: mean radial velocity. Top middle: mean vertical velocity. Top right: tilt angle of the velocity ellipsoid. Bottom left: radial velocity dispersion. Bottom middle: vertical velocity dispersion. Bottom right: correlated second velocity moment. In the latter four panels, the open symbols show the case for which we assume $\overline{v_R} = \overline{v_z} = 0$ and the filled symbols show the case where $\overline{v_R}$ and $\overline{v_z}$ are free parameters in the likelihood function (equation 3.1).

Table 3.2: Measured tilt angle (in degrees) as function of height in pc from Figure 3.4. The last column shows halo contamination fraction (in %). Their errors are estimated from the standard-deviations of the post-burn parameter distributions.

z (pc)	α_{tilt} (deg)	ϵ (%)	z (pc)	α_{tilt} (deg)	ϵ (%)
425	-4.70 ± 2.00	2.8 ± 0.8	1159	-9.60 ± 2.20	3.6 ± 1.1
520	-4.50 ± 2.10	3.3 ± 0.9	1265	-8.40 ± 2.80	4.7 ± 1.2
587	-4.80 ± 2.10	4.1 ± 1.0	1393	-8.80 ± 2.50	4.7 ± 1.4
657	-4.40 ± 2.20	3.4 ± 0.9	1545	-10.20 ± 2.80	3.7 ± 1.4
715	-7.20 ± 2.10	2.5 ± 0.8	1724	-7.70 ± 2.70	4.2 ± 1.3
777	-8.30 ± 1.90	2.4 ± 0.8	1953	-10.60 ± 2.30	5.7 ± 1.5
838	-6.70 ± 2.20	3.2 ± 0.9	2194	-15.90 ± 2.60	9.4 ± 3.1
1064	-7.90 ± 2.60	3.0 ± 1.1	2306	-18.20 ± 2.60	6.7 ± 2.9

mid-plane, Figure 3.4 shows that both measurements are consistent with our findings especially when taking into account the large range in heights around the mean $|z| \sim 1$ kpc.

Over a similar range in heights $1 < |z|/\text{kpc} < 2$, [Carollo et al. \(2010\)](#) found, based on a sample of more than ten thousand calibration stars from SDSS DR7, a consistent tilt angle of $7.1 \pm 1.5^\circ$ for stars with metallicity $-0.8 < [\text{Fe}/\text{H}] < -0.6$, but a larger tilt angle of $10.3 \pm 0.4^\circ$ for more metal-poor stars with $-1.5 < [\text{Fe}/\text{H}] < -0.8$. However, given that more metal-poor stars are relatively more abundant at larger heights, it is likely that both values are fully consistent with the $> 10^\circ$ change in tilt angle we find over this large range in height. [Smith et al. \(2012\)](#) also used SDSS DR7 data, but restricted to Stripe 82, to exploit the high-precision photometry and proper motions. They measured the tilt angle in four bins in the height range $0.5 < |z|/\text{kpc} < 1.7$ for stars with metallicity $[\text{Fe}/\text{H}] < -0.6$ and more metal-poor stars with $-0.8 < [\text{Fe}/\text{H}] < -0.5$, and concluded that, despite larger uncertainties, the tilt angles are consistent with spherical alignment of the velocity ellipsoid; the few measurements that appear at larger (negative) tilt angles they believe to be an artefact.

Recently, [Binney et al. \(2014\)](#) used $> 400,000$ stars from the fourth data release of RAVE to infer, under the assumed tilt angle variation $\alpha_{\text{tilt}} \propto \arctan(|z|/R_\odot)$, a proportionality constant of ~ 0.8 except for hot dwarfs with ~ 0.2 . The former gradient is consistent with our measurements in Figure 3.4 and the corresponding best-fit relation given in equation (3.16), but the hot-dwarfs gradient appears too shallow, although a more quantitative comparison is unfortunately not possible due to missing uncertainties on the inferred gradients.

3.4 DISCUSSION AND CONCLUSION

In this chapter, we have accurately measured the velocity ellipsoid of the Milky Way disk near the Sun. To do this, we used a well-characterised sample of >16,000 G-type dwarf stars from the *SEGUE* survey and fit their discrete kinematic data using a likelihood method that accounts for halo star contaminants. In combination with Markov Chain Monte Carlo (MCMC) sampling, we have robustly measured the velocity ellipsoid components as a function of height away from the Galactic mid-plane for a number of chemically-distinct sub-samples.

To begin, we separated our sample into two sub-samples based on their metallicity and α -element abundances. As these sub-samples are tracers of the same underlying gravitational potential, fitting Jeans models to the vertical density and dispersion profiles for each sub-sample independently should yield the same constraint on the local dark matter density. Instead, we found large variations: metal-rich, low- α -abundant stars require a significant local dark matter density, while metal-poor, high- α -abundant stars do not need any dark matter. As the latter stars are relatively more abundant at larger vertical heights, we believe this is the consequence of a coupling between vertical and radial motions that becomes stronger with height. In turn, this should be detectable as an increase in the tilt angle of the velocity ellipsoid with height.

Next, we measured the velocity ellipsoid components in the meridional plane as function of height, for seven chemically-distinct sub-samples. We found radial and vertical dispersions, σ_R and σ_z , that are approximately constant with height, consistent with the isothermally profiles found in earlier studies (e.g. Liu & van de Ven 2012; Bovy et al. 2012b). Between the sub-samples, the amplitudes of both σ_R and σ_z increase when the stars are less metal-rich and more α -abundant, in line with the age-velocity relation observed in the Solar neighbourhood (e.g. Casagrande et al. 2011). The cross term $\overline{v_R v_z}$ together with σ_R and σ_z yields a tilt angle of the velocity ellipsoid that is clearly non-zero and its amplitude indeed increasing with height.

For modelling the contamination by halo stars, we adopted a canonical single-component Galactic halo (e.g. Schönrich et al. 2011). However, several studies have suggested a two-component halo structure (e.g. Carollo et al. 2007, 2010; de Jong et al. 2010; Nissen & Schuster 2010; Kinman et al. 2012; An et al. 2013; Hattori et al. 2013). Carollo et al. (2007, 2010) showed that the outer-halo component is only dominant beyond ~ 15 -20 kpc and at metallicities $[\text{Fe}/\text{H}] < -2.0$; as our sample does not extend above 3 kpc in height, we expect negligible contamination from this component. Nevertheless, to ensure that our results are not sensitive to the particular choice of contamination model, we repeat the calculations using the inner component of the dual-halo model from Carollo et al. (2010); that is, we use dispersions $\sigma_{R,\text{halo}} = 150 \pm 2 \text{ km s}^{-1}$ and $\sigma_{z,\text{halo}} = 85 \pm 1 \text{ km s}^{-1}$ in equation (3.2). we show the results of this test in Figure 3.7; the left panel shows the contamination fraction and the right panel shows the tilt angle, both as a function of distance from the Galactic plane. In both cases, the differences in the results from the

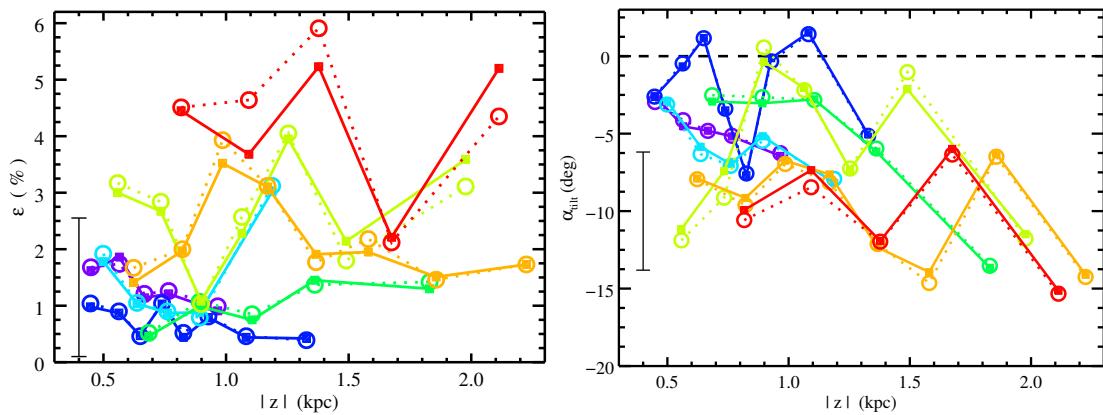


Figure 3.7: Halo contamination fraction (left panel) and tilt angle (right panel) as a function of distance from the Galactic plane for two different contamination models. The colours reflect the sub-samples as illustrated in the top-left panel of Figure 3.3. The square symbols joined with solid lines use the inner-component of the dual-halo model described in [Carollo et al. \(2010\)](#) to describe the expected halo contamination; for comparison, we show the canonical single-component halo model from [Schönrich et al. \(2011\)](#) that we adopted for this study as the open circles joined with dashed lines. The contamination fractions are very similar, regardless of the particular contamination model used, and, in turn, that the effect on the tilt angles inferred is minimal. In both panels, any differences are well within the uncertainties indicated by the error bars.

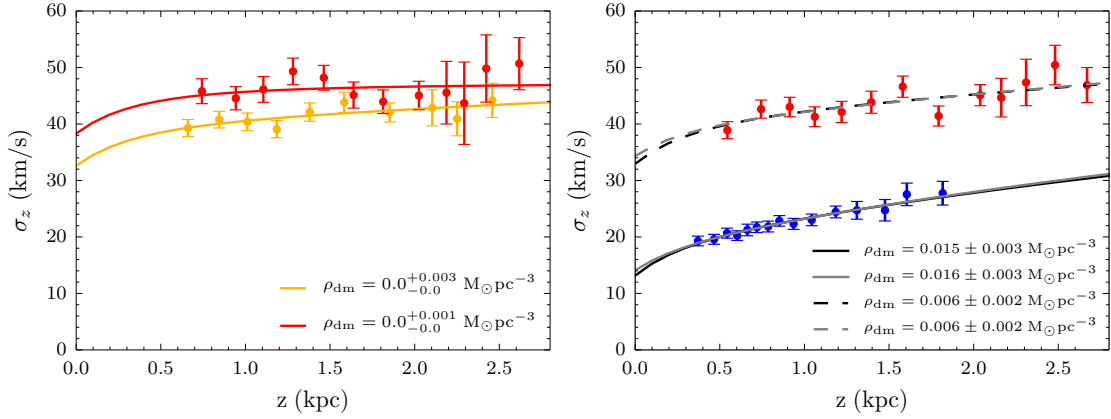


Figure 3.8: Vertical velocity dispersion as function of height; similar to Figure 3.2 where α -young and α -old stars are separately fitted by vertical Jeans models. The plots explore the effect of the metal-weak thick disk on the vertical Jeans models. **Left:** The orange and red dispersions are extracted from the subsamples coloured orange and red in Figure 3.3. The red subsample is more metal-poor and so more susceptible to the presence of metal-weak thick disk stars. The shapes of the two fitted profiles are very similar, as are the inferred local dark matter densities, indicating that the results obtained for the α -old sample are largely insensitive to metallicity (see also Figure 3.3) and, hence, to the presence of a metal-weak tail to the thick disk. **Right:** Dispersion profiles for the same α -young (blue) and α -old (red) subsamples as shown in the bottom-right panel of Figure 3.2. Dashed lines show fits to the α -old subsample and solid lines show fits to the α -young subsample. The black lines are the original fits, also shown in Figure 3.2. The grey lines are fits with the metal-weak thick disk explicitly added to the gravitational potential. Once again, there is no significant difference in the fits or the inferred local dark matter density.

two different halo models are well within the uncertainties and, thus, the results from our vertical Jeans models remain unchanged.

Some studies have also found indications of a metal-weak tail of the thick disk (MWTD; e.g. Chiba & Beers 2000 and references therein). If MWTD stars are present in our sample, they would be found among the α -old thick-disk stars, primarily at lower metallicities. To test the effect they have on our results, we repeat the analysis from Section 3.2.3 using the red and orange sub-samples selected in Figure 3.3 as these two subsamples have similar (high) α abundances but different metallicities. We show the results of this test in the left panel of Figure 3.8: the more metal-poor red subsample is shown as red points and the fitted Jeans model as a red line; the more metal-rich orange subsample is shown as orange points and the fitted Jeans model as an orange line. The shapes of the two fitted profiles are very similar, indicating that the presence of any MWTD stars will have a negligible effect on the vertical Jeans model results.

Even so, we perform a further test to verify this expectation: We repeat the full Section 3.2.3 analysis, but now consider the MWTD as an independent stellar population as suggested by

Carollo et al. (2010) and include a second thick disk component with exponential scale height 1.3 kpc and scale length of 2 kpc, in addition to a thick disk with 0.51 kpc and 2.2 kpc as exponential scale height and length. We show the results of this test in the right panel of Figure 3.8. As before, the red and blue points show the dispersion profiles calculated from the α -old and α -young subsamples. The black lines show the original fits from Section 3.2.3 and the grey lines show the new Jeans model fits with the MWTD explicitly included. It is clear that adding the extra MWTD component does not change our results. This further supports our conclusion that the differences between the α -old and α -young subsamples is due to the incorrect assumption regarding the separability of the radial and vertical motions and not because of missing components in our Galactic model.

As the tilt angle measurements between the sub-samples are fully consistent within the error bars, we were able to decrease the statistical uncertainties by combining all G dwarfs. This yields a tilt angle as function of height that is consistent with previous determinations, but significantly improved. The resulting measurements given in Table 3.2 are very well fitted by the relation $\alpha_{\text{tilt}} = (-0.90 \pm 0.04) \arctan(|z|/R_{\odot}) - (0.01 \pm 0.005)$, which is close to alignment with the spherical coordinate system and hence a velocity ellipsoid pointing to the Galactic centre.

In the case of a Stäckel potential, the tilt of the velocity ellipsoid is directly coupled to the shape of the gravitational potential and thus *must* be the same for any sub-sample. In case of oblate axisymmetry the velocity ellipsoid is then aligned with the prolate spheroidal coordinate system. The resulting expression for the tilt angle (eq. 3.17) can describe the tilt angle measurements as long as the focus of the latter coordinate systems is significantly smaller than the solar radius. Even if the Stäckel potential is only a good approximation locally, this brings a convenient, and often fully analytical, expression of dynamical aspects that otherwise, even numerically, are very hard to achieve. One such example is the use of a local Stäckel approximation to infer the integral of motions or actions (Binney 2012).

In the next chapter, we obtain a solution of the axisymmetric Jeans equations along curvilinear coordinates that allows us to construct in a computationally efficient way models that allow for a non-zero tilt of the velocity ellipsoid. In this way, we can overcome the assumption of decoupled motion in the vertical Jeans models, while still being able to do a discrete likelihood fit with MCMC parameter inference, even for many thousands of stars at the same time. Among other benefits, this will enable a much more accurate measurement of the local dark matter density, especially with upcoming data from Gaia and spectroscopic follow-up surveys such as Gaia-ESO (Gilmore et al. 2012) and 4MOST (de Jong et al. 2012).

THE DARK MATTER DENSITY IN THE SOLAR NEIGHBOURHOOD FROM AXISYMMETRIC JEANS MODELS

The local dark matter density is of special interest for direct detection experiments, because they require an independent determination of it to precisely estimate the interaction rate of dark matter particles in the detectors. A successful detection would bring us considerably closer to the nature of dark matter. Moreover, the local dark matter density can give insights into the shape of the local halo. A flattened oblate shape, for example, and a concentrated dark matter distribution along the Galactic disk would suggest the presence of a dark matter disk in the Milky Way (Read et al. 2009; Bruch et al. 2009), setting constraints on galaxy formation models and cosmological simulations (e.g. Macciò et al. 2007; Lux et al. 2012), if a Milky Way-like spiral galaxy should be reproduced.

The accuracy of local dark matter density measurements improved a lot after the launch of the Hipparcos space telescope (Perryman et al. 1997). Hipparcos provided for the first time accurate parallaxes and proper motions for $\approx 100,000$ stars with distances up to 100 pc. Before, distance estimates to stars relied on “photometric” distances, which were not well calibrated. Moreover, early samples used to trace the vertical gravitational potential were contaminated with young, dynamically not well-mixed stars and authors often treated the stellar populations as isothermal. As a possible consequence in the early analyses of the local mass density, the results on the local dark matter density were strongly scattered - from a significant contribution of dark matter of the order $\sim 40\%$ (Jeans 1922; Oort 1960; Bahcall et al. 1992) to no explicit need for a dark component (Kapteyn (1922); Oort (1932); Bienayme et al. (1987); Flynn & Fuchs (1994)). It is interesting to note, that Bahcall et al. (1992) and Flynn & Fuchs (1994) obtained contradicting results although they used similar datasets. Kuijken & Gilmore (1989a) did not find evidence for substantial amounts of dark matter in the disk as well, but they estimated the most precise total surface density of $\Sigma_{1,1} = 71 \pm 6 M_{\odot} \text{pc}^{-2}$ at that time and accounted for various previously ignored biases. They collected an almost volume-complete sample of K-type stars and added a

correction for the tilt-term in the Jeans-equation by assuming spherical alignment of the velocity ellipsoid, which is normally neglected in the derivation of the vertical Jeans model.

After the data from Hipparcos became available, the significance of the dark matter measurements were boosted, but [Holmberg & Flynn \(2000, 2004\)](#) and [Bienaymé et al. \(2006\)](#) did not find a discernable dark matter fraction. Until then, the common concensus was that the local disk contains, if at all, only very little dark matter. This picture has changed with the advent of SDSS/SEGUE ([Yanny et al. 2009](#)), when a large number of stellar tracers became available sampling a much large volume around the sun, reaching heights $z > 1$ kpc. Since the disk near the Galactic mid-plane is dominated by baryonic matter, we have to use tracers above $z = 1$ kpc to disentangle the disk and dark halo contribution to the gravitational potential. This is also known as the disk-halo degeneracy, which was one reason why earlier studies could not find a significant dark matter fraction. [Zhang et al. \(2013\)](#) estimated in a recent analysis of SEGUE K dwarfs the dark matter density $\rho_{\text{dm}} = (0.0065 \pm 0.0023) M_{\odot}\text{pc}^{-3}$, which is small but significantly different from zero. [Bovy & Tremaine \(2012\)](#); [Bovy & Rix \(2013\)](#) attained similar results. Also, [Bovy & Rix \(2013\)](#) determined from 16,000 SEGUE G dwarfs the best estimated total surface density and scale length of the disk to date, which are $\Sigma(z = 1.1 \text{ kpc}) = 68 \pm 4 M_{\odot} \text{pc}^{-2}$ and $h_R = 2.15 \pm 0.14$ kpc, respectively. However, [Garbari et al. \(2012\)](#) and [Bienaymé et al. \(2014\)](#) determined a larger dark matter density of $\rho_{\text{dm}} = (0.022 \pm 0.014) M_{\odot}\text{pc}^{-3}$ and $\rho_{\text{dm}} = (0.014 \pm 0.001) M_{\odot}\text{pc}^{-3}$, respectively. Despite the different current results, it is promising that the estimates on the local dark matter will slowly converge with better and better data. The recent estimates already agree within a 2σ confidence interval.

Almost all of the past local dark matter studies are one dimensional, relying on the vertical Jeans equation (e.g. [Zhang et al. 2013](#); [Garbari et al. 2012](#)) or a 1D distribution function (e.g. [Kuijken & Gilmore 1989a](#); [Flynn & Fuchs 1994](#)). In this case they can only use tracers below $z = 1$ kpc. Above this height, the correlation between the radial and vertical motion leads to a decrease in the vertical velocity dispersion, as seen in [Figure 3.2](#). Hence, we would underestimate the resulting dark matter density. [Statler \(1989\)](#) used distribution functions based on Stäckel potentials to estimate the effect to be about 10% at $z = 1$ kpc. Some authors corrected for this effect either by adding an approximated correction term to the vertical Jeans equation ([Kuijken & Gilmore 1989a](#)) or by using Stäckel potentials ([Bienaymé et al. 2014](#)), in which they specified the tilt of the velocity ellipsoid. On the other hand, [Bovy & Rix \(2013\)](#) and [McMillan \(2011\)](#) used axisymmetric distribution functions based on action integrals in order to model the distribution of tracers along the radius and the height of the disk. These models going beyond a 1D approximation are still quite rare. Cappellari's [2008](#) axisymmetric Jeans model neglects the tilt of the velocity ellipsoid and is therefore only used for external stellar systems, where it is assumed that correlated motions within these systems have little effect on the observed line-of-sight velocities. There are also solutions to the axisymmetric and triaxial Jeans equations with the assumptions of Stäckel potentials (e.g. [van de Ven et al. 2003](#)). They should be a good ap-

proximation to the true potential as long as we do not use tracer objects near the Galactic centre, where the Stäckel potentials with a central core might not be able to represent the expected cuspy total density distribution.

We have already introduced in Section 2.4 a solution to the axisymmetric Jeans equations that uses the prolate spheroidal coordinate system¹ and allows for an arbitrary gravitational potential. Furthermore, we can fit the tilt of the velocity ellipsoid together with the potential due to the flexibility of the spheroidal coordinates. We explain how we applied it to the SEGUE G dwarfs in Section 4.1. Several parameters are usually degenerate in a dynamical model. Therefore we properly explore the parameter space with the help of a MCMC. We present our results on the local dark matter density in Section 4.2 and we discuss them in light of other work in Section 4.3.

4.1 SETUP OF THE JEANS MODEL

4.1.1 TRACER POPULATION

A Jeans model relates the velocity dispersion and the density distribution of a tracer population to the gravitational potential. But in contrast to other dynamical models outlined in Section 1.3, only kinematical information, in particular the second velocity moment, is used to recover the potential. We can either fit the density distribution separately and then substitute the parameterised density into the Jeans model, or fit the density and the second moments simultaneously. In this way, the model takes care of the needs of the kinematics regarding the density profile as well. As an example, a steeper slope of the density profile shifts the vertical velocity dispersion $\sigma_z(z)$ as function of vertical height uniformly to a larger value. For the application of the model to the G dwarfs we adopt the approach to simultaneously fit the tracer density and kinematics. The strongest constraint on the density parameters comes from the measured density profile itself, because it can be measured more accurately. The density parameters are degenerate with the gravitational potential or the total mass. However, we can break this degeneracy by using multiple tracer (sub-)populations. Then the velocity dispersion of each population is independently shifted by the gradient of its density profile, but changing the total mass of the system shifts the velocity dispersion of all tracers equally.

Bovy et al. (2012c,b) discovered that mono-abundance populations have quite simple density and velocity dispersion profiles. The density takes the form of a single exponential and the velocity dispersion is isothermal. They splitted their G-type dwarf sample in small bins of α -element and iron abundance. If we want to determine the local fraction of dark matter, we

¹This is the same coordinate system in which the Stäckel models are used. But we do not restrict ourselves to Stäckel potentials.

should divide the tracer population into sub-samples with different ages in general. A population containing stars with a large spread of ages can mimic a large amount of dark matter, since the velocity dispersion is age dependent and older stars with a larger velocity dispersion are mainly found at larger vertical height, where the contribution of dark matter also increases.

For these reasons, we split the SEGUE G-type dwarf sample, that we presented in Section 2.2, into 7 sub-samples in $[\alpha/\text{Fe}]$ - $[\text{Fe}/\text{H}]$ space, as already done for the measurement of the local velocity dispersions in Section 3.3.1. Now, since the axisymmetric Jeans models take into account both the height and radius, we use the full sample that spans from around 6 to 12 kpc in radius. So, each of the 7 abundance bins contains more stars, see Figure 4.6. As in Chapter 3, we use the terms “ α -young” and “ α -old” to distinguish between the more metal-rich, lower α -abundant stars and the more metal-poor, higher α -abundant stars. Figure 4.1 shows the spatial distribution of the abundance bins in the R-z plane. The sun is located at $(R, z) = (8, 0)$ kpc. Because the three α -young sub-samples in the bottom panel contain younger stars, they are more concentrated to the mid-plane. There is also a mild tendency that the stars in the α -younger bins are preferentially located to the outer part of the disk with respect to the sun, in contrast to the α -older bins. The majority of α -young stars is located closer to mid-plane of the disk than the α -old stars. As light-absorbing dust is concentrated to the mid-plane with increasing density to the inner part of the galaxy, we observe this directional unbalance of α -young stars.

After the separation in the abundance sub-samples, we divide each sub-sample on a grid in R and z . Then we calculate the number density of every (R, z) -bin by using the method outlined in Section 2.2.2 for the estimation of the effective volume, which includes explicitly the selection function. The number density is then simply the ratio of the number of stars in the (R, z) -bin and of the effective volume: $\nu_{\star}(R_i, z_j) = N_{ij}/V_{ij,\text{eff}}$. We approximate the density profile of sub-sample s with a double exponential:

$$\nu_{\star,s}(R, z) = \nu_{0,s} e^{-|z|/\zeta_{z,s}} e^{-R/\zeta_{R,s}}, \quad (4.1)$$

where $\zeta_{R,s}$ and $\zeta_{z,s}$ are the exponential scale length and height, respectively. We calculate the normalisation $\nu_{0,s}$ from the requirement that the Chi-Squared $\chi^2 = \sum_i \frac{(v_{\text{obs},i,s} - \nu_{\star,s})^2}{\Delta v_{\text{obs},i,s}^2}$ is independent of $\nu_{0,s}$, since the normalisation itself is difficult to determine directly and it cancels out in the Jeans model. Solving for the normalisation in the equation $\frac{\partial \chi^2(\nu)}{\partial \nu_{0,s}} = 0$ gives

$$\nu_{0,s} = \frac{\sum_i^{N_s} \exp(-R - z) \frac{v_{\text{obs},i,s}}{\Delta v_{\text{obs},i,s}}}{\sum_i^{N_s} \frac{\exp\left[-R\left(1 - \frac{1}{\zeta_{R,s}}\right)\right] \cdot \exp\left[-z\left(1 - \frac{1}{\zeta_{z,s}}\right)\right]}{\Delta v_{\text{obs},i,s}}} \quad (4.2)$$

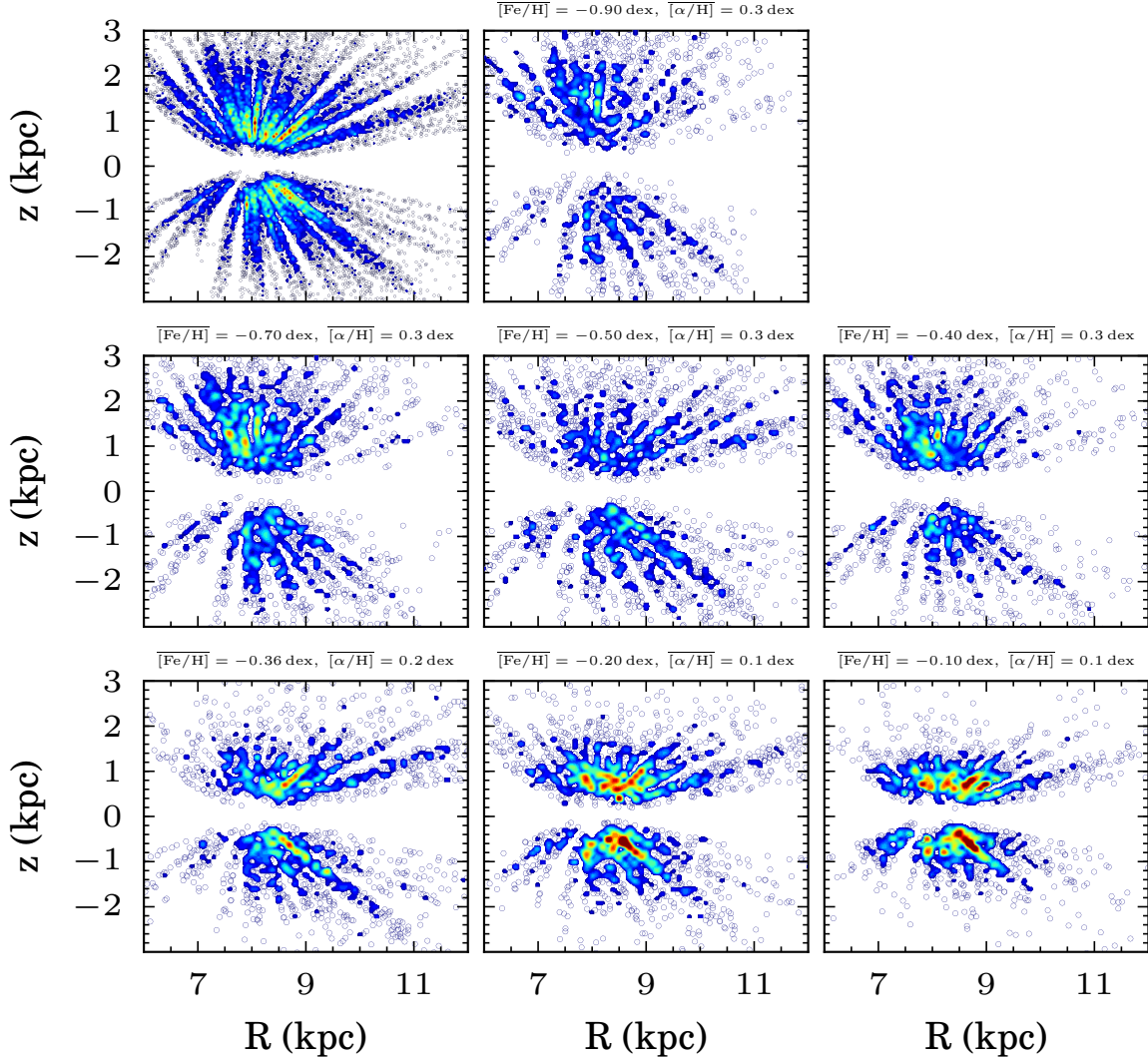


Figure 4.1: Radial and vertical extent of the 7 abundance sub-samples, displayed as coloured contours in regions of higher density, otherwise single stars are plotted. The top right panel shows the extend of the whole sample and the other panels the stars in the 7 abundance bins, starting with the α -oldest sub-sample in the middle of the top row to the α -youngest one in the bottom left corner. The mean metallicity and α -abundance of the sub-sample is indicated on top of each panel.

with the sum over all (R,z)-bins of the specific sub-sample, in which the density $v_{\text{obs},s}$ and its uncertainty $\Delta v_{\text{obs},s}$ is measured. The resulting log-likelihood of the density distribution is given by

$$\ln \mathcal{L}_v = \ln \mathcal{L}(\zeta_R, \zeta_z | v_{\text{obs}}, \Delta v_{\text{obs}}) = \sum_s \sum_i^{N_s} -\ln \left(\sqrt{2\pi} \Delta v_{\text{obs},i,s} \right) - \frac{1}{2} \left(\frac{v_{\star,s}(R_i, z_i) - v_{\text{obs},i,s}}{\Delta v_{\text{obs},i,s}} \right)^2 \quad (4.3)$$

The use of the likelihood fitting technique allows to add the likelihood of the tracer density to the likelihood of the velocity distribution (see Section 3.1.2), thus linking the axisymmetric Jeans model to the underlying density distribution. Each sub-sample carries its two free density parameters, the scale height and scale length, in the likelihood fitting, which already makes 14 free parameters in the model on 7 sub-samples.

Another set of 8 free parameters connected to the tracer population comes from the velocity anisotropy, which is defined in equation 2.19 with respect to the prolate spheroidal velocities v_λ and v_ν . These 8 parameters consist of the 7 κ_s and p^2 . The latter, p^2 , controls the gradient of the anisotropy with respect to the spheroidal coordinate λ , for which the anisotropy will be equal to κ_s if $p^2 = 1$. Otherwise, the anisotropy of the sub-sample increases with radius to κ_s at large radii. The cylindrical velocity dispersions σ_R and σ_z are deduced from both σ_λ and σ_ν (see equation 2.16), but the largest contribution to σ_z comes from σ_ν . Thus, σ_z strongly depends on the velocity anisotropy.

If the assumption in equation 2.19 of an increasing anisotropy with radius is correct, we should be able to determine the shape of the velocity anisotropy in the range $6 < R/\text{kpc} < 12$. This makes a total of 22 free parameters for the tracer sub-samples. If we splitted the G-type dwarf sample into smaller abundance bins as done in Bovy & Rix (2013), it would not be feasible anymore to fit the density and velocity anisotropy of all tracer sub-samples simultaneously.

4.1.2 GRAVITATIONAL POTENTIAL

We use two different sets of potentials for the disk and the dark halo. Both sets have only the bulge component in common, for which we adopt a spherical exponential density, given by Dwek et al. (1995).

$$\rho_{\text{bulge}} = \rho_{b,0} \cdot \exp \left(-\frac{\sqrt{R^2 + z^2}}{a} \right) \quad (4.4)$$

where $\rho_{b,0}$ is the density normalisation with respect to the Galactic centre and a marks the scale radius. This density profile is actually based on the luminosity. Therefore we assume a constant mass-to-light ratio for the bulge to convert the luminosity into a mass density. We fix the mass of the bulge to $M_b = 6 \cdot 10^9 M_\odot$ and $a = 0.8 \text{ kpc}$. Cao et al. (2013) determined the scale lengths of the triaxial bulge to be smaller than 1 kpc for all three axes; therefore the scale radius of the ‘‘spherical’’ bulge would be smaller than 1 kpc as well. There is of course little possibility to

constrain any of the bulge parameters from our data that only reaches $R > 6$ kpc. Moreover, the bulge is made of a triaxial rotating bar and we have only an axisymmetric model, so that it is not possible to fully model the details of its triaxial shape. [Wegg & Gerhard \(2013\)](#) found that the density distribution falls off exponentially. Therefore a spherical exponential density distribution is sufficient to account for the contribution of the bulge to the total potential. From equation 2.28 in [Binney & Tremaine \(2008\)](#), the potential follows as

$$\Phi_{\text{bulge}}(r) = -4\pi G\rho_{b,0} \left[\frac{2a^3}{r} \left(1 - \exp\left(-\frac{r}{a}\right) \right) - a^2 \exp\left(-\frac{r}{a}\right) \right] \quad (4.5)$$

with $r = \sqrt{R^2 + z^2}$.

The first set of potentials includes only analytical forms, that are quick to calculate, so that we can use them to test the model. The stellar disk component of this set is represented by a Miyamoto-Nagai potential ([Miyamoto & Nagai 1975](#))

$$\Phi_{\text{disk}} = -\frac{GM_d}{\sqrt{R^2 + \left(h_R + \sqrt{z^2 + h_z^2}\right)^2}} \quad (4.6)$$

where the scale height $h_z = 0.4$ kpc is fixed and the disk mass M_d and the disk scale length h_R are free parameters. We cannot constrain h_z with our data, because we would rather need more data at lower latitudes to be sensitive enough to the mass distribution of the disk. Likewise, we assume a Miyamoto-Nagai potential with fixed parameters $M_{\text{gas}} = 1 \cdot 10^{10} M_{\odot}$ and $h_{z,\text{gas}} = 0.1$ kpc for the gaseous disk. The scale length of the gas disk is coupled with twice the scale length of the stellar disk $h_{R,\text{gas}} = 2h_R$ as suggested by [Binney & Tremaine \(2008\)](#).

The dark halo is approximated with the logarithmic, spherical potential

$$\Phi_{\text{DM}} = v_0^2 \ln \left(1 + \frac{R^2 + z^2}{d^2} \right), \quad (4.7)$$

which is cored in the centre and the scale radius is fixed to $d = 12$ kpc. The velocity v_0 measures the dark matter density.

The second set of potentials are more realistic, especially the disk component. The latter is described by an exponential distribution $\rho_{\text{disk}}(R, z) = \Sigma_0 / (2h_z) e^{-R/h_R - |z|/h_z}$, where the corresponding potential is numerical and contains a Bessel function of the first kind of order zero.

$$\Phi_{\text{disk}} = -2\pi G\Sigma_0 h_R^2 \int_0^{\infty} dk J_0(kR) \left(1 + k^2 R^2 \right)^{-3/2} \frac{e^{-k|z|} - kh_z e^{-\frac{|z|}{h_z}}}{1 - (kh_z)^2} \quad (4.8)$$

The scale height is fixed to be $h_z = 0.4$ kpc, while h_R is a free parameter again. The mass of the disk is computed from the simple relation $M_d = 2\pi\Sigma_0 h_R^2$. The gaseous disk is similarly described by an exponential density, where the local surface density is $13 M_{\odot} \text{pc}^{-2}$, $h_{z,\text{gas}} = 0.1$ kpc and

again $h_{R,\text{gas}} = 2h_{R,\text{disk}}$. The second dark halo potential takes the form of a spherical Navarro-Frenk-White (NFW) profile (Navarro et al. 1996):

$$\rho_{\text{NFW}} = \frac{\rho_{0,h}}{\frac{r}{r_h} \cdot \left(1 + \frac{r}{r_h}\right)^2}, \quad (4.9)$$

with a central density $\rho_{0,h}$ and a characteristic radius r_h . The mass of the NFW profile is often expressed in terms of the virial mass M_{vir} . The characteristic radius is replaced by the ratio of the virial radius r_{200} and the mass concentration c_{200} . There, r_{200} is defined as the radius where the mean density within that radius is 200 times larger than the critical density $\rho_c = \frac{3H_0^2}{8\pi G}$. H_0 is the Hubble constant and the mass within r_{200} is defined as

$$M_{200} = \frac{200r_{200}^3 H_0^2}{2G}, \quad (4.10)$$

yielding the NFW potential

$$\Phi_{\text{NFW}} = -\frac{GM_{200}}{\ln(1 + c_{200}) - \frac{c_{200}}{1+c_{200}}} \frac{\ln\left(1 + \frac{rc_{200}}{r_{200}}\right)}{r} \quad (4.11)$$

Of course, there is also a stellar component in the halo. But since in mass it is less than 0.1%, it can be neglected. To keep the functional form of the potentials in this section short and for a better recognition, the potentials are given in cylindrical or spherical coordinates. However, our axisymmetric Jeans model uses the prolate spheroidal coordinate system (λ, ϕ, ν) .

4.1.3 VELOCITY DISTRIBUTION

Pure Jeans models only allow to recover the potential from binned data². If we want to find the best fitting model by comparing it with the position and velocities of every star individually and assigning a specific likelihood to each star, we will need some kind of velocity distribution for the tracer population. Then, the predicted second moment of the Jeans model corresponds to the standard deviation of the velocity distribution.

We assume a bi-variate Gaussian, as already successfully applied to a sub-sample of this data set in Chapter 3 to measure the tilt angle as function of height. Such a two dimensional distribution also allows for the measurement of the tilt of the velocity ellipsoid through the cross-term $\overline{v_R v_z}$. The likelihood for the disk is given in equation 3.1. The second likelihood function 3.2 accounts for the broader velocity distribution of possible halo stars in our sample. The fraction of halo stars has been a free parameter in the model for every abundance bin and in principle

²The observed velocity dispersion is an average property of an ensemble of stars and cannot be measured for a single star. Only with the help of dynamical models, one can assign to every star a specific velocity dispersion that depends on the position of the star.

we should make it as a free parameter in the axisymmetric Jeans model as well. However, this would unnecessarily increase the number of free parameters by seven, as the fraction does not strongly vary from one sub-sample to another. In Section 3.3.1, we have estimated the fraction of halo stars for the 7 abundance bins. The scatter is moderate throughout the abundance bins, but the metal-poor sub-samples definitely contain a larger fraction of halo stars than the metal-rich sub-samples. On the other side, it is expected that the fraction increases with the height above the Galactic mid-plane. This is roughly visible in Figure 4.2, where the halo fractions of the abundance bins are shown as a function of z between $7 < R/\text{kpc} < 9$. The fractions are coloured in the same way as indicated in Figure 4.6. Therefore, we adopt two linear functions ($\epsilon = ax + b$) to the metal-poor bins and metal-rich bins³ Those are fitted to the halo contamination fractions in Figure 4.2 with a linear-least-square routine (black solid and dashed lines) and yield

$$\begin{aligned}\epsilon_{\text{mr}} &= (0.004 \pm 0.006) \cdot z + (0.006 \pm 0.006) \\ \epsilon_{\text{mp}} &= (0.016 \pm 0.011) \cdot z + (0.012 \pm 0.012)\end{aligned}\tag{4.12}$$

where ϵ_{mr} and ϵ_{mp} are the contamination fractions of the metal-rich and the metal-poor sub-samples, respectively. The errors are obtained with the bootstrap method. When including them in the likelihood 3.2 and the MCMC, the values of ϵ_{mr} and ϵ_{mp} are sampled from their Gaussian error distribution. In this way, we can marginalise over the large uncertainty in them.

Theoretically, it should also be feasible to measure the tilt of velocity ellipsoid, since we use a multivariate Gaussian and we can adjust the focal point of the prolate spheroidal coordinate system to match the variations of the tilt angle throughout the disk, at least, if the absolute tilt rises linearly with z . In Section 3.3, we showed that this is a good approximation. The parameter q^2 is free to control the tilt and α , the other parameter of the coordinate system, is fixed to -150 kpc^2 . Both directly constrain the tilt via the focal point $\Delta^2 = -\alpha \cdot (1 - q^2)$ in equation 2.17.

The link between the axisymmetric Jeans model and the velocity distribution are the velocity dispersions. The axisymmetric Jeans model returns the velocity dispersions in prolate spheroidal coordinates. we convert them to the cylindrical dispersions σ_R , σ_z and $\overline{v_R v_z}$ using equation 2.16 and insert them into the likelihood 3.1. The combined disk and halo likelihood for a single star is given in equation 3.3. The product of the likelihoods for all stars results in the total likelihood 3.4 of the velocity distribution.

4.1.4 ACCELERATED COMPUTATION

With the help of the MCMC likelihood approach, we can fit the data in a discrete way, avoiding spatial binning of the data in any way. Binning always means a loss of information, as it smears

³In this case, the cyan, lime green, orange and red abundance bins belong to the metal-poor sub-samples and the purple, blue and green abundance bins to the metal-rich sub-samples.

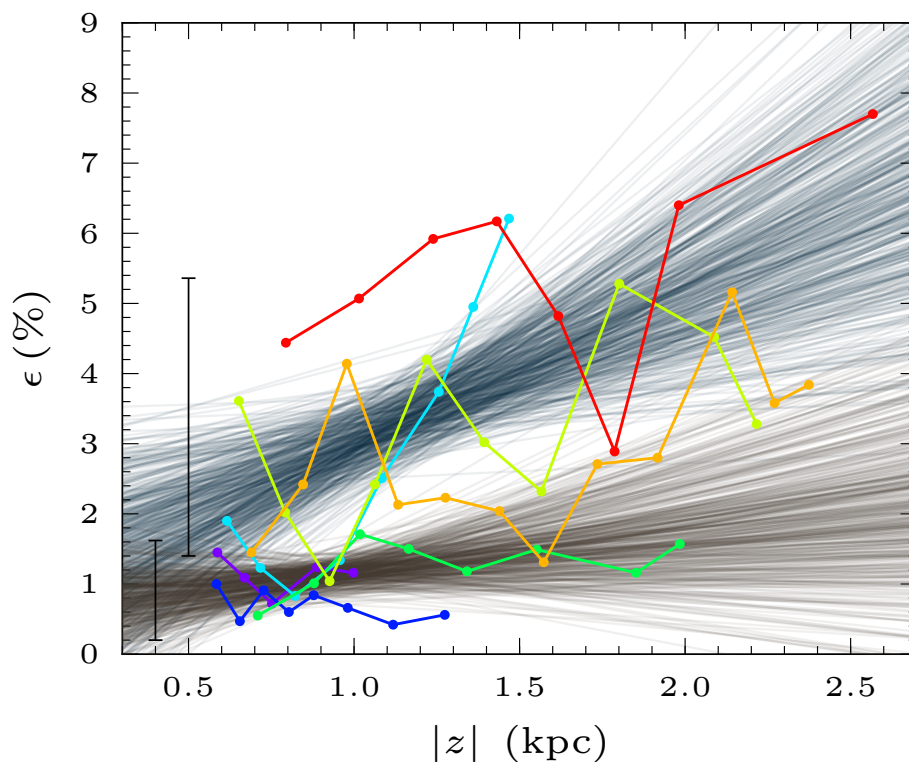


Figure 4.2: Halo contamination fractions of the 7 abundance sub-samples, that are coloured like in Figure 4.6. The transparent brown lines reflect the uncertainty in the linear fit to the metal-rich sub-samples (purple, blue, green) and the transparent blue-grey lines reflect the uncertainty in the linear fit to the more metal-poor sub-samples (cyan, lime green, orange, red). These linear relations are used for the velocity distribution to calculate the approximate probability of halo contamination for each star based on its vertical height above the mid-plane.

out individual features or it weights regions in data space with a large outlier fraction similarly as other regions. But the discrete handling of the data also means that we have to evaluate the model as many times as we have stars, instead of evaluating it just for few bins. This provides an additional challenge for the computing costs, especially if we have to deal with millions of stars, which will be the case when the Gaia data will be released. The axisymmetric Jeans model is quite fast with analytic potential; it takes about 6 hours for 1000 steps with 100 walkers each and 25,000 stars on 50 CPUs. The use of a numerical potential implies a double-integral to be solved, which increases the workload by a factor 50 - 100. Therefore we implemented our code into the GPU framework, that can compute many more processes in parallel than the CPU. This has speeded up the code significantly, such that a MCMC takes ~ 1 hour on 1 GPU for the analytical potentials and ~ 4.5 hours on 10 GPUs for the numerical potential with the same number of stars and steps as in the above quoted CPU case. If our sample contains several million stars in the near future, one can implement a grid in the spatial coordinates on which the velocity dispersions of every star is interpolated. So the computation time should not increase due to an increase of tracer objects.

4.2 LOCAL DARK MATTER DENSITY

In this section, we present the results of the axisymmetric Jeans model on the G-type dwarf sample. We show that separate fitting of the tracer densities might lead to different results in comparison to simultaneous fits of the density and kinematics. First, we use the analytic potential to be able to efficiently investigate various aspects of the model. After we present the fiducial analytic model and show the difference with the exponential-disk model, we test the influence of various parameters on the dark matter density. Throughout the different model runs, we fix certain parameters, that are marked with an * in Table 4.1. In general, there are 26 free parameters, among them 3 belong to the potential and 21 to the tracer sub-samples. The remaining 2 are the anisotropy turnover p^2 and the tilt q^2 . To ensure that all these parameters converge, we run the MCMC for 3500 iterations with 100 walkers. We use for all the tests the analytic potential and marginalise over the fixed scale lengths of the tracer sub-samples that we estimate in the fiducial run⁴. Thus, we can reduce the number of steps taking less time per run.

4.2.1 TRACER DENSITY AND KINEMATICS: SEPARATE VERSUS SIMULTANEOUS FIT

As we explained in Section 4.1.1, we fit the tracer densities simultaneously with the kinematics. Figure 4.3 shows the number densities of all sub-samples as a function of height for the solar

⁴We checked before that this will not introduce a bias in the results of the test runs.

cylinder and the resulting fits from the MCMC. The α -age⁵ of the sub-sample increases from the bottom to the top panel, while the corresponding mean $[\alpha/\text{Fe}]$ and $[\text{Fe}/\text{H}]$ values are given within each plot together with the scale height of the best model. The fits are almost all acceptable with the exception of the most metal-rich and the most metal-poor sub-sample - these are the bottom left and top left panel.

The metal-rich sub-sample indicates a similar dichotomy as already known for the thin and thick disk, that is the slope of the number density is smaller at $z \gtrsim 1.6$ kpc. A similar behaviour with a weaker magnitude also occurs in the next abundance bin, while it fades away the α -older the sub-samples become. This suggests that the density of our metal-rich bins would probably be better described by a double exponential. [Bovy et al. \(2012c\)](#) found that single exponentials well describe all monoabundance populations, but our bin sizes in $[\alpha/\text{Fe}]$ - $[\text{Fe}/\text{H}]$ are larger, so that it is likely that the break will vanish if we subdivide the abundance bins further.

The α -oldest sub-sample seems to underestimate the density slope, giving rise to a larger scale height, because the kinematics demand a larger vertical velocity dispersion and hence a larger scale height. The simultaneous fit with the MCMC yields $\zeta_z(\overline{[\text{Fe}/\text{H}]} = -0.95) = 1.15 \pm 0.05$ kpc. When we fit the density distribution directly the scale height is $\zeta_z(\overline{[\text{Fe}/\text{H}]} = -0.95) = 0.83$ kpc. We can verify the model if we compare the predicted velocity dispersion with the direct measurement from [Chapter 3](#). [Figure 4.4](#) plots the directly measured vertical velocity dispersion of the two α -oldest subsamples (orange and red circles) as a function of z at $R = 8$ kpc, which we have measured in [Chapter 3](#) from direct fits of the velocity distribution function. The solid lines show the best fit axisymmetric Jeans model, where we fit the kinematics together with the number densities. Then we do an alternative run, where we adopt for the two α -oldest sub-samples the scale heights from the direct fit to the densities. The dashed lines show that the model cannot fit the velocity dispersion of the α -oldest sub-sample with the smaller scale height, which underestimates the dispersions. For this reason, it is of benefit to model the density and kinematics together. It might also be that the selection function is biased. Such a bias can be a large source of errors, if it is not properly accounted for. Therefore, it would be more sensible to include the estimation of the selection function for the number density into the likelihood fitting, as implemented by [Bovy et al. \(2012c\)](#).

4.2.2 PARAMETER RANGES

We start with a minimal set of priors in the MCMC. These include flat priors in the range $[0,1]$ for the parameters q^2 and p^2 to avoid that they step out of their allowed range. These models have a serious problem as they prefer a large scale length ($h_R = 5.9 \pm 0.7$ kpc) and a small disk

⁵The combination of $[\alpha/\text{Fe}]$ and $[\text{Fe}/\text{H}]$ is a proxy for age ([Loebman et al. 2011](#)), which increases from the metal-rich, low α -abundant stars to the metal-poor, high α -abundant stars.

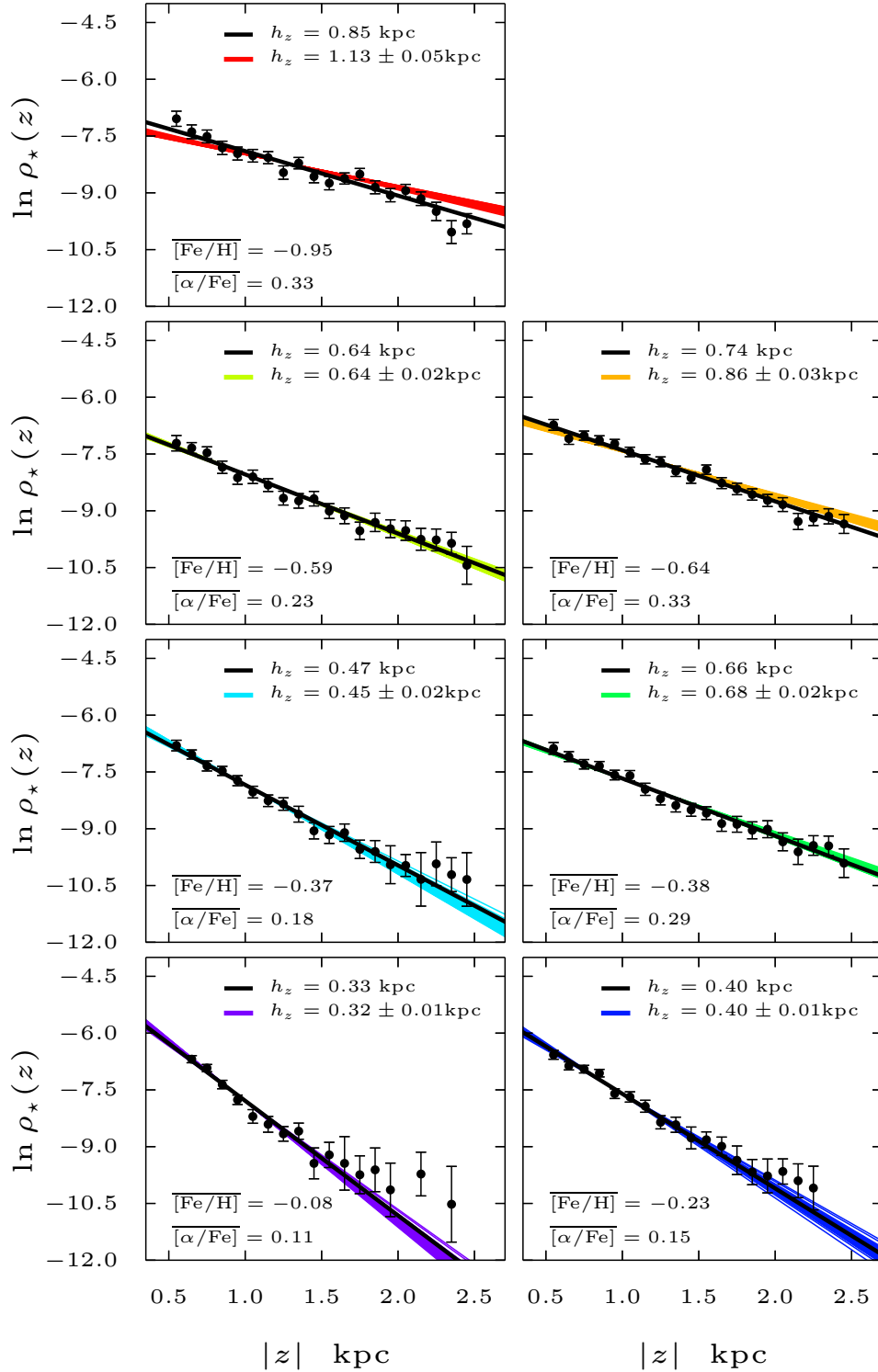


Figure 4.3: The density profiles (black circles) of the seven abundance bins in dependence of height at $R = R_\odot$. The profiles are fitted with a double exponential simultaneously with the kinematics. The fits are coloured according to their colour in Figure 4.6 and the black solid line is a direct fit to the density profiles. The α -younger sub-samples show evidence for a thick disk component in the slope, but the fits are acceptable in all bins, though there is a clear difference between the simultaneously and directly fitted profile in the α -oldest abundance bin.

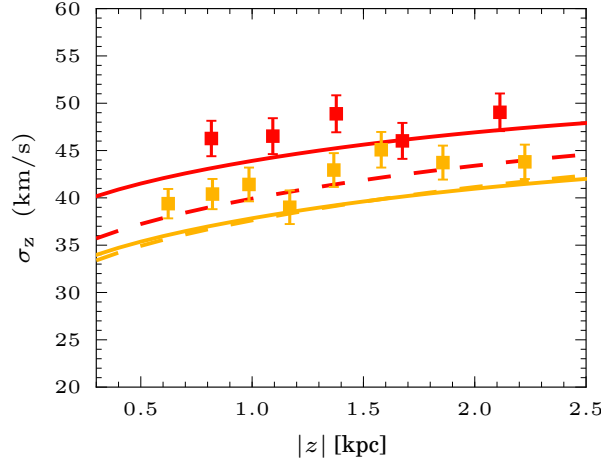


Figure 4.4: Vertical velocity dispersion as function of height at $R = R_{\odot}$ for the α -oldest abundance bin. The squares are direct measurements from Section 3.3.1, the solid lines are predictions of the model that fits the tracer densities simultaneously and the dashed lines are predictions of the model with fixed scale heights. In the latter model, the density profile was directly fitted, which results in a very poor prediction of the vertical velocity dispersion (red). The model fitting the tracer density together with the kinematics performs better in this case.

mass ($M_d = 3.4 \pm 0.4 M_{\odot}$), that is partially responsible for the resulting large dark matter density $\rho_{\text{dm}} = (0.02 \pm 0.002) M_{\odot} \text{pc}^{-3}$. The corresponding rotation curve in the left panel of Figure 4.5 reveals a strong positive gradient of $\left. \frac{d \ln v_c}{d \ln R} \right|_{R=8 \text{kpc}} = 0.47 \pm 0.03$ at the solar position, that is not at all supported by direct rotation curve measurements (Bovy et al. 2012d), which suggest an almost flat rotation curve. So we emphasise the need for a moderate rotation curve prior for our models. Hereby, we just limit the logarithmic slope $\frac{d \ln v_c}{d \ln R}$ and the absolute value V_c of the rotation curve at solar position. The slope is free to vary in the range $-0.12 < \frac{d \ln v_c}{d \ln R} < 0.12$ and V_c is restricted to $190 < V_c / \text{km s}^{-1} < 245$.

After implementing these constraints, the rotation curve in the right panel of Figure 4.5 is almost flat near the sun with a minimal positive slope. Only $V_c(R = 8 \text{kpc}) = 196 \pm 4 \text{ km s}^{-1}$ is smaller than the widely accepted $V_c \approx 220 \pm 20 \text{ km s}^{-1}$ (Binney & Tremaine 2008). The disk mass increase a bit to $M_d = (4.1 \pm 0.2) \cdot 10^{10} M_{\odot}$, while the disk scale length decreases tremendously to $h_R = 2.5 \pm 0.3 \text{ kpc}$. A similar strong drop happens in the dark matter density. It converges to $\rho_{\text{dm}} = (0.013 \pm 0.002) M_{\odot} \text{pc}^{-3}$.

Figure 4.6 is similar to Figure 3.3 as it displays the directly measured velocity dispersion profiles of the sub-samples. In addition, we overplot the predicted profiles of the axisymmetric Jeans model with the same colours. The transparent lines correspond to models from samples of the MCMC posterior distribution. We just want to clarify that the lines are not fitted to the binned velocity dispersion, but instead to the velocities and positions of all stars individually. The top panel shows the radial velocity dispersion and the bottom panel the vertical velocity dispersion.

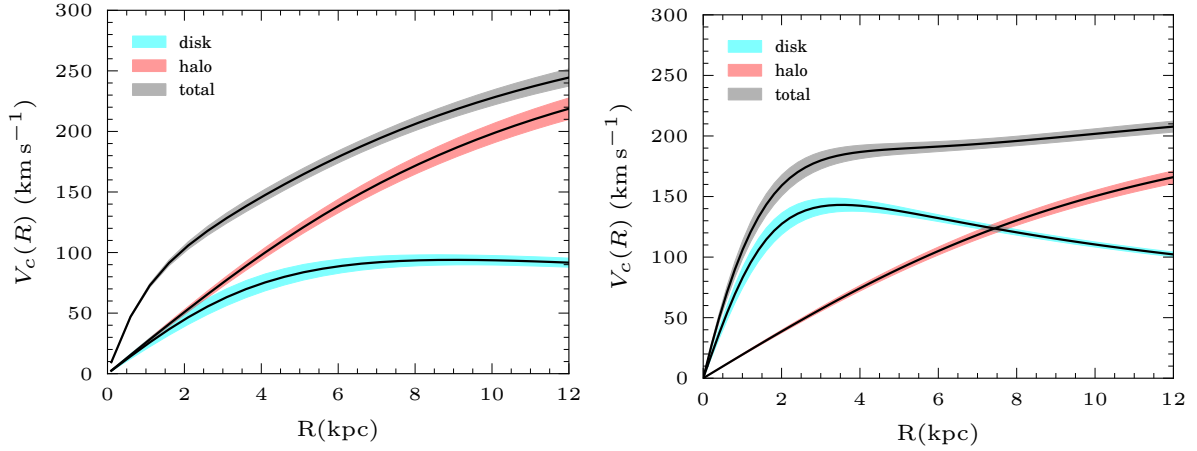


Figure 4.5: Rotation curve derived from the Miyamoto-Nagai disk and logarithmic halo as result of the axisymmetric Jeans modelling. The colour filled areas around the curves represent the uncertainty, the grey total rotation curve is separated into its main components: the aqua coloured disk contribution and the red coloured halo contribution. *Left:* resulting rotation curve as deduced from the G-type tracers without a prior on the flatness of the rotation curve. The dark matter already dominates beyond 2 kpc, leading to a rising rotation curve proportional to the dark matter part. *Right:* Rotation curve as obtained with a weak prior on the flatness of the rotation curve.

The predicted dispersions from the model largely agree with the binned dispersion measurements within the given uncertainties. We indicate the errorbars on the left side in the plot averaged on the binned measurements of each sub-sample.

The local stellar surface density at $|z| = 1.1$ kpc is with $\Sigma_* = 27 \pm 3 \text{ M}_\odot \text{ pc}^{-2}$ significantly smaller than that what for example [Bovy & Rix \(2013\)](#) found using an exponential mass density for the disk. This is explained by the different density shapes of the Miyamoto-Nagai and the exponential disk. The latter has a shallower fall-off in the inner part of the disk regarding the radius, but a steeper one in the outer part. So depending on the disk scale length and the radius at which the surface density is measured, the Miyamoto-Nagai disk generates a smaller or larger surface density. However, the total measured surface density $\Sigma_{1.1} = 64 \pm 6$ agrees with the measurement of [Bovy & Rix \(2013\)](#).

Even though the analytical set of potentials and the numerical set have a quite different shape, they are supposed to match on the mass of the disk and the local dark matter density. Replacing the Miyamoto-Nagai disk and the logarithmic halo potential with the exponential disk and the NFW halo, gives a comparable dark matter density but a smaller disk mass. The disk mass reduces to $M_d = (3.4 \pm 0.2) \cdot 10^{10} \text{ M}_\odot$. In contrary, the stellar surface density $\Sigma_* = (39 \pm 3) \text{ M}_\odot \text{ pc}^{-2}$ is much larger than in the case of the analytic potentials. The results of the other parameters are given in [Table 4.1](#) and we discuss them in the light of other results in the literature in [Section 4.3](#). The output of the MCMC for this particular run is shown in [Figure 4.7](#). The top panel presents

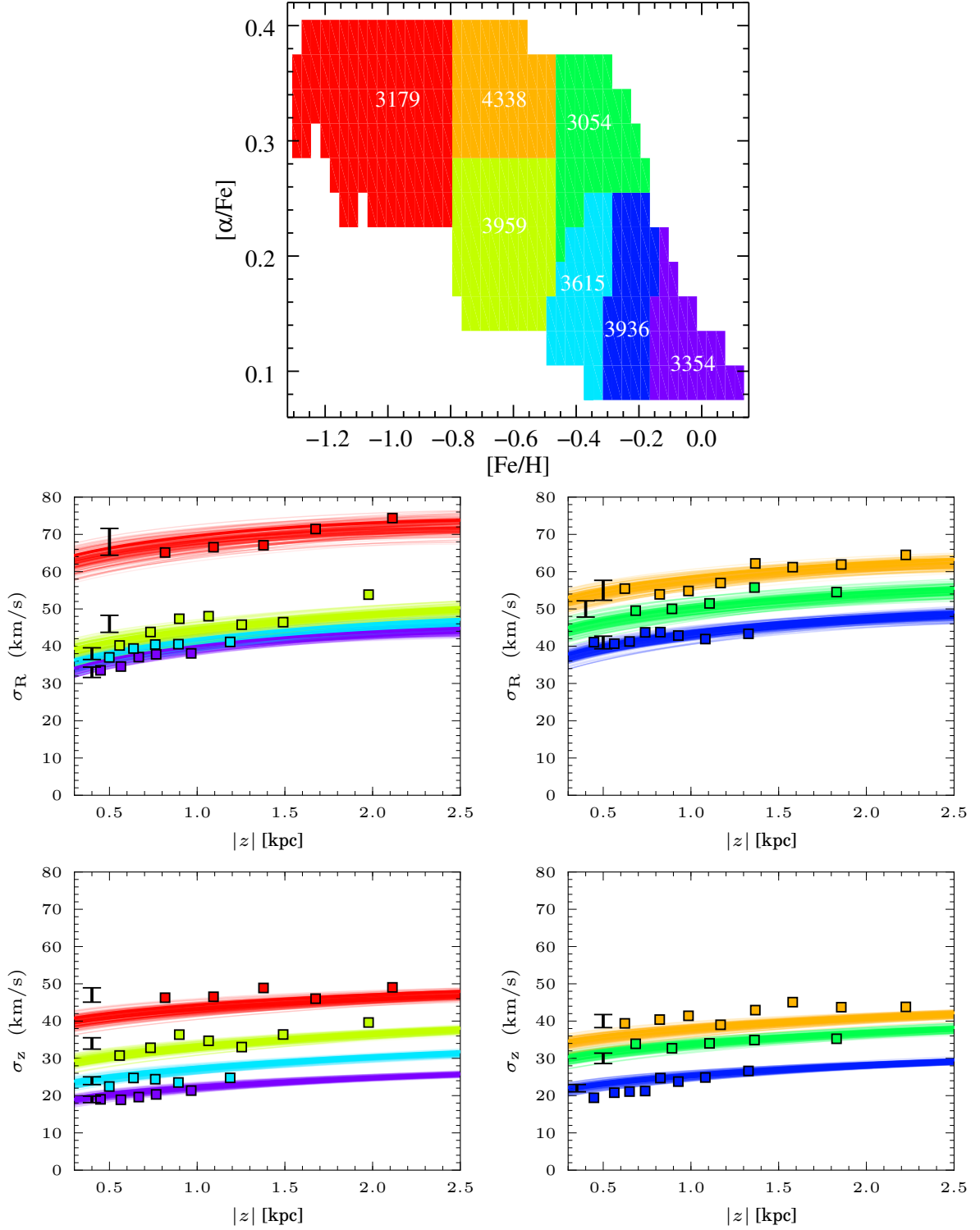


Figure 4.6: We compare the radial and vertical velocity dispersions as predicted by the axisymmetric Jeans model using the analytic potential with the directly measured velocity dispersion for the seven abundance bins illustrated in the top panel, that are separated in $[\text{Fe}/\text{H}]$ - $[\alpha/\text{Fe}]$ space.

the evolution of the parameters in the MCMC and the bottom panel shows the marginalised posterior distribution of the parameters. The latter plot visualises possible correlations between parameters and shows the $1-3\sigma$ regions enclosed by ellipses. The colours correspond to the individual likelihood of each model. We only display a third of the parameters in the model as not to overload the figure. All parameters converge and most of them are not degenerate. There are just the correlations between the disk and the halo parameters and the sub-sample dependent anisotropies κ_s are correlated with the gradient p^2 of the anisotropy. However, the MCMC makes sure that the parameter space is fully explored and the correlations only marginally affect the parameter estimates, if at all.

Figure 4.8 compares again the predicted radial and vertical velocity dispersions with the measurements of Chapter 3. They match well the vertical dispersion of the metal-poor sub-samples, but midly overestimate it in the metal-rich sub-samples. Similarly, the model slightly overestimates the radial dispersion in some abundance bins. From this point of view, the analytical potentials surprisingly seem to fit better the dispersions.

4.2.3 THE VELOCITY ELLIPSOID TILT

The use of the prolate spheroidal coordinate system gives us the opportunity to measure the tilt of the velocity ellipsoid as well. We gave an upper limit for the focal point Δ in Section 3.3.2 using equation 2.17, which is $\Delta \sim 3.4$ kpc. However, the Jeans model gives $\Delta = 6.8_{-1.0}^{1.7}$ kpc for the analytic potential and even $\Delta = 9.2_{-1.3}^{1.7}$ kpc for the exponential-NFW potentials. This raises the question if the model is really able to determine the tilt angle in general. The number statistics might be too low, so that a lot more stars are needed in comparison to a direct measurement as done in Chapter 3. Figure 4.9 gives in its left panel the tilt measurements of Section 3.3.2 (black squares) overplotted with the predicted tilt of the Jeans model with the analytic potential (red lines). The predicted tilt does not match well, although it roughly reproduces the gradient of the measurements. As demonstrated in the right panel, if we shift the predicted tilt by -3.4° , it will better fit the majority of the tilt measurements except of the last two measurement points. In addition, we overplot for comparison an arctan fit (grey, dashed line) to the points below 2 kpc as well as the resulting tilt from the exponential-NFW model (dark red, dashed line), where we fix the y-intercept to the one of the shifted tilt. The point is that the slope of the reddish lines almost reproduce the slope of the tilt measurements below 2 kpc, hinting that the model could have treated the stronger correlation in the motion of the stars above 2 kpc as outlier, hence mainly accounting for the contribution of the other stars to the tilt.

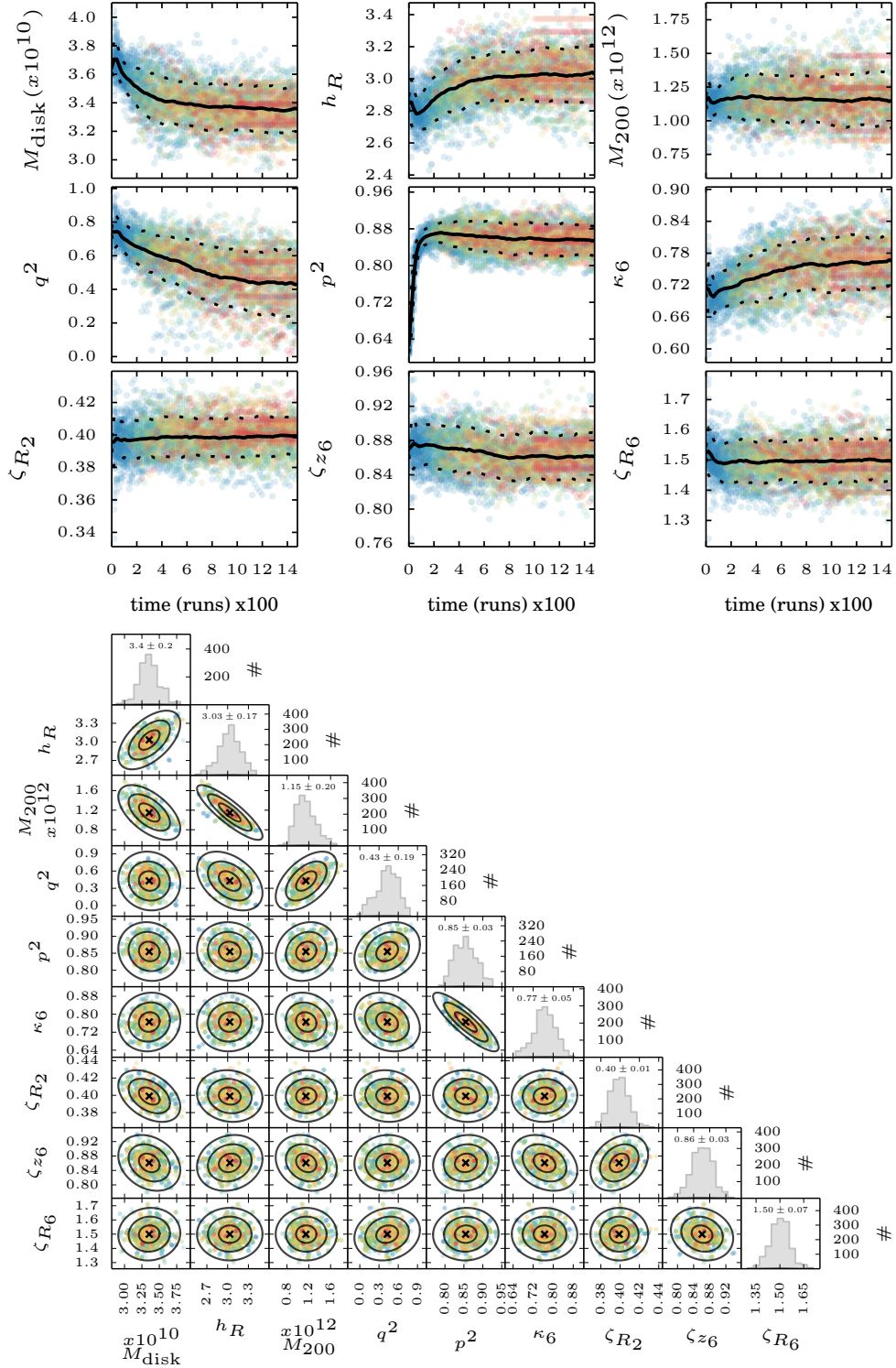


Figure 4.7: Parameter evolution (*top*) and post-burn parameter distributions (*bottom*) of the MCMC run from the axisymmetric Jeans model with the exponential-NFW potential pair. Each walker is colour-coded with its likelihood. The disk and halo mass are given in solar masses and the scale parameters like the disk scale length h_R and the tracer scale heights ζ_{z_i} and scale lengths ζ_{R_i} in kpc.

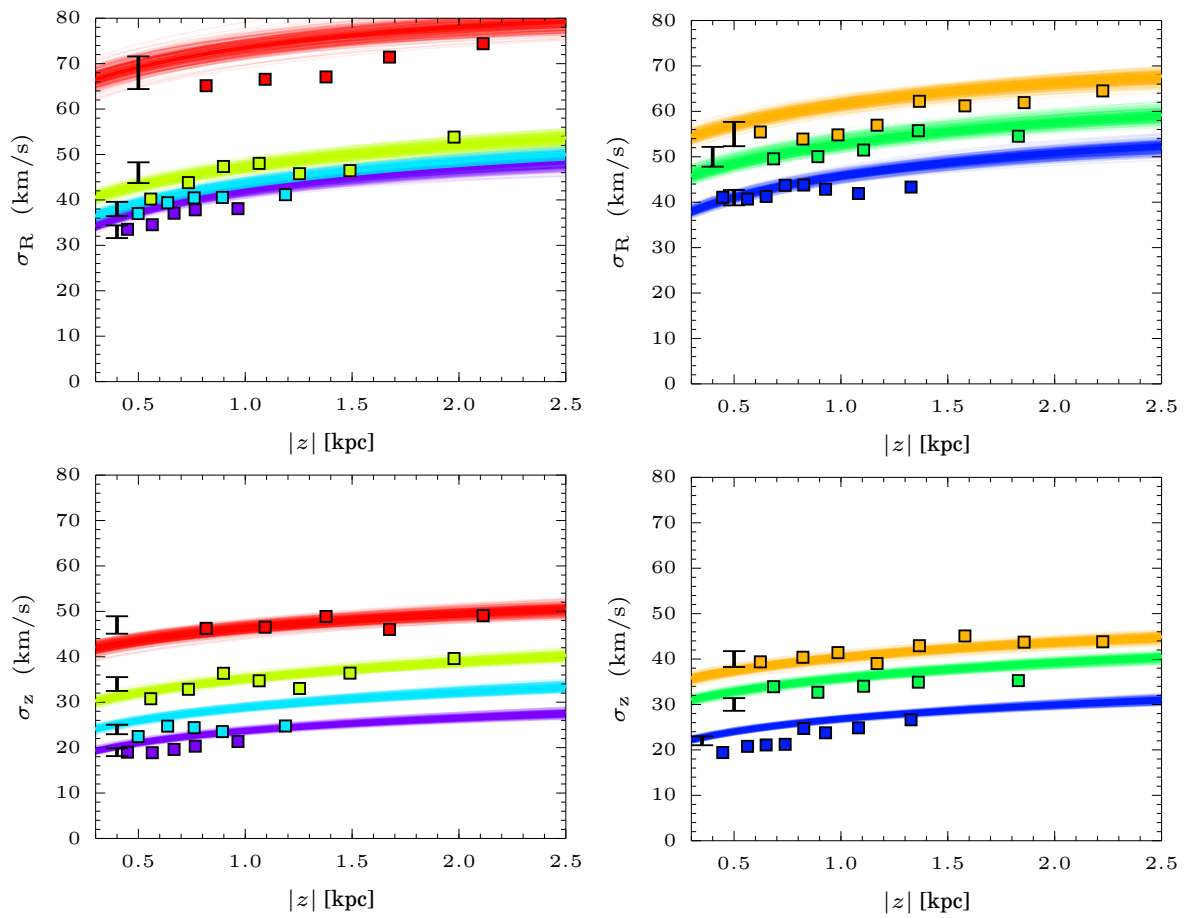


Figure 4.8: Similar to Figure 4.6; this time, the exponential-NFW potential pair is used in the model and the resulting velocity dispersions are computed in this potential.

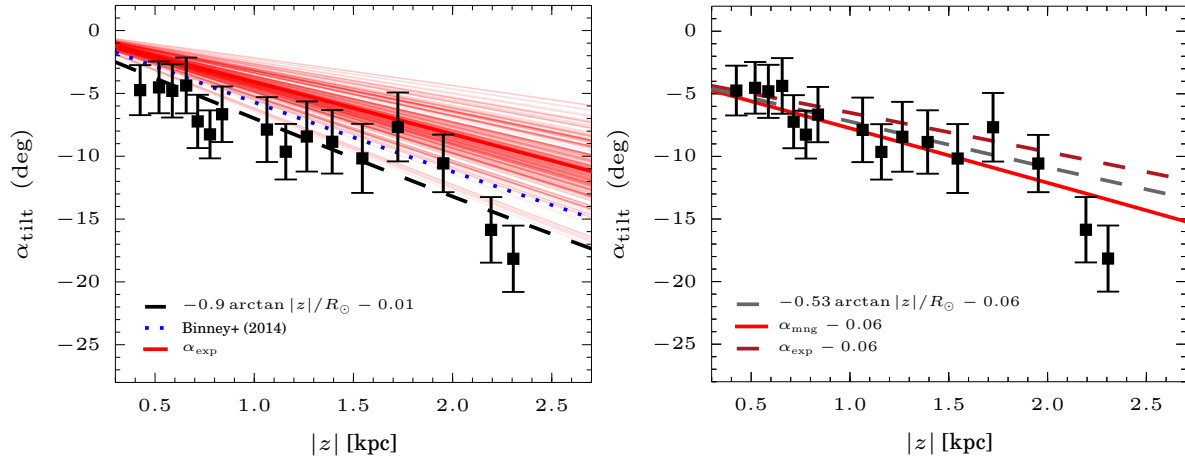


Figure 4.9: *Left:* Tilt angle as function of z at $R = R_{\odot}$ as directly measured (black squares) and as constrained by the axisymmetric Jeans model using the analytic potential (red lines). The latter samples the posterior distribution of the tilt from the MCMC. The blue dotted line represents a reference measurement of Binney et al. (2014). *Right:* The tilt of the best fit axisymmetric Jeans model from the left panel (red solid line) is shifted by -3.4° to better match the direct measurement below 2 kpc in height. The corresponding tilt for the model with the exponential-NFW potential pair is shown as dark red dashed line and a simple arctan fit to the tilt below 2 kpc is displayed as grey dashed line. It looks like that the two predicted trends in the tilt could fairly reproduce the slope of the directly measured tilt angles with the exception of the two measurements above 2 kpc.

4.2.4 INFLUENCES OF PARAMETERS

We keep almost all parameters in the model free to avoid strong priors and to investigate the performance of the model when giving it a large freedom. On the other hand, it is hard to define a reasonable prior for some parameters. For example, the disk scale length is usually measured in terms of an exponential disk, but not for a Miyamoto-Nagai disk. The radial gradient of the anisotropy is also not well known.

The parameter q^2 controlling the tilt has a strong influence on the dark halo potential. We test the latter by running the model with both the tilt that we measured in Section 3.3.2 and a cylindrically aligned velocity ellipsoid. The remaining parameter configuration is the same for both models. The resulting dark matter density differs by a factor 2. We estimate in the no-tilt case $\rho_{\text{dm}} = (0.008 \pm 0.002) M_{\odot} \text{pc}^{-3}$ and in case of a strong tilt $\rho_{\text{dm}} = (0.016 \pm 0.001) M_{\odot} \text{pc}^{-3}$.

Since the disk scale height is not constrained by the data, we fix it to the mass-weighted scale height $h_z = 0.4$ kpc found by Bovy et al. (2012c). Thus, the results of the axisymmetric Jeans model can be better compared to Bovy & Rix (2013), who also used G-type dwarf stars from SEGUE and this scale height in their dynamical models as well. However, the estimate of the scale height in Bovy et al. (2012c) is quite uncertain, spreading between 0.2 - 1 kpc. Therefore,

we test how the result would change if we picked a smaller or larger scale height. We make two test runs with $h_z = 0.25$ kpc and $h_z = 0.6$ kpc and find that the mass and the scale length of the disk are proportional to the scale height, that is the scale length and the mass decreases as the scale height decrease to 0.25 kpc. But the differences are just within the 1σ confidence interval. As a consequence, the dark matter density slightly increases by roughly 10%, because the model acutally measures the total mass and if the disk mass decreases the dark halo mass will have to increase to keep the total mass constant. Nevertheless, the increase in ρ_{dm} is still within the uncertainty. In contrast, the dark matter density is less sensitive to an increase of the scale height. The scale height would be better constrained overall, if the data reached lower latitudes.

Finally, we fix those parameters that are not well constrained by the model, and for which there are precise measurements available in the literature. These are the scale length of the disk that [Bovy & Rix \(2013\)](#) recently estimated to be $h_R = 2.15 \pm 0.15$ kpc and the tilt angle that we measure in [Section 3.3](#) to be $\Delta \approx 3$ kpc. This time, we use the exponential-NFW potential pair to get a realistic estimate of the local dark matter density and the disk surface density. The scale length and scale height of the tracer sub-samples are also free parameters in the model. As a result we obtain $\rho_{\text{dm}} = (0.0135 \pm 0.001) \text{ M}_{\odot}\text{pc}^{-3}$ and $\Sigma_* = (30 \pm 2) \text{ M}_{\odot}\text{pc}^{-2}$. The dark matter density will be a little larger and disk surface density will be smaller as if the disk scale length and the tilt angle are free parameters.

4.3 DISCUSSION AND CONCLUSION

In this chapter, we have introduced a novel axisymmetric Jeans model that is fully general under the assumption of axisymmetry. It additionally relies on the assumptions that the velocity ellipsoid is aligned with the prolate spheroidal coordinate system and that the velocity anisotropy mainly changes with radius (see [Figure 2.3](#)). However, the anisotropy distribution can be changed to any other functional form, e.g. having a main dependence on the vertical height. The gravitational potential in our model can be freely chosen. It does not need to be separable as in the [Stäckel](#) solution of the Jeans equations and it does not need to be self-consistent, such that it reproduces the underlying density distribution. As with all solutions of the Jeans equations, we can not guarantee that our solution is everywhere physically meaningful, i.e. it corresponds to a positive defined distribution function.

We applied this model to a sample of $\sim 25,000$ G-type dwarf stars from the [SEGUE](#) survey using a Markov Chain Monte Carlo (MCMC) likelihood approach to fit the positions and velocities of the stars in a discrete way without any spatial binning. The likelihood approach also includes the consideration of halo stars contaminating the sample of disk stars. We selected sub-samples based on their metallicity and α -element abundances to minimise the effect of different stellar ages on the velocity dispersion, thus avoiding an artificial overestimation of the dark mat-

ter fraction. We used two different sets of potentials - a Miyamoto-Nagai disk plus a logarithmic halo and an exponential disk plus a Navarro-Frenk-White (NFW) halo. The density profiles of the tracers were fitted at the same time with the kinematics.

The tests with the axisymmetric Jeans model have shown that the tilt is an important aspect when using data over a large range in height. Neglecting the tilt completely in our analysis would lead to a $\approx 40\%$ smaller dark matter density than we actually get. If we fixed the tilt to $\Delta = 3$ kpc, which we measure in Section 3.3.2, then we would get a significantly larger dark matter density ($\rho_{\text{dm}} = (0.016 \pm 0.001) M_{\odot} \text{pc}^{-3}$). Hence it is crucial to describe the tilt and its variations with z in dynamical models correctly.

We will estimate for the NFW halo a local dark matter density of $\rho_{\text{dm}} = (0.012 \pm 0.001) M_{\odot} \text{pc}^{-3}$ and for the logarithmic halo $\rho_{\text{dm}} = (0.013 \pm 0.002) M_{\odot} \text{pc}^{-3}$, if we give the model the freedom to decide on the disc scale length and the tilt angle. If we instead use the estimated scale length of [Bovy & Rix \(2013\)](#) and our tilt angle of Chapter 3, we will estimate $\rho_{\text{dm}} = (0.0135 \pm 0.001) M_{\odot} \text{pc}^{-3}$ with the NFW potential. Combining both measurements of the NFW potential, we conclude that the local dark matter density is $\rho_{\text{dm}} = (0.013 \pm 0.0015) M_{\odot} \text{pc}^{-3}$. This is larger than what other authors found. [Zhang et al. \(2013\)](#) estimated from ~ 9000 K dwarfs of the SEGUE survey $\rho_{\text{dm}} = (0.0065 \pm 0.0023) M_{\odot} \text{pc}^{-3}$ that are located at $|z| < 1.2$ kpc. This is just the range in which the invoked uncertainty by neglecting the tilt term in the Jeans equation is smaller than the statistical uncertainty of the model.

[Bovy & Tremaine \(2012\)](#) re-analysed the sample of [Moni Bidin et al. \(2012\)](#) containing 412 stars and determined a similar $\rho_{\text{dm}} = (0.008 \pm 0.003) M_{\odot} \text{pc}^{-3}$. As their sample is located at heights larger than 1 kpc, they used the cylindrical axisymmetric Jeans equation and several simplifying assumptions. The least recent measurement of ρ_{dm} , that is below the canonical standard value $0.01 M_{\odot} \text{pc}^{-3}$ usually adopted by particle physicists, was done by [Bovy & Rix \(2013\)](#). They used an action based distribution function and $\sim 16,000$ G dwarfs from SEGUE to measure $\rho_{\text{dm}} = (0.008 \pm 0.0025) M_{\odot} \text{pc}^{-3}$.

A few authors found larger values. [Garbari et al. \(2012\)](#) re-analysed the sample of K stars of [Kuijken & Gilmore \(1989a\)](#) and augmented it with more precise distances. While [Kuijken & Gilmore \(1989a\)](#) did not find a significant dark matter fraction in the disk, [Garbari et al. \(2012\)](#) estimated $\rho_{\text{dm}} = (0.022 \pm 0.014) M_{\odot} \text{pc}^{-3}$, which is a larger value for the dark matter density near the sun than determined by most other studies. However, the uncertainty in their value is quite large, so that it is still consistent with them within 2σ . [Bienaymé et al. \(2014\)](#) found from nearby red clump stars in RAVE $\rho_{\text{dm}} = (0.014 \pm 0.001) M_{\odot} \text{pc}^{-3}$, where they applied a Stäckel based distribution function to model the vertical velocity distribution and its density. This is very similar to our result, especially to the one where we fixed the disk scale length to 2.15 kpc and the tilt to $\Delta = 3$ kpc. From this point it is interesting that the adopted tilt parameter of [Bienaymé et al. \(2014\)](#) ($\Delta = 2$ kpc) in their model is almost the same.

Our exponential surface density at 1.1 kpc height, $\Sigma_{<1.1} = (79 \pm 2) \text{ M}_\odot \text{pc}^{-2}$, is on the upper end of estimates in the literature. It only fits within the 2σ confidence interval to the measurements of [Kuijken & Gilmore \(1991\)](#) $\Sigma_{<1.1} = (71 \pm 6) \text{ M}_\odot \text{pc}^{-2}$ or [Zhang et al. \(2013\)](#) ($\Sigma_{<1.1} = (68 \pm 6) \text{ M}_\odot \text{pc}^{-2}$). This larger total surface density is mostly due to our larger dark matter fraction because the baryonic surface density $\Sigma_b = (52 \pm 3) \text{ M}_\odot \text{pc}^{-2}$, from which $13 \text{ M}_\odot \text{pc}^{-2}$ are attributed to interstellar gas, matches to the other estimates. [Kuijken & Gilmore \(1991\)](#) determined $\Sigma_b = (48 \pm 8) \text{ M}_\odot \text{pc}^{-2}$, [Bovy & Rix \(2013\)](#) $\Sigma_b = (51 \pm 4) \text{ M}_\odot \text{pc}^{-2}$ and [Read \(2014\)](#) concluded $\Sigma_b = (55 \pm 5) \text{ M}_\odot \text{pc}^{-2}$.

Our smaller disk mass of $M_d = (3.4 \pm 0.2) \cdot 10^{10} \text{ M}_\odot$ comes along with a larger disk scale length of $h_R = 3.0 \pm 0.2 \text{ kpc}$ in comparison to $M_d = (4.6 \pm 0.3) \cdot 10^{10} \text{ M}_\odot$ and $h_R = (2.15 \pm 0.15) \text{ kpc}$ ([Bovy & Rix 2013](#)). [Robin et al. \(2014\)](#) estimated a smaller scale length of the thick disk ($h_R = 2.3$) from the Besançon Galaxy model, for which they compared the star counts in the model to star counts in photometric data of SDSS and the Two Micron All Sky Survey (2MASS, [Skrutskie et al. 2006](#)). On the other hand, [Jurić et al. \(2008\)](#) estimated a larger thick disk scale length of $h_R = 3.6 \text{ kpc}$ from photometric SDSS star counts. But the result of [Polido et al. \(2013\)](#) on the thick disk matches best with our result, where they applied a star count model to the 2MASS survey. In conclusion, recent works suggest that the disk scale length is between 2 and 3.5 kpc. [Bovy et al. \(2012c\)](#) ascertained that the scale length varies with metallicity and α -abundance in their monoabundance populations. The more α -enhanced and older stars are the smaller is their scale length. From that, it appears possible that the axisymmetric Jeans model puts more weight on the α -young stars in our sample, which favours a larger scale length.

A small disk scale length would strongly support the hypothesis of a maximal disk. We say the disk will be maximal, if it dominates the rotation curve at $R = 2.2 h_R$ with the maximum possible amount. This is defined as 75% - 95% of the disk contribution to the rotation curve ([Sackett 1997](#)), i.e. $0.75 < \frac{V_{c,*}}{V_c} < 0.95$. The 2.2 scale lengths are the empirically deduced radius at which the rotation curve usually peaks ([Gnedin et al. 2007](#)). [Bovy & Rix \(2013\)](#) inferred from their measurement of the Galactic potential, that the disk is maximal. Whereas [Bershady et al. \(2011\)](#) analysed 30 spiral galaxies with different rotational velocities and luminosities and did not find a galaxy with a maximum disk. Given the fact that even the disks of their brightest fast rotating galaxies were sub-maximal, they concluded that spiral galaxies should be sub-maximal in general. [Courteau & Dutton \(2015\)](#) recently suggested that all disks are maximal in their inner part, but a transition occurs at a certain radius between the inner baryon-dominated part and the outer dark matter dominated part. They confirmed that the transition radius is near 2.2 scale lengths for low-mass galaxies and at a larger radius for high-mass ($V_c > 200$) km s^{-1} galaxies. Our results indicate however a rather sub-maximal disk having $\frac{V_{c,*}}{V_c} = 0.62 \pm 0.02$ with $V_c(R = 8 \text{ kpc}) = 220 \pm 6 \text{ km s}^{-1}$. So it is not fully decided yet, whether the Milky Way has a maximum disk or not.

Table 4.1: Best fit and fixed parameters in the axisymmetric Jeans model, in particular for the models: (A) exponential-NFW potential pair; (B) exponential-NFW potential pair with fixed disk scale length h_R (Bovy & Rix 2013) and fixed tilt Δ (Section 3.3.2); (C) Miyamoto-Nagai disk + logarithmic halo; (D) Miyamoto-Nagai disk + logarithmic halo with fixed (large) tilt Δ (Section 3.3.2); (E) Miyamoto-Nagai disk + logarithmic halo with (almost) zero tilt. The * specifies a fixed parameter. If the tracer scale length is marked with *, it will be sampled from a gaussian distribution with the given standard deviation. The first column contains the mean metallicity and α element abundance for the various abundance bins coloured as in Figure 4.6. Every sub-sample is described by its velocity anisotropy κ , its scale height ζ_z and its scale length ζ_R .

			(A)	(B)	(C)	(D)	(E)
	ρ_{dm}	$M_{\odot} \text{pc}^{-3}$	0.0124 ± 0.0013	0.0135 ± 0.001	0.0125 ± 0.001	0.016 ± 0.01	0.0085 ± 0.002
	c_{200}		15.0*	15.0*			
	d_{halo}	kpc			12.0*	12.0*	12.0*
	Σ_*	$M_{\odot} \text{pc}^{-2}$	39 ± 3	30 ± 2	27 ± 2.5	23 ± 2.3	33 ± 4.4
	h_R	kpc	3 ± 0.2	2.2*	2.5 ± 0.3	1.9 ± 0.2	3.2 ± 1.8
	h_z	kpc	0.4*	0.4*	0.4*	0.4*	0.4*
	Σ_{gas}	$M_{\odot} \text{pc}^{-2}$	13*	13*	9.5	8.8	9.4
	$h_{z,\text{gas}}$	kpc	0.1*	0.1*	0.1*	0.1*	0.1*
	ρ_{bulge}	$M_{\odot} \text{pc}^{-3}$	0.47*	0.47*	0.47*	0.47*	0.47*
	a_{bulge}	kpc	0.8*	0.8*	0.8*	0.8*	0.8*
	Δ	kpc^2	$6.7^{+2}_{-1.3}$	3.0*	$6.7^{+2}_{-1.3}$	3.0*	500*
	p^2		0.85 ± 0.03	0.8 ± 0.04	0.9 ± 0.03	0.8 ± 0.1	$1^{0.0}_{-0.7}$
	κ_1		0.92 ± 0.05	0.91 ± 0.05	0.89 ± 0.05	0.81 ± 0.05	0.81 ± 0.1
$[\text{Fe}/\text{H}] = -0.08 \text{ dex}$ $[\alpha/\text{Fe}] = 0.11 \text{ dex}$	ζ_{R1}	kpc	1.7 ± 0.1	1.7 ± 0.1	1.7 ± 0.1	$1.7^* \pm 0.1$	$1.7^* \pm 0.1$
	$\zeta_{z,1}$	kpc	0.32 ± 0.01	0.34 ± 0.01	0.32 ± 0.01	0.32 ± 0.01	0.34 ± 0.03
	κ_2		0.88 ± 0.04	0.88 ± 0.04	0.86 ± 0.05	0.78 ± 0.05	0.76 ± 0.1
$[\text{Fe}/\text{H}] = -0.23 \text{ dex}$ $[\alpha/\text{Fe}] = 0.15 \text{ dex}$	ζ_{R2}	kpc	2.2 ± 0.15	2.2 ± 0.14	2.2 ± 0.15	$2.2^* \pm 0.15$	$2.2^* \pm 0.15$
	$\zeta_{z,2}$	kpc	0.4 ± 0.01	0.42 ± 0.01	0.40 ± 0.01	0.4 ± 0.01	0.41 ± 0.04
	κ_3		0.76 ± 0.04	0.76 ± 0.04	0.73 ± 0.04	0.67 ± 0.04	0.68 ± 0.1
$[\text{Fe}/\text{H}] = -0.37 \text{ dex}$ $[\alpha/\text{Fe}] = 0.18 \text{ dex}$	ζ_{R3}	kpc	2.8 ± 0.23	2.7 ± 0.22	2.8 ± 0.24	$2.8^* \pm 0.2$	$2.8^* \pm 0.2$
	$\zeta_{z,3}$	kpc	0.45 ± 0.01	0.47 ± 0.01	0.45 ± 0.01	0.45 ± 0.01	0.45 ± 0.02
	κ_4		0.73 ± 0.05	0.72 ± 0.05	0.71 ± 0.05	0.64 ± 0.05	0.62 ± 0.05
$[\text{Fe}/\text{H}] = -0.38 \text{ dex}$ $[\alpha/\text{Fe}] = 0.29 \text{ dex}$	ζ_{R4}	kpc	1.6 ± 0.1	1.6 ± 0.1	1.6 ± 0.1	$1.6^* \pm 0.1$	$1.6^* \pm 0.1$
	$\zeta_{z,4}$	kpc	0.68 ± 0.02	0.71 ± 0.02	0.69 ± 0.02	0.68 ± 0.02	0.67 ± 0.03
	κ_5		0.60 ± 0.04	0.60 ± 0.04	0.58 ± 0.05	0.52 ± 0.04	0.49 ± 0.6
$[\text{Fe}/\text{H}] = -0.59 \text{ dex}$ $[\alpha/\text{Fe}] = 0.23 \text{ dex}$	ζ_{R5}	kpc	3.0 ± 0.26	2.9 ± 0.23	2.9 ± 0.21	$2.9^* \pm 0.2$	$2.9^* \pm 0.2$
	$\zeta_{z,5}$	kpc	0.64 ± 0.02	0.65 ± 0.02	0.64 ± 0.02	0.63 ± 0.02	0.63 ± 0.04
	κ_6		0.77 ± 0.05	0.75 ± 0.05	0.74 ± 0.05	0.67 ± 0.05	0.62 ± 0.08
$[\text{Fe}/\text{H}] = -0.64 \text{ dex}$ $[\alpha/\text{Fe}] = 0.33 \text{ dex}$	ζ_{R6}	kpc	1.5 ± 0.07	1.5 ± 0.08	1.5 ± 0.07	$1.5^* \pm 0.07$	$1.5^* \pm 0.07$
	$\zeta_{z,6}$	kpc	0.86 ± 0.03	0.91 ± 0.03	0.86 ± 0.02	0.88 ± 0.02	0.83 ± 0.03
	κ_7		0.81 ± 0.05	0.79 ± 0.05	0.78 ± 0.05	0.71 ± 0.05	0.61 ± 0.06
$[\text{Fe}/\text{H}] = -0.95 \text{ dex}$ $[\alpha/\text{Fe}] = 0.33 \text{ dex}$	ζ_{R7}	kpc	1.6 ± 0.09	1.6 ± 0.09	1.6 ± 0.09	$1.6^* \pm 0.1$	$1.6^* \pm 0.1$
	$\zeta_{z,7}$	kpc	1.13 ± 0.05	1.24 ± 0.05	1.14 ± 0.05	1.17 ± 0.05	1.1 ± 0.04
	\mathcal{L}		-248,313	-248,341	-255,089	-255,077	-255,135

MASS OF THE DARK HALO

Cosmological simulations have contributed a lot to the understanding of galaxy formation. In conjunction with hydrodynamical simulations including also baryonic particles, they can shed light on the evolution of galaxies as well. However, the evolution depends strongly on the (initial) mass of a galaxy and we can only draw inferences from these simulations, if we compare their outcome with the structure and dynamical properties of real galaxies with the same size and mass as the simulated ones. Two of the big discrepancies between observations and simulations are known as the “missing satellites” problem (Klypin et al. 1999; Moore et al. 1999) and the “too big to fail” problem (Boylan-Kolchin et al. 2011), that are explained in Section 1.1.3. Since the number of sub-halos and the size of the largest ones depends on the mass of the host halo, these two problems would be solved if the Milky Way had a mass less than $\approx 10^{12} M_{\odot}$ (Wang et al. 2012). Although the qualified tracer objects of the Milky Way are much closer than for any other galaxy, the available estimates of the virial mass in the literature spread over a factor of 5 difference, $(0.5 - 2.5) \cdot 10^{12} M_{\odot}$, with the error on each estimate often larger than 40%.

A few authors used single satellite galaxies such as the Magellanic Clouds (Busha et al. 2011; González et al. 2013) or Leo I (Li & White 2008; Boylan-Kolchin et al. 2013). However, it is questionable whether Leo I is really bound to the Milky Way (Mateo et al. 2008). Including Leo I generally leads to a larger derived halo mass, whereas if it was unbound system, the results would not be reliable.

Sales et al. (2007); Barber et al. (2014) compared the velocities and positions or the orbital ellipticity of several Milky Way satellites with sub-halos around N-body galaxies. In contrast, Watkins et al. (2010) did not use N-body simulations, but instead derived the mass from a simple mass estimator, which relates the velocities and radial positions of their 26 galaxies to the mass of the Milky Way. Stellar streams offer another opportunity to estimate the mass (e.g. Gibbons et al. 2014; Küpper et al. 2015; Sanderson et al. 2015) by following the orbit of one or several streams along the gravitational potential of the host. But the most used tracers are stars, as they

are much more numerous. [Xue et al. \(2008\)](#) used 2400 BHB stars at distances up to $r_{gc} \approx 60$ kpc and similarly, [Gnedin et al. \(2010\)](#) used 552 BHB stars up to 80 kpc. [Kafle et al. \(2014\)](#) used a larger sample consisting of BHBs and giants with each of ≈ 5000 stars and reaching up to $r_{gc} \approx 100$ kpc. Most of the studies that use discrete tracers applied (spherical) Jeans models to estimate the mass; some applied instead a distribution function method ([Sakamoto et al. 2003](#); [Deason et al. 2012](#)).

There are three main reasons that can explain the large spread in the estimated masses: (i) For most tracers only line-of-sight velocities are available. For an accurate determination of the kinematics, we will need proper motions as well, that allow to constrain the velocity anisotropy in the models, which is a significant factor of uncertainty. (ii) Due to magnitude limits, especially for spectroscopic surveys, the available samples of tracers are usually quite small, i.e. < 1000 objects or only one stream. This affects generally the Jeans models as well as the distribution function methods. (iii) The accuracy to determine the tracer density profile is partially connected to the small sample size, but also to the accuracy of the parallaxes and the detailed knowledge of the selection function. The mass is proportional to the logarithmic slope of the tracer density according to the Jeans equations. This means, that the error in the tracer density sets an upper limit for the accuracy of the mass estimate. That is why, it is of special importance to determine the density profile as accurate as the data allows.

The density profile is often measured via star counts and volume corrected for completeness. In the past, almost all studies (e.g. [Sommer-Larsen 1987](#); [Sluis & Arnold 1998](#); [Robin et al. 2000](#); [De Propriis et al. 2010](#)) found that the density is well described by a single power law with index $n = 2.5 - 3.5$, only [Saha \(1985\)](#) discovered an evidence for a broken power law. Then, [Carollo et al. \(2007, 2010\)](#); [Beers et al. \(2012\)](#) put forward the idea of a broken density profile, which they interpreted as the existence of two distinct populations in the halo. Another explanation came from [Deason et al. \(2013a\)](#), who found an unusual amount of stars at their apocentres causing the break in the density profile. However, [Schönrich et al. \(2011\)](#) doubted that the broken profile is a real feature and ascribed it to distance uncertainties and contaminations by substructures. On the other hand, the density profile of M31 was measured out to 200 kpc and no broken profile was found ([Ibata et al. 2014](#)). This may point out, that the broken density profile in the Milky Way halo is indeed an observational bias or that the Milky Way has a different accretion history than M31. Only regarding the shape of the stellar halo, it crystallises that the mass distribution is not spherical but rather flattened with a flattening parameter $q > 0.5$. Moreover, [Preston et al. \(1991\)](#) found variable flattening changing with radius with a spherical halo beyond 20 kpc, that becomes more flattened towards the centre with $q = 0.54$.

In this chapter, we use a sample of SEGUE-2 K-giants to trace the mass profile of the Galactic halo. The sample originates from [Xue et al. \(2015\)](#) and is described in [Section 2.3](#) with regard to its selection criteria. [Section 5.1](#) explains how we extract the second moment from the line-of-sight velocity (LOS v) taking special care of the contamination by the Sagittarius stream. Then,

we outline in Section 5.2 the procedure to estimate the halo mass with the axisymmetric Jeans model and introduce different density profiles to check their influence on the mass estimates. Finally, we present and discuss the results of the LOSV dispersion profile and the inferred halo mass in Sections 5.3 and 5.4. Hereby, we first inspect the fits of five models, given in Section 5.2, to the velocity distribution, which handle the contribution of substructures differently. Then we analyse the predictions of the LOSV dispersion and the halo mass estimated by the density profiles. We also compare the halo mass estimated by the five models, before we present and discuss the final result.

5.1 EXTRACTING THE LINE-OF-SIGHT VELOCITY DISPERSION

After applying the axisymmetric Jeans model (introduced in Section 2.4), we compare the resulting radial velocity dispersion profile with the measured velocity dispersion profile in radial bins. In this way, we are able to judge how accurate the model matches the data. Moreover, we can inspect the LOSV distribution itself in light of substructures in the stellar halo. In fact, we expect the stellar halo to have a Gaussian velocity distribution, but substructures in the halo will distort the distribution causing non-Gaussianities. If we assume a Gaussian distribution, we will over- or underestimate the velocity dispersion, which will lead to a biased halo mass. We extract the velocity dispersion for each bin as described in Section 3.1.2. But this time, we only have LOSVs, so we only need a one-dimensional Gaussian to describe the velocity distribution. The likelihood, that star i belongs to the field halo stars, is predicted by Gaussian j with mean velocity \bar{v}_j and velocity dispersion σ_j .

$$\mathcal{L}_{ij}^{\text{halo}} = \mathcal{L}(v_i | \bar{v}_j, \sigma_j, \Delta_i) = \frac{1}{\sqrt{2\pi}\hat{\sigma}_j} \exp\left(-\frac{(v_i - \bar{v}_j)^2}{2\hat{\sigma}_j^2}\right) \quad (5.1)$$

where $\hat{\sigma}_j^2 = \sigma_j^2 + \Delta_i^2$ results from the convolution of the intrinsic variance of the Gaussian and the observed uncertainty. \bar{v}_j and σ_j are unknown parameters, even though we set $\bar{v} = 0$ in the axisymmetric Jeans model. As we show in Section 5.3.1, some radial bins suffer strongly from a contamination by Sagittarius stars, that have a different mean velocity and velocity dispersion. A second Gaussian accounts for the LOSV distribution of the Sagittarius stream

$$\mathcal{L}_{i,\text{sgr}} = \mathcal{L}(v_i | \overline{v_{i,\text{sgr}}}, \sigma_{j,\text{sgr}}, \Delta_i) = \frac{1}{\sqrt{2\pi}\hat{\sigma}_{j,\text{sgr}}} \exp\left(-\frac{(v_i - \overline{v_{i,\text{sgr}}})^2}{2\hat{\sigma}_{j,\text{sgr}}^2}\right), \quad (5.2)$$

where $\overline{v_{i,\text{sgr}}}$ is the mean LOSV velocity of Sagittarius at the position of star i and $\hat{\sigma}$ is again the convolved dispersion $\hat{\sigma}_{j,\text{sgr}}^2 = \sigma_{j,\text{sgr}}^2 + \Delta_i^2$. If ϵ_i is the probability that star i belongs to the

Sagittarius stream, and $(1 - \epsilon_i)$ the probability of star i belonging to the halo field stars, then the total likelihood of star i in bin j is in equivalence to equation 3.3:

$$\mathcal{L}_{ij} = (1 - \epsilon_i) \mathcal{L}_{ij}^{\text{halo}} + \epsilon_i \mathcal{L}_i^{\text{sgr}} \quad (5.3)$$

The fraction of Sagittarius stars on the sky is strongly position dependent. Thus, $\epsilon(\tilde{\Lambda}_\odot)$ is a function of the position $\tilde{\Lambda}_\odot$ along the stream, that we explain in more detail in the next section. To maximise the likelihood equation 5.3 and to find the best fitting σ_j , $\overline{v_{i,\text{sgr}}}$ and $\sigma_{j,\text{sgr}}$ we use the EMCEE package as before.

5.1.1 SAGITTARIUS MEMBERSHIP PROBABILITY

The largest substructure contributing most to the giants is the Sagittarius stream. The goal is therefore to estimate for each star the probability that it belongs to the stream. The probability is determined by comparing the LOSV and 3-dimensional position of each star to the LOSV and position of the Sagittarius stream. Following Belokurov et al. (2014), we transform the equatorial Right Ascension α and Declination δ into the heliocentric $\tilde{\Lambda}_\odot$ and \tilde{B}_\odot .

$$\begin{aligned} \tilde{\Lambda}_\odot = \arctan2 &(-0.936 \cos \alpha \cos \delta - 0.319 \sin \alpha \cos \delta + 0.149 \sin \delta, \\ &0.212 \cos \alpha \cos \delta - 0.8485 \sin \alpha \cos \delta - 0.485 \sin \delta) \end{aligned} \quad (5.4)$$

$$\tilde{B}_\odot = \arcsin(0.281 \cos \alpha \cos \delta - 0.422 \sin \alpha \cos \delta + 0.862 \sin \delta)$$

The $\tilde{\Lambda}_\odot$ coordinate has the equator aligned with the Sagittarius trailing arm and it increases in the direction of the streaming motion. Belokurov et al. (2014) provide a complete map of the leading and trailing arm in position and LOSV. The map was constructed using BHB stars, sub-giants and red clump stars. We fit the distance of the leading (trailing) arm as a function of $\tilde{\Lambda}_\odot$ with a log-normal (smoothed spline of degree 2) and the LOSV of the leading (trailing) arm with a smoothed spline of degree 2 (4th order polynomial). This allows to simply calculate the mean distance $\overline{d_{i,\text{sgr}}}$ and the mean LOSV $\overline{v_{i,\text{sgr}}}$ to the stream for an arbitrary $\tilde{\Lambda}_\odot$ in the range $30^\circ < \tilde{\Lambda}_\odot < 300^\circ$.

Figure 5.1 shows these fits in regions of position and velocity space, where it was possible to estimate the membership, together with the K-giant sample (black dots) in comparison to the measurements of Belokurov et al. (2014) (green & red points). The probability that star i belongs to the stream is composed of the probability that star i has a similar LOSV to the stream stars and of the probability that it has a similar distance. We assume that the probability in the LOSV is Gaussian shaped, centred on $\overline{v_{i,\text{sgr}}}$ at the angular position of star i . The standard deviation of the Gaussian reflects the LOSV dispersion $\sigma_{j,\text{sgr}}$ of the stream in $\tilde{\Lambda}_\odot$ -bin j .

The LOSV of the candidate i is of course not infinitely precisely measured, instead it has an error Δv_i . When approximating the probability, we have to consider that the true LOSV of the

candidate could be closer to or further away to the mean LOSV of Sagittarius. Therefore, the probability distribution is convolved with a Gaussian kernel, where the standard deviation equals the LOSV error:

$$p_v(\tilde{\Lambda}_{i\odot}, v_i) = \exp\left(-\frac{1}{2} \frac{(v_i - \overline{v_{i,\text{sgr}}})^2}{\sigma_{j,\text{sgr}} + \Delta v_i^2}\right) \quad (5.5)$$

The distribution of Sagittarius members in distance space is much broader, so that many members further away would have a low probability if represented by a Gaussian. We describe it with a rectangular function for simplicity and to make sure that likely members in velocity space have a distance close to other stream stars at their given sky position $\tilde{\Lambda}_{i\odot}$.

$$p_d(\tilde{\Lambda}_{i\odot}, d_i) = \begin{cases} 1 & \text{for } |d_i - \overline{d_{i,\text{sgr}}}| < 20 \text{ kpc} \\ 0 & \text{otherwise} \end{cases} \quad (5.6)$$

where all stars outside a band of 20 kpc around the mean distance to the stream are rejected to be a member and within this distance band only the LOSV information determines the probability. The total probability P_i then computes to $P_i \equiv \epsilon_i = p_{i,d} \cdot p_{i,v}$. In the case in which the leading and trailing arm of the stream overlap in $\tilde{\Lambda}_{i\odot}$, we have to take into account both the probability that star i might be a member of the leading arm and the probability that it might be a member of the trailing arm. Then we have as combined probability

$$\tilde{\epsilon}_i = P_{i,\text{lead}} + P_{i,\text{trail}} - P_{i,\text{lead}} \cdot P_{i,\text{trail}}. \quad (5.7)$$

In Addition, the likelihood $\mathcal{L}_i^{\text{sgr}}$ in equation 5.3 contains both likelihoods of the leading and trailing arm.

$$\mathcal{L}_i^{\text{sgr}} = \frac{P_{i,\text{lead}}}{P_{i,\text{lead}} + P_{i,\text{trail}}} \mathcal{L}_{i,\text{lead}} + \frac{P_{i,\text{trail}}}{P_{i,\text{lead}} + P_{i,\text{trail}}} \mathcal{L}_{i,\text{trail}} \quad (5.8)$$

$P_{i,\text{lead}}$ and $P_{i,\text{trail}}$ are the probabilities that star i belongs to the leading and trailing arm respectively. Their likelihoods $\mathcal{L}_{i,\text{lead}}$ and $\mathcal{L}_{i,\text{trail}}$ are defined in equation 5.2 with their mean LOSVs $\overline{v_{i,\text{lead}}}$ and $\overline{v_{i,\text{trail}}}$ and dispersions $\sigma_{j,\text{lead}}$ and $\sigma_{j,\text{trail}}$. As we do not have constraints outside of the range $30^\circ < \tilde{\Lambda}_{i\odot} < 300^\circ$, we set $\epsilon_i = 0$ for those stars. [Belokurov et al. \(2014\)](#) found from observations and [Law & Majewski \(2010\)](#) from N-body models that the stream is confined to the range $-15^\circ < \tilde{B}_{i\odot} < 15^\circ$. In order to avoid miss-assignments we set $\epsilon_i = 0$ for stars with $|\tilde{B}_{i\odot}| > 15^\circ$.

$\sigma_{j,\text{sgr}}$ at a given $\tilde{\Lambda}_{i\odot}$ is not known a priori, because there are no reliable measurements of the LOSV dispersion along the stream in the literature. That is why, it is a free parameter when estimating the probability. We estimate it by applying the likelihood method described in Section 5.1 to the K-giant sample binned in $\tilde{\Lambda}_{i\odot}$. We adapt the bin-size to contain 250 stars each, where the bin-size is not allowed to exceed $\tilde{\Lambda}_{i\odot} > 20^\circ$. The likelihood is given by equation 5.3 having 3 free parameters: σ_j , $\sigma_{j,\text{lead}}$ and $\sigma_{j,\text{trail}}$. In general, we assume for the mean velocity of the field stars $\mu_j = 0$. The MCMC method is applied separately on each $\tilde{\Lambda}_{i\odot}$ bin. The right panel of Figure 5.1 shows the result in terms of the velocity dispersion coloured according to

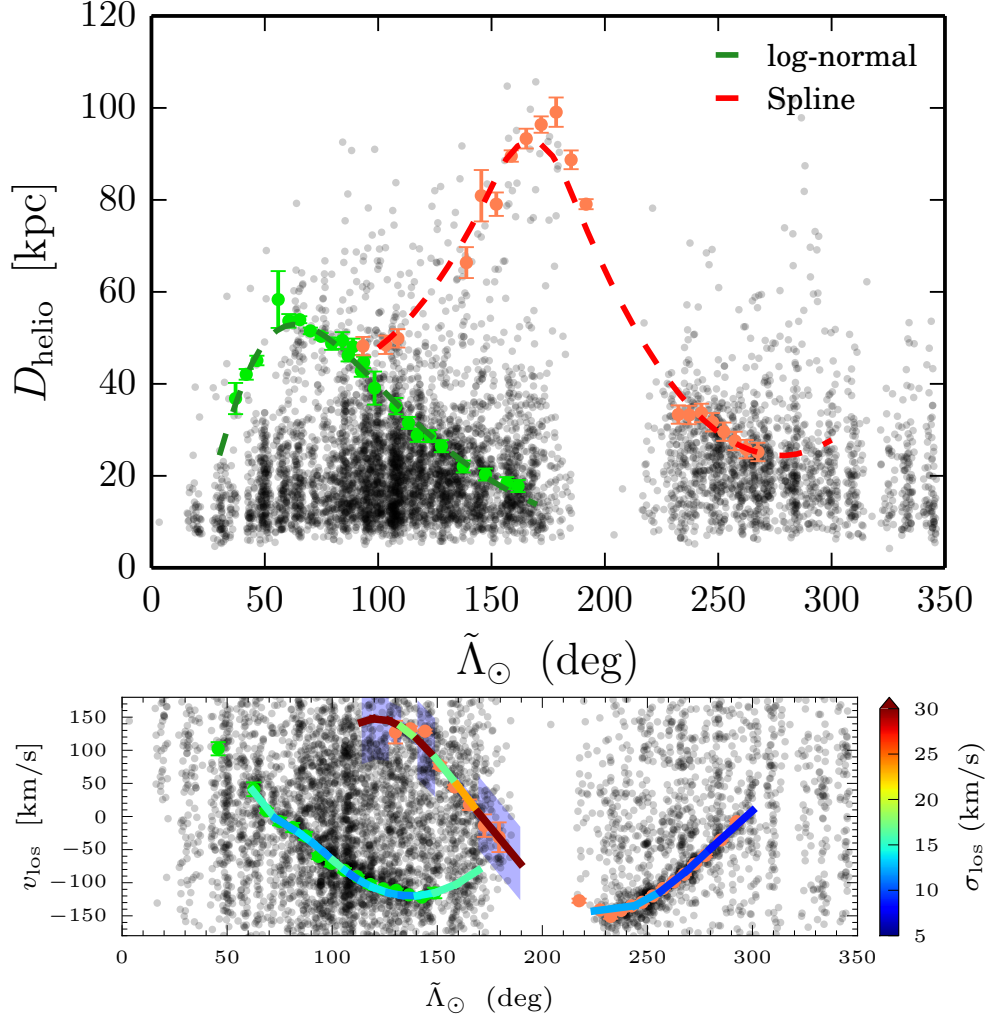


Figure 5.1: The *top* and the *bottom* panel show the distance and the LOSV along the stream coordinate $\tilde{\Lambda}_{\odot}$. The green circles are distances and LOSVs of the leading arm measured from BHB and sub-giant stars. The red circles belong to the trailing arm measured from BHB and red clump stars. The measurements are adopted from Belokurov et al. (2014, their Figure 6). The solid curves show fits to the data points, where the distances of the leading arm are fitted by a log-normal, the distances of the trailing arm and the LOSVs of the leading arm are fitted by a smoothed spline of degree 2 and the LOSVs of the trailing arm are fitted by a 4th order polynomial. The colour codes in the velocity map specify the LOSV dispersion in the direction of the line-of-sight and the violet shaded region around them indicate its uncertainty. If some violet shaded regions are not visible, the uncertainty will be smaller than the thickness of the line. The distances and LOSVs of the K-giants are overplotted as black dots to help the reader comparing the locations of the stream to the sample.

their estimated value along $\tilde{\Lambda}_\odot$. The violet shaded region around the spline and polynomial fits of the stream data visualise the error in the velocity dispersion. The displayed dispersion is equal to the optimised parameters $\sigma_{j,\text{lead}}$ and $\sigma_{j,\text{trail}}$. The LOSV dispersion is in general below 20 km/s with a statistical uncertainty smaller than 4 km/s. In contrast, the dispersion of Branch A¹ of the trailing arm is hard to measure with the K-giant sample in the range $110^\circ < \tilde{\Lambda}_\odot < 180^\circ$, because the sample only contains very few stars close to the spatial position of the trailing arm in this $\tilde{\Lambda}_\odot$ -range (see the left panel of Figure 5.1). Moreover it is striking that the LOSV dispersions of the Branch B trailing arm for $\tilde{\Lambda}_\odot > 255^\circ$ are below 10 km/s.

The left panel of Figure 5.2 illustrates the parameter evolution of a typical MCMC run in one of the $\tilde{\Lambda}_\odot$ -bins. The leading arm LOSV dispersion converges nicely, while the mentioned low sample density near the Branch A trailing arm cannot constrain the corresponding LOSV dispersion. However, the LOSV dispersion of the Branch B trailing arm converges quickly again. The right panel of Figure 5.2 reveals the post-burn parameter distribution coloured according to the likelihood and we do not identify any significant correlations between the parameters.

Note, that we pass the posteriors of the membership probabilities directly to the dynamical model outlined in Section 5.2 and do not use the averaged value of the posterior distribution.

This model is mainly based on the LOSV along the stream, but we can also use the position instead. In this case, the membership probability in distance space is represented by a Gaussian convolved with the distance error Δd_i in analogue to equation 5.5.

$$p_d(\tilde{\Lambda}_{i\odot}, d_i) = \exp\left(-\frac{1}{2} \frac{(d_i - \overline{d_{i,\text{sgr}}})^2}{\delta_{j,\text{sgr}} + \Delta d_i^2}\right) \quad (5.9)$$

$\delta_{j,\text{sgr}}$ represents the distance spread and $\overline{d_{i,\text{sgr}}}$ the mean distance of the stream at $\tilde{\Lambda}_{i\odot}$. The probability regarding the velocity is expressed as a rectangular function.

$$p_v(\tilde{\Lambda}_{i\odot}, v_i) = \begin{cases} 1 & \text{for } |v_i - \overline{v_{i,\text{sgr}}}| < 60 \text{ km/s} \\ 0 & \text{otherwise} \end{cases} \quad (5.10)$$

We will call this model Sgr2 and the velocity based analogue Sgr1. The model Sgr2 has 5 free parameters: σ_j , $\sigma_{j,\text{lead}}$, $\sigma_{j,\text{trail}}$, $\delta_{j,\text{lead}}$ and $\delta_{j,\text{trail}}$. The LOSV dispersions $\sigma_{j,\text{lead}}$ and $\sigma_{j,\text{trail}}$ enter through equation 5.2, but they are not involved in the determination of the membership probability. In the maximum likelihood fitting, we have to put a prior on $\delta_{j,\text{lead}}$ and $\delta_{j,\text{trail}}$, that is $\delta_{j,\text{lead}} < 50$ kpc and $\delta_{j,\text{trail}} < 50$ kpc, in order to avoid too many stars getting an unlikely, high membership probability ($P_i > 0.8$). Figure 5.3 plots again the LOSV and distance of the stream from Belokurov et al. (2014) as function of $\tilde{\Lambda}_\odot$. The log-normal, spline and polynomial fits are coloured according to the distance spread (left panel) and the LOSV dispersion (right panel). The

¹We arbitrary define the trailing arm in the range $110^\circ < \tilde{\Lambda}_\odot < 180^\circ$ as Branch A and in the region $\tilde{\Lambda}_\odot > 210^\circ$ as Branch B

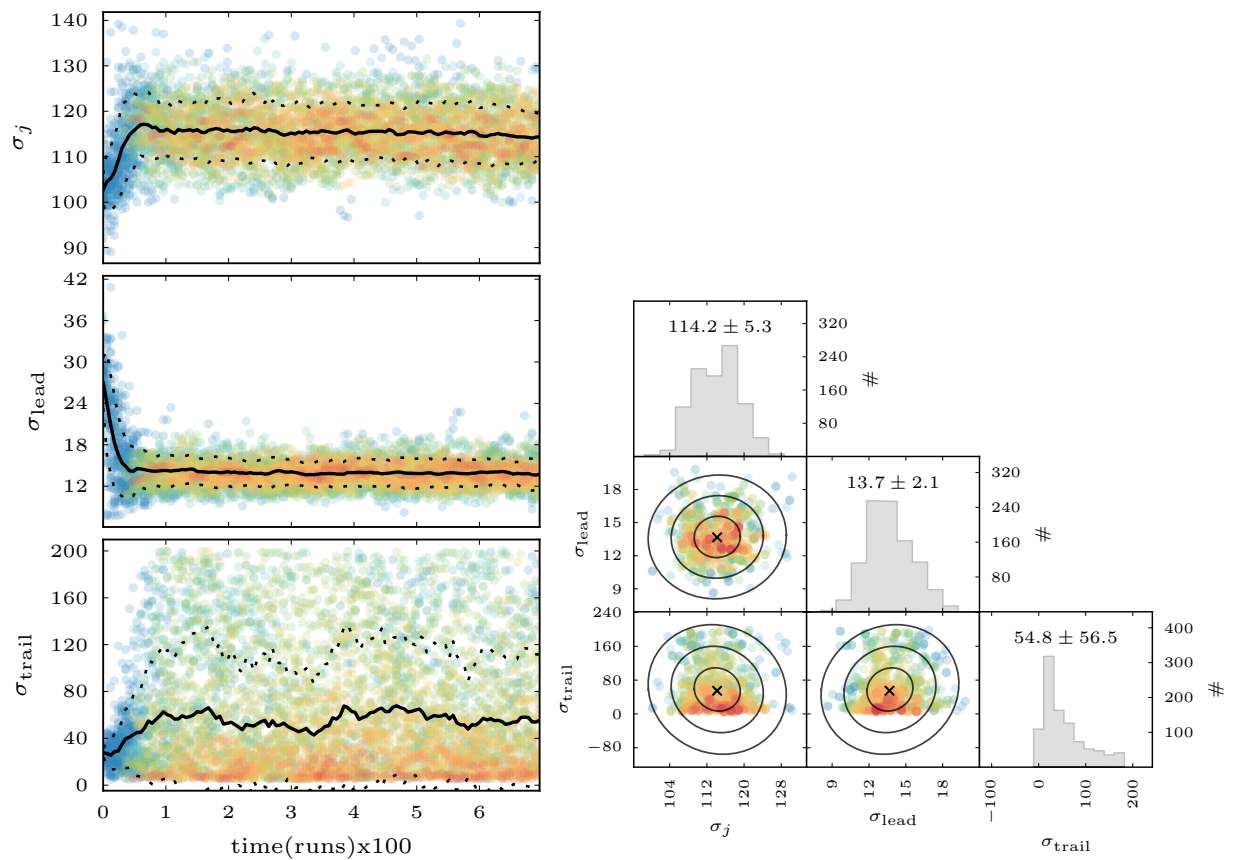


Figure 5.2: Parameter evolution (*left*) and post-burn parameter distributions (*right*) of an exemplary MCMC run that optimises the probability distributions of equation 5.5 in a given $\tilde{\Lambda}_{\odot}$ -bin (see also the caption of Figure 3.1 for a more detail description for this kind of Figure).

Gaussian distance spread is larger than 40 kpc in the leading arm as well as in the trailing arm at $\tilde{\Lambda}_{\odot} > 220^{\circ}$. Again, there are just too few stars at the position of the Branch A trailing arm to provide a reliable constraint on δ_{trail} . The LOSV dispersion is as double as large as in the model Sgr1, but the overall trend is consistent. The dispersions in the Branch A trailing arm are largest, while the Branch B trailing arm has the smallest dispersions with 10 - 25 km/s. The leading arm has an intermediate dispersion of 20 - 35 km/s, but its tails seem to have a little larger dispersion than its body.

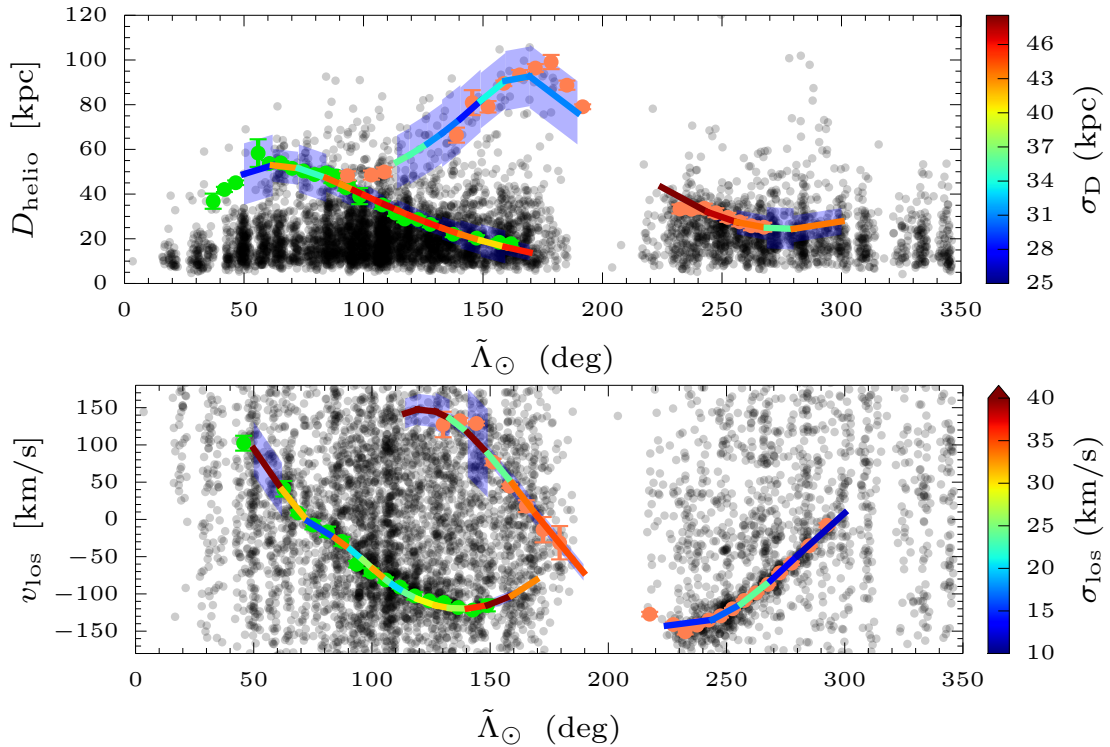


Figure 5.3: Similar to Figure 5.1; Results of the model Sgr2 for the distance spread (*top*) and the LOSV dispersion (*bottom*) as colour-coded onto the solid fit-lines.

Janesh et al. (2015) investigated the amount of substructures in the stellar halo as well. They applied the 4-distance estimator technique in combination with a friends-of-friends algorithm to identify stars of substructures in the halo. The 4-distance uses the angular position on the sky, the LOSV and the distance information of two individual stars to estimate whether the two stars move together in a group.

William Janesh has analysed our K-giant sample with their method and identified all possible candidates that could belong to a substructure. He identified 683 stars as members of Sagittarius and 944 stars as members of other substructures. This corresponds to 27% of the total sample. This approach should be more reliable than the Gaussian probability distribution around the LOSV or distance, in the sense that our method produces a significantly larger number of possible

miss-assigned halo field stars. If we assume that all stars with $P_i > 0.8$ are likely Sagittarius candidates and match these stars with Janesh’s candidates, the candidates of the model Sgr1 will match to 48% and the one of the Sgr2 will match to 69%.

Figure 5.4 compares Janesh’s candidates (black circles) with the ones from the model Sgr1 (light orange circles) in \tilde{B}_\odot , distance and LOSV as function of $\tilde{\Lambda}_\odot$. The two samples match well in most cases. There are of course some candidates of the model Sgr1 that are outside the regions where Janesh’s candidates are located. These are 34% of the possible candidates identified by the model Sgr1 and 43% regarding the Sgr2 model. Even though the model Sgr2 has a high hit ratio, it has also a larger error rate than the model Sgr1.

In the right panel, where the LOSV in dependence of $\tilde{\Lambda}_\odot$ is compared, the candidates of the model Sgr1 do not spread as wide as Janesh’s candidates due to the nature of the Gaussian used to estimate the probability of each candidate. When excluding Janesh’s candidates from the sample, the derived halo mass should be comparable to the estimates with the Sgr models, if the Sgr models correctly reproduce the LOSV distribution of Sagittarius. The Sgr models are of course applied to the whole sample.

5.2 DYNAMICAL MODEL INGREDIENTS

The stellar motions in the halo should be strongly affected by the tilt of the velocity ellipsoid. [Smith et al. \(2009\)](#) measured the tilt from a sample of ≈ 1600 sub-dwarfs in the inner halo. They confirmed that the velocity ellipsoid in the inner halo is almost pointing to the Galactic centre as we find for the thick disk as well (see Chapter 3). For this reason, we have to use a dynamical model that incorporates the correlated motion between R and z. The developed axisymmetric Jeans model from Chapter 4 is perfectly suited for this task. It should also be possible to measure the velocity anisotropy from the LOSVs, because the sample extends not only in the vertical direction towards the North Galactic Pole, but also in radial direction towards the centre and anticentre. The LOSV in the vertical direction gives a direct measure of the vertical velocity, whereas the LOSV in the radial directions gives a direct measurement of the radial velocity.

We use 5 different models throughout the chapter that we abbreviate with the following tags: (*simple*) includes all K-giants and has no contamination model, whereby equation 5.1 describes the full likelihood; (*simple_noSgr*) is the same as the model “simple”, except that it has Janesh’s 683 Sagittarius candidates excluded; (*simple_noSub*) is the same as the model “simple” as well, but this time all K-giants are excluded that belong to any substructure identified by William Janesh; (*Sgr1*) uses all K-giants and includes the Sagittarius model that is mainly based on the LOSV and is described by the likelihood 5.3; (*Sgr2*) is similar to the “Sgr1” model with the difference that it uses the Sagittarius model that is mainly based on position.

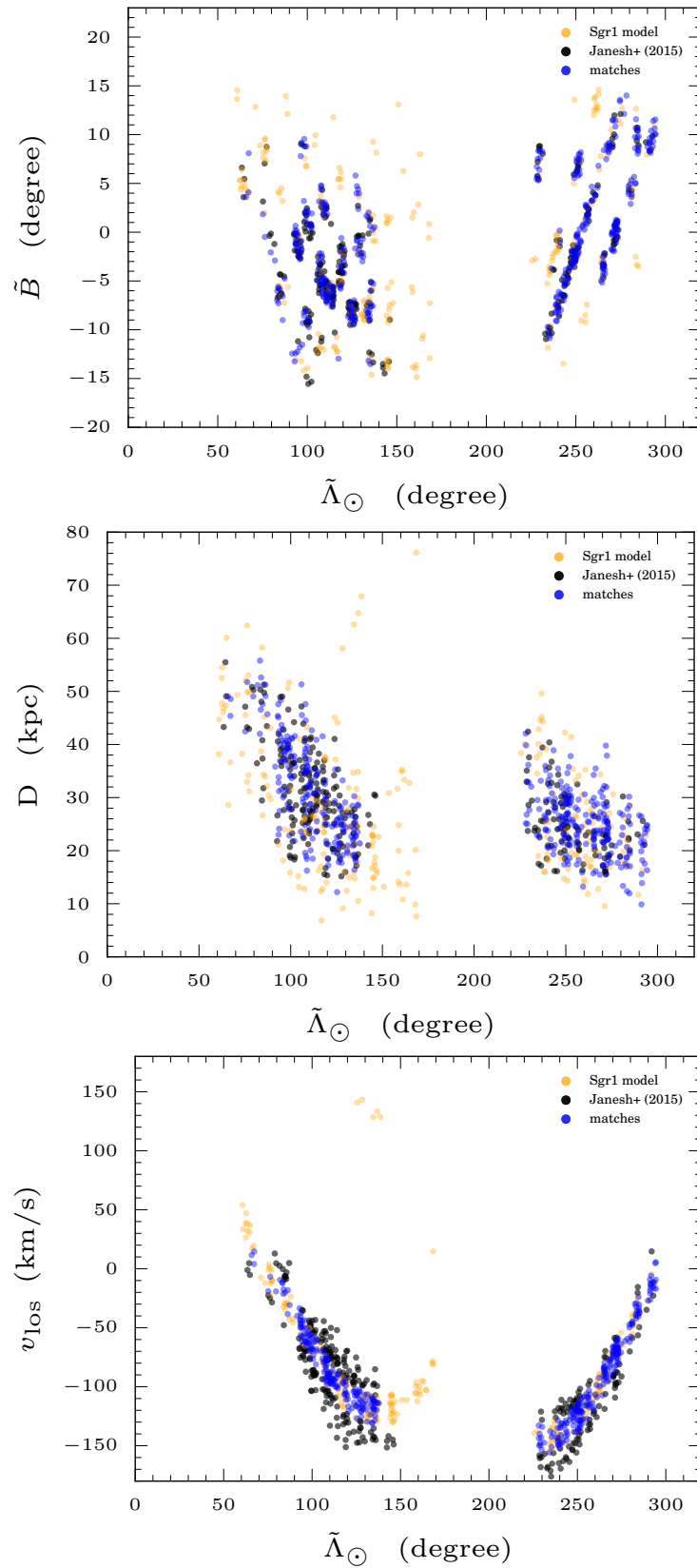


Figure 5.4: Comparison of the candidates identified by the model Sgr1 (light orange circles) and Janesh’s method (black circles) with the matches coloured in blue: *Left:* in the space of the Sagittarius stream coordinates \tilde{B}_{dot} and $\tilde{\Lambda}_{\odot}$; *Middle:* in distance versus $\tilde{\Lambda}_{\odot}$; *Right:* in LOSV versus $\tilde{\Lambda}_{\odot}$.

5.2.1 FLATTENED DENSITY PROFILES AND THE GRAVITATIONAL POTENTIAL

The currently most adopted density profile to study the structure of the stellar halo has been the broken power law (Saha 1985; Beers et al. 2012; Deason et al. 2011, 2014). So we adopt it as a step function:

$$v_{\star}(r_q) = \begin{cases} r_q^{-\alpha_{\text{in}}}, & r_q \leq r_{\text{break}} \\ r_{\text{break}}^{\alpha_{\text{out}} - \alpha_{\text{in}}} \cdot r_q^{-\alpha_{\text{out}}}, & r_q > r_{\text{break}}, \end{cases} \quad (5.11)$$

with the break radius r_{break} that marks the break between two distinct mass distributions (the inner and the outer halo) and α_{in} and α_{out} as the power law indices of the inner and the outer halo. The prefactor $r_{\text{break}}^{\alpha_{\text{out}} - \alpha_{\text{in}}}$ ensures that the two power laws are continuous at the break radius. The coordinate of choice is r_q , which describes a spheroidal distribution.

$$r_q = \sqrt{R^2 + \left(\frac{z}{q}\right)^2} \quad (5.12)$$

where $R = \sqrt{x^2 + y^2}$ and q control the flattening. A spheroidal distribution should be a good approximation to the shape of the halo, although the present substructures in the stellar halo might perturb this shape. Therefore, Xue et al. (2015) followed a “straightforward and rigorous approach to determine the posterior probability distributions of the halo parameters in light of the given data, their knowledge of the SEGUE selection function and well-established astrophysical priors on the luminosity function of giant stars”.

Sesar et al. (2011); Deason et al. (2011); Xue et al. (2015) investigated beside the broken power law an Einasto profile and concluded that the density is equally well fitted. The Einasto profile (Einasto & Haud 1989) is the 3D analogue to the Sérsic law (Sérsic 1963), which is often used to describe the surface brightness of bulges. The Einasto profile reads

$$v_{\star}(r_q) = \exp\left(-d_n \left[\left(\frac{r_q}{r_{\text{eff}}}\right)^{1/n} - 1\right]\right), \quad (5.13)$$

where $d_n \approx 3n - \frac{1}{3} + \frac{0.0079}{n}$, for $n \geq 0.5$, r_{eff} is the effective scale radius and n the concentration index. So far we have assumed that the flattening in equation 5.12 is constant. Despite of several attempts to detect a variable flattening with radius (Sluis & Arnold 1998; Sesar et al. 2011; Deason et al. 2011), only Preston et al. (1991) found an evidence for it. Thereupon it looks like that the innermost part of the halo is more flattened, which would make sense due to the vicinity and gravitational accretion from the Galactic disk.

A second confirmation comes now from Xue et al. (2015). They adopted three formulas for the variation of q , as there is obviously no consensus regarding the form of variation. We try two of them to check if they make any difference in the estimation of the halo mass. The first,

$$q(r) = q_{\text{inf}} - (q_{\text{inf}} - q_0) \exp\left(1 - \frac{\sqrt{r^2 + r_0^2}}{r_0}\right), \quad (5.14)$$

has an exponential form and q_0 sets the flattening at the centre while changing to q_{inf} at large radii on a scale radius r_0 . The second form is based on the velocity anisotropy profiles introduced by [Osipkov \(1979\)](#); [Merritt \(1985\)](#),

$$q(r) = \sqrt{q_0^2 + (q_{\text{inf}}^2 - q_0^2) \frac{r^2}{r^2 + r_0^2}} \quad (5.15)$$

and has a similar behaviour of the parameters q_0 , q_{inf} and r_0 as the exponential form 5.14. The parameters of these density models are given in [Table 5.3](#).

[Xue et al. \(2015\)](#) fit these density profiles to 3 sub-samples: First, to all SEGUE-2 K-giants in their sample; second, to a sub-sample from which Janesh’s Sagittarius candidates are removed; third, to a sub-sample from which all identified substructures are removed. We use for the model simple their density results of the whole sample. For the models simple_noSgr, Sgr1 and Sgr2, we use their density results, where Janesh’s Sagittarius candidates are removed and for the model simple_noSub, we use their results where all stars in substructures are removed. [Table 5.1](#) gives an overview on which model is used with which dataset.

Table 5.1: Overview of the models, their included likelihood and which sub-sample is used for the dynamical model (*data* column) and on which particular sub-sample the density profile is determined (*density data* column).

model	\mathcal{L}	data	data density
simple	eq. 5.2	all	all
simple_noSgr	eq. 5.2	w/o Sagittarius	w/o Sagittarius
simple_noSub	eq. 5.2	w/o any substructure	w/o any substructure
Sgr 1	eq. 5.3	all	w/o Sagittarius
Sgr 2	eq. 5.3	all	w/o Sagittarius

The gravitational potential in the model contains 3 components. We describe the stellar and the ISM component of the disk with the Miyamoto-Nagai potential given by [equation 4.6](#) and list the parameters in [Table 5.2](#), because it can be computed analytically contrary to the more realistic, numerical exponential profile. The exact shape of the potential is not as important, since the K-giants are located outside of the disk at $|z| > 3$ kpc and therefore only feel the total potential of the disk+ISM. As a consequence, we fix the parameters of these components throughout the whole analysis, unless stated otherwise.

Furthermore, we choose a spherical Navarro-Frenk-White (NFW) potential given by [equation 4.11](#) for the halo component. The spherical shape of the potential sufficiently approximate the true potential, as the velocity ellipsoid is almost spherically aligned, hence the shape of the

potential should not strongly deviate from spherical symmetry, even though the distribution function will affect the shape as well. Secondly, it is hard to distinguish the shapes of the potential with LOSV alone. The two parameters, mass M_{200} and mass-concentration c_{200} , are free parameters in the model. It is well-known that both parameters are highly degenerate, but we show in Section 5.2.3 that it is possible to break this degeneracy. The third free parameter is the velocity anisotropy κ . There is no hope to constrain the tilt of the velocity ellipsoid in the halo due to the fact that we only have LOSVs.

Given the cylindrical coordinates R and z , the velocity dispersion is computed with equation 2.22, which returns the dispersion in the λ direction. This has to be transformed into the LOSV dispersion in order to calculate the likelihood of the observed LOSV distribution, which is given by equation 5.3. The projection is described in Section 5.2.2. The likelihood of the velocity distribution uses the determined probabilities of Sagittarius members in case of the models Sgr1 and Sgr2 and assumes $\overline{v_{\text{los}}} = 0$.

Table 5.2: Fixed parameters in the gravitational potential, Δ as a measure of the tilt of the velocity ellipsoid and the velocity gradient p^2 .

M_{disk} (M_{\odot})	h_z (kpc)	h_R (kpc)	M_{gas} (M_{\odot})	$h_{z,\text{gas}}$ (kpc)	Δ (kpc)	p^2
$5.4 \cdot 10^{10}$	0.5	2.6	$1.0 \cdot 10^{10}$	0.1	3	0.7

Table 5.3: Parameters of the density profiles for the complete sample and the two sub-samples, where only Sagittarius or all substructures are removed. (These parameters are adopted from Xue et al. (2015))

	Einasto	Broken power law	Einasto exponential $q(r)$	Einasto Osipkov-Merritt $q(r)$
all data (N = 6036)	$n = 2.4 \pm 0.3$ $r_{\text{eff}} = 18 \pm 1$ kpc $q = 0.77 \pm 0.02$	$\alpha_{\text{in}} = 2.8 \pm 0.1$ $\alpha_{\text{out}} = 4.2 \pm 0.2$ $r_{\text{break}} = 30 \pm 2$ kpc $q = 0.77 \pm 0.02$	$n = 6.5 \pm 2.1$ $r_{\text{eff}} = 4 \pm 2$ kpc $q_0 = 0.3 \pm 0.1$ $q_{\text{inf}} = 0.9 \pm 0.04$ $r_0 = 9 \pm 2$ kpc	$n = 5.8 \pm 1.9$ $r_{\text{eff}} = 4 \pm 2$ kpc $q_0 = 0.2 \pm 0.1$ $q_{\text{inf}} = 0.96 \pm 0.05$ $r_0 = 15 \pm 3$ kpc
w/o Sagittarius (N = 5353)	$n = 2.8 \pm 0.5$ $r_{\text{eff}} = 16 \pm 1.4$ kpc $q = 0.72 \pm 0.02$	$\alpha_{\text{in}} = 2.1 \pm 0.4$ $\alpha_{\text{out}} = 3.9 \pm 0.1$ $r_{\text{break}} = 19 \pm 2$ kpc $q = 0.72 \pm 0.02$	$n = 7.4 \pm 1.8$ $r_{\text{eff}} = 3 \pm 1.6$ kpc $q_0 = 0.2 \pm 0.1$ $q_{\text{inf}} = 0.8 \pm 0.03$ $r_0 = 6 \pm 1$ kpc	$n = 6.6 \pm 1.8$ $r_{\text{eff}} = 3 \pm 2$ kpc $q_0 = 0.1 \pm 0.1$ $q_{\text{inf}} = 0.87 \pm 0.04$ $r_0 = 12 \pm 1.8$ kpc
w/o any substructures (N = 4409)	$n = 4.0 \pm 1.1$ $r_{\text{eff}} = 13 \pm 2.5$ kpc $q = 0.70 \pm 0.02$	$\alpha_{\text{in}} = 2.1 \pm 0.4$ $\alpha_{\text{out}} = 3.8 \pm 0.1$ $r_{\text{break}} = 18 \pm 1$ kpc $q = 0.71 \pm 0.02$	$n = 8 \pm 1.7$ $r_{\text{eff}} = 2.5 \pm 1.4$ kpc $q_0 = 0.2 \pm 0.1$ $q_{\text{inf}} = 0.78 \pm 0.04$ $r_0 = 6 \pm 1.5$ kpc	

5.2.2 PROJECTION OF THE VELOCITY DISPERSION TENSOR

As we do not additionally have proper motions available and accordingly the full 3-dimensional velocity information, we have to project the 3-dimensional dispersion tensor of the model given in prolate spheroidal coordinates on the line-of-sight. The second moment transforms in a similar way like the velocity. First, the prolate spheroidal velocities v_λ , v_ϕ and v_ν are transformed into Cartesian velocities:

$$\begin{aligned} v_x &= A \cos(\phi)v_\lambda - \sin(\phi)v_\phi - B \cos(\phi)v_\nu \\ v_y &= A \sin(\phi)v_\lambda + \cos(\phi)v_\phi - B \sin(\phi)v_\nu \\ v_z &= Bv_\lambda + Av_\nu \end{aligned} \quad (5.16)$$

The azimuthal velocity v_ϕ , as well as the angular position ϕ , in the prolate spheroidal coordinate system are identical to the ones in cylindrical coordinates. The parameters A and B depend on the position of the star

$$A^2 = \frac{(\lambda - q^2)(\nu - 1)}{(\lambda - \nu)(q^2 - 1)} \quad B^2 = \frac{(\lambda - 1)(\nu - q^2)}{(\lambda - \nu)(1 - q^2)},$$

where λ and ν are the prolate spheroidal coordinates. q^2 controls the bending of the coordinate system and in this way the tilt of the velocity ellipsoid. After the transformation to Cartesian velocities, the dot product between the Cartesian velocity vector and the normalised position vector yields the LOSV.

$$v_{los} = \vec{v} \cdot \frac{\vec{x}_{hel}}{d} = \frac{1}{d} \begin{pmatrix} v_x \\ v_y \\ v_z \end{pmatrix} \cdot \begin{pmatrix} x_{hel} \\ y \\ z \end{pmatrix} = \frac{1}{d} (v_x x_{hel} + v_y y + v_z z) \quad (5.17)$$

The position is in heliocentric coordinates with x toward the Galactic centre, y pointing in the direction of Galactic rotation ($l = 90^\circ$) and z towards the North Galactic Pole. Finally, the LOSV dispersion is obtained by inserting equation 5.16 into equation 5.17 and pulling the prolate spheroidal velocities out.

$$\begin{aligned} \overline{v_{los}^2} &= \frac{1}{d^2} \left[(A(x \cos \phi + y \sin \phi) + Bz)^2 \overline{v_\lambda^2} + (y \cos \phi - x \sin \phi)^2 \overline{v_\phi^2} \right. \\ &\quad \left. + (Az - B(x \cos \phi + y \sin \phi))^2 \overline{v_\nu^2} \right] \end{aligned} \quad (5.18)$$

5.2.3 BREAKING THE DEGENERACY BETWEEN M_{200} AND c_{200}

The virial mass M_{200} and the mass concentration c_{200} are highly degenerate parameters in the NFW potential. In equivalence to the degeneracy between the disk surface density and the disk

scale length (Bovy & Rix 2013) we can break the degeneracy between M_{200} and c_{200} by transforming the mass into a surface density Σ_{200} and measuring the surface density at that radius at which the correlation between the parameters vanishes. We define the surface density of the halo as function of the cylindrical radius R as given by

$$\Sigma_{200}(R) = \int_{-\infty}^{\infty} dz \rho_{\text{NFW}}(R, z) \quad (5.19)$$

$$= \int_{-\infty}^{\infty} dz \frac{25M_{200}a^3}{2\pi \left(\ln(1 + c_{200}) - \frac{c_{200}}{1+c_{200}} \right)} \frac{1}{a \sqrt{R^2 + z^2} \left(1 + a \sqrt{R^2 + z^2} \right)^2}, \quad (5.20)$$

where $a \equiv \frac{c_{200}}{r_{200}}$ and $r_{200}^3 = \frac{M_{200}G}{100H_0^2}$ with $H_0 = 70 \text{ km s}^{-1} \text{ Mpc}^{-1}$ being the Hubble constant and G the gravitational constant. Then we use the fact that the correlation between Σ_{200} and c_{200} depends on the cylindrical radius at which Σ_{200} is measured. So we have to run the MCMC twice, the first time with the M_{200} parameter. From the posterior distributions of the two parameters M_{200} and c_{200} , we determine the radius R_{best} at which the correlation between Σ_{200} and c_{200} vanishes. Finally, we run the MCMC a second time with Σ_{200} measured at the radius R_{best} instead of M_{200} to obtain the uncorrelated result on the halo mass.

5.3 MILKY WAY'S HALO MASS

5.3.1 LINE-OF-SIGHT VELOCITY DISPERSION

Before we look at the velocity dispersion, we should check if the velocity distribution is really Gaussian as we assume in the dynamical model. We bin the sample in radius so that each bin contains 500 stars. Beyond $r_{\text{gc}} = 40 \text{ kpc}$, the number density strongly decreases so that the bin size will be too large, if we keep the 500 stars minimum. So we reduce it first to 100 stars between 40 to 60 kpc and finally to 40 stars beyond 60 kpc. This ensures that the velocity dispersion profile is not smeared out and variations are still visible.

As a first step we determine the LOSV dispersion for each bin using the method described in Section 5.1. In particular, the likelihood is given by equation 5.1 and we omit any additional contamination term.

The left most column in Figure 5.5 shows the LOSV histograms for four typical radial bins where the radial range is indicated inside each plot. The estimated Gaussians from the maximum likelihood fitting are overplotted as black line. The top histogram reveals that below $r_{\text{gc}} \approx 20 \text{ kpc}$ the distribution is well approximated by a Gaussian.

The two middle histograms are in the range between 20 and 45 kpc, where the contribution of substructures with different velocity distributions is strongest and skews the whole distribution. The same is also partially true for $r_{\text{gc}} \gtrsim 50 \text{ kpc}$, but the skewness is weaker for most bins. It is

clear from the histograms that a single Gaussian is insufficient to describe the LOSV distribution of the halo K-giants. Since Sagittarius is responsible for about 30-70% of substructures beyond 20 kpc (Janesh et al. 2015), we include the model for the Sagittarius stream stars outlined in Section 5.1.1. Before we fit the actual velocity distribution in the radial bins, we estimate the membership probability for each star in the sample by fitting the velocity distribution along the stream given by the coordinate $\tilde{\Lambda}_\odot$. The detailed procedure is described in Section 5.1.1. The likelihood is modified according to equations 5.1-5.3 and 5.8 and includes the fixed membership probabilities.

The third column in Figure 5.5 shows the result with the model Sgr1 included for the same four radial bins as before. The fits are strongly improved in comparison to the first column, although the Sagittarius model is fixed in the fits and the LOSV dispersion of the halo (field) stars is the only free parameter. The fourth column shows the histograms and the fit with the model Sgr2. The predicted velocity distributions fit the observed histogram even better than with the model Sgr1. The second column shows the histograms when all identified stars in substructures by Janesh et al. (2015) are removed from the sample. The stars responsible for the strong skewness in the two middle histograms vanishes and the distribution becomes Gaussian-like.

The velocity dispersion profile of the three models, simple, simple_noSgr and Sgr1 as function of radius is shown in Figure 5.6. At first it stands out that the difference between the measured dispersions of the three models is smaller than their uncertainty. The dispersion decreases from 134 km/s at $r_{gc} = 10$ kpc to 70 km/s at $r_{gc} = 95$ kpc, but the slope is steeper in the inner part and becomes a bit shallower at $r_{gc} \approx 18$ kpc. Note also the small drop of 10 km/s within 1 kpc at this radius. The model Sgr1 (red) often estimates a slightly larger dispersion than the other two models, but it agrees generally better with the model simple_noSgr (green) than the model simple (black). The dispersions of the model simple are mostly lower than the ones of the model simple_noSgr, which already hints to a smaller estimated halo mass with the model simple.

So far, we have always assumed that the LOSV has a zero mean. Figure 5.7 shows the mean as function of radius if the mean LOSV \bar{v}_j in the likelihood 5.1 is a free parameter as well. The Figure compares $\overline{v_{los}}$ of the model simple (black) with the model simple_noSgr (green) and the model simple_noSub (blue). $\overline{v_{los}}$ is clearly non-zero, which is not surprising in case of the model simple. There, the substructures are thought to be the reason for the deviation from zero. Removing the substructures reduces the mean LOSV of the other two models in the range $20 \text{ kpc} < r_{gc} < 50 \text{ kpc}$ where most of Sagittarius' stars sit. But it leaves the radial bins outside this range unchanged and a smaller non-zero component in the range $25 \text{ kpc} < r_{gc} < 50 \text{ kpc}$ remains. The simplest explanation would be that still some stars residing in substructures are present. Nevertheless, we will assume $\overline{v_{los}} = 0$ in the dynamical model. $\overline{v_{los}}$ is small compared to the dispersion, so that this assumption does not bias the results.

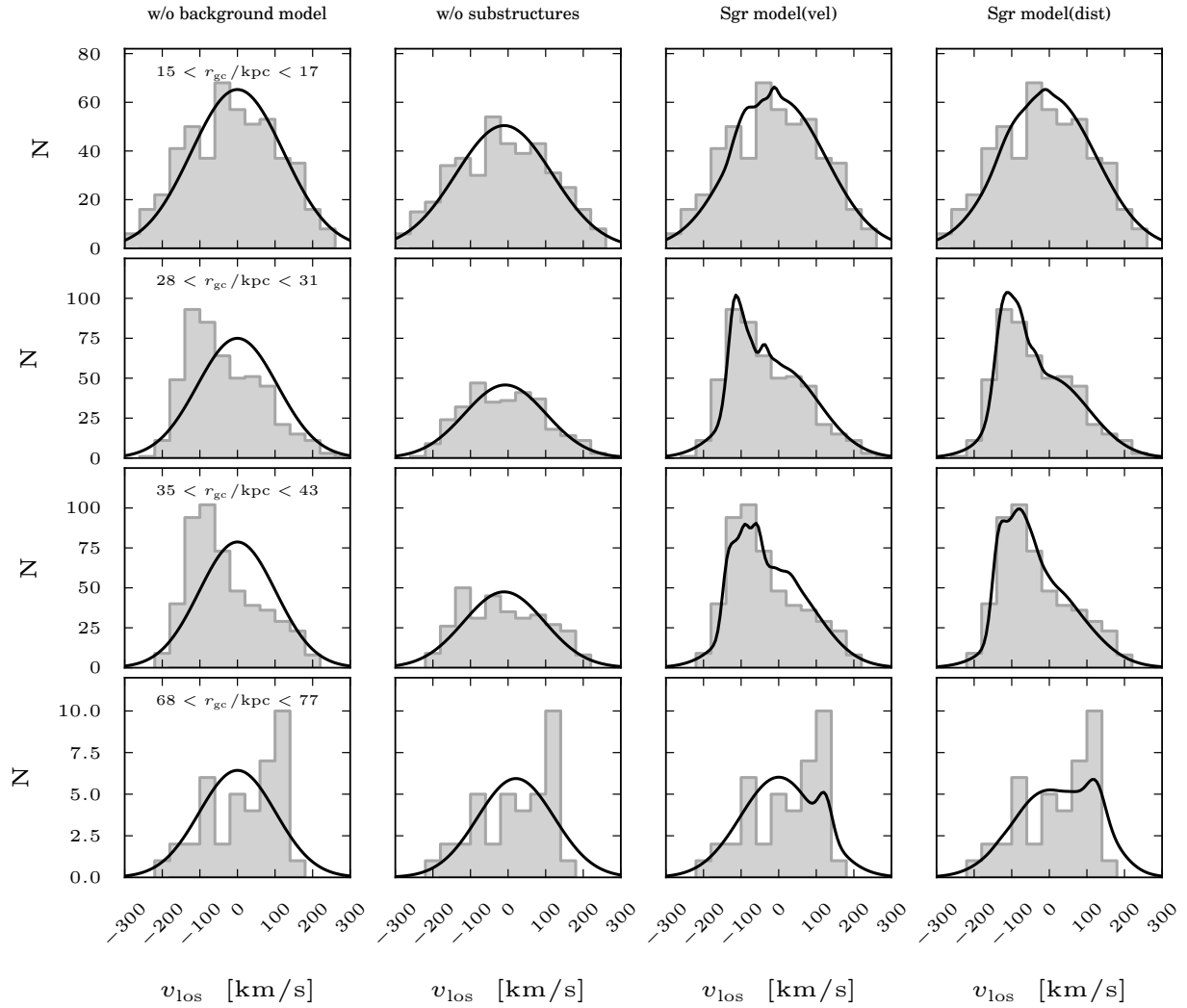


Figure 5.5: LOSV histograms of four radial bins (*rows*) overplotted with the fitted distribution as black line of the four models for the velocity distribution used in this chapter. The fits of each model are presented in a separate *column*. The range of the four radial bins is displayed inside the panels of the left most column. This column shows the fits of the model simple that has no contamination model included. The Gaussian models clearly do not fit to the skewed histograms, except marginally for the top row maybe. The middle left column shows the fits of a single Gaussian to the reduced sample without substructures. The big improvement towards a more Gaussian distribution is especially visible in the two middle rows. Most of the removed stars in this radial range belong to the Sagittarius stream. The model in the middle right column has the Sagittarius model primarily based on the LOSV included, while the included Sagittarius model displayed in the right most column is primarily based on the position. The Sagittarius models are able to match the histograms quite well, especially in the two middle rows.

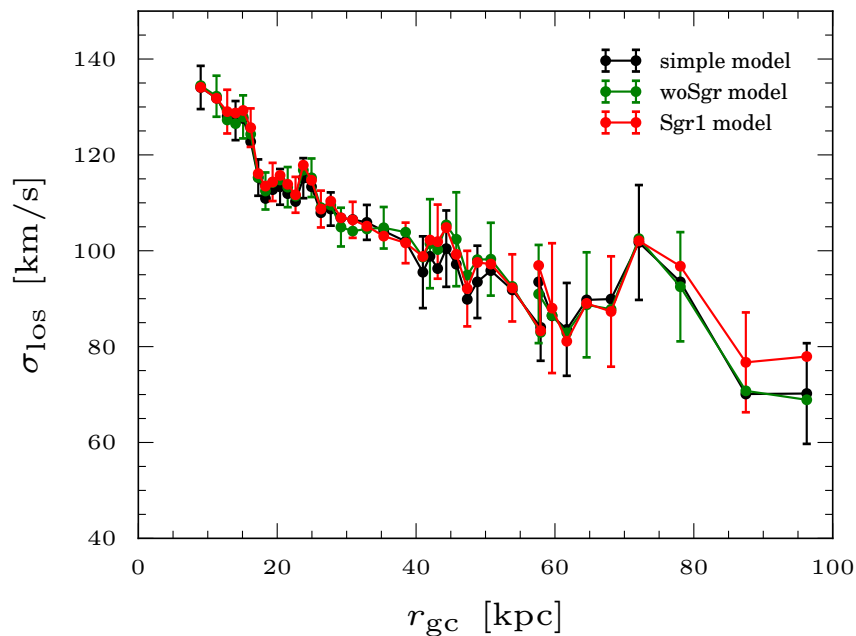


Figure 5.6: LOSV dispersion profile of the K-giants in dependence of the galactocentric distance. The three profiles compare the model simple (black), the model simple_noSgr (green) and the model Sgr1 (red).

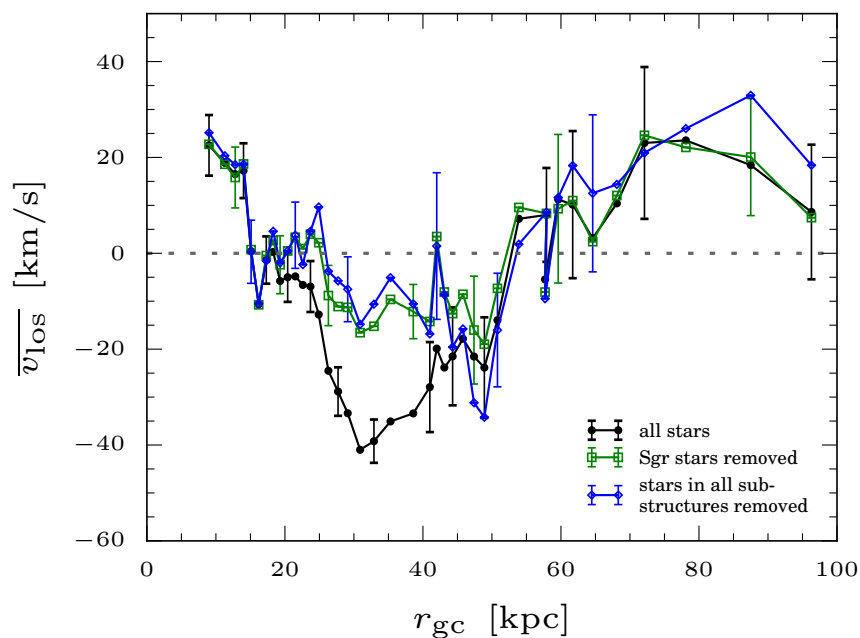


Figure 5.7: Mean LOSV of the K-giants in dependence of the galactocentric distance. The three profiles compare the model simple (black), the model simple_noSgr (green) and the model simple_noSub (blue). The dashed zero line is drawn to guide the eye.

5.3.2 THE HALO MASS

We start to investigating the effect of substructures on the mass estimates by running the models with and without the substructure candidates in the sample. Those correspond to the models `simple`, `simple_noSgr` and `simple_noSub`. Furthermore, we use the models `Sgr1` and `Sgr2` to model the velocity distribution of the Sagittarius stream when all stars are included. Figure 5.8 shows the result on the virial and total mass for the five models. The left panel plots the virial mass versus its concentration and the right panel shows the mass profile as function of radius. The total mass is the sum of $M_{\text{tot}} = M_{\text{halo}} + M_{*} + M_{\text{gas}}$ at a given radius. In order to obtain a robust result for each model, we marginalise over the three density profiles, broken power law, Einasto and Einasto with variable flattening. The flattening of the latter is given in equation 5.14.

As already indicated in the LOSV dispersion profiles in the previous sub-section, ignoring the substructures leads to a little smaller inferred halo mass within 100 kpc, because the assumed Gaussian velocity distribution mildly underestimates the actual velocity dispersion due to its skewness. The difference in the mass profile between the `simple` and the `simple_noSub` model is mainly due to their different mass concentrations, but still within their individual uncertainty range. Moreover, the match between the model `simple_noSgr` and the two `Sgr` models is absolutely remarkable. The virial mass M_{200} is the same as in the model `simple_noSgr` and the mass concentration c_{200} matches very well too. The three models are not distinguishable in their mass profile. Besides, it is striking that the two `Sgr` models also match among themselves. Of course, as the models `Sgr1` and `Sgr2` only account for the Sagittarius stream, they cannot match the model `simple_noSub`, which has all substructures removed. The model `simple_noSub` has a larger mass concentration and predicts therefore a slightly larger mass below $r_{\text{gc}} \approx 80$ kpc. Nevertheless, the mass profiles are very similar and match again at $r_{\text{gc}} \approx 100$ kpc.

For these measurements, we have decorrelated the virial mass and the concentration with the technique explained in Section 5.2.3. Figure 5.9 demonstrates the success of this technique. The bottom panel shows the MCMC posterior distribution of the three free parameters, M_{200} , c_{200} and κ . There is a severe correlation between M_{200} and c_{200} in the left panel, whereas the correlation vanishes in the run displayed in the right panel after transforming the mass into a surface density. It does not give a different result, but at least it reduces mildly the uncertainty and one can be sure that the result is not degenerate. For the subsequent analysis we choose the model `Sgr1`, because removing stars will often lead to a loss of information that can result in a systematical bias as for example a large mass concentration in the model `simple_noSub`. The model `Sgr1` accounts well for the Sagittarius stars and fits the velocity distribution accurately. Therefore, we think that it is not necessary to cut the sample.

The density distribution of the tracer stars is a very important aspect in dynamical models. Its uncertainty can sometimes be larger than the uncertainty in velocities or the statistical uncertainty of the modelling process and thus it can amount to the largest factor in the uncertainty of mass

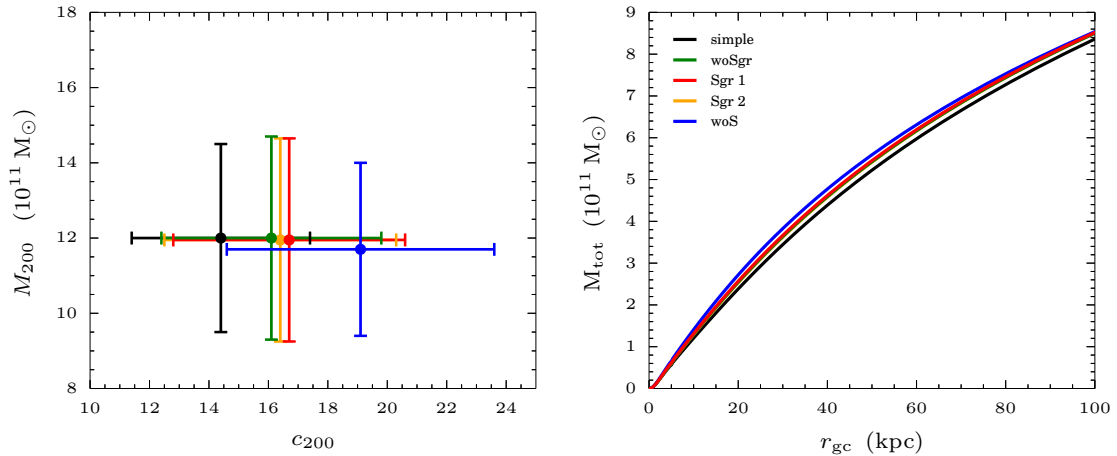


Figure 5.8: *Right:* Total mass of the galaxy as function of galactocentric radius for 5 different models with or without a background model as indicated in the legend. The model simple slightly underestimates the mass and the model simple_noSub measures a mildly larger mass in the intermediate range, but agrees again at $r_{\text{gc}} = 100$ kpc with the models that account for Sagittarius. *Left:* Virial mass versus mass concentration for the previously stated 5 models. The measurements have the same colour as in the right plot. The main differences in the mass profiles originate from different mass concentrations. The model simple_noSub has the largest mass concentration, while the model simple has the smallest one. In contrast, the three models that only account for Sagittarius match each other well.

estimates. Xue et al. (2015) compared the various density profiles of the K-giants and concluded that most of them agree well. These are in particular the in already introduced broken power law and Einasto profile (Section 5.2.1), in which the latter can be either with constant or variable flattening. We estimate the halo mass with all of them, first one by one and then we marginalise over all three within the dynamical model.

The left panel of Figure 5.10 present the virial masses M_{200} and mass concentrations c_{200} . The model with the broken power law tracer density clearly estimates the lowest mass, but largest concentration, while the Einasto profile produces the highest mass and smallest concentration. This translates into $M(r < 100 \text{ kpc}) = (6.9 \pm 0.5) \cdot 10^{11} M_{\odot}$ and $M(r < 100 \text{ kpc}) = (8.1 \pm 0.7) \cdot 10^{11} M_{\odot}$ respectively within a 100 kpc sphere. The two mass estimates are even not consistent with each other given the 1-sigma errors. Marginalizing over the three density profiles put the mass roughly in the middle of the two estimates.

The Einasto profiles with variable flattening are on the other side both close to the marginalized estimate. Despite of their different functional form of the flattening $q(r)$ they give the same result. This becomes even more explicit in the radial total mass profile shown in the right panel of Figure 5.10. The colour coding is the same as in the left panel. Until $r_{\text{gc}} \approx 60$ kpc the marginalised profile and the two Einasto profiles with variable flattening are indistinguishable. Afterwards the two Einasto profiles continue to a minimal larger mass. In the following, we only

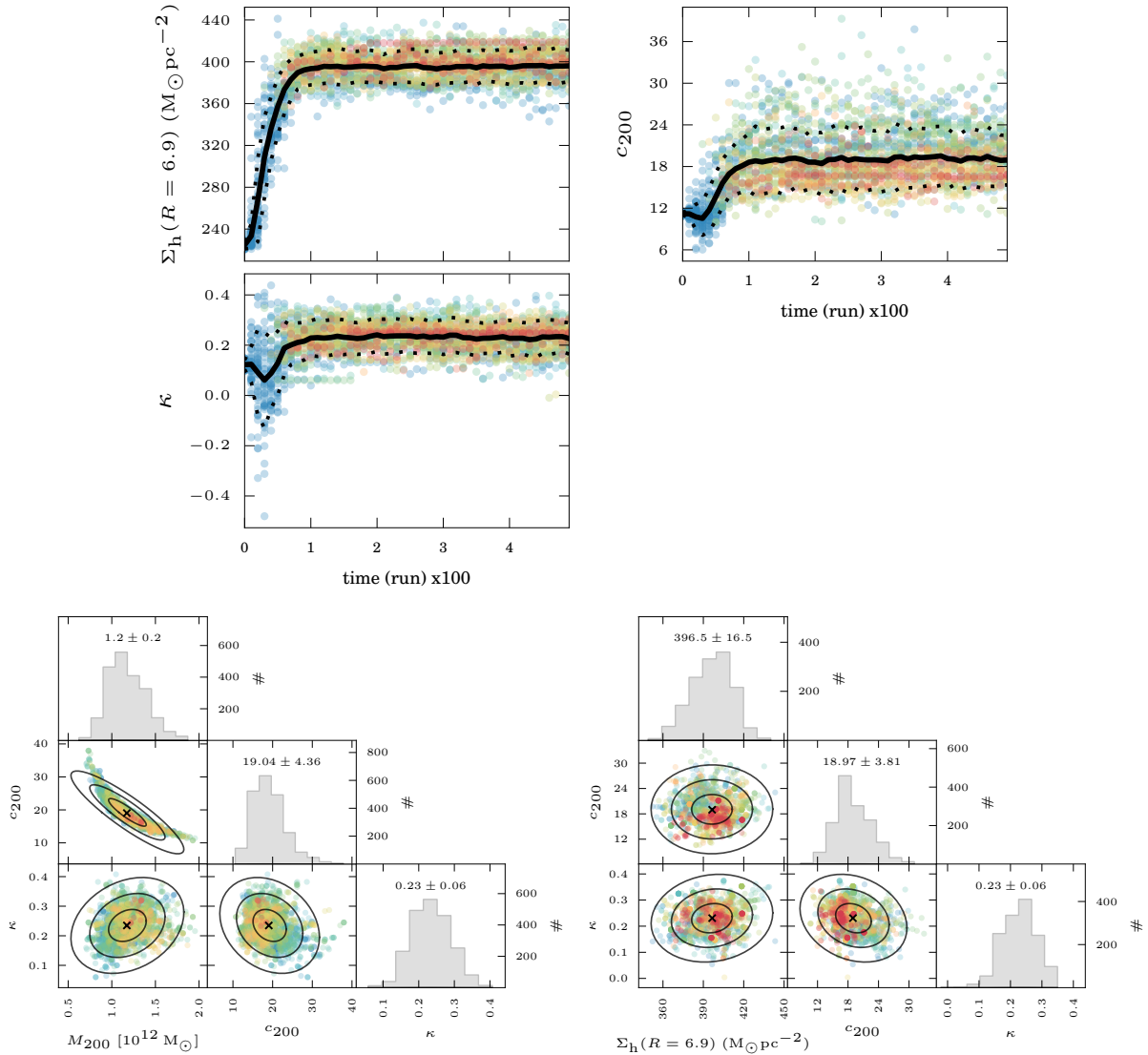


Figure 5.9: These two MCMC runs use the model `simple_noSub`. *Top:* Evolution of the parameters Σ_{200} , c_{200} , κ for 100 walkers running 500 steps, colour-coded according to the likelihood. The parameters converge very quickly after only ≈ 120 steps. *Bottom right:* Marginalised posterior distributions of the parameters coloured with the likelihood and their histograms of the last 15 steps, where the virial mass is used as free parameter. M_{200} and c_{200} are highly correlated. *Bottom left:* This is similar to the left panel, but instead the surface density Σ_{200} is used. The transformation of M_{200} into Σ_{200} dissolves the strong correlation and even weakens the small correlation between Σ_{200} and κ .

consider the exponential form in equation 5.14 as the standard functional form of the variable flattening.

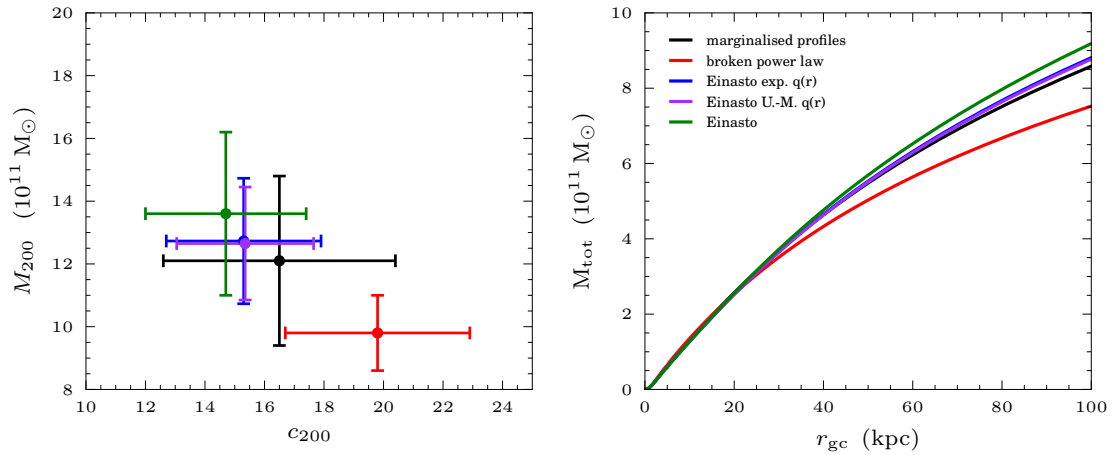


Figure 5.10: These runs are done using the model Sgr1. *Right:* Total mass of the galaxy as function of galactocentric radius for 5 different tracer density profiles: broken power law (red), Einasto (green), Einasto with variable flattening given by equation 5.14 (blue), Einasto with variable flattening given by equation 5.15 (purple) and marginalised over broken power law, Einasto and Einasto with variable q of equation 5.14 (black). Only one mass profile of the two Einasto density profiles with variable q is visible, because they cover each other. The profiles regarding the broken power law and the Einasto provide the two extrema, where the marginalised model is roughly in between and the two Einasto profiles with variable flattening are close by. *Left:* Virial mass versus mass concentration for the previously stated 5 tracer density profiles. The measurements have the same colour as in the right plot.

The best fit parameters of the various models displayed in Figures 5.10 and 5.8 are listed in Table 5.4. Figure 5.11 shows the best fit total mass profile (black line) of the model Sgr1 with its error range (dark grey lines) and additionally compares the predicted LOSV dispersion of the axisymmetric Jeans model for the three density profiles (green corresponds to Einasto, blue to Einasto with variable flattening and red to the broken power law) with the measured LOSV dispersion (black circles). The dispersion profile corresponding to the Einasto with variable flattening falls off steeper in the inner part and is a little shallower in the outer part than the Einasto with constant flattening due to a more flattened tracer density distribution in the inner part and a rounder distribution in the outer part. The dispersion profile predicted from the broken power law density matches the measured dispersion at $r_{gc} > 30$ kpc, but it does not match in the inner halo.

A similar picture emerges from the velocity anisotropy. The model with the broken power law density measures an anisotropy $\kappa = 0.16 \pm 0.06$, while the model with the Einasto density measures $\kappa = 0.21 \pm 0.06$.

κ gives the maximum velocity anisotropy and p^2 controls the anisotropy gradient, where $p^2 = 1$ means isotropic and $p^2 = 0$ the maximum possible gradient (see also equation 2.19). Because only a few stars have measured proper motions and LOSVs beyond 10 kpc, there are no real measurements of this gradient so far out and p^2 will influence the fitted value of κ in the models at least a little. That is why we marginalise over the likely values of p^2 by freeing the parameter in the model. In this way, we get a reasonably robust measurement of κ . As expected, p^2 is not constraint by the model and varies between 0 and 1 with a mean of $p^2 = 0.49 \pm 0.31$. The anisotropy is radial supported and the result $\kappa = 0.19 \pm 0.06$ indicates that the velocity in the stellar halo is definitely not isotropic on a $\sim 3\sigma$ level.

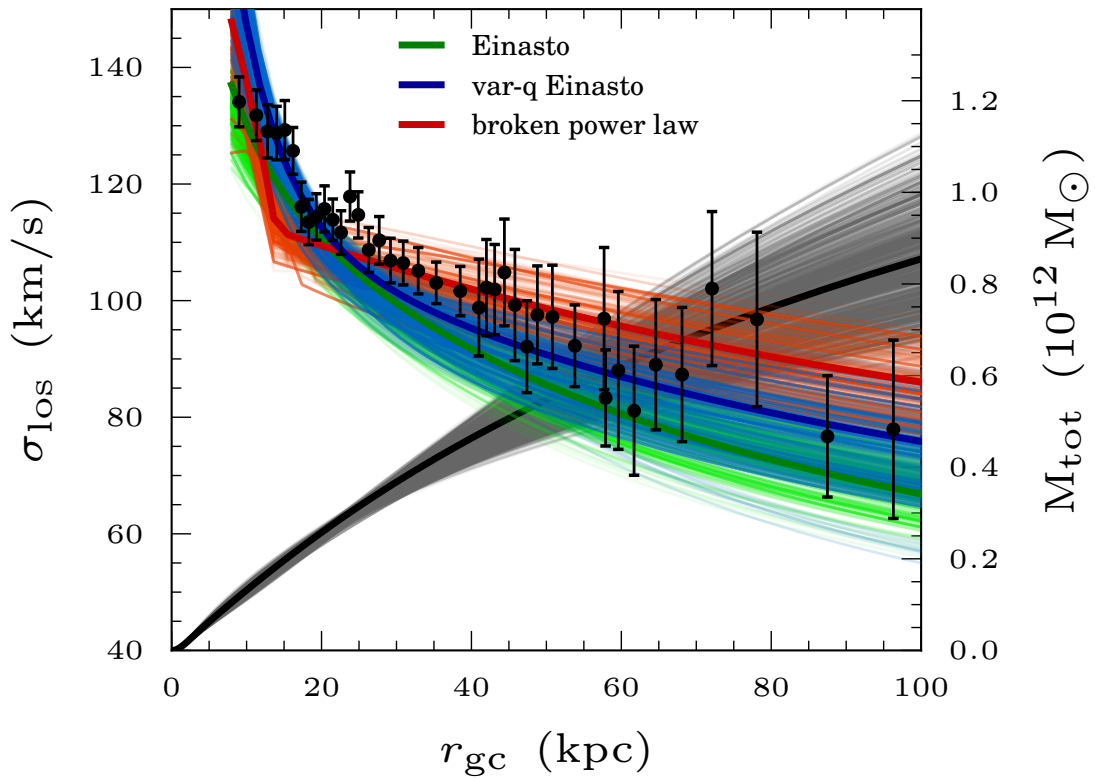


Figure 5.11: The total mass (black solid line) and the LOSV dispersion as function of galactocentric radius as predicted by model Sgr1 and marginalised over the tracer density profiles, broken power law (red), Einasto (green) and its variable flattening version (blue). The mass profiles from the MCMC posterior distribution of the parameters Σ_{200} and c_{200} are plotted in lighter colours and with thinner lines. The prediction of the model with the broken power law does clearly not fit with the measured LOSV dispersion in the inner halo.

Figure 5.12 summarises the models of the three different substructure contributions and the three different density profiles with respect to the mass profile and the best fit LOSV dispersion. The model Sgr2 is not shown, because it gives the same result as the model Sgr1. The

black/grey lines and the blue lines in the background represent the model Sgr1 with variable flattened Einasto density as reference for the other models which are not explicitly marked and just displayed as dashed lines. The virial mass for the model Sgr1 is $M_{200} = (12.7 \pm 2.0) \cdot 10^{11} M_{\odot}$ with a mass concentration of $c_{200} = 15.3 \pm 2.6$ which translates to a pure halo mass of $M(r < 100 \text{ kpc}) = (8.2 \pm 0.8) \cdot 10^{11} M_{\odot}$ within 100 kpc. The comparison makes clear that the various models yields comparable results within the range of their uncertainty.

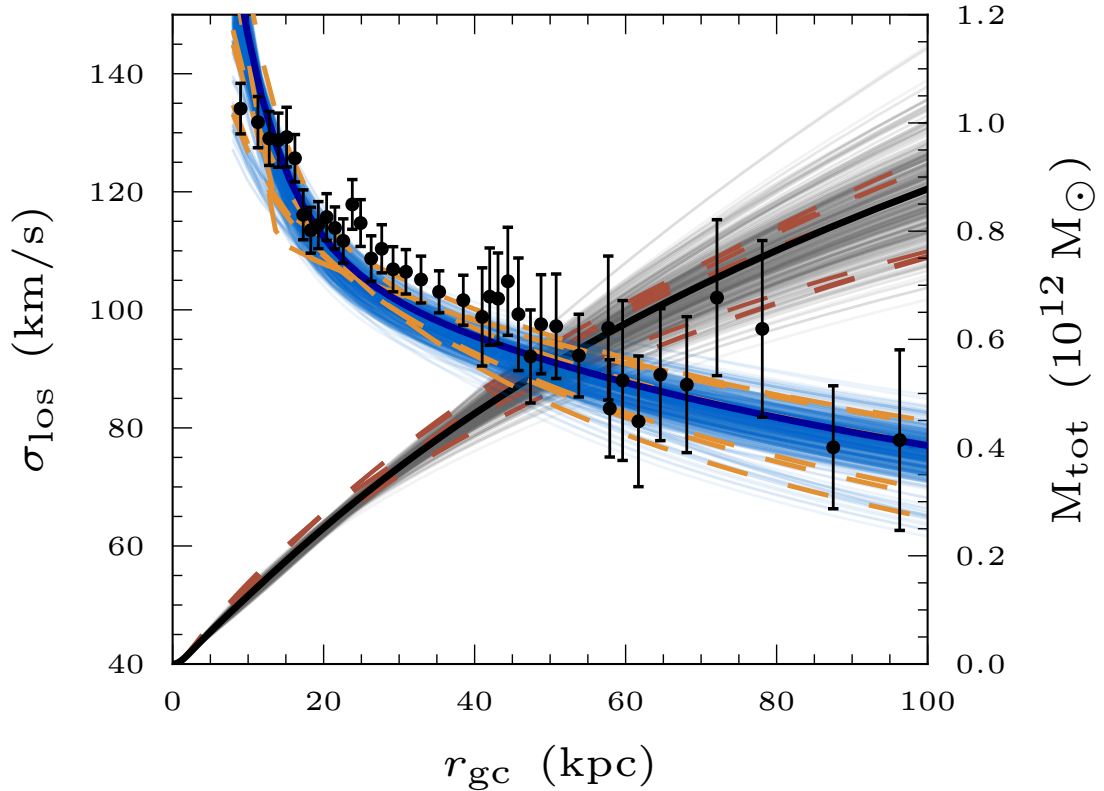


Figure 5.12: The total mass (black solid line) and the LOSV dispersion (blue solid line) as function of galactocentric radius as predicted by Sgr1 model including the variable flattened Einasto tracer density profile. The thinner lines are predictions from the MCMC posterior parameters. The dashed lines represent combinations of the three different substructure models simple_noSgr, simple_noSub and Sgr1 with the three relevant density profiles, broken power law, Einasto and its variable flattening version. All these models agree with the above mentioned reference model.

Table 5.4: Best fit parameters of the various models. The total mass within 100 kpc and the likelihood of the model is also listed, in addition to the parameters of the models.

	density	M_{200} ($10^{11} M_{\odot}$)	c_{200}	$M(r < 100 \text{ kpc})$ ($10^{11} M_{\odot}$)	κ	\mathcal{L}
simple	marginalised	11.2 ± 2.6	17.2 ± 4.2	8.1 ± 1.0	0.16 ± 0.06	-37092
	broken power law	9.9 ± 1.1	19.0 ± 2.7	7.5 ± 0.5	0.15 ± 0.06	-32983
simple_noSgr	Einasto	14.2 ± 2.9	13.8 ± 2.7	9.4 ± 1.0	0.2 ± 0.05	-32975
	Einasto exponential q(r)	12.7 ± 1.9	15 ± 2.2	8.8 ± 0.7	0.17 ± 0.06	-32971
	marginalised	12.0 ± 2.7	16.4 ± 4	8.5 ± 1.1	0.17 ± 0.06	-32975
simple_noSub	broken power law	9.7 ± 1.1	24.4 ± 4.3	7.6 ± 0.5	0.21 ± 0.06	-27306
	Einasto	12.0 ± 1.9	19.7 ± 3.7	8.7 ± 0.8	0.27 ± 0.06	-27298
	Einasto exponential q(r)	12.8 ± 1.8	18.0 ± 3.1	9.1 ± 0.7	0.23 ± 0.06	-27296
	marginalised	11.7 ± 2.1	19 ± 4	8.5 ± 0.9	0.23 ± 0.06	-27298
	broken power law	9.8 ± 1.2	19.8 ± 3	7.5 ± 0.6	0.16 ± 0.06	-35019
Sgr 1	Einasto	13.6 ± 2.6	14.7 ± 2.7	9.2 ± 1	0.21 ± 0.06	-35011
	Einasto exponential q(r)	12.7 ± 2	15.3 ± 2.6	8.8 ± 0.8	0.18 ± 0.06	-35008
	Einasto Osipkov-Merrit q(r)	12.6 ± 1.8	15.3 ± 2.3	8.7 ± 0.7	0.17 ± 0.05	-35004
Sgr 2	marginalised	12.0 ± 2.7	16.7 ± 4	8.5 ± 1.1	0.18 ± 0.06	-35006
	marginalised	12.0 ± 2.7	16.1 ± 3.7	8.5 ± 1.1	0.19 ± 0.06	-35146

5.4 DISCUSSION AND CONCLUSION

We estimate the mass of the Galactic halo by applying the axisymmetric Jeans model derived in Section 2.4 to a set of 6036 SEGUE-2 K-giants. Their selection function is well understood, they are numerous in the halo and bright enough to allow for realistic distances. We incorporate the tracer density profiles of the same sample determined by Xue et al. (2015) in our dynamical models. The sample ranges from 5 - 95 kpc in radius and includes a non-negligible amount of stars in substructures. These stars cause the velocity distribution to skew in some radial bins.

We fit the LOSV distribution in a discrete way, in which we predict its dispersion from the axisymmetric Jeans model. The assumption that the LOSV distribution is Gaussian overall, is problematic because of the large variety of substructures in the halo and hence also in the K-giant sample. It is already widely accepted that the halo contains a variety of substructures, from disrupted satellite streams to overdensities of stars (e.g. Belokurov et al. 2006). The Sagittarius stream is the largest substructure among them and contributes $\approx 42\%$ of the substructures in our sample. Kafle et al. (2012) investigated the effect of substructures on the velocity dispersion, but only in the range 5 - 20 kpc. We also check the LOSV distribution and dispersion. As we assume in the dynamical model that the LOSV distribution is Gaussian, a strong deviation from that might bias the estimated LOSV dispersion.

We binned the sample in radius and fitted the distribution in each bin with a maximum likelihood approach. Moreover, Janesh et al. (2015) reliably identified with their method those stars in our sample that originate from Sagittarius and other substructures. After excluding all these substructured stars, the measured dispersions should be different to the ones measured on the whole sample. We do not notice a discernible effect on the LOSV distribution or dispersion in the range 5 - 20 kpc. However, the substructures perceptibly skew the distribution in the range 20 - 45 kpc. The dispersions are a little larger when the substructures are excluded, but still in the range of uncertainty. Xue et al. (2015) studied the effect of these substructures on the density profiles and discovered that the substructures steepen the profiles and make the halo slightly rounder.

Next, we create a model to evaluate the LOSV distribution of Sagittarius in dependence of the position and to predict the probability for each star to belong to Sagittarius. The model can either determine the membership probability primarily based on the LOSV (Sgr1) of the star or primarily based on the 3D position (Sgr2) in relation to the LOSV or position of the stream. The kinematical model defined in Section 5.1 can accurately reproduce the skewed LOSV distribution of the K-giants. From this point of view, we also find that it does not matter whether the membership probabilities are mainly obtained by the velocities or positions with respect to the stream. Both models, Sgr1 and Sgr2, fit the LOSV distribution equally well and they also give the same result on the estimated halo mass. The LOSV dispersion measured from these models decrease from $\sigma_{\text{los}} \approx 135$ km/s at $r_{\text{gc}} = 10$ kpc to $\sigma_{\text{los}} \approx 75$ km/s at $r_{\text{gc}} = 90$ kpc.

Kafle et al. (2014) observed a strong drop from $\sigma_{\text{los}}(r_{\text{gc}} = 5 \text{ kpc}) = 160 \text{ km/s}$ to $\sigma_{\text{los}}(r_{\text{gc}} = 20 \text{ kpc}) = 100 \text{ km/s}$ that we cannot confirm in our data, although the slope is indeed a little steeper below 20 kpc. The gradient subsequently becomes shallower in their data, what they associated with the transition between inner and outer halo in the density profile. Using ~ 2400 BHB stars, Xue et al. (2008) conversely measured a smaller gradient from $\sigma_{\text{los}}(r_{\text{gc}} = 10 \text{ kpc}) = 108 \text{ km/s}$ to $\sigma_{\text{los}}(r_{\text{gc}} = 50 \text{ kpc}) = 96 \text{ km/s}$, which is also in contrast to our measurements. However, the ~ 900 BHBs and blue stragglers of Brown et al. (2010) coincide nicely with the dispersions of our K-giants in their measurement range of $15 < r_{\text{gc}} < 75 \text{ kpc}$. Battaglia et al. (2005) measured the LOSV dispersion directly from a set of very different objects consisting of BHB stars, red giants, globular clusters and satellite galaxies, in total 240 objects situated between 10 and 120 kpc. Their profile declining from $\sigma_{\text{los}}(r_{\text{gc}} = 10 \text{ kpc}) = 130 \text{ km/s}$ to $\sigma_{\text{los}}(r_{\text{gc}} = 90 \text{ kpc}) = 80 \text{ km/s}$ is in good agreement with our findings again. Given the very different velocity dispersions for the various sub-populations in the Galactic disk, the halo seems in contrary to have a quite uniform dispersion profile with respect to its different populations.

In order to estimate the halo mass, we fit the LOSV distribution in a discrete way using an MCMC without any binning, in which we predict the LOSV dispersion from the axisymmetric Jeans model. We additionally adopt the density profile of the K-giants reported by Xue et al. (2015). They tried five different functional forms of the density, which include the Einasto profile, the broken power law and Einasto profiles with three different variable flattening functions. We analyse to what extent the mass estimates with these profiles² differ.

The two variable flattened profiles give comparable results and the fits to the LOSV dispersion are slightly better than with the normal Einasto profile, which still gives a good fit. The model with the broken power law can only fit the outer halo, whereas the fit in the inner halo is very poor. To be more precise, both slopes of the broken power law do not agree with the slope of the dispersion profile, neither in the inner nor in the outer part. The inner slope of the power law should be steeper and the outer one a little shallower, so that it is questionable if the broken power law is the correct density distribution to describe the dynamics of the halo, albeit Xue et al. (2015) shows that the broken power law fits the density distribution of the K-giants as equally well as the Einasto profiles. When marginalising over all three profiles they can fully cover the range of measured LOSV dispersions and actually complement one another nicely in the outer halo. This suggests that the broken power law should not be adopted in the determination of the halo mass from kinematic tracers, at least not as the only density profile in the model. Maybe, adopting a variable flattening in the broken power law might change the picture, such that the velocity dispersion profile in the inner halo will be better fitted.

We can quantitatively verify the two Sagittarius models by comparing their results on the mass profile with the case where all stars identified as Sagittarius members are excluded. The three models agree pretty well on the estimated halo mass, for which we get a virial mass of

²We only use four profiles: Einasto, broken power law and two with variable flattening

$M_{200} = (12.0 \pm 2.7) \cdot 10^{11} M_{\odot}$ and a mass concentration of $c_{200} = 16.3 \pm 3.9$. As the mass and the concentration are degenerate³ and the virial mass is often extrapolated, since it is not measured within the radius in which the tracer objects are located, it is more robust to specify the mass within the radius that is still covered by the tracer objects. So the mass that we estimate within 100 kpc from the Galactic centre is $M(r < 100 \text{ kpc}) = (8.5 \pm 1.1) \cdot 10^{11} M_{\odot}$, when we only take Sagittarius as disturbing substructure into account.

Janesh et al. (2015) also identified other substructures than Sagittarius in our sample. When excluding these stars as well, the axisymmetric Jeans model estimates $M_{200} = (11.7 \pm 2.1) \cdot 10^{11} M_{\odot}$, $c_{200} = 19.0 \pm 3.8$ and hence $M(r < 100 \text{ kpc}) = (8.5 \pm 0.9) \cdot 10^{11} M_{\odot}$. The virial mass as well as the total mass within 100 kpc are in good agreement with the estimate on the whole sample and including one of the Sagittarius models. The mass concentration, however, increases due to a more concentrated tracer density. So, the concentration index n of the Einasto profile changes from $n = 2.4$ to $n = 4.0$. In addition, we estimate the halo mass $M_{340} = (10.6 \pm 2.0) \cdot 10^{11} M_{\odot}$ and its concentration $c_{340} = 16 \pm 4.3$ for the model that excludes all substructures.

Our mass estimate is slightly larger than most other determinations. Gnedin et al. (2010) applied a spherical Jeans model to hypervelocity stars in the range 25 - 80 kpc assuming a single power law. They find a mass of $M(r < 80 \text{ kpc}) = 6.9_{-1.2}^{+3} \cdot 10^{11} M_{\odot}$ within 80 kpc, that agrees with our estimate of $M(r < 80 \text{ kpc}) = (7.5 \pm 0.7) \cdot 10^{11} M_{\odot}$. It is also consistent with the results of Wilkinson & Evans (1999) ($M(r < 50 \text{ kpc}) = 5.4_{-3.6}^{+0.2} \cdot 10^{11} M_{\odot}$) and Sakamoto et al. (2003) ($M(r < 50 \text{ kpc}) = 5.5_{-0.4}^{+0.1} \cdot 10^{11} M_{\odot}$). They adopted a distribution function to 27 satellite galaxies and globular clusters and to a sample of 561 objects consisting of field Horizontal-Branch stars, globular clusters and satellites, respectively.

Another work that used a set of different objects was done by Battaglia et al. (2005). They applied a spherical Jeans model on binned data to estimate a virial mass $M_{200} = 0.8_{-0.2}^{+1.2} \cdot 10^{11} M_{\odot}$ with a mass concentration $c_{200} = 18$. Their model favours a high mass concentration as well, similar to our model, where all substructures are removed. The distribution function model of Deason et al. (2012) also prefers a higher mass concentration ($c_{\text{vir}} = 20$) with a virial mass $M_{\text{vir}} \sim 10^{12} M_{\odot}$. Authors normally adopt or find a mass concentration between 5 and 12. For example, Piffl et al. (2014) get $c_{340} \approx 5$ from high-velocity stars of the RAVE survey, which is on the lower end, but their virial mass of $M_{340} = 1.3_{-0.3}^{+0.4} \cdot 10^{12} M_{\odot}$ is consistent with ours again. On the other side, Xue et al. (2008) estimated the virial mass from 2400 BHB stars and comparisons to cosmological simulations yielding $M_{340} = 0.91_{-0.18}^{+0.27} \cdot 10^{12} M_{\odot}$ with the mass concentration ($c_{340} = 12.0 \pm 0.3$) on the upper end. The mass concentration, that we get with the same definition of the virial mass and the model simple_noSub, just agrees with their estimate due to its large uncertainty. If we use instead the model Sgr1 with the variable flattened Einasto density profile only, the resulting concentration ($c_{340} = 13.3 \pm 2.4$) is already close to their estimate. Of course,

³One can get the same mass within a specific radius either from a larger virial mass and a lower concentration or from a smaller virial mass and a higher concentration

because the additional substructures in the model Sgr1 makes the density profile of the stellar halo shallower, the dark halo will be more concentrated after removing them. Furthermore, the mass concentration is generally larger when including the broken power law density, although its density profile itself matches well with the Einasto profiles. Cosmological simulations support intermediate concentrations suggesting $c \sim 10$ (Macciò et al. 2008). However, this constraint comes from dark matter only simulations and there are evidences from simulations (e.g. Davis et al. 2014) that baryons in the bulge and the Galactic disk can gravitationally interact with dark matter leading to a contraction of the dark matter halo. Hence, the dark halo would be more concentrated.

Another possibility to infer the halo mass is the fitting of orbits of streams, in which the mass within the galactocentric distance of the stream can be determined. Küpper et al. (2015) fitted the orbit of the Palomar 5 stream that is at a distance of ≈ 19 kpc to the Galactic centre. They find $M(r < 19\text{kpc}) = (2.1 \pm 0.4) \cdot 10^{11} M_{\odot}$ slightly smaller than $M(r < 19\text{kpc}) = (2.6 \pm 0.1) \cdot 10^{11} M_{\odot}$ of our model. Some authors (Sakamoto et al. 2003; Boylan-Kolchin et al. 2013) also included the distant satellite galaxy Leo I in their analysis. Leo I is at a distance of $D \approx 260$ kpc and it is still a subject of debates whether this dSph galaxy is bound or unbound to the Milky Way. Piffl et al. (2014) provide lower limits for the pair $(M_{\text{vir}}, c_{\text{vir}})$ below which Leo I would be unbound. Given the small virial mass with respect to the large concentration that we estimate, the gravitational force would be too weak at the distance of Leo I to keep it on a bound orbit.

Moreover, it is unlikely that this halo mass is small enough to solve the “Too Big To Fail” problem. Wang et al. (2012) computed the probability that a galaxy like the Milky Way would have at maximum three massive satellites given the mass of the host galaxy. This probability is about 0.45, if $M_{200} \approx 12 \cdot 10^{11} M_{\odot}$. Nevertheless, several other authors (Kafle et al. 2014; Vera-Ciro & Helmi 2013; Gibbons et al. 2014) claims to have estimated a mass small enough to be consistent with the prediction of Λ CDM.

There are just a few attempts in the literature to measure the velocity anisotropy of the Galactic halo. We constrain the anisotropy⁴ in the outer halo to be $\kappa = 0.19 \pm 0.06$, which is radially biased and significantly different from isotropic. Deason et al. (2012) measured a larger anisotropy ($\beta \sim 0.5$) from ~ 2000 BHB stars at distances between 20 to 40 kpc. On the other hand, Deason et al. (2013b) used proper motions from the Hubble Space Telescope to measure $\beta = 0.0^{+0.2}_{-0.4}$ in the range $18 < D/\text{kpc} < 30$. The anisotropy near the disk is around 0.6 (Bond et al. 2010) and Kafle et al. (2012) found a dip of the anisotropy at $r_{\text{gc}} \approx 17$ kpc, where it first declines from $\beta \sim 0.6$ to $\beta \approx -1.1 \pm 0.8$ and then rises to $\beta \approx 0.0$ again. So, Deason et al. (2013b) argued that it would be indeed possible that the anisotropy first declines to zero and rises again at $r_{\text{gc}} \sim 20$ kpc, which would be interestingly in the same region as the break of the stellar density profile. Substructures might be able to influence the anisotropy strongly. It is interesting

⁴Note, that κ is not the anisotropy in the spherical coordinate system as mostly reported in literature, but the one in prolate spheroidal coordinates. However, it is almost identical to the spherical anisotropy at these large radii.

from this regard, that we will estimate a smaller anisotropy ($\kappa = 0.16 \pm 0.06$), if we ignore all substructures and use the model simple instead of the model Sgr1, and we will estimate a large anisotropy ($\kappa = 0.23 \pm 0.06$), if we cut all substructures and use the model simple_noSub.

The majority of parameters in our dynamical model are set to a fixed value. In such a case, it is always good to check how robust the halo mass estimate is for these parameters. The disk mass M_{disk} and the turnover of the velocity anisotropy p^2 are probably the most critical parameters. Therefore we checked if the halo mass estimate substantially changes when the two parameters are varied. Beside the moderate turnover $p^2 = 0.7$, we test a stronger turnover with $p^2 = 0.4$ and a constant anisotropy where $p^2 = 1$. Furthermore, we increase the disk mass by $\sim 20\%$ from $M_* = 5.3 \cdot 10^{10} M_{\odot}$ to $M_* = 6.4 \cdot 10^{10} M_{\odot}$. It turns out that p^2 has a negligible effect on the mass estimate and if at all, then a stronger gradient in the anisotropy minimally increases the maximum anisotropy κ . The model is similarly robust to moderate changes of the disk mass. M_{200} increase by 5% and c_{200} decreases by 8%, but the radial mass profile remains almost unchanged.

We do not include a bulge in the above analysis, since the K-giants are at least 5 kpc away from the centre. We repeat the run with the model Sgr1 and test whether the inclusion of a bulge would change the results. If we include a spherical exponential bulge described by equation 4.5 with a mass $M_b = 7 \cdot 10^9 M_{\odot}$ and a radial scale length $r_s = 0.8$ kpc and at the same time conserve the total baryonic mass of the previous results by diminishing the stellar disk mass to $M_* = 4.6 \cdot 10^{10} M_{\odot}$, the mass concentration will decrease a little from $c_{200} \approx 15.3$ to $c_{200} = 14.7 \pm 2.5$, which is still higher than expected, but the virial mass remains the same and the small change in c_{200} is still within the uncertainty of the result without the bulge. So, the presence of the bulge in the adopted potential does not alter the interpretation of our results.

Dark matter exists on large scales like in galaxy clusters as well as on small scales like in Galactic halos or in disks of galaxies. It makes up $\sim 85\%$ of all matter and accounts for 26% of the energy budget in the universe. However, its nature is still unknown. We know that it must interact gravitationally and we expect it to interact weakly, but it has not been detected yet. The success of such a direct detection is inevitably linked to our knowledge of the local dark matter density. Dynamical models are the essential tools to uncover the amount of dark matter surrounding us. They are also key to learn about the intrinsic properties of our Galaxy.

My thesis presents advancements in our understanding of the coupled motion in radial and vertical direction between stars in the Galactic disk and in the characterisation of the effect of the so-called tilt of the velocity ellipsoid on the dynamically inferred mass. After we constructed an axisymmetric Jeans model that accounts for the coupled motion, we measured the local dark matter density. Finally, we applied this model to stars in the Galactic halo to determine the mass profile of the dark halo. At the same time, we qualified the effect of substructures in our sample of tracer stars on the halo mass estimate.

In the following, We summarise the work we have presented in this thesis and give an outlook to the next steps in dynamical modelling.

6.1 TILT OF THE VELOCITY ELLIPSOID

In [Chapter 3](#), we characterised the tilt of the velocity ellipsoid in the disk. We motivated the measurement of the tilt with contradictory results of the vertical Jeans model on two chemically-distinct sub-samples. We started from a sample of $\sim 16,000$ G-type dwarf stars from the Sloan Extension for Galactic Understanding and Exploration survey (SEGUE, [Yanny et al. 2009](#)) described in [Chapter 2](#), that cover a vertical distance between 0.3 and 2.5 kpc. We then extracted two sub-samples, a metal-rich, low α -abundant (α -young) and a metal-poor, high α -abundant

(α -old). For both sub-samples, we robustly measured the velocity ellipsoid as function of height above the Galactic mid-plane, by fitting the velocity distribution in height z and radius R with a multi-variate normal distribution. We employed a Markov Chain Monte Carlo (MCMC) likelihood method that accounts for contaminants of halo stars. Due to the careful selection of our sample, the fraction of halo stars is well below 10%.

Then, we constructed vertical Jeans models with a gravitational potential consisting of an exponential disk and a constant dark matter contribution in the solar neighbourhood. When applied separately to the two sub-samples the vertical Jeans model should give the same answer as every star in our sample traces the same underlying potential. However, the results show that the α -young stars require a substantial amount of dark matter in the disk, while the α -old stars do not need any dark matter. The convenience of the vertical Jeans models is that they are simple and straightforward to apply. Unfortunately, this simplicity comes along with several assumptions, including that the stellar motion is decoupled in height z and radius R or, in other words, a zero tilt of the velocity ellipsoid.

However, we expect the tilt to increase with the height above the mid-plane (e.g. [Smith et al. 2012](#)) and the α -old stars are more abundant at larger heights in comparison to the α -young stars. Therefore, we believe that the incorrect assumption regarding the separability of the radial and vertical motions caused the discrepancy between the two vertical Jeans models.

To investigate if the coupling of the radial and vertical motion is stronger for older stars, we splitted the sample into seven bins in the α -abundance-metallicity space. These two combined pieces of chemical properties can be seen as a proxy for the age of the stars ([Loebman et al. 2011](#)). The stars are on average older as they become more metal-poor and high- α -abundant. We use the same MCMC likelihood method as before to estimate the velocity dispersion tensor. We found that the radial and vertical velocity dispersion profiles are nearly isothermal, with the more metal-poor, alpha-enhanced stars having larger radial and vertical velocity dispersions. This observation reflects the age-velocity relation of stars in the solar neighbourhood. We also verified that the tilt of the velocity ellipsoid is non-zero and increases almost linearly with height. However, we could not detect a significant difference in the trend of the tilt for the individual sub-samples mostly due to the large statistical uncertainty in the tilt measurement. The lack of deviations between the sub-samples would suggest a unique tilt for the population of G-type dwarf stars, if not even for all stellar populations. Therefore we decided to measure the tilt as function height using all stars together, in order to improve the accuracy of each measurement. This led to the most precise vertical profile of the tilt angle in the solar neighbourhood in the literature. The fit of this profile with an arctan function gives us the relation $\alpha_{\text{tilt}} = (-0.90 \pm 0.04) \arctan(|z|/R_{\odot}) - (0.01 \pm 0.005)$. This means that the velocity ellipsoid is almost spherically aligned, pointing to the Galactic centre. The result is consistent with other studies (e.g. [Siebert et al. 2008](#); [Casetti-Dinescu et al. 2011](#); [Smith et al. 2012](#)), who measured the individual tilt angles over a broader range in height and with larger errorbars.

We also tested the robustness of our results. To account in the likelihood method for contaminating stars from the halo, we previously applied a single-component halo model with velocity dispersions determined [Schönrich et al. \(2011\)](#). Several studies found evidence for a second component in the halo from an analysis of the stellar density profile (e.g. [Carollo et al. 2010](#)). As their outer halo dominates only beyond ~ 15 -20 kpc, this additional component does not affect our measured velocity dispersions. Also, the velocity dispersions of the inner component do not differ much from the previously adopted single-component halo. Some authors also claimed the discovery of a metal-weak tail of the thick disk (MWTD; e.g. [Chiba & Beers 2000](#) and references therein). This additional component might have an effect on our vertical Jeans analysis, if present. Since the MWTD stars are very metal-poor they should only be present in our most metal-poor abundance bin. So, we repeated the vertical Jeans analysis including an additional component for the MWTD and confirmed our previous results.

The conclusion from this chapter is that we will need more general and sophisticated dynamical models if we want to use data that extends beyond 1 kpc in height. [Statler \(1989\)](#), for example, assessed the bias to be around 10% at $z \sim 1$ kpc in models that assume decoupled motions. If we have more general models, we can use our accurate measurement of the tilt as a prior on the velocity distribution, because this tilt will be quite hard to infer from dynamical models themselves given the dozens of other free parameters.

6.2 LOCAL DARK MATTER DENSITY

In [Chapter 4](#), we derived a novel axisymmetric Jeans model in prolate spheroidal coordinates and applied it to a sample of $\sim 25,000$ SEGUE G-type dwarf stars to determine the local dark matter density. Our G-type dwarf stars cover from 6 - 12 kpc in radius and 0.3 - 3 kpc in height. We give an overview of the sample and of the SEGUE survey in [Section 2.2](#).

The motion of these stars is sensitive to the underlying gravitational potential, which through [Poisson's equation 1.3](#) is related to the density of all matter, including possible dark components. We learned from [Chapter 3](#) that we need the full velocity dispersion tensor of the stars to reliably recover the mass distribution. The prolate spheroidal coordinate system has the benefit that the model can account for the coupling of vertical and radial motions. Moreover, the model includes a non-constant velocity anisotropy for which we chose a functional form such that the anisotropy increases much stronger with radius than it decreases with height. The only other assumptions we imposed to derive the solution of the axisymmetric Jeans equations are, that the stellar system is in dynamical equilibrium and of course, that it is axisymmetric. Taking those together, the model overcomes most of the assumptions made in previous models and in particular the vertical Jeans models.

The prediction from Jeans models are usually compared to either the number density counts or the velocity dispersion of tracer objects, which are both spatially averaged quantities. Since the binning of data to estimate a certain quantity often means a loss of information, we combine the axisymmetric Jeans model with a bi-variate normal velocity distribution function in order to fit our data in a discrete way. We also account for the contamination of our sample with halo stars by adopting a normal velocity distribution for every coordinate direction with velocity dispersions given by Schönrich et al. (2011). In doing so, we fit the velocity distribution of the tracer in combination with axisymmetric Jeans models by applying the likelihood method described in Section 3.1.2.

The number density of the tracers is, beside the kinematics, another important input to the Jeans model. As the velocity dispersions are proportional to the density profile, we fit the number density simultaneously with the kinematics using a double exponential function of the radius and the height above the mid-plane. In this way, the kinematics can partly compensate biases in the number density profile due to the complex selection function of the SEGUE survey.

We chose two different sets of gravitational potentials, the first fully analytic and the second partly numerical. The analytic set consists of a stellar and a gaseous Miyamoto-Nagai disk, a spherical exponential bulge and a spherical, logarithmic halo potential. The numerical set consists of a stellar and a gaseous exponential disk, a spherical exponential bulge (Dwek et al. 1995) and a spherical Navarro-Frenk-White potential (NFW, Navarro et al. 1996). Analytic potentials are much quicker to compute and thus are advantageous for testing purposes.

During the testing phase, we found that some parameters were consistently over or underestimated, such as the scale length and the scale height of the disk. These unnatural parameter values generated a steeply rising rotation curve in the outer part of the galaxy, that is observed neither in the Milky Way nor in other spiral galaxies. Therefore we included a prior that restricts the amplitude and the flatness of the rotation curve at the solar radius within the ranges $190 < V_c/\text{kms}^{-1} < 245$ and $-0.12 < \frac{d \ln v_c}{d \ln R} < 0.12$.

We fixed the bulge and the gaseous disk because we cannot constrain them from our data, as the stellar sample does not extend to the regions where these components dominate. We could also not constrain the scale height of the disk as most of our data starts at 500 pc above the Galactic mid-plane. The scale radius of the halo is the last parameter in the potential that we fixed, because it is strongly degenerate with the halo mass. We assumed different values for the disk scale height and the scale radius of the halo to test the influence of our chosen values for these parameters on the results. We find that a modest variation of the halo scale radius does not change the results, and similarly for a change in the scale height as long as it is larger than 0.25 kpc.

During our tests, we discovered that the tilt of the velocity ellipsoid has indeed a strong impact on the determination of the local dark matter density. Using the Miyamoto-Nagai disk

and the logarithmic halo potential, we will estimate $\rho_{\text{dm}} = (0.016 \pm 0.001) M_{\odot}\text{pc}^{-3}$, if we use our measurement of the tilt from Chapter 3. If we, however, align the velocity ellipsoid with the cylindrical coordinate system, we will get $\rho_{\text{dm}} = (0.008 \pm 0.002) M_{\odot}\text{pc}^{-3}$ which is a factor two different from the model with the strong tilt. This highlights the importance of the correct assumptions on the tilt of the velocity ellipsoid in the determination of the local dark matter density.

The model with the exponential disk yielded the following results for the dark matter density, the disk mass, the stellar surface density and the total surface density at $|z| \leq 1.1$ kpc

$$\begin{aligned}\rho_{\text{dm}} &= 0.012 \pm 0.001 M_{\odot}\text{pc}^{-3} \\ M_* &= (3.4 \pm 0.2) \cdot 10^{10} M_{\odot} \\ \Sigma_* &= 39 \pm 3 M_{\odot}\text{pc}^{-2} \\ \Sigma_{\text{tot}} &= 79 \pm 2 M_{\odot}\text{pc}^{-2},\end{aligned}$$

if we allow the disk scale length and the tilt parameter to vary in our model.

6.3 MASS PROFILE OF THE DARK HALO

In Chapter 5, we applied our axisymmetric Jeans model to a sample of $\sim 6,000$ SEGUE K-giants located in the Galactic halo between 5 and 100 kpc away from the Galactic centre. The aim was to estimate the mass of the dark halo, for which we considered a spherical NFW halo potential as well as fixed disk, gas and bulge components. Xue et al. (2015) measured the density profile of the K-giants and considered the selection effects of SEGUE. They tested three different density profiles: a broken power law, an Einasto profile with constant flattening and an Einasto profile with variable flattening. All of them were able to fit the density profile equally well. Because it is not guaranteed that the Jeans models can fit the kinematics with these density profiles equally well, we used all them to determine the halo mass. The Jeans models with the two Einasto profiles provide similar good fits to the velocity dispersion profile, whereas we could not fit the inner halo velocity dispersion with the broken power law. We also used all three profiles in the likelihood fitting at the same time in order to obtain a robust estimate of the mass profile. Since the model with the Einasto density profile and variable flattening was close to the combined result and the broken power law produced a poor fit to the line-of-sight velocity (LOS) dispersion of the inner halo, we adopted the Einasto profile with variable flattening as our fiducial density profile of the K-giants for the subsequent analysis.

As described in the Sections 3.1 and 4.1, we assume a Gaussian velocity distribution in our model. When looking at the velocity distribution of the K-giants, we noticed that it deviates strongly from a Gaussian shape for a large part of our sample due to a significant contamination by substructures. Those often have a different mean velocity and a smaller velocity dispersion

than field halo stars. The by far largest substructure in our sample is the Sagittarius stream. Roughly 11% of our stars belong to it (William Janesh, private communication) and they induce the strongest non-Gaussianities in the sample¹.

Therefore we created two models based on the 3D position and LOSV along the stream, as determined by [Belokurov et al. \(2014\)](#), to model accurately its LOSV distribution as function of the distance from the Galactic centre. The first model is primarily based on the LOSV of the stream and only weakly on its position, while the second model is primarily based on the position of the stream rather than the LOSV (see [Section 5.1.1](#) for more details on the two models). We also tried a model that matches both position and LOSV, but we got too small a fraction of stars in the sample assigned to the stream, so that we were not able to properly fit the LOSV velocity distribution of the sample. Both of the Sagittarius models performed equally well in fitting the velocity distribution. Next, we checked if the predicted mass profiles from the axisymmetric Jeans model are consistent in combination with the two Sagittarius (contamination) models as well as a third model in which we did not apply a contamination model, but instead cut all Sagittarius stars identified by William Janesh (private communication). The resulting halo masses matched very well, which supports the validity of the two Sagittarius models. For the final analysis we chose the model that is mainly based on the LOSV of the stream, because it has a lower fraction of miss-assigned stars. We tested that after cutting all stars that presumably belong to substructures, the LOSV distribution became almost Gaussian. However, cutting a sample would unnecessarily remove information, when instead we have a model accounting for these outliers, so that the MCMC can decide what the best model will be on the basis of the total sample.

We estimated the virial mass, the mass concentration and the mass within 100 kpc from the Galactic centre with the Einasto density profile with variable flattening and our chosen Sagittarius model:

$$\begin{aligned} M_{200} &= (1.26 \pm 0.18) \cdot 10^{12} M_{\odot} \\ c_{200} &= 15.3 \pm 2.3 \\ M(< 100 \text{ kpc}) &= (8.8 \pm 0.7) \cdot 10^{11} M_{\odot} \end{aligned}$$

The estimated masses in the literature vary between $(0.5 - 2.5) \cdot 10^{12} M_{\odot}$, but the majority of estimates range from $(0.7 - 1.5) \cdot 10^{12} M_{\odot}$ and most of them agree with our estimate, not the least due to the often large uncertainty of individual estimates.

Now that we have determined the halo potential, we can toss in new arguments on the open debates of Leo I being bound or not to the Milky Way and the “too big to fail” problem. Leo I is of interest for dynamical modelling of the halo potential, because the distance to Leo I is

¹William Janesh identified for us with his 4-distance - friend of friend code ([Janesh et al. 2015](#)) those stars in our sample that most likely belong to Sagittarius or other substructures. After cutting the Sagittarius stars the strong skewness mostly vanished.

large compared to individual stars, globular clusters and other satellite galaxies in Milky Way halo used as tracers for the halo potential. As we can only determine the mass within the orbit of such a tracer object, it will make the large distance to Leo I of special importance in measuring the mass profile of the dark matter halo - provided this galaxy is bound. We infer from our mass estimate that Leo I is unbound, because of the large mass concentration of the halo in its inner part.

The “too big to fail” problem originates from cosmological dark matter only simulations (Boylan-Kolchin et al. 2011), in which the most massive sub-halos as seen in simulations should host luminous components, which we do not detect in the Milky Way halo. The mass of the most massive satellites and its frequency in the dark matter halo of any galaxy depends on the mass of the galaxy itself. So if the Milky Way had a mass smaller than $\approx 1 \cdot 10^{12} M_{\odot}$, we could match it to a less massive halo in the simulations, that host fewer massive satellites with masses comparable to the large Magellanic Cloud or the Sagittarius dwarf spheroidal galaxy. However, we do not see that the problem can be solved in this way, because the mass of the Milky Way is clearly larger than this imposed upper limit.

6.4 FUTURE PROSPECTS

After we had introduced a novel axisymmetric Jeans model to overcome limitations of the vertical Jeans model, like the assumption of a coupled motion, we combined it with a maximum likelihood method to make the optimal use of the data by avoiding the unnecessary loss of information through binning. Of course, we had to make some assumptions, like axisymmetry or the functional form of the velocity anisotropy, to solve the Jeans equations. The next step will be to test the effect of these assumptions with a set of mock catalogues. The use of mock simulations has the advantage that we already know all parameters and properties of the galaxy including the density distribution, the velocity distribution and the gravitational potential. We could start with an unevolved disk, that generates a smooth potential, before moving on to more realistic mock catalogues that include non-axisymmetric features, like spiral arms, a bar or perturbations due to a merger. From these simulations, we can also estimate how accurate the data or how large the volume has to be, in which the tracer objects reside, in order to successfully recover the potential. Several mock catalogues with different levels of “difficulty” for dynamical models to determine the true properties are gathered in the “Gaia Challenge” project², which was initiated to provide dynamicists a platform to refine their dynamical models of the Milky Way and to prepare the models for data from the Gaia survey (Perryman et al. 2001) in the coming years.

Gaia is an optical space telescope that has been designed to observe about 1 billion stars in the Milky Way with unprecedented parallaxes and proper motions with a brightness limit of

²Gaia Challenge Wiki: <http://astrowiki.ph.surrey.ac.uk/dokuwiki/doku.php?id=tests:discs>

$r \sim 20$ mag. Gaia will extensively enhance our knowledge about the Milky Way system due to its high accuracy and enormous amount of observed stars³. It will measure for example the distances of G stars up to 2 kpc to better than 10% and line-of-sight velocities to better than 6 km s⁻¹ for G stars brighter than $r \sim 16$ mag. The proper motions will have a similar uncertainty as the distances. Nevertheless, we will not be able to use every star in the catalogue for our study of the gravitational potential. About 150 million stars will have line-of-sight velocities from the Doppler shifts of their spectra, and about 2 million bright stars will have chemical abundances measured. To increase the number of stars with chemical abundances or to extend the brightness limit, Gaia requires follow-up surveys like Gaia-ESO (Randich et al. 2013) to complement it with high-resolution spectra, or the Large Synoptic Survey Telescope (Ivezic et al. 2008) to extend Gaia beyond its faint end.

The immense progress in stellar number statistics will also help us to measure the tilt of the velocity ellipsoid with much higher accuracy and it will probably be finally possible to clarify if there is a fundamental difference in the tilt between different stellar populations. We had too few stars per population, so that the possible variations in the tilt between these (sub-)populations were smaller than the uncertainty of the tilt. We have recognised that it is hard to determine the tilt with dynamical models (at least with the axisymmetric Jeans model), so that it will be a more reasonable approach to use our direct measurement of the tilt as a prior for the models. For example, Bienaymé et al. (2014) used our tilt measurement to estimate the local dark matter density and derived a larger value than most other recent studies, but in good agreement with our estimate.

Regarding the estimate of the dark matter density near the Sun we differentiate between two kinds: local and global. We will denote such a measurement as local, if we can probe the dark matter density from a sample of tracers close to the Sun and we denote it as global, if we do not trace the local distribution of matter but instead have to extrapolate it from a sample-volume further away under the assumption of a spherical halo. By comparing the dark matter density near the sun of the local and the global estimate we can discriminate between a prolate and an oblate halo. If the local estimate is smaller than the global one, it will point to a prolate shape. If the local estimate is larger, it will point to an oblate shape or an additional dark matter disc in the Milky Way.

According to the local/global definition, the measurement of the halo mass in Chapter 5 is definitely of global kind, while the measurement of the dark matter density in Chapter 4 may be in between, because the sample covers a larger volume but it still contains local tracers. The comparison of our extrapolated dark matter density $\rho_{\text{dm}}^{\text{global}} = 0.0135 \pm 0.003 \text{ M}_{\odot} \text{ pc}^{-3}$ with our local measurement of $\rho_{\text{dm}}^{\text{local}} = 0.013 \pm 0.0015 \text{ M}_{\odot} \text{ pc}^{-3}$ does not yield a clear result on either shape. The approximate equality of both estimates would rather suggest a spherical halo. However, the comparison of our globally derived dark matter density with the estimate of $\rho_{\text{dm}}^{\text{local}} \approx 0.007$

³Gaia will be volume-complete for stars brighter than $G = 20$ mag.

$M_{\odot} \text{pc}^{-3}$ by Zhang et al. (2013) would indicate a prolate halo. On the other hand, the comparison of our measurement to $\rho_{\text{dm}}^{\text{local}} \approx 0.022 M_{\odot} \text{pc}^{-3}$ by Garbari et al. (2012) would indicate an oblate halo. We expect to achieve a closer agreement between the dark matter measurements with larger sample sizes and more precise data.

Given the wealth of future Gaia data, we ought to use more advanced modelling techniques like the Schwarzschild orbit-superposition method or the 'made-to-measure' particle method. They require less assumptions, albeit need more computing time, which we can reduce if faster methods like the axisymmetric Jeans models can provide a first appropriate guess. However, these kind of dynamical models are just starting to transit from applications to external galaxies, where the data is binned by nature, to the application in the solar neighborhood, where we have discrete tracers available. The Gaia data release with appropriate full 6D phase space information is still some years ahead⁴, so that we can use this time to develop more advanced models.

⁴The distances and 3D velocities for some faint stars will be released soonest in 2017; distances and 3D velocities for brighter stars maybe a little earlier. But distances and proper motions to $\approx 100,000$ stars should already be available in 2016. The final catalogue is intended to be published in 2021.

ACKNOWLEDGEMENTS

At first, I like to express my special appreciation and thanks to my advisor Glenn van de Ven, who has been a tremendous mentor for me, and allowed me to grow as a research scientist. I also like to thank Laura for giving me advices in scientific writing and listening over these years. I am grateful to Xiangxiang and Hans-Walter Rix for their support in my last project. Another thanks goes to Chao and Lan helping me with the data. Thanks also to Justin Read that he accepted to be the second referee.

Moreover, I have found many new friends, who made my time unique in Heidelberg and took my mind off when I was stuck in work.

A special acknowledgement to my family. Words cannot express how grateful I am for all of the sacrifices they have made on my behalf. Their unfailing love and support has put me where I am today.

Alex Büdenbender
Heidelberg, May 2015

BIBLIOGRAPHY

- Abadi, M. G., Navarro, J. F., Steinmetz, M., & Eke, V. R. 2003, *ApJ*, 597, 21
- Adams, J. J., et al. 2014, *ApJ*, 789, 63
- Agertz, O., Teyssier, R., & Moore, B. 2011, *MNRAS*, 410, 1391
- An, D., et al. 2013, *ApJ*, 763, 65
- Anderson, L., et al. 2014, *MNRAS*, 441, 24
- Arnold, R. 1995, *MNRAS*, 276, 293
- Bahcall, J. N., Flynn, C., & Gould, A. 1992, *ApJ*, 389, 234
- Barber, C., Starkenburg, E., Navarro, J. F., McConnachie, A. W., & Fattahi, A. 2014, *MNRAS*, 437, 959
- Battaglia, G., et al. 2005, *MNRAS*, 364, 433
- Beers, T. C., et al. 2012, *ApJ*, 746, 34
- Begeman, K. G., Broeils, A. H., & Sanders, R. H. 1991, *MNRAS*, 249, 523
- Belokurov, V., Evans, N. W., Irwin, M. J., Lynden-Bell, D., Yanny, B., Vidrih, S., Gilmore, G., & Seabroke, G. 2007, *ApJ*, 658, 337
- Belokurov, V., et al. 2006, *ApJ*, 647, L111
- . 2014, *MNRAS*, 437, 116
- Bensby, T., Feltzing, S., & Lundström, I. 2004, *A&A*, 421, 969
- Bensby, T., et al. 2013, *A&A*, 549, A147
- Bershady, M. A., Martinsson, T. P. K., Verheijen, M. A. W., Westfall, K. B., Andersen, D. R., & Swaters, R. A. 2011, *ApJ*, 739, L47
- Betoule, M., et al. 2014, *A&A*, 568, A22
- Bienayme, O., Robin, A. C., & Creze, M. 1987, *A&A*, 180, 94

- Bienaymé, O., Soubiran, C., Mishenina, T. V., Kovtyukh, V. V., & Siebert, A. 2006, *A&A*, 446, 933
- Bienaymé, O., et al. 2014, *A&A*, 571, A92
- Binney, J. 2010, *MNRAS*, 401, 2318
- . 2012, *MNRAS*, 426, 1324
- Binney, J., & Mamon, G. A. 1982, *MNRAS*, 200, 361
- Binney, J., & McMillan, P. 2011, *MNRAS*, 413, 1889
- Binney, J., & Tremaine, S. 2008, *Galactic Dynamics* (Princeton, NJ, Princeton University Press)
- Binney, J., et al. 2014, *MNRAS*, 439, 1231
- Bissantz, N., Debattista, V. P., & Gerhard, O. 2004, *ApJ*, 601, L155
- Bond, N. A., et al. 2010, *ApJ*, 716, 1
- Borde, A., Palanque-Delabrouille, N., Rossi, G., Viel, M., Bolton, J. S., Yèche, C., LeGoff, J.-M., & Rich, J. 2014, *JCAP*, 7, 5
- Bosma, A. 1981, *AJ*, 86, 1825
- Bournaud, F., Elmegreen, B. G., & Martig, M. 2009, *ApJ*, 707, L1
- Bovy, J., & Rix, H.-W. 2013, *ApJ*, 779, 115
- Bovy, J., Rix, H.-W., & Hogg, D. W. 2012a, *ApJ*, 751, 131
- Bovy, J., Rix, H.-W., Hogg, D. W., Beers, T. C., Lee, Y. S., & Zhang, L. 2012b, *ApJ*, 755, 115
- Bovy, J., Rix, H.-W., Liu, C., Hogg, D. W., Beers, T. C., & Lee, Y. S. 2012c, *ApJ*, 753, 148
- Bovy, J., & Tremaine, S. 2012, *ApJ*, 756, 89
- Bovy, J., et al. 2012d, *ApJ*, 759, 131
- Boylan-Kolchin, M., Bullock, J. S., & Kaplinghat, M. 2011, *MNRAS*, 415, L40
- Boylan-Kolchin, M., Bullock, J. S., Sohn, S. T., Besla, G., & van der Marel, R. P. 2013, *ApJ*, 768, 140
- Brook, C., Richard, S., Kawata, D., Martel, H., & Gibson, B. K. 2007, *ApJ*, 658, 60
- Brown, W. R., Geller, M. J., Kenyon, S. J., & Diaferio, A. 2010, *AJ*, 139, 59
- Bruch, T., Read, J., Baudis, L., & Lake, G. 2009, *ApJ*, 696, 920
- Büdenbender, A., van de Ven, G., & Watkins, L. L. 2015, *ArXiv e-prints*
- Bullock, J. S., & Johnston, K. V. 2005, *ApJ*, 635, 931
- Bullock, J. S., Stewart, K. R., Kaplinghat, M., Tollerud, E. J., & Wolf, J. 2010, *ApJ*, 717, 1043
- Burkert, A. 1997, *ApJ*, 474, L99
- Busha, M. T., Marshall, P. J., Wechsler, R. H., Klypin, A., & Primack, J. 2011, *ApJ*, 743, 40
- Cao, L., Mao, S., Nataf, D., Rattenbury, N. J., & Gould, A. 2013, *MNRAS*, 434, 595
- Cappellari, M. 2008, *MNRAS*, 390, 71
- Cappellari, M., & Copin, Y. 2003, *MNRAS*, 342, 345

- Carlberg, R. G., & Sellwood, J. A. 1985, *ApJ*, 292, 79
- Carollo, D., et al. 2007, *Nature*, 450, 1020
- . 2010, *ApJ*, 712, 692
- . 2012, *ApJ*, 744, 195
- Casagrande, L., Schönrich, R., Asplund, M., Cassisi, S., Ramírez, I., Meléndez, J., Bensby, T., & Feltzing, S. 2011, *A&A*, 530, A138
- Casetti-Dinescu, D. I., Girard, T. M., Korchagin, V. I., & van Altena, W. F. 2011, *ApJ*, 728, 7
- Chanamé, J., Kleyna, J., & van der Marel, R. 2008, *ApJ*, 682, 841
- Chiba, M., & Beers, T. C. 2000, *AJ*, 119, 2843
- Combes, F., & Sanders, R. H. 1981, *A&A*, 96, 164
- Courteau, S., & Dutton, A. A. 2015, *ApJ*, 801, L20
- Cretton, N., de Zeeuw, P. T., van der Marel, R. P., & Rix, H. 1999, *ApJS*, 124, 383
- Davis, A. J., Khochfar, S., & Dalla Vecchia, C. 2014, *MNRAS*, 443, 985
- Dawson, K. S., et al. 2013, *AJ*, 145, 10
- de Jong, J. T. A., Yanny, B., Rix, H.-W., Dolphin, A. E., Martin, N. F., & Beers, T. C. 2010, *ApJ*, 714, 663
- de Jong, R. S., et al. 2012, in *Society of Photo-Optical Instrumentation Engineers (SPIE) Conference Series*, Vol. 8446, *Society of Photo-Optical Instrumentation Engineers (SPIE) Conference Series*
- de Lorenzi, F., Debattista, V. P., Gerhard, O., & Sambhus, N. 2007, *MNRAS*, 376, 71
- De Propriis, R., Harrison, C. D., & Mares, P. J. 2010, *ApJ*, 719, 1582
- de Zeeuw, T. 1985, *MNRAS*, 216, 273
- Deason, A. J., Belokurov, V., & Evans, N. W. 2011, *MNRAS*, 416, 2903
- Deason, A. J., Belokurov, V., Evans, N. W., & An, J. 2012, *MNRAS*, 424, L44
- Deason, A. J., Belokurov, V., Evans, N. W., & Johnston, K. V. 2013a, *ApJ*, 763, 113
- Deason, A. J., Belokurov, V., Koposov, S. E., & Rockosi, C. M. 2014, *ApJ*, 787, 30
- Deason, A. J., Van der Marel, R. P., Guhathakurta, P., Sohn, S. T., & Brown, T. M. 2013b, *ApJ*, 766, 24
- Dehnen, W., & Binney, J. J. 1998, *MNRAS*, 298, 387
- Dehnen, W., & Gerhard, O. E. 1993, *MNRAS*, 261, 311
- Dejonghe, H., & de Zeeuw, T. 1988, *ApJ*, 333, 90
- Dicke, R. H., Peebles, P. J. E., Roll, P. G., & Wilkinson, D. T. 1965, *ApJ*, 142, 414
- Dobbs, C., & Baba, J. 2014, *PASA*, 31, 35
- Duffau, S., Zinn, R., Vivas, A. K., Carraro, G., Méndez, R. A., Winnick, R., & Gallart, C. 2006, *ApJ*, 636, L97

- Dutton, A. A., et al. 2011, *MNRAS*, 417, 1621
- Dwek, E., et al. 1995, *ApJ*, 445, 716
- Einasto, J., & Haud, U. 1989, *A&A*, 223, 89
- Eisenstein, D. J., et al. 2005, *ApJ*, 633, 560
- Evans, N. 1990, *Intern. J. Computer Math.*, 34, 105
- Faure, C., Siebert, A., & Famaey, B. 2014, *MNRAS*, 440, 2564
- Fellhauer, M., et al. 2006, *ApJ*, 651, 167
- Feng, J. L. 2010, *ARA&A*, 48, 495
- Flynn, C., & Fuchs, B. 1994, *MNRAS*, 270, 471
- Foreman-Mackey, D., Hogg, D. W., Lang, D., & Goodman, J. 2013, *PASP*, 125, 306
- Förster Schreiber, N. M., et al. 2009, *ApJ*, 706, 1364
- Freeman, K. C. 2014, in *Lessons from the Local Group*, ed. K. Freeman, B. Elmegreen, D. Block, & M. Woolway
- Fuchs, B., & Flynn, C. 1994, *MNRAS*, 270, 471
- Fuchs, B., & Wielen, R. 1987, in *NATO ASIC Proc. 207: The Galaxy*, ed. G. Gilmore & B. Carswell, 375–398
- Garbari, S., Liu, C., Read, J. I., & Lake, G. 2012, *MNRAS*, 425, 1445
- Gavazzi, R., Treu, T., Rhodes, J. D., Koopmans, L. V. E., Bolton, A. S., Burles, S., Massey, R. J., & Moustakas, L. A. 2007, *ApJ*, 667, 176
- Gibbons, S. L. J., Belokurov, V., & Evans, N. W. 2014, *MNRAS*, 445, 3788
- Gilmore, G., & Reid, N. 1983, *MNRAS*, 202, 1025
- Gilmore, G., et al. 2012, *The Messenger*, 147, 25
- Gnedin, O. Y., Brown, W. R., Geller, M. J., & Kenyon, S. J. 2010, *ApJ*, 720, L108
- Gnedin, O. Y., Weinberg, D. H., Pizagno, J., Prada, F., & Rix, H.-W. 2007, *ApJ*, 671, 1115
- Gómez, F. A., Helmi, A., Brown, A. G. A., & Li, Y.-S. 2010, *MNRAS*, 408, 935
- Gómez, F. A., et al. 2012, *MNRAS*, 423, 3727
- González, R. E., Kravtsov, A. V., & Gnedin, N. Y. 2013, *ApJ*, 770, 96
- Goodman, J., & Weare, J. 2010, *Commun. Appl. Math. Comput. Sci.*, 5, 65
- Grand, R. J. J., Kawata, D., & Cropper, M. 2015, *MNRAS*, 447, 4018
- Guth, A. H. 1981, *Phys. Rev. D*, 23, 347
- Hattori, K., Yoshii, Y., Beers, T. C., Carollo, D., & Lee, Y. S. 2013, *ApJ*, 763, L17
- Helmi, A. 2004, *ApJ*, 610, L97
- Helmi, A., & White, S. D. M. 1999, *MNRAS*, 307, 495
- Holmberg, J., & Flynn, C. 2000, *MNRAS*, 313, 209
- . 2004, *MNRAS*, 352, 440

- Hunt, J. A. S., & Kawata, D. 2013, *MNRAS*, 430, 1928
— . 2014, *MNRAS*, 443, 2112
- Ibata, R. A., Gilmore, G., & Irwin, M. J. 1994, *Nature*, 370, 194
- Ibata, R. A., et al. 2014, *ApJ*, 780, 128
- Ivezić, Ž., Sesar, B., Jurić, M., Bond, N., Dalcanton, J., & Rockosi, C. M. 2008, *ApJ*, 684, 287
- Ivezic, Z., et al. 2008, *ArXiv e-prints*
- Janesh, W., et al. 2015, *ArXiv e-prints*
- Jeans, J. H. 1915, *MNRAS*, 76, 70
— . 1922, *MNRAS*, 82, 122
- Jurić, M., et al. 2008, *ApJ*, 673, 864
- Kafle, P. R., Sharma, S., Lewis, G. F., & Bland-Hawthorn, J. 2012, *ApJ*, 761, 98
— . 2014, *ApJ*, 794, 59
- Kapteyn, J. C. 1922, *ApJ*, 55, 302
- Kauffmann, G., White, S. D. M., & Guiderdoni, B. 1993, *MNRAS*, 264, 201
- Kerr, F. J., & Lynden-Bell, D. 1986, *MNRAS*, 221, 1023
- Kinman, T. D., Cacciari, C., Bragaglia, A., Smart, R., & Spagna, A. 2012, *MNRAS*, 422, 2116
- Klypin, A., Kravtsov, A. V., Valenzuela, O., & Prada, F. 1999, *ApJ*, 522, 82
- Koda, J., Milosavljević, M., Shapiro, P. R., Nagai, D., & Nakar, E. 2008, in *Astronomical Society of the Pacific Conference Series*, Vol. 393, *New Horizons in Astronomy*, ed. A. Frebel, J. R. Maund, J. Shen, & M. H. Siegel, 223
- Koposov, S. E., Belokurov, V., Torrealba, G., & Wyn Evans, N. 2015, *ArXiv e-prints*
- Kordopatis, G., et al. 2013, *AJ*, 146, 134
- Kormendy, J., & Illingworth, G. 1982, *ApJ*, 256, 460
- Kuijken, K., & Gilmore, G. 1989a, *MNRAS*, 239, 605
— . 1989b, *MNRAS*, 239, 571
— . 1991, *ApJ*, 367, L9
- Küpper, A. H. W., Balbinot, E., Bonaca, A., Johnston, K. V., Hogg, D. W., Kroupa, P., & Santiago, B. X. 2015, *ArXiv e-prints*
- Laevens, B. P. M., Martin, N. F., Ibata, R. A., Rix, H.-W., Bernard, E. J., Bell, E. F., & Sesar, B. 2015, *ApJ*, 802, L18
- Law, D. R., & Majewski, S. R. 2010, *ApJ*, 714, 229
- Lee, Y. S., et al. 2008, *AJ*, 136, 2022
— . 2011, *AJ*, 141, 90
- Li, Y.-S., & White, S. D. M. 2008, *MNRAS*, 384, 1459
- Liu, C., & van de Ven, G. 2012, *MNRAS*, 425, 2144

- Loebman, S. R., Roškar, R., Debattista, V. P., Ivezić, Ž., Quinn, T. R., & Wadsley, J. 2011, *ApJ*, 737, 8
- Long, R. J., Mao, S., Shen, J., & Wang, Y. 2013, *MNRAS*, 428, 3478
- Lux, H., Read, J. I., Lake, G., & Johnston, K. V. 2012, *MNRAS*, 424, L16
- Macciò, A. V., Dutton, A. A., & van den Bosch, F. C. 2008, *MNRAS*, 391, 1940
- Macciò, A. V., Dutton, A. A., van den Bosch, F. C., Moore, B., Potter, D., & Stadel, J. 2007, *MNRAS*, 378, 55
- Mandelbaum, R., Slosar, A., Baldauf, T., Seljak, U., Hirata, C. M., Nakajima, R., Reyes, R., & Smith, R. E. 2013, *MNRAS*, 432, 1544
- Markevitch, M., Gonzalez, A. H., David, L., Vikhlinin, A., Murray, S., Forman, W., Jones, C., & Tucker, W. 2002, *ApJ*, 567, L27
- Martig, M., Bournaud, F., Croton, D. J., Dekel, A., & Teyssier, R. 2012, *ApJ*, 756, 26
- Massey, R., et al. 2007, *ApJS*, 172, 239
- Mateo, M., Olszewski, E. W., & Walker, M. G. 2008, *ApJ*, 675, 201
- McMillan, P. J. 2011, *MNRAS*, 414, 2446
- McMillan, P. J., & Binney, J. J. 2008, *MNRAS*, 390, 429
- McWilliam, A., & Zoccali, M. 2010, *ApJ*, 724, 1491
- Merritt, D. 1980, *ApJS*, 43, 435
- . 1985, *AJ*, 90, 1027
- Minchev, I., Chiappini, C., & Martig, M. 2013, *A&A*, 558, A9
- Minchev, I., Chiappini, C., Martig, M., Steinmetz, M., de Jong, R. S., Boeche, C., Scannapieco, C., & Binney, J. J. 2014, *ApJ*, 781, L20
- Minchev, I., & Famaey, B. 2010, *ApJ*, 722, 112
- Miyamoto, M., & Nagai, R. 1975, *PASJ*, 27, 533
- Momany, Y., Zaggia, S., Gilmore, G., Piotto, G., Carraro, G., Bedin, L. R., & de Angeli, F. 2006, *A&A*, 451, 515
- Moni Bidin, C., Carraro, G., Méndez, R. A., & Smith, R. 2012, *ApJ*, 751, 30
- Moore, B., Ghigna, S., Governato, F., Lake, G., Quinn, T., Stadel, J., & Tozzi, P. 1999, *ApJ*, 524, L19
- Morganti, L., & Gerhard, O. 2012, *MNRAS*, 422, 1571
- Munn, J. A., et al. 2004, *AJ*, 127, 3034
- Nath, B. B., & Silk, J. 2009, *MNRAS*, 396, L90
- Navarro, J. F., Frenk, C. S., & White, S. D. M. 1996, *ApJ*, 462, 563
- Ness, M., Debattista, V. P., Bensby, T., Feltzing, S., Roškar, R., Cole, D. R., Johnson, J. A., & Freeman, K. 2014, *ApJ*, 787, L19

- Ness, M., et al. 2013, *MNRAS*, 430, 836
- Nguyen, D. D., Seth, A. C., Reines, A. E., den Brok, M., Sand, D., & McLeod, B. 2014, *ApJ*, 794, 34
- Nissen, P. E., & Schuster, W. J. 2010, *A&A*, 511, L10
- Norberg, P., et al. 2002, *MNRAS*, 332, 827
- Oort, J. H. 1932, *Bull. Astron. Inst. Netherlands*, 6, 249
— . 1960, *Bull. Astron. Inst. Netherlands*, 15, 45
- Osipkov, L. P. 1979, *Pisma v Astronomicheskii Zhurnal*, 5, 77
- Paraficz, D., Kneib, J.-P., Richard, J., Morandi, A., Limousin, M., & Jullo, E. 2012, *ArXiv e-prints*
- Peñarrubia, J., et al. 2005, *ApJ*, 626, 128
- Penzias, A. A., & Wilson, R. W. 1965, *ApJ*, 142, 419
- Perlmutter, S., et al. 1999, *ApJ*, 517, 565
- Perryman, M. A. C., et al. 1997, *A&A*, 323, L49
— . 2001, *A&A*, 369, 339
- Peter, A. H. G. 2011, *Phys. Rev. D*, 83, 125029
- Piffl, T., Scannapieco, C., Binney, J., Steinmetz, M., Scholz, R.-D., Williams, M. E. K., & de Jong, R. S. 2014, *A&A*, 562, A91
- Planck Collaboration et al. 2011, *A&A*, 536, A1
— . 2014, *A&A*, 571, A15
— . 2015, *ArXiv e-prints*
- Polido, P., Jablonski, F., & Lépine, J. R. D. 2013, *ApJ*, 778, 32
- Portail, M., Wegg, C., Gerhard, O., & Martinez-Valpuesta, I. 2015, *MNRAS*, 448, 713
- Posacki, S., Cappellari, M., Treu, T., Pellegrini, S., & Ciotti, L. 2015, *MNRAS*, 446, 493
- Preston, G. W., Shectman, S. A., & Beers, T. C. 1991, *ApJ*, 375, 121
- Purcell, C. W., Bullock, J. S., Tollerud, E. J., Rocha, M., & Chakrabarti, S. 2011, *Nature*, 477, 301
- Quinn, P. J., Hernquist, L., & Fullagar, D. P. 1993, *ApJ*, 403, 74
- Randich, S., Gilmore, G., & Gaia-ESO Consortium. 2013, *The Messenger*, 154, 47
- Read, J. I. 2014, *Journal of Physics G Nuclear Physics*, 41, 063101
- Read, J. I., Mayer, L., Brooks, A. M., Governato, F., & Lake, G. 2009, *MNRAS*, 397, 44
- Richstone, D. O. 1982, *ApJ*, 252, 496
- Robin, A. C., Reylé, C., & Crézé, M. 2000, *A&A*, 359, 103
- Robin, A. C., Reylé, C., Fliri, J., Czekaj, M., Robert, C. P., & Martins, A. M. M. 2014, *A&A*, 569, A13

- Rocha-Pinto, H. J., Majewski, S. R., Skrutskie, M. F., & Crane, J. D. 2003, *ApJ*, 594, L115
- Rubin, V. C., & Ford, Jr., W. K. 1970, *ApJ*, 159, 379
- Sackett, P. D. 1997, *ApJ*, 483, 103
- Saha, A. 1985, *ApJ*, 289, 310
- Sakamoto, T., Chiba, M., & Beers, T. C. 2003, *A&A*, 397, 899
- Sales, L. V., Navarro, J. F., Abadi, M. G., & Steinmetz, M. 2007, *MNRAS*, 379, 1475
- Sanders, J. 2012, *MNRAS*, 426, 128
- Sanders, J. L., & Binney, J. 2014, *MNRAS*, 441, 3284
- Sanderson, R. E., Helmi, A., & Hogg, D. W. 2015, *ApJ*, 801, 98
- Schönrich, R., Asplund, M., & Casagrande, L. 2011, *MNRAS*, 415, 3807
- Schwarzschild, M. 1979, *ApJ*, 232, 236
- Searle, L., & Zinn, R. 1978, *ApJ*, 225, 357
- Sellwood, J. A., & Binney, J. J. 2002, *MNRAS*, 336, 785
- Sérsic, J. L. 1963, *Boletin de la Asociacion Argentina de Astronomia La Plata Argentina*, 6, 41
- Sesar, B., Jurić, M., & Ivezić, Ž. 2011, *ApJ*, 731, 4
- Siebert, A., et al. 2008, *MNRAS*, 391, 793
- Skrutskie, M. F., et al. 2006, *AJ*, 131, 1163
- Sluis, A. P. N., & Arnold, R. A. 1998, *MNRAS*, 297, 732
- Smith, M. C., Evans, N. W., & An, J. H. 2009, *ApJ*, 698, 1110
- Smith, M. C., Whiteoak, S. H., & Evans, N. W. 2012, *ApJ*, 746, 181
- Sommer-Larsen, J. 1987, *MNRAS*, 227, 21P
- Springel, V., Frenk, C. S., & White, S. D. M. 2006, *Nature*, 440, 1137
- Springel, V., et al. 2005, *Nature*, 435, 629
- . 2008, *MNRAS*, 391, 1685
- Statler, T. S. 1989, *ApJ*, 344, 217
- Strigari, L. E. 2013, *Phys. Rep.*, 531, 1
- Syer, D., & Tremaine, S. 1996, *MNRAS*, 282, 223
- The DES Collaboration et al. 2015, *ArXiv e-prints*
- van de Ven, G., Falcón-Barroso, J., McDermid, R. M., Cappellari, M., Miller, B. W., & de Zeeuw, P. T. 2010, *ApJ*, 719, 1481
- van de Ven, G., Hunter, C., Verolme, E. K., & de Zeeuw, P. T. 2003, *MNRAS*, 342, 1056
- van den Bosch, R. C. E., van de Ven, G., Verolme, E. K., Cappellari, M., & de Zeeuw, P. T. 2008, *MNRAS*, 385, 647
- Vera-Ciro, C., & Helmi, A. 2013, *ApJ*, 773, L4
- Villalobos, Á., & Helmi, A. 2008, *MNRAS*, 391, 1806

- Wadepuhl, M., & Springel, V. 2011, MNRAS, 410, 1975
- Walsh, S. M., Willman, B., & Jerjen, H. 2009, AJ, 137, 450
- Wang, J., Frenk, C. S., Navarro, J. F., Gao, L., & Sawala, T. 2012, MNRAS, 424, 2715
- Wang, W., Han, J., Cooper, A., Cole, S., Frenk, C., Cai, Y., & Lowing, B. 2015, ArXiv e-prints
- Watkins, L. L., Evans, N. W., & An, J. H. 2010, MNRAS, 406, 264
- Watkins, L. L., Evans, N. W., Belokurov, V., Smith, M. C., Hewett, P. C., Bramich, D. M., & Gilmore, G. F. 2009, MNRAS, 398, 1757
- Watkins, L. L., van de Ven, G., den Brok, M., & van den Bosch, R. C. E. 2013, MNRAS, 436, 2598
- Wegg, C., & Gerhard, O. 2013, MNRAS, 435, 1874
- Wetterer, C. J., & McGraw, J. T. 1996, AJ, 112, 1046
- Wilkinson, M. I., & Evans, N. W. 1999, MNRAS, 310, 645
- Williams, M. E. K., et al. 2013, MNRAS, 436, 101
- Willman, B. 2010, *Advances in Astronomy*, 2010, 21
- Willman, B., et al. 2005, ApJ, 626, L85
- Xue, X.-X., Rix, H.-W., Ma, Z., Morrison, H. L., Bovy, J., & Sesar, B. 2015, In preparation
- Xue, X. X., et al. 2008, ApJ, 684, 1143
- Xue, X.-X., et al. 2014, ApJ, 784, 170
- Yanny, B., Rockosi, C., Newberg, H. J., Knapp, G. R., Adelman-McCarthy, J. K., Alcorn, B., & Allam, S. 2009, AJ, 137, 4377
- York, D. G., et al. 2000, AJ, 120, 1579
- Zehavi, I., et al. 2002, ApJ, 571, 172
- Zhang, L., Rix, H.-W., van de Ven, G., Bovy, J., Liu, C., & Zhao, G. 2013, ApJ, 772, 108
- Zoccali, M., et al. 2003, A&A, 399, 931
- Zwicky, F. 1937, ApJ, 86, 217

LIST OF TABLES

3.1	Velocity dispersion and tilt angle measured in various bins of height z for seven abundance bins	53
3.2	Tilt angle as derived from the total G-type dwarf sample	59
4.1	Best fit parameters of the axisymmetric Jeans models in the determination of the local dark matter density	88
5.1	Overview of the halo models	101
5.2	Fixed parameters in the halo model	102
5.3	Parameters of the halo density profiles concerning the K-giants	102
5.4	Best fit parameters of the various models. The total mass within 100 kpc and the likelihood of the model is also listed, in addition to the parameters of the models.	114

LIST OF FIGURES

1.1	Orbital energy versus angular momentum of simulated particles in the halo as observed by Gaia	3
1.2	Exemplary rotation curve and the Bullet cluster: Two evidence for the existence of dark matter	4
1.3	Anisotropy map and power spectrum of the Cosmic Microwave Background radiation	7
1.4	Sketch of the Milky Way	11
2.1	Distribution of the G-type dwarf sample in the R - z plane	27
2.2	Distribution of K-giants in position and velocity space	33
2.3	Typical gradient of the cylindrical and the prolate spheroidal anisotropy	38
3.1	MCMC posterior distribution and evolution of the kinematical bi-variate Gaussian model	44
3.2	Abundance map of the G-type dwarf sample and results of the vertical Jeans models concerning the density and vertical velocity dispersion profiles	49
3.3	Radial and vertical velocity dispersions as well as the tilt angle for the abundance selected sub-samples as a function of height above the Galactic mid-plane	54
3.4	Measurements of the tilt of the velocity ellipsoid as function of height at the solar radius	55
3.5	Mean azimuthal velocities and comparison of the bi-variate Gaussian velocity model to a multi-variate Gaussian model of rank 3	57

3.6	Testing the assumption of zero radial and vertical mean motion on the results of the velocity ellipsoid	58
3.7	Halo contamination fraction and tilt angle for two different contamination models	61
3.8	Testing the contribution of the metal-weak thick disk on the vertical velocity dispersion of our G-type dwarf sample	62
4.1	Radial and vertical extend of the 7 abundance sub-samples	69
4.3	Density profiles of the abundance selected sub-samples as function of height at $R = R_{\odot}$	77
4.4	Vertical velocity dispersion of the α -oldest abundance bin for two models, in which the tracer densities are either fitted separately or simultaneously with the kinematics	78
4.5	The resulting rotation curve from the axisymmetric Jeans model with and without prior	79
4.6	Radial and vertical velocity dispersion as predicted by the axisymmetric Jeans model with analytic potential	80
4.7	MCMC posterior distribution of the axisymmetric Jeans model in the solar neighbourhood	82
4.8	Same as Figure 4.6 with velocity dispersions derived from the exponential-NFW potential pair	83
4.9	Predicted tilt of the axisymmetric Jeans model using the analytic potential . . .	84
5.1	Position and velocity of the Sagittarius stream coloured with the its velocity dispersion deduced from the model based on the velocity of the stream	94
5.2	MCMC posterior distribution of the Sagittarius model	96
5.3	Position and velocity of the Sagittarius stream coloured with the its velocity dispersion deduced from the model based on the position of the stream	97
5.4	Comparison of stream candidates from the model with William Janesh's identified candidates in position and velocity space	99
5.5	Line-of-sight velocity distributions of the K-giants predicted by various models and compared to the measured distributions	106
5.6	Line-of-sight velocity dispersion of the K-giants as measured with different models	107
5.7	Mean line-of-sight velocity of sub-samples of the K-giants with different fractions of stars belonging to substructures	107

5.8	Estimates and radial profile of the halo mass from models that contain different fractions of substructures or account for them in a different way	109
5.9	MCMC posterior distribution and evolution of the axisymmetric Jeans model applied to halo K-giants	110
5.10	Estimates and radial profile of the halo mass for different tracer densities	111
5.11	Total mass profile of the galaxy and comparison of the measured line-of-sight velocity dispersion with the prediction of the fiducial model	112
5.12	Comparison of the different substructure and density models of the halo with respect to their mass profile and predicted line-of-sight velocity dispersion . . .	113